RELATING GYROKINETIC ELECTRON TURBULENCE TO PLASMA CONFINEMENT IN THE NATIONAL SPHERICAL TORUS EXPERIMENT

JAYSON DEAN LUCIUS PETERSON

A DISSERTATION

PRESENTED TO THE FACULTY

OF PRINCETON UNIVERSITY

IN CANDIDACY FOR THE DEGREE

OF DOCTOR OF PHILOSOPHY

RECOMMENDED FOR ACCEPTANCE

BY THE DEPARTMENT OF

ASTROPHYSICAL SCIENCES

PROGRAM IN PLASMA PHYSICS

ADVISERS: G. W. HAMMETT AND D. R. MIKKELSEN

NOVEMBER 2011

Abstract

Unraveling the relationship between plasma turbulence and transport is an important step in the development of magnetic fusion energy. In a magnetic fusion experiment, naturally occurring gradients in temperature and density profiles drive plasma turbulence. This turbulence can effectively transport heat and particles throughout the machine, thereby modifying the plasma's profiles. The result is a feedback system, with turbulence driving transport and transport altering the turbulent drive. Understanding this system is as important to development of fusion energy as it is challenging.

The relationship between gyrokinetic electron temperature gradient (ETG) driven turbulence and thermal confinement is particularly poorly understood. Empirical evidence suggests that ETG turbulence can not only exist in the National Spherical Torus Experiment (NSTX) but that it can also sometimes drive enough thermal transport to limit machine performance. Electron-scale (high-k) density fluctuations increase when the ETG mode is predicted to be active. Reversing the device's magnetic shear not only suppresses these fluctuations, but also triggers high electron confinement modes in NSTX known as electron internal transport barriers (e-ITBs). Controlling ETG turbulence with magnetic shear significantly enhances plasma confinement.

This dissertation supplements these experimental observations with numerical simulations. Applying the nonlinear gyrokinetic code GYRO to NSTX confirms the possibility of strong ETG-driven turbulent transport within the experiment. The associated thermal flux can indeed be high, accounting for at least one half of the inferred experimental level; however, the link between high-k fluctuations and ETG turbulence is less firm. Additionally, the first nonlinear simulations of an NSTX e-ITB confirm that magnetic shear suppresses ETG turbulence and establishes transport barriers. While ETG turbulence can be strong in NSTX, its detrimental effects can be controlled with magnetic shear.

How turbulence governs the performance of fusion experiments cannot be determined without an understanding of plasma transport. To that end, this work develops new algorithms for solving the steady-state plasma transport problem, integrating them into and testing them with the `TGYRO` code. An application of the new algorithms to a proposed ETG experiment on NSTX shows that adding impurities to radio-frequency heated plasmas can reduce turbulent transport and improve plasma performance.

Acknowledgements

The higher your structure is to be, the deeper must be its foundation.

Saint Augustine of Hippo

I've been helped along this journey by many people. Though Saint Augustine writes of piercing the firmament, even the tiniest blades of grass need roots to grow. I would like to take this opportunity to thank at least some of this work's roots.

First of all, thank you to my advisers, Prof. Greg Hammett and Dr. David Mikkelsen. Your guidance as mentors, teachers, colleagues and friends has made this work possible. Thank you for letting me explore new ideas, telling me when those ideas are crazy and directing me towards more realistic ones, when necessary. Thank you for allowing me to find my own mistakes, even when they're obvious to you. Thank you for teaching me and for teaching me to teach myself.

I would also like to thank the many collaborators who have worked with me on this work, especially those of the Princeton Plasma Physics Laboratory and the NSTX research staff. In particular, Dr. Stan Kaye, on top of always finding my results interesting and worth exploring, offered me formal feedback on this thesis as an official reader. Dr. Howard Yuh kept me grounded in experimental reality while simultaneously letting me scribble wholly unrealistic ideas all over his white board. The prettiest pictures in this thesis are likely due to the help of Dr. Walter Guttenfelder. I'm also indebted to Dr. Ben LeBlanc for his TRANSP analysis of the NSTX shots I examined, to Dr. Ron Bell for his discussions about plasma impurities, to Drs. Dave Smith, Yang Ren and Francesca Poli for their explanations of the high-k scattering system and to the late Mr. Doug McCune for his assistance in creating `transp2gyro`, his universal willingness to answer my TRANSP-related questions and his general kindness. He touched many lives and careers, even one as nascent as mine, and will be truly missed.

I couldn't stand, and for believing in me when I wouldn't believe in myself. Thank you for being my biggest fan, my best friend and the love of my life. I really could not have done this without you. Quite simply, if you weren't here, I wouldn't be either. I thank you not from the bottom of my heart, but from its entirety.

To Meg, my most important discovery.

Contents

List of Tables

List of Figures

Chapter 1

Introduction:

The Necessity of Nuclear Fusion

1.1 Meltdown

On March 11, 2011 at 2:46:23 PM local time, 231 miles northeast of Tokyo and 19.9 miles below the floor of the Pacific Ocean, the fault line between the North American and Pacific tectonic plates slipped. The resulting magnitude 9.0 Tohoku earthquake shook the ground as far away as Taipai for six minutes [1]. It also triggered a massive tsunami that struck coastal Japan with waves up to 124 feet high [2].

The combined damage from the earthquake and tsunami was both enormous and tragic. Despite strict Japanese anti-earthquake building codes, 125,000 structures were destroyed. Over 20,000 people were killed or went missing [3]. On March 21, 2011, the World Bank estimated the total economic damage could approach 235 billion dollars [4], but the total cost of this tragedy may not be fully known for years.

Soon after the earthquake, international attention quickly focused on the town of Okuma, in the Fukushima Prefecture, on the eastern coast of the island of Honshu. This town is home to the

Fukushima Daiichi Nuclear Power Plant, a fission power complex of 6 nuclear reactors. Operated by the Tokyo Electric Power Company, these light water reactors had a combined electrical output of 4.7 gigawatts, making the Fukushima Daiichi complex one of the largest nuclear power stations in the world [5].

At the time of the earthquake, reactors 1-3 were operational, 4 had been de-fueled, while 5 and 6 were shutdown for planned maintenance. As soon as the ground began to shake, the three working reactors automatically shut down, and emergency diesel generators ran water pumps to keep the reactors cool. In all, the plant's emergency safety features worked as planned [5].

However, 15 minutes after the earthquake, the tsunami overtook the plant's protective seawall, flooded the nuclear complex, disabled the emergency generators, and severed the plant's electrical connection to the power grid. The plant's emergency batteries lasted eight hours, until the plant lost power entirely. Without electricity to run the cooling systems, the reactors began to overheat, despite being offline, because of the natural decay of the fission byproducts still in the reactors [5].

The lack of electricity at the plant created a dangerous situation that quickly deteriorated. With neither water pumps nor ventilation fans the water in the reactors began to boil. As the water levels fell, the melting casings around the exposed fuel rods reacted with the water to form hydrogen that began to leak out of the reactors and into their containment buildings. On March 12, hydrogen in the reactor 1 building exploded. The same happened to reactor 3 the following day and to reactor 4 on March 15. Reactor 2 also exploded on March 15, due likely to a build-up of hydrogen within the containment vessel itself. Though power was eventually restored to part of the plant, the damage to reactors 1-4 was too great to allow them to restart [5], leaving decommissioning the only option, a process that could take decades [6].

With a level 7 ranking on the International Nuclear Event Scale, the Fukushima incident sits alongside the Chernobyl meltdown as one of the two worst nuclear disasters in history [5].

The repercussions of the events in Japan could last years. However, the partial meltdown at the Fukushima Daiichi plant has already done significant environmental, economic, psychological and political damage, not only to the Japanese people, but to communities around the globe.

Firstly, the incident at Fukushima Daiichi harmed the environment, most notably within Japan. A combination of deliberate events, such as the venting of gas and the discharging of coolant water, and accidental events, such as explosions, released radioactive material from the plant and forced the Japanese government to evacuate the surrounding countryside. Although negligible radiation escaped Japan, elevated levels of radioactive isotopes within the country led to restrictions on the consumption of certain agricultural products, such as spinach and milk, and drinking water [5]. While the disaster at the Fukushima Daiichi plant did not immediately impact the environment outside of Japan, and while the Japanese drinking water and agricultural contaminations were short-lived, the cleanup of the radioactive debris, coolant water and radioactive waste at the site itself could take decades [6].

Although the environmental effects of the Fukushima Daiichi disaster were largely contained to Japan, the psychological reverberations quickly spread throughout the globe. Protests against nuclear power emerged worldwide, from Germany, where in March 200,000 demonstrators helped elevate the Greens party to a majority in the industrial state of Baden-Wuerttemberg for the first time [7], to India, where in April one man was shot by police during violent protests against a new nuclear power plant [8]. The protests in India were fueled not only by a general opposition to nuclear power, but also by a renewed fear that seismic activity could cause an accident similar to that in Japan, even though India is far less seismically at risk than Japan.

The fear expressed in India also reverberated in the United States, where, in the wake of the Fukushima tsunami, consumers began buying large supplies of iodine tablets to counter-act the effects of radiation exposure, even as local health officials emphasized the negligible risk of radiation several thousand miles outside of the Japanese evacuation zone [9]. The run on potassium iodide pills was so severe in the United States that some states began worrying about shortages [9]. The

Building More Nuclear Power Plants
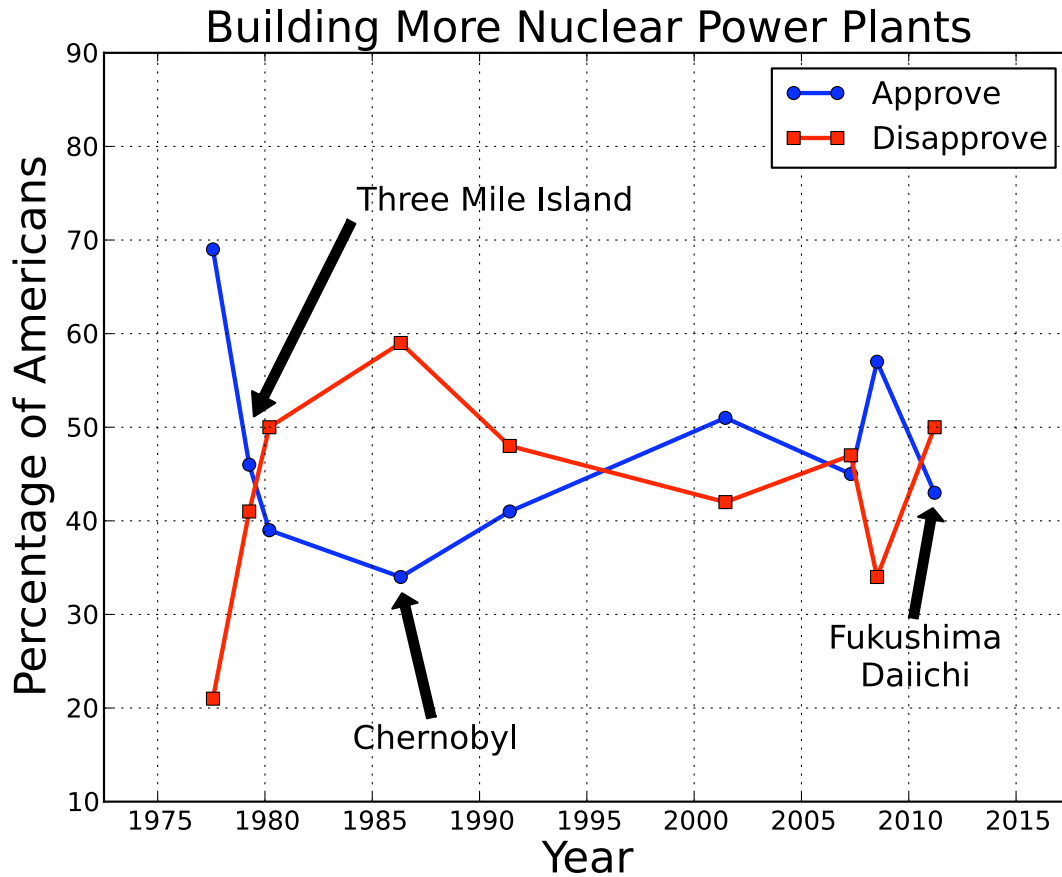
Figure 1.1: History of United States public opinion of nuclear power. Polling errors are ±3%. Data: CBS News Poll [12].

perceived risk of radiation exposure from the Japanese plant was very high in the United States, irrespective of factual evidence to the contrary.

While the fears of radiation exposure from the accident itself eventually died down, the renewed fears of nuclear power in general are likely to last much longer. Fukushima Daiichi immediately jeopardized the future of nuclear fission as an energy source. On March 15, amid massive demonstrations against nuclear power, Germany took the oldest seven of its 17 nuclear power plants temporarily offline for safety checks [10]. And on May 31, the country announced plans to eliminate its dependence on nuclear power entirely by 2022 [11].

In the United States, like elsewhere, public opinion of nuclear power dropped after the Fukushima Daiichi incident. This can be seen in Fig. 1.1, a timeline composite of CBS News polling data [12] asking Americans if they approve or disapprove of building new nuclear power plants. Polling errors are $\pm 3\%$. (As a caveat, these data ask if people approve of building plants in general, not plants in their community, against which there is significantly higher resistance [12].) In the mid 1970's, nearly 70% of those asked approved of the construction of new plants. However, this number plummeted to below 50% with the core meltdown at the Three Mile Island power plant near Harrisburg, PA in March, 1979. Approval for new nuclear power plants reached its low point with the Chernobyl meltdown in April, 1986, with under 35% in favor of expanding nuclear power. Yet, public attitudes began to change over time. As the memories of those accidents faded from the public psyche, nuclear power seemed poised to enter a renaissance. Prior to the earthquake and tsunami in Japan, nearly 60% of Americans were in favor of building new nuclear power plants. This is significant because for the first time in three decades a majority of citizens approved of an expansion of nuclear power. Yet after the events at Fukushima Daiichi, this changed, with approval dropping by 14 percentage points. This polling data is telling, as the expansion of nuclear power in the United States is closely tied to public opinion. Construction of new power stations came to halt with Three Mile Island; the US has not broken ground on a new nuclear reactor since 1974 [13]. Considering the time it took for opinion to recover from the events of Three Mile Island and Chernobyl, the political future of nuclear power in the United States is uncertain.

Additionally, the economic fallout of this environmental tragedy is both extensive and extensively complicated. Within Japan alone, the total cleanup from the earthquake and tsunami could cost $235 billion [4], but the global economic damage could be much more. Germany's temporary shutdown of its oldest reactors not only cost the German utility company E.ON AG around $370 million in profits [14], but also threatened to raise overall energy prices within Germany, since the country's energy supply dropped overnight. To combat rising prices and without a suitable substi-

tute for the missing nuclear power, Germany had to import electricity from neighboring countries. Ironically enough, this included nuclear power from France and the Czech Republic. Alternatively, Germany proposed to produce more electricity from renewable sources, such as wind power. But unfortunately, while German citizens strongly opposed nuclear energy, they also strongly opposed erecting the high-voltage cables needed to transport the renewable energy across the country from where it's produced in the north to where it's needed in the south [15]. How the country will replace the electricity lost by eliminating nuclear power entirely by 2022 remains to be seen. Germany's experience shows not only the complicated economic consequences of the events in Japan, but also of energy policy in general. A country cannot merely eliminate an energy supply overnight without finding a suitable replacement. And there is no guarantee that replacement will be both cheap and politically tenable.

While it may take years to realize the full consequences of the tragedy at Fukushima Daiichi, one lesson is clear: meeting global demands for energy consumption will not be easy. Finding an energy source that is technologically possible, environmentally friendly, politically popular, socially acceptable and economically feasible is no small feat. However, it is a necessary endeavor, albeit a difficult one, simply for the reason that world needs energy. It needs a lot of it, and it needs it fast.

1.2   Energy Scarcity

Simply speaking, a high quality of life stems from a high use of energy. Industrial societies use more energy than agrarian societies. From the simple heating of a home to the complex design of novel drugs, modern life revolves around the consumption of energy. In 2007 total global energy consumption rate averaged 16.5 terrawatts [16]. However, that consumption of energy is not uniform, disproportionally coming not only from non-renewable energy sources, but also from a relatively few number of countries, namely the industrialized world. As developing countries

seek to improve their quality of life up to that enjoyed in developed countries, they will use more energy. That energy must come from somewhere. Finding a sustainable energy source that can meet growing demands will be a grand challenge of the 21st century.
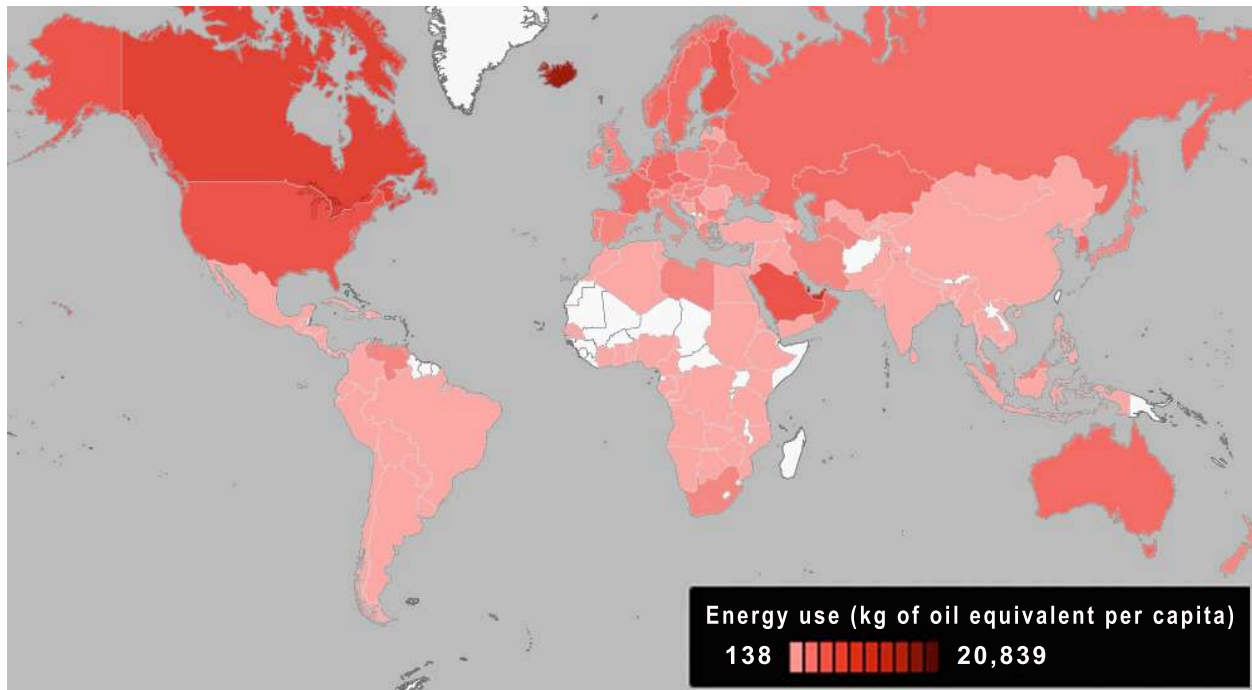
Figure 1.2: Per capita energy consumption by country, in equivalent kilograms of oil [17].

Industrialized citizens use much more energy than their counterparts in the developing world. Figure 1.2 shows a map of per capita energy use in 2007 in units of equivalent kilograms of oil [17]. The uneven per capita distribution of energy usage is clear. Industrialized countries use significantly more energy per person than do developing countries: those in North America, Europe and Australia consume much more energy per person than do those in Latin America, Africa and Asia.

To quantify this further, Table 1.1 lists average energy consumptions and the ratio of this use to the global average for select countries. This includes all energy use, from electricity generation to transportation. The citizens of the United States, in 2007, consumed on average 7758.9 kilograms of oil equivalent (koe) energy. To put this in perspective, (1 koe)=(41.9 MJ), so using 1 koe in one

Table 1.1: Average per capita energy consumption during 2007 [17].

	per capita energy usage (kg oil equivalent)	ratio to global average
US	7758.9	4.2
Russia	4730.0	2.6
OECD Members[a]	4600.5	2.5
EU	3555.6	2.0
World	1819.2	1.0
China	1484.0	0.8
India	528.9	0.3

[a] Australia, Austria, Belguim, Canada, Chile, Czech Republic, Denmark, Estonia, Finland, France, Germany, Greece, Hungary, Iceland, Ireland, Israel, Italy, Japan, Korea, Luxembourg, Mexico, Netherlands, New Zealand, Norway, Poland, Portugal, Slovak Republic, Slovenia, Spain, Sweden, Switzerland, Turkey, UK, US

year averages to an energy use rate of about 1.33 watts. A U.S. citizen, who used 7758.9 koe in 2007, consumed energy at a rate roughly equal to 10 kilowatts. This is akin to having 100 lightbulbs constantly burning for each person. It is also 4.2 times the world average. Like the U.S., developed countries tend to consume more energy than the world average; OECD Members [1] and Russia use less energy per person than does the United States, but still consume energy at a rate that is still roughly 2.5 times the world average. Large developing countries, such as China and India, help to bring down this average. For every 100 lightbulbs that an American burns, a Chinese citizen burns 19. An Indian burns 7. This is a large deficit, considering the large populations of these countries. Should these populations want a standard of living enjoyed by developed countries, they will most likely consume much more energy.

Just how much energy is this? Within the next 25 years, global energy use is projected to rise by 50 percent, primarily as China continues its push for industrialization [16]. Other countries will likely follow suit. As a thought experiment, suppose that world energy consumption rises to that of the OECD Member states. Although still less than 60 percent of the U.S. rate, this would constitute an increase of 250 percent from present-day use. Instead of 16.5 terawatts, the world

[1]Australia, Austria, Belguim, Canada, Chile, Czech Republic, Denmark, Estonia, Finland, France, Germany, Greece, Hungary, Iceland, Ireland, Israel, Italy, Japan, Korea, Luxembourg, Mexico, Netherlands, New Zealand, Norway, Poland, Portugal, Slovak Republic, Slovenia, Spain, Sweden, Switzerland, Turkey, UK, US

would then use energy at a rate of 41.3 terawatts. This high-use scenario would, obviously, take time, but considering the pace of current projected increases, may not be outlandish at the end of the century.

World Energy Use by Fuel Type
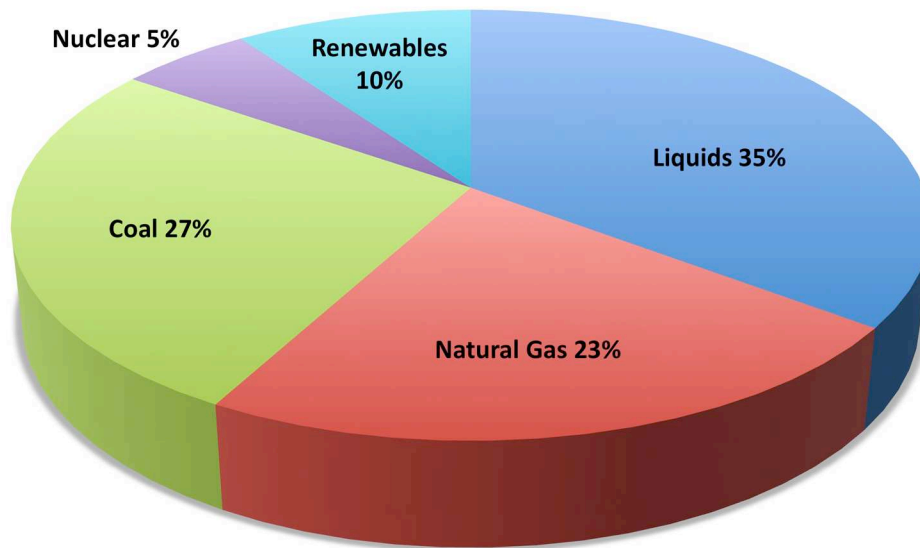
Data: U. S. Energy Information Administration, "International Energy Outlook 2010."

Figure 1.3: Global energy consumption by fuel source for the year 2007. Total consumption rate for 2007 was 16.5 terrawatts [16].

From where will all of this extra energy come? Currently, the world generates the vast majority of its energy from non-renewable fossil fuel sources, such as liquid fuels (like oil) and coal. The breakdown of current energy production can be seen in Fig. 1.3. Nuclear fission, such as that generated at Fukushima Daiichi, constitutes only 5% of total global energy use. All renewable resources, like hydroelectric, wind and solar power, make up another 10%. The other 85% comes from fossil fuels. Beyond the environmental impact of fossil fuels, these resources are, above all, finite. Table 1.2 lists the energy content of known fuel reserves alongside their usage rates and the

Table 1.2: Energy sources, consumption rates and known reserves [16]. Current total global consumption rate is 16.5 terawatts. High use scenario represents global per capita consumption at industrialized levels (41.3 terawatts). Oil contains both known supply and maximum estimates of undiscovered global reserves. Nuclear fuel is based on uranium using current generation once-through technology and fast breeder technology.

Fuel Source		Consumption (TW)		Supply (ZJ)	Supply (Years)	
		Current	High Use		Current	High Use
	Coal	4.5	11.2	19.8	140	56
Oil	Known Supply	5.8	14.5	8.1	44.3	17.7
	Max Estimate			57	312.5	125
	Natural Gas	3.8	9.5	8.1	67.5	27
Nuclear	Once Through	0.8	2	17	672.5	269
	Fast Breeders			2500	99,028	39,611
	Renewables	1.6	4.1	—	—	—

global supply in years. In addition to current consumption rates, Table 1.2 also shows estimates for the high-use scenario presented above, assuming the distribution of energy sources remains constant, i.e. 85% of that energy will still come from fossil fuels.

Despite the uncertainties in this estimate (such as the potential increase in renewable energy sources), these data in Table 1.2 are telling. Should the world average energy usage increase to industrialized levels, the global supply of natural gas, which supplies 23% of the world's energy, will be gone in under 30 years. Even at current consumption rates, it will not last the century. Coal will follow suit. Oil may last a little longer, or it may not, depending on whether additional sources are found in accessible locations, if at all. The salient point is that fossil fuels reserves, which supply over 85% of the world's energy, are unlikely to last much into the 22nd century.

To make up for this impending shortage, there exist a few options. One is an increased dependence on renewable resources, such as wind and solar power, although these will likely require a restructuring of energy grids to allow for their transient, distributed nature. Recent objections [15] to Germany's plans to run high-power cables across the countryside to deliver wind energy from

the North Sea to the factories in its south illustrate potential obstacles facing large-scale adoption of wind and solar power.

Another option could be an increased reliance on nuclear power. After all, Table 1.2 shows that uranium could last hundreds of years at current consumption rates. If new plants were built to take advantage of fast-breeding technology, which can use the more abundant uranium-238 or thorium instead of relying on uranium-235, the fuel could seeming last millennia.

Assume that new fission plants could be built to replace the lost power from vanishing fossil fuels. Our high-use scenario implies that after 30 years, natural gas will be depleted. To make up for the missing 9.5 TW of power, one would need to build 9,500 gigawatt reactors within the next 30 years, at a rate of one reactor every 28 hours. Then the pace would have to pick up to anticipate the exhaustion of coal: to displace 11.2 TW in 20 years would mean a new reactor every 16 hours. Assuming oil lasts that long, the last 75 years of this energy transformation would be relatively relaxed: one would only need a new reactor every 45 hours. This is in addition to expanding nuclear power to maintain a 5% share of the higher-use energy market, which would require an additional new reactor every 3 weeks.

Obviously this is a little extreme, as it assumes a higher-than-current rate of energy consumption and that fission will bear the brunt of this. If in the next 30 years renewable energy resources can expand to 20% of the total market, that would replace 8.3 of the 9.5 TW lost from the depletion of natural gas. This alleviates the demands on the construction of nuclear plants, so one would only need 1,200 new reactors within in the next 30 years, or one every 9 days. (The pace of construction would then have to pick back up to prepare for the shortage of coal and oil.) Again, this assumes a growth scenario. If instead energy use is held constant, fuel supplies last 2.5 times longer, so to replace missing fossil fuels, one would only need a brand new fission power plant every 23 days for the next 30 years. Even still, this is an unprecedented expansion of nuclear power. In a time of heightened opposition to nuclear power, amid fears of safety and proliferation, this would be no small feat.

Human societies depend upon the consumption of energy. Some societies consume more than others. As developing countries play catch-up to the industrialized world, the demand for energy is going to soar. With this increased demand must come an energy revolution. The single major source of energy use in the world has a limited lifetime. Beyond the potential environmental effects of their increased consumption, fossil fuels will disappear in the next few centuries. New energy sources must emerge to displace these depleted resources. Because of the scope of the problem, the development and deployment of new energy sources cannot wait until fossil fuels vanish. Renewable resources and nuclear fission could potentially fill the gap left by fossil fuels, but expanding these on a sufficiently large scale will likely be met with economic, environmental and political opposition. In any case, humanity needs to find a solution to this impending crisis. We need an energy source that is abundant, cheap, deployable on mass-scales, backed by the public and environmentally friendly. Find such a source may not be easy, but it is absolutely necessary.

1.3   Nuclear Fusion

To find a potentially game-changing energy source, one need only to look to the sun. By providing heat and light, it is the source of all energy on earth. No creature, no plant, no civilization, from the Aztec to the Zulu, could exist without this awesome solar power plant. Harnessing the power of the sun is tapping into the universe's most impressive power source: nuclear fusion (see Fig. 1.4).

The core of the sun is an intense environment. It is essentially a gigantic ball of hydrogen gas with densities ten times that of lead and temperatures of over ten million degrees kelvin. Under these conditions a phenomenal process occurs: nuclear fusion. Two hydrogen nucleii, that is single protons, normally repel each other, both being positively charged. However, if the two protons can get close enough together, they can fuse. This fusion reaction produces an isotope of hydrogen,

Figure 1.4: Schematic of a fusion reactor: the Aztec sun calendar, ca. 1480. [18].

deuterium, plus a positron and an electron neutrino:

$$H_1^1 + H_1^1 \longrightarrow H_1^2 + e^+ + \nu_e. \tag{1.1}$$

Once deuterium is formed, it can fuse together with another proton to form a new element: helium-3, two of which can fuse together into helium-4. One possible chain reaction is:

$$H_1^2 + H_1^1 \longrightarrow He_2^3 + \gamma, \tag{1.2}$$

$$He_2^3 + He_2^3 \longrightarrow He_2^4 + 2\,H_1^1. \tag{1.3}$$
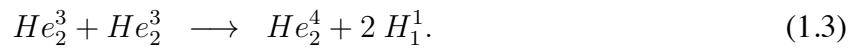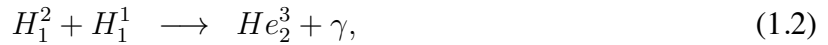
This whole process, known as the proton-proton chain, powers the sun. To see how, consider the first step in the process, Eq. 1.1, which converts hydrogen into deuterium. Deuterium is made up of a proton and a neutron. A proton has a mass of 1.0073 atomic mass units (u), while a neutron has a mass of 1.0087 u. The sum of these is 2.0160 u. Yet, deuterium has a mass of only 2.0141 u. The mass of deuterium is less than the sum of the mass of its components. It seems as if mass has disappeared in this reaction (the positron, with a mass of 5.5×10^{-4} u, cannot make up the difference). However, while mass can be neither created nor destroyed, it can be changed into energy. A mass, m has an energy content E, given by the relation:

$$E = mc^2. \tag{1.4}$$

The fundamental constant relating mass and energy is the speed of light, c. Measuring roughly 3×10^8 m/s, c is a very large number. c^2 is astronomical. It implies that a small amount of mass has a very large equivalent amount of energy. One gram, roughly the mass of a paper clip, has the energy content of 9×10^{13} Joules. At 22 kilotons TNT-equivalent, this is more than the amount of energy released by the atomic bombs of the Second World War. Equation 1.4 says that the small fraction of mass lost in the fusion of hydrogen into deuterium gets converted into energy.

Each step in the reaction, just like the first, releases energy. In whole, the proton-proton chain is a nuclear reaction that takes as fuel four hydrogen nucleii and produces a helium nucleus. Since the mass of the helium is less than that of the four hydrogens, the missing mass gets converted into energy:

$$4 \, H_1^1 \longrightarrow He_2^4 + \text{energy}. \tag{1.5}$$

The nuclear fusion of light atoms into heavier atoms is the energy source of every star. The sun is a furnace that converts hydrogen to helium, releasing energy in the process.
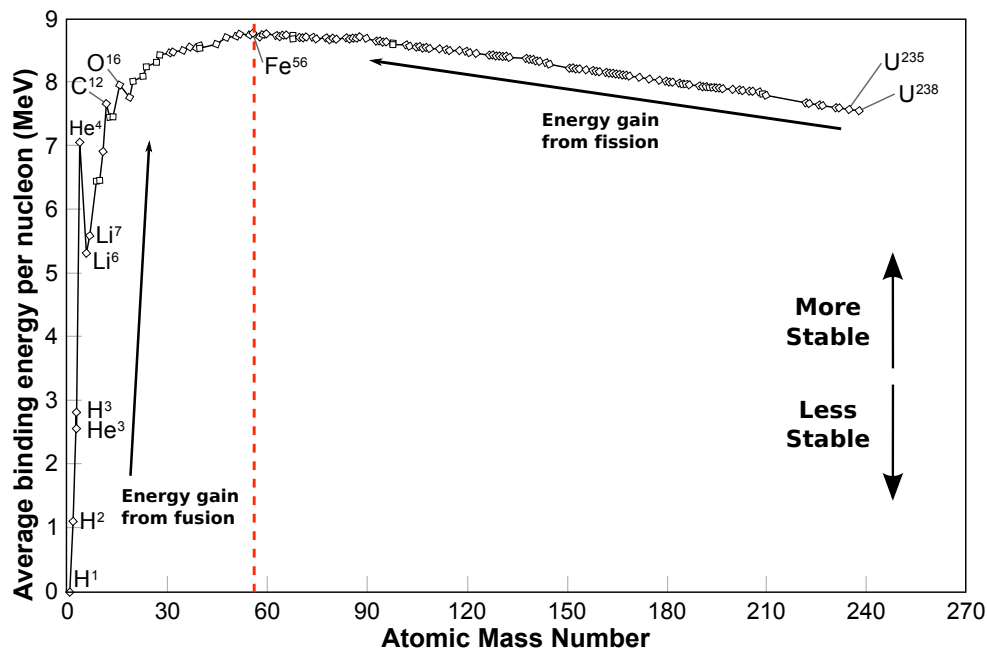
Figure 1.5: Average nuclear binding energy per nucleon for select isotopes. Isotopes with a higher average binding energy are more stable, with iron being the most stable element. Isotopes lighter than iron can release energy from fusion; heavier isotopes, like uranium, release energy from fission.

The amount of energy released from nuclear fusion depends upon the reaction. Every element, like helium, is actually lighter than its components. That difference in mass represents the binding energy of the nucleus. To break apart a nucleus (like helium) into its building blocks (like protons and neutrons) requires energy. The more stable the nucleus, the more energy it takes to break it

apart. Fig. 1.5 shows the average binding energy per nucleon for a number of elemental isotopes. The curve rises sharply for light elements, reaches a maximum at iron, and slowly falls of as the mass of the nucleus gets larger. Iron-56 is the most tightly bound, most stable, element. Moving from a lower binding energy to a higher binding energy is a favorable reaction and will release energy (since the product is more stable). Nuclear fusion, combining lighter elements into heavier elements, is represented by moving to the right in Fig. 1.5. Nuclear fission, represented by moving to the left, takes heavier elements (like uranium) and lets them decay to smaller, more stable ones. So, elements lighter than iron will tend to fuse, and elements heavier than iron will tend to fissile.

The energy binding curve in Fig. 1.5 tells why fusion is such a powerful energy source. Nuclear processes that move to higher points on the binding curve transform elements into more stable ones. Moving to a more stable state releases energy, as a ball nudged from the top of a hill will gain speed as it begins to roll. The amount of energy released per nucleon is the difference in the two points on the graph. For instance, fusing deuterium H^2 and tritium H^3 into helium-4 He^4 releases $7 \times 4(He^4) - 1 \times 2(H^2) - 2.8 \times 3(H^3) = 17.6$ MeV of energy. Fusing light elements into heavier ones can release a large amount of energy per nucleon.

The sun is a working fusion reactor that converts hydrogen into helium. In so doing, it releases an enormous amount of energy, sustaining life on Earth. If it were possible to control nuclear fusion in a laboratory, humanity could tap into that same awesome power source.

1.3.1   What is Fusion Power?

Nuclear fusion is the process that powers the universe. Every star, including our sun, is a power plant that fuses light elements into heavier ones, a process that releases an enormous amount of energy. Bringing this star power to Earth is the goal of fusion research. What, then, would a terrestrial fusion power plant look like?
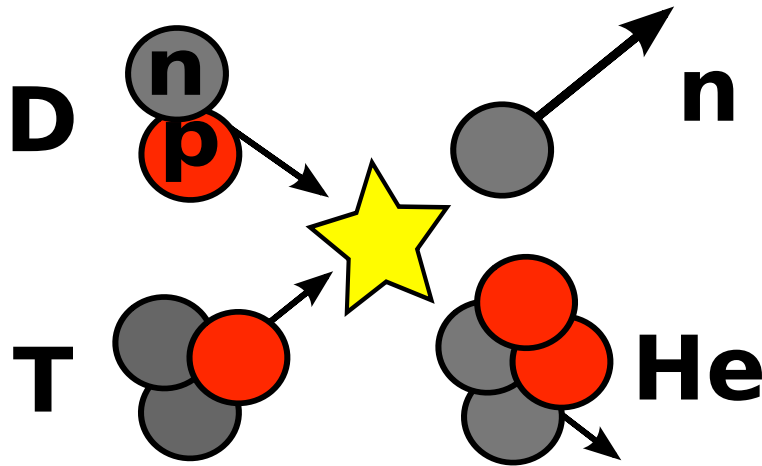
Figure 1.6: The Deuterium-Tritium Fusion Reaction. When the hydrogen isotopes deuterium and tritium overcome their repulsive forces, they can fuse into helium and a high energy neutron: $H_1^2 + H_1^3 \longrightarrow He_2^4 \, (3.5 \; MeV) + n_0^1 \, (14.1 \; MeV)$

First of all, the power plant would have a reactor core of plasma. Plasma is a gas that is hot enough to ionize. The core of the sun has a temperature of several million degrees. At these temperatures, electrons have enough energy to move freely, unbounded to a nucleus. The fusion plasma is a high energy soup of electrons and ions. The ions in the first fusion reactor would most likely be isotopes of hydrogen: deuterium ($D = H_1^2$) and tritium ($T = H_1^3$). The goal would be the D-T fusion reaction (Fig. 1.6):

$$D + T \longrightarrow He^4 \; (3.5 \; MeV) + n \; (14.1 \; MeV) \, . \tag{1.6}$$
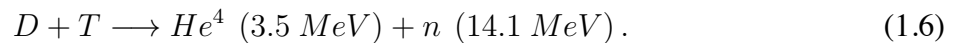
The reaction produces helium and a high-energy neutron from deuterium and tritium. Generally speaking, for fusion to occur at sufficient quantities, hot plasma needs to be held together for a long time. Since like-charged particles repel, the fusion fuel must have enough energy to overcome the repulsive force. As such, the fusion plasma should be at a high temperature. Similarly, the closer the fuel atoms are to one another, the more likely they are to fuse. Therefore, the plasma should be dense. Finally, the fuel must be held in these conditions for a long enough time to allow them

to interact, making the final ingredient in a fusion reaction time. One would want to maximize, therefore, the temperature, density and confinement time of plasma. This is the idea behind the fusion triple product: $n_e T \tau_E$. n_e is the plasma density, T its mean temperature and τ_E its energy confinement time, defined as the energy content of the plasma, W divided by the rate of energy loss, P_{loss}:

$$\tau_E = \frac{W}{P_{loss}} \tag{1.7}$$

The level at which a fusion plasma's self heating exceeds its losses is known as the Lawson Criterion. Although J. D. Lawson's initial calculation only involved the product of n_e and τ_E [19], placing limits on plasma pressure introduces T. For a D-T plasma, self heating outpaces energy losses around

$$n_e T \tau_E \geq 10^{21} keV s/m^3. \tag{1.8}$$

While a commercial fusion reactor need not necessarily reach this level to operate, as this assumes all heating in the plasma comes from fusion reactions and discounts, for instance, the idea of a driven system whose goal is to merely gain more energy than put in, the triple product is still a good figure of merit for a fusion plasma. The higher it is, the more fusion power one can get out of the system.

The $D - T$ reaction, while not the source of the sun's energy, is attractive in a terrestrial fusion plant because its reaction rate is very high and peaks at lower temperatures than other reactions. This is illustrated in Fig. 1.7, which shows the reaction rate parameter $\langle \sigma v \rangle$ as a function of temperature for a variety of fusion reactions. (The total number of reactions per second for two fusing particle species a and b is $n_a n_b \langle \sigma v \rangle_{ab}$.) The $D - T$ reaction rate peaks at just shy of a billion degrees kelvin, however the Lawson criterion is most easily achieved when $\langle \sigma v \rangle / T^2$ is minimized. This occurs for $D - T$ at roughly 10 keV. This means that a $D - T$ fusion plasma would actually be hotter than the core of the sun. The $D - T$ reaction, while primary, would not be the only reaction occurring in a $D - T$ plasma. Deuterium and tritium each have self interactions.
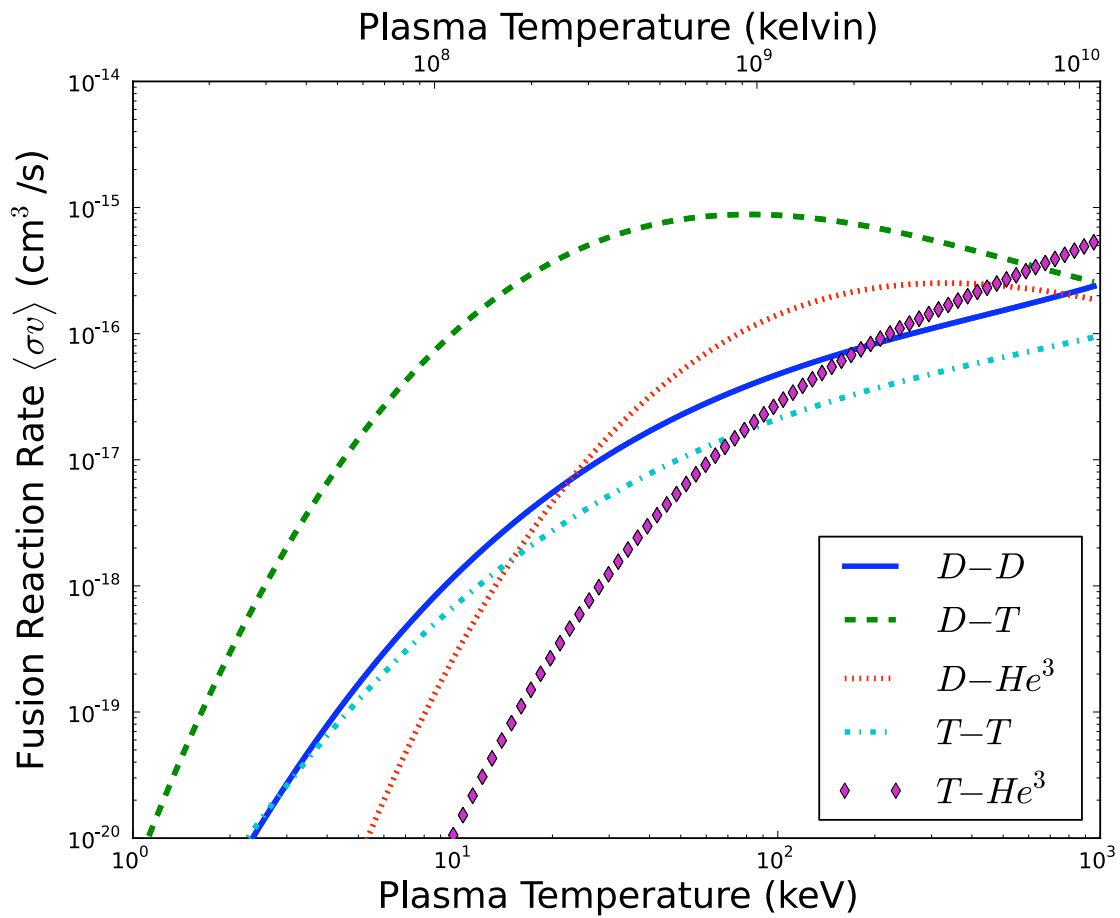
Figure 1.7: Reaction rates for a variety of fusion reactions as a function of bulk plasma temperature [20].

Table 1.3: Some energy-relevent fusion reactions, with their byproducts and released energy. Branching ratios are for energies near cross-section peaks. Isotopes of hydrogen are labeled as: $H^1 = p$; $H^2 = D$; $H^3 = T$ [20].

			Neutronic Reactions in a $D - T$ plasma	
$D + D$	$\longrightarrow$	[50%]	T $(1.01\ MeV) + p$ $(3.02\ MeV)$	
	$\longrightarrow$	[50%]	He^3 $(0.82\ MeV) + n$ $(2.45\ MeV)$	
$D + T$	$\longrightarrow$		He^4 $(3.5\ MeV) + n$ $(14.1\ MeV)$	
$T + T$	$\longrightarrow$		$He^4 + 2\,n + (11.3\ MeV)$	
			Advanced Fuels	
$D + He^3$	$\longrightarrow$		He^4 $(3.6\ MeV) + p$ $(14.7\ MeV)$	
$T + He^3$	$\longrightarrow$	[51%]	$He^4 + p + n + (12.1\ MeV)$	
	$\longrightarrow$	[43%]	He^4 $(4.8\ MeV) + D$ $(9.5\ MeV)$	
	$\longrightarrow$	[6%]	He^5 $(2.4\ MeV) + p$ $(11.9\ MeV)$	
$p + B^{11}$	$\longrightarrow$		$3\,He^4 + (8.7\ MeV)$	
			Tritium Breeding	
$n + Li^6$	$\longrightarrow$		He^4 $(2.1\ MeV) + T$ $(2.7\ MeV)$	

The $D - D$ reaction can create He^3, which can fuse with tritium or deuterium. $T - T$ reactions are also possible.

Table 1.3 lists a number of energy-relevant fusion reactions, broken into three categories: Neutronic reactions, advanced fuels and tritium breeding. The first category lists reactions that produce neutrons and includes the main $D - T$ reaction. The second category includes so-called "advanced fuels." These reactions are attractive because their direct byproducts are all charged particles, which means they can be controlled with electromagnetic fields. However, since their reaction cross-sections peak at very high temperatures, a fusion power plant based on these reactions will likely be a second- or third-generation technology.

The last category, tritium breeding, includes a crucial reaction for the $D - T$ power plant. Neutrons can fuse with lithium to produce helium and tritium. This allows for the prospect of a

closed tritium fuel cycle. Deuterium and tritium react to produce a neutron, which can react with lithium to produce another tritium ion. In this sense, the neutron plays a double role. It not only contains the energy produced by the reaction, but also replenishes the fuel supply.

At this point, the conceptual $D - T$ plant begins to take shape. Its fuel would be deuterium and lithium. Its waste would be helium. It would have to use neutrons to replenish the supply of tritium, extracting the neutrons' energy in the process to produce electricity. One method to do this would be similar to existing fission plants: use the neutrons to heat up a fluid, which passes through a heat-exchanger to produce steam and drive a turbine. These neutrons are both dangerous and precious: dangerous, because they can harm equipment and personnel, and precious, because they contain both the reaction's energy and the means to replenish its fuel supply. In this respect, the fusion reactor core would have to be surrounded by a neutron shield, such as a meter-thick slab of lead, and a neutron multiplier, such as beryllium, to maximize the breeding potential of each neutron, as in the reaction:

$$Be_4^9 + n \longrightarrow 2\,He_2^4 + 2\,n \tag{1.9}$$

Figure 1.8 shows an illustration of the conceptual $D - T$ power plant. At its core lies a high-temperature plasma of deuterium and tritium. Their fusion produces neutrons that pass through the first wall, which isolates the core from the rest of the plant. These neutrons must then be multiplied and used to breed more tritium, which is collected and recycled into the core. The neutrons deposit their energy in the blanket and a neutron shield, which protects sensitive equipment and personnel from neutron damage. Flowing coolant passes the absorbed heat to a heat exchanger to produce steam, which runs the turbines of a power generator.

1.3.2 Why Fusion Power?

With the conceptual power plant in mind, the benefits of fusion-based energy economy emerge. The fuel, waste, safety and integrability of a fusion plant make it an attractive power source.

neutrons

Fusion
Core

First Wall

Neutron
Multiplier

Tritium Breeder

Neutron Shield
Coolant
Heat Exchanger
Power Generator
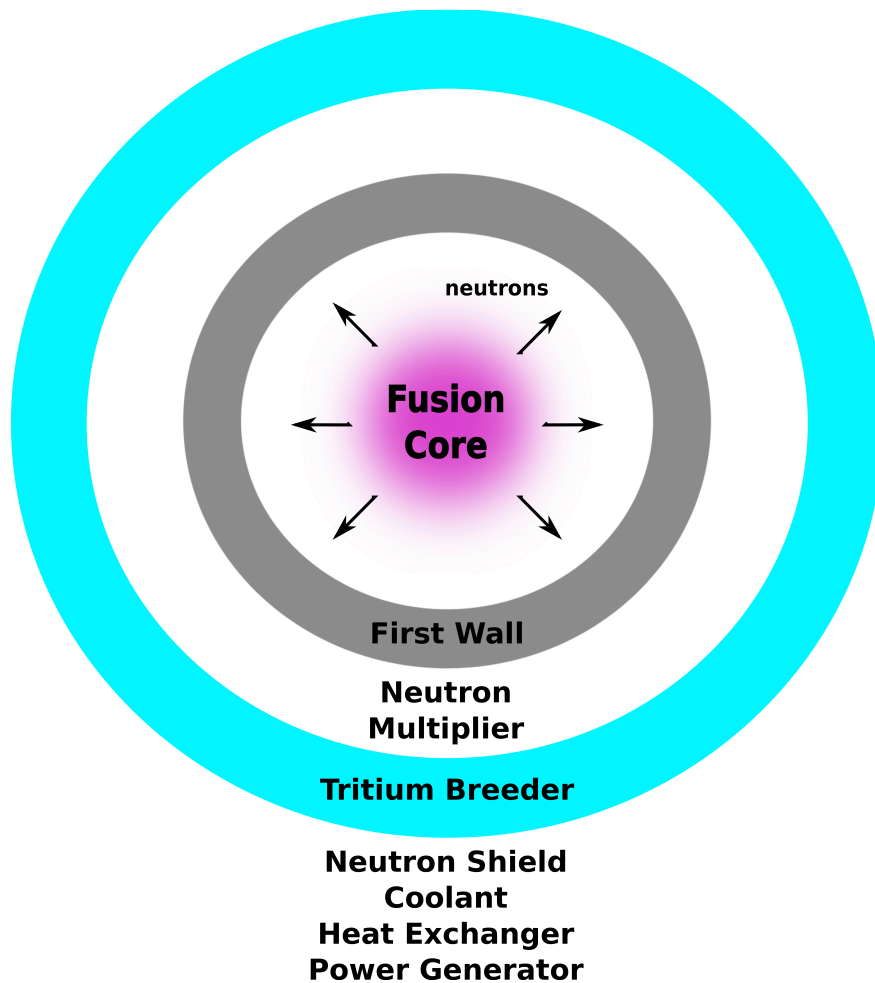
Figure 1.8: Concept of a D-T fusion reactor. The fusion core generates neutrons, which pass through the first wall of the reactor into a blanket. The blanket serves to generate tritium and electricity. Neutronic multiplication and interaction with lithium can breed more tritium to fuel the reactor. The neutrons' energy appears as heat, which can be extracted to drive a steam turbine, much like in a fission plant.

Table 1.4: Estimates of fusion fuel supplies on Earth, with their estimated lifetimes, assuming all-fusion powered society at high use (41.3 terawatt) global consumption.

Reaction	Fuel	Reserves (kg)	Energy Content (ZJ)	Supply (Years)
$D-T$	D (seawater)	4.6×10^{16}	5.1×10^{10}	3.9×10^{10}
	Li^6 (crust)	7.6×10^8	273.6	209.9
	Li^6 (seawater)	1.4×10^{13}	5.0×10^6	3.8×10^6
$D-D$	D (seawater)	4.6×10^{16}	4.1×10^9	3.1×10^9

Firstly, the fusion fuel supply is attractive. As mentioned, since the tritium necessary for the $D-T$ reaction would be produced in-house from neutron-lithium fusion, the plant's primary fuels would be deuterium and lithium. Both of these elements are in abundant natural supply. Deuterium is found in seawater, as heavy water: D_2O. Approximately one in every 6,400 seawater hydrogen atoms is deuterium [21]. This amounts to roughly 4.6×10^{16} kg in Earth's oceans. Lithium exists in the Earth's crust and in seawater. Current estimates put world reserves of crust-based lithium at around 11.8×10^9 kg [22]. Much more is thought to exist in seawater, with a total estimated supply of 2.2×10^{14} kg [23]. The crust and oceans contain roughly 7.6×10^8 kg and 1.4×10^{13} kg, respectively, of the tritium-breeding isotope, Li^6. Since deuterium and lithium are found abundantly in seawater, no single group of countries would control the fusion fuel source.

From a supply point of view, the $D-T$ reaction can be thought as requiring one atom of lithium-6 and one atom of deuterium to produce roughly 22.4 MeV (or 3.6×10^{-12} J) of energy. Each reaction would consume 3.3×10^{-27} kg of deuterium and 1×10^{-26} kg of lithium-6. Similary, $D-D$ fusion would produce 5.9×10^{-13} J of energy from 6.6×10^{-27} kg of deuterium. In all, this means that the energy content of terrestrial supplies of fusion fuels is very large, as summarized in Table 1.4. The limiting fuel for $D-T$ fusion is lithium. Yet the lithium in seawater would still last close to 4 million years, even when using fusion to supply all of humanity's power needs at the high-use scenario presented in Sec. 1.2. Should second- or third- generation reactors employ

$D - D$ fusion, enough fuel exists in Earth's oceans to power humanity for over 3 billion years. Doubtlessly, these are rough estimates that do not consider such externalities as the increased use of lithium for batteries, but the abundance of naturally occurring fusion fuel makes it an essentially limitless supply of energy.

Additionally, the waste stream from a fusion power plant is attractive. The byproducts of the $D - T$ fusion reaction are neutrons and helium. Helium, being an inert gas, is not harmful to the environment. It neither traps greenhouse gases nor reacts chemically with other elements. Neutrons, however, pose more of a challenge. The materials of a power plant, particularly those inside the neutron shield, will transmute and become radioactive over time, due to their interactions with neutrons. This will require the safe replacement and storage of damaged materials. However, the careful choice of low-activation materials could allow fusion plant waste to be safe enough for near-surface burial, negating the need for long-term deep geological storage of waste [24]. Aneutronic reactors could be designed to be even cleaner than $D - T$ reactors. In either case, the waste from a fusion power plant is environmentally appealing.

Fusion plants would be relatively safe to operate. They could not suffer a runaway reaction, as only small amounts of fuel are in the reactor at any given time. To shut down the reaction, one need simply turn off the fuel supply. The proliferation risks of a fusion plant are far less than those of a fission plant. It would be very difficult to covertly use a fusion reactor to generate weapons material [25]. A fusion plant would be relatively safe and secure, making it politically attractive.

Finally, a fusion-based energy economy needn't look drastically different from that of the present day. Fusion plants could be integrated into existing electrical grid networks, near the population centers that use the electricity. Unlike solar and wind power, fusion power would not depend on weather conditions, allowing it to provide a constant, predictable, base supply. Furthermore, since a plant's effectiveness would not depend on its geographic location, the incremental cost of adding more plants decreases, instead of increases, with time. To illustrate this effect, consider wind power. As the most energy-valuable land gets populated with wind turbines, the remaining

useable land becomes more expensive, so the incremental cost of adding more turbines increases with time. A fusion plant, on the other hand, would likely become cheaper to construct over time, as second- and third-generation plants could take advantage of technological advances learned in the construction and operation of first-generation plants. Fusion's final attractive feature is that it would act much like existing conventional energy sources: power generation is concentrated in a plant that can be located near demand and integrated into the currently existing grid infrastructure.

Fusion power is sustainably, environmentally and politically attractive. It holds the prospects of a nearly limitless supply of safe, clean, energy. Fusion works already: it powers not only our sun, but also every star in the universe. If we can harness that same energy source in a laboratory, we bring star power to Earth.

1.4 Laboratory Fusion

Three possible methods can contain plasma undergoing nuclear fusion. They are gravitational, inertial and magnetic. Nature unanimously uses gravitational pressure to hold hot plasma in thermonuclear conditions. The enormous weight of the sun keeps its hot core compressed long enough to undergo fusion.

Terrestrial fusion scientists do not have the luxury of astronomical gravitational fields. Instead, laboratory fusion occurs from one of two methods: inertial and magnetic confinement. In the inertial approach, a plasma is compressed while its own inertia holds the fusion fuel at very high densities for short periods of time, maximizing the triple product through the plasma's density. The magnetic approach instead uses magnetic fields to contain a less dense plasma for much longer times. An inertial fusion system might undergo compression for nanoseconds, while a magnetic system could have confinement times of seconds.

1.4.1 Inertial Fusion Energy
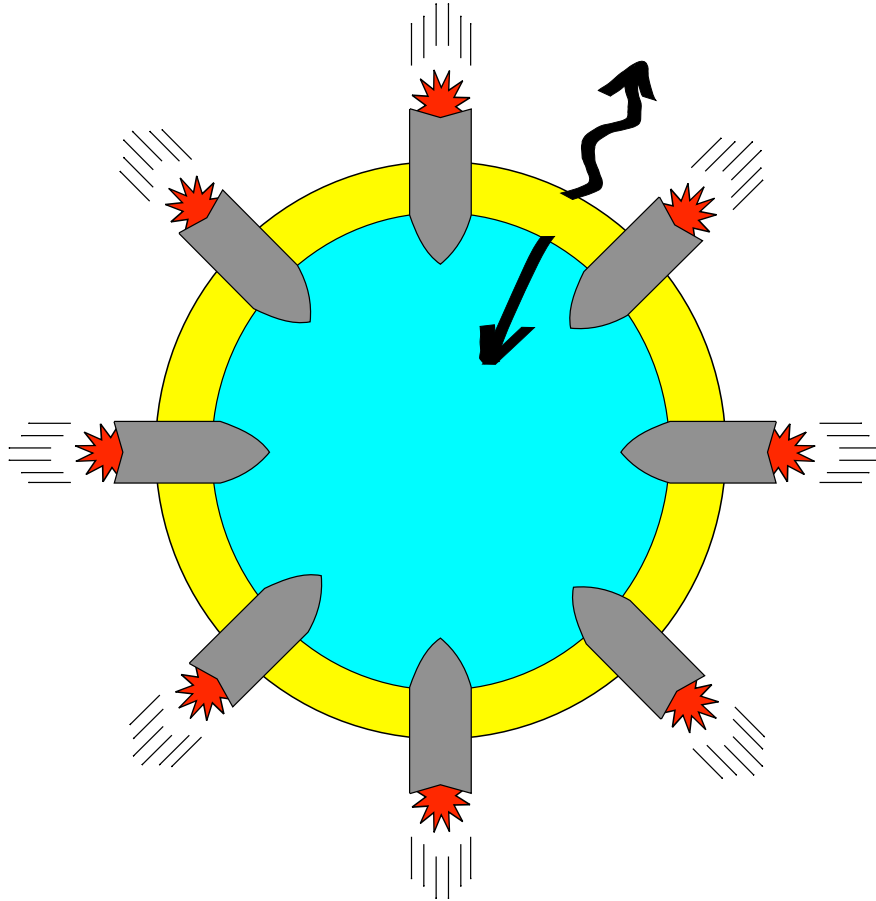
Figure 1.9: The compression of an inertial fusion pellet by the rocket effect. As the outer layer of the pellet ablates, conservation of moment forces the pellet to compress, much like the expulsion of fuel by a rocket engine moves the spacecraft forward.

One method of achieving nuclear fusion in a laboratory uses a plasma's own inertia to maximize the fusion triple product. This is known as Inertial Confinement Fusion (ICF). An Inertial Fusion Energy (IFE) system compresses tiny pellets of $D - T$ fuel to extremely high densities to achieve a fusion burn and energy gain. The principle idea behind IFE is the rocket effect, illustrated in Fig. 1.9. An external driver strikes the outer layer of a spherical pellet of fusion fuel. As this outer layer ablates off, conservation of momentum forces the fuel to compress, much like the ejection of

rocket fuel from a spaceship propels the craft forward. The ablative layer acts like many connected rocket ships all firing their engines at once. This crushes the pellet. As the pellet shrinks, the fuel density and temperature increase. Eventually, the fuel gets hot and dense enough for fusion to occur. Once the core ignites, a nuclear burn propagates through the rest of the pellet. The goal of IFE is to fuse as much of the fuel as possible before the pellet blows itself apart.

The leading method of achieving inertial confinement fusion is with lasers. High-energy laser light focuses onto the target pellet to burn of the pellet's ablation layer. When the lasers themselves strike the pellet, the method is known as direct drive. The alternative is known as indirect drive [26]. In this case, the spherical fuel pellet rests inside a metal cylinder, known as a holhraum (from German for "hollow area"). Instead of striking the pellet directly, the lasers heat the inner walls of the holhraum, which begins to emit x-rays. This x-ray bath serves as the ablative trigger for the fuel pellet. Indirect drive is attractive because, among other reasons, it provides a more uniform compression. Furthermore, higher-energy x-rays can penetrate deeper into plasma than can visible laser light, allowing for a more robust coupling to the fuel as it ionizes.

The flagship experiment for the indirect drive approach to laser inertial fusion is the National Ignition Facility, or NIF, at Lawrence Livermore National Laboratory [27]. The goal of NIF is to gain more energy from fusion than delivered to the pellet. To achieve this net energy gain, NIF focuses 192 laser beams, each of cross-sections of about one square meter, into a centimeter-sized holhraum containing a two-millimeter-diameter pellet. The pellet compresses in a matter of nanoseconds, crushing the fuel to ten times the density of lead. The hope is that the fuel will fuse enough to release 10-20 times the incident x-ray energy.

Although achieving a break-even "ignition" would be a key step in the advancement of laser inertial fusion, much work would be needed to adopt NIF's technology to a power plant. The millimeter-sized pellets would have to be mass-produced to within tolerances of microns for less than a dollar a piece. An IFE power plant would have to fire several times per second, compared

with the once-every-few-hours design of NIF. In any case, however, energy gain from a fusion reaction in a terrestrial laboratory would be a phenomenal achievement.

1.4.2   Magnetic Fusion Energy

An alternative to inertial confinement uses magnetic fields to contain fusion plasmas. While the inertial approach to fusion maximizes the fusion triple product through density, magnetic fusion energy (MFE) research maximizes instead the confinement time.

The key to the magnetic confinement of plasmas is that charged particles spiral around magnetic field lines. An MFE reactor would use this phenomenon to create a magnetic bottle for the charged fusion fuel. The tricky part is designing the bottle. In the simplest magnetic field, particles gyrate
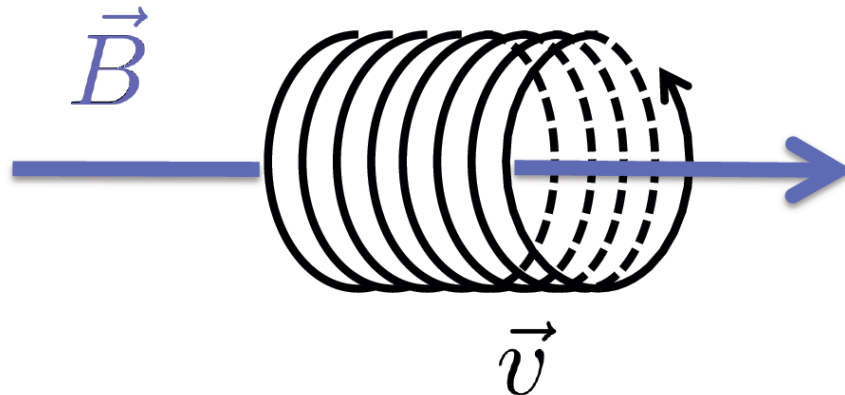
Figure 1.10: The helical gyration of a charged particle, moving with velocity $\vec{v}$, in a uniform magnetic field, $\vec{B}$. The particle's velocity parallel to the magnetic field remains unchanged, but its perpendicular motion is that of a circular orbit of radius ρ and period $mc/\left(2\pi eB\right)$.

around straight magnetic field lines, as in Fig. 1.10. Given a unidirectional magnetic field, like that generated by a solenoid, plasma will follow the field lines right out the end of the solenoid. One kind of magnetic bottle is known as a magnetic mirror. It uses the magnetic mirror effect to "plug" the ends of the solenoid, in which conservation of magnetic moment and energy cause particles to bounce away from regions of stronger magnetic field.

A machine that uses this effect to plug the ends of a solenoid is known as a mirror machine. Although it is one of the simplest magnetic confinement devices, consisting at the basic level of a solenoid with extra strong magnetics near the ends, MFE research has found greater success with different kinds of machines. In particular, instead of trying to plug the ends of a straight magnetic field, the most successful fusion devices wrap the straight magnetic field into a torus. This way, particles are free to stream along the direction of the magnetic field, merely zipping around in circles.

Solely having a donut-shaped magnetic field, however, cannot contain plasma very well. Particles still spiral around field lines. Yet the geometry introduces an effective force on the particle. Just as a car driving around a racetrack feels an outwardly directed force, so do plasma particles traveling around a torus. This force causes particles' gyration centers to drift vertically very quickly. For fusion plasma conditions, these drifts could cause a particle could leave the machine in milliseconds. The losses could be even quicker under the influence of instabilities.

The key idea to combat particle drifts in toroidal fusion devices is to twist the magnetic field. Since a particle follows a magnetic field line, a twisting magnetic field can guide the particle either up or down, counteracting the drift effect. This method has proven very successful in toroidal devices.

The first type of machine to do this is in a stable way is known as a stellarator. A stellarator uses complex magnetic field coils to create a twisting field. Stellarators have a long history and many attractive features. However, their coils can be very difficult to manufacture, and they've received far less attention than the most successful MFE design: the tokamak.

The tokamak, shown in Fig. 1.11, is a toroidal device with an externally applied toroidal magnetic field. This field has no twist and does not contain plasma very well. However, by driving an electric current in the toroidal direction, the plasma creates its own poloidal magnetic field, which gives the total magnetic field the requisite twist. This current also serves to kick-start the plasma's temperature. Just as a wire resistively heats up when pumped with an electric current, so too
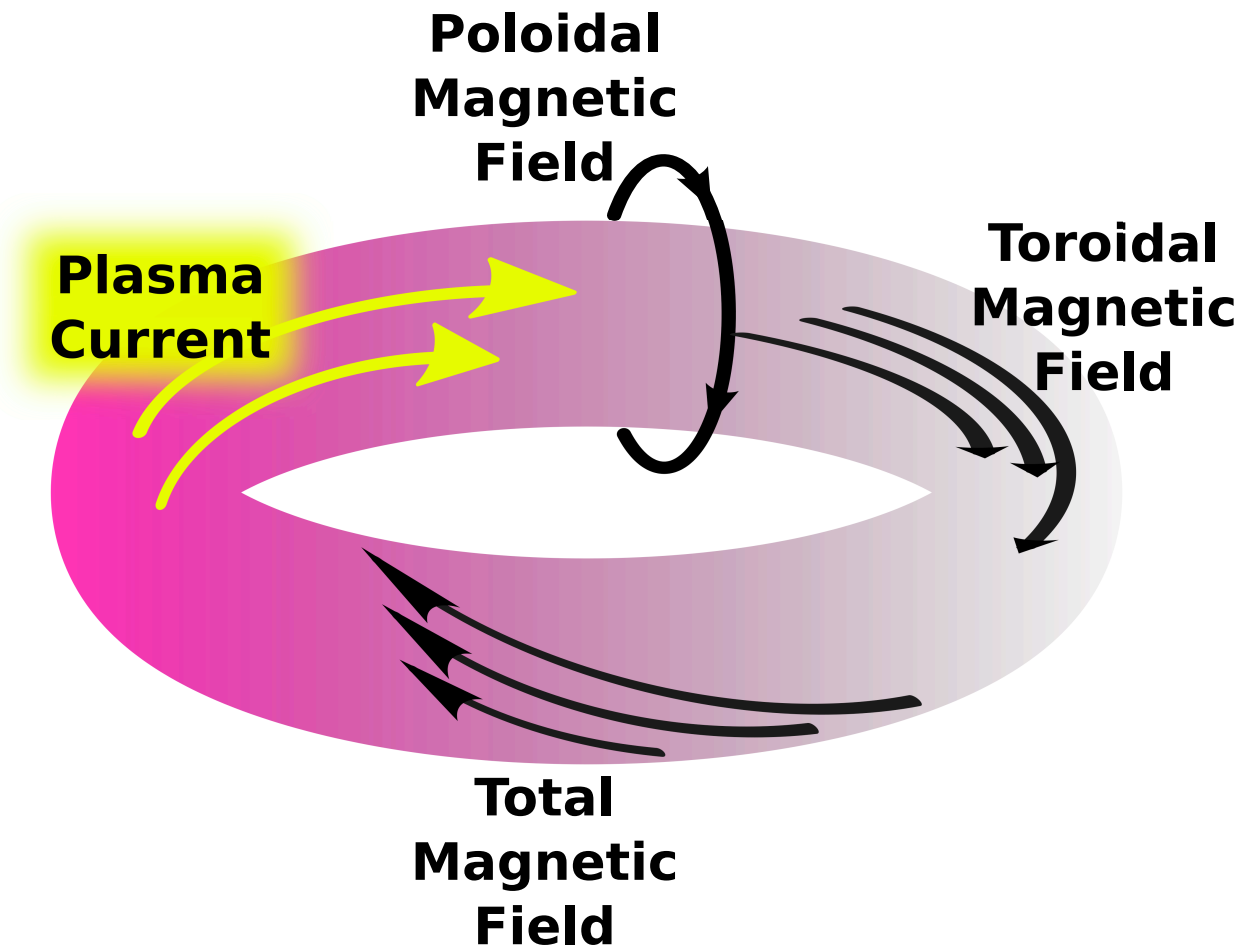
Figure 1.11: A conceptual tokamak. In a tokamak, an internal toroidal plasma current creates a poloidal magnetic field that combines with an externally applied toroidal field. The total field's spiral counteracts the effects of magnetic drifts, improving overall confinement.

does plasma. Such ohmic heating allowed even the earliest tokamaks to achieve very impressive temperatures.

Since its invention, magnetic fusion research has focused largely on the tokamak. Great advances in the science and technology of magnetic fusion have brought the field from infancy to the cusp of net energy gain.

1.5   A Brief History of (Confinement) Time
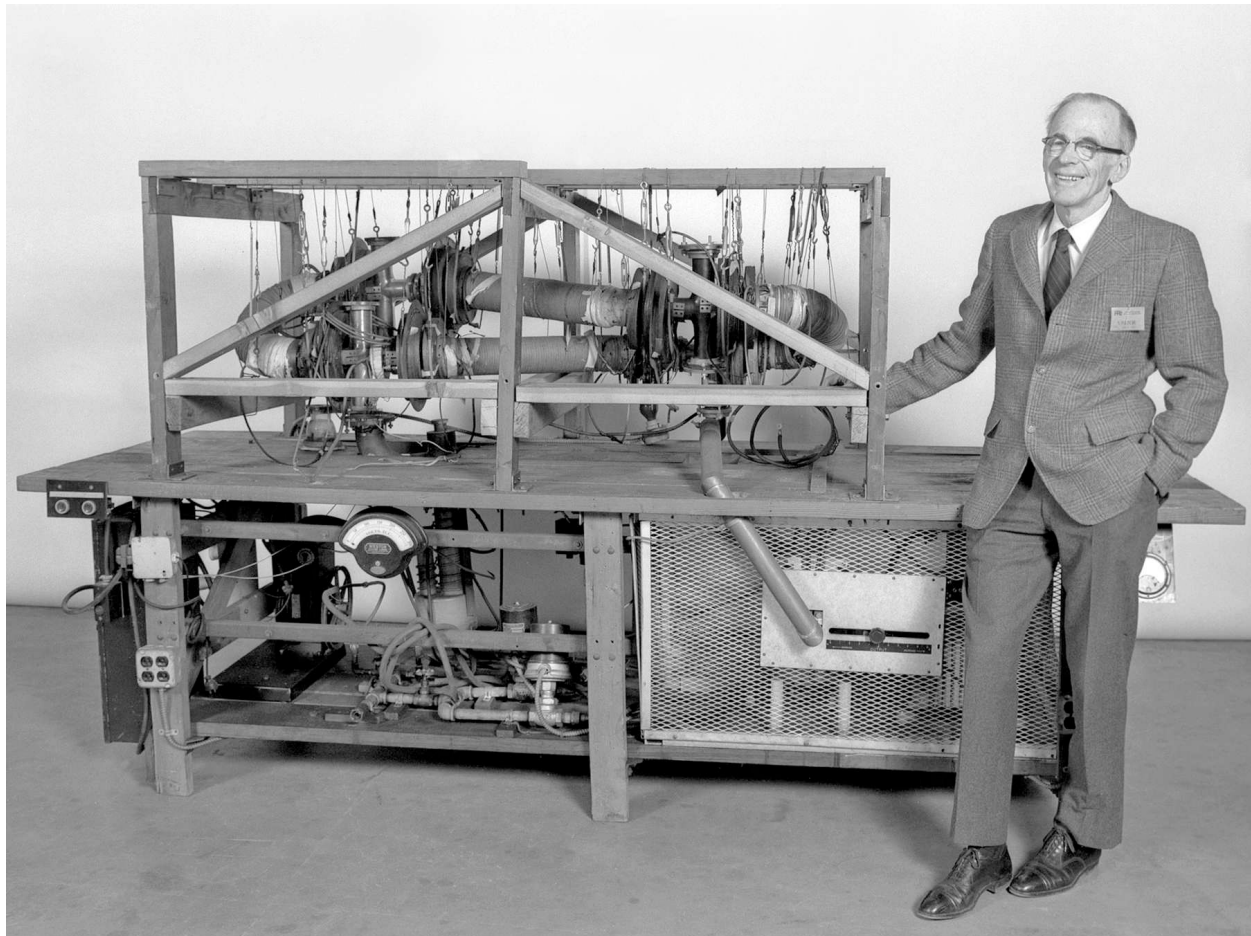
Figure 1.12: Lyman Spitzer with an early stellarator. Photo: Princeton Plasma Physics Laboratory.

Magnetic fusion research began shortly after the Second World War as a classified project, since a nearly limitless supply of energy would be a colossal advantage to a post-war superpower. A peaceful fusion program was envisioned before the end of the war; Edward Teller, the "father of the Hydrogen Bomb," called for academic discussions on the idea at Los Alamos as early as 1942 [28]. Yet, research in the United States didn't pick up until 1951, under the auspices of Princeton University Professor of Astrophysical Sciences, Lyman Spitzer (Fig. 1.12). Spitzer was on a ski trip in Aspen, thinking about particle guiding center drifts (as one is apt to do on vacation) when he came upon the concept of the stellarator. He successfully pitched the idea to the Atomic Energy Commission and named the newly established program "Project Matterhorn," after the famous Swiss mountain and his inspirational ski trip [29].

Early work on the stellarator paralleled MFE work in other countries, with researchers expecting early success but encountering unforeseen obstacles. In September 1958, the countries involved in fusion research agreed that a unified approach would work best and declassified their fusion research at the Second International Atoms for Peace Conference in Geneva [30]. Despite the Cold War climate, research continued on under an air of international collaboration, with US researchers focused largely on stellarators.

Magnetic fusion took a dramatic turn in 1968, when scientists at the Kurchatov Institute outside Moscow claimed that they had achieved electron temperatures in excess of 1 keV in the T3 tokamak. For contrast, stellarator researchers at Princeton considered 200 eV to be "hot" [31]. The tokamak, invented by the Soviet Physicists Igor Tamm and Andrei Sakharov in the 1950's, had until this point been largely ignored by researchers outside the iron curtain. However, the impressive results quickly drew interest, if not skepticism. Plans began at Princeton to convert the Model-C stellarator to a tokamak in the summer of 1969, in an attempt to reproduce the Russian experiments with a better set of diagnostics [31]. When a team of English researchers traveled to the T3 tokamak and independently confirmed the Russian results [32], skeptics took note. The

Model-C upgrade was changed to be more like T3, and in May 1970, the Symmetric Torus (ST) began operation.

Scaling experiments on the ST showed a favorable extrapolation to a reactor, unlike similar experiments on the Model-C stellarator [31]. Temperatures could reach 1 keV and confinement times lasted tens of milliseconds. With impressive results in hand, tokamak research gained momentum, both in the United States and Europe. A series of tokamaks dominated magnetic fusion research through the 1970's and 1980's, culminating in the US with the Tokamak Fusion Test Reactor (or TFTR), which operated from 1982 to 1997. In 1993, TFTR became the first magnetic fusion device to perform extensive experiments with a 50-50 $D - T$ fuel mixture, producing over 5 megawatts of fusion power [33]. Tokamaks also dominated research abroad.
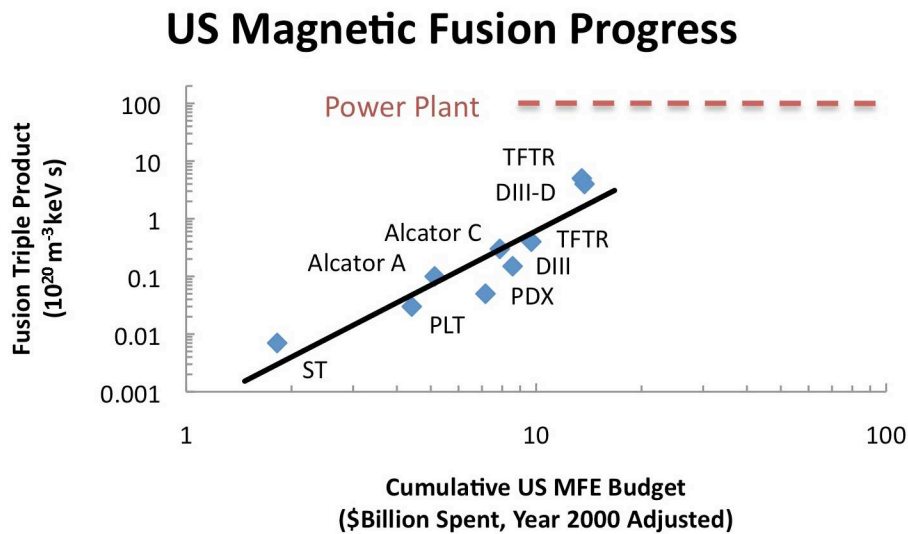
Figure 1.13: The fusion triple product, $nT\tau$, achieved by United States tokamaks as a function of total dollars spent on U.S. MFE research. Dollars are actual spent, adjusted to year 2000 equivalent dollars. Data are from Fusion Power Associates [34] and Fusenet [35].

Tokamaks in the United States brought with them a steady march of the Lawson criterion toward reactor regimes. Figure 1.13 displays this figure of merit for a variety of US tokamaks against cumulative domestic spending on magnetic fusion research, normalized to year-2000 equivalent

dollars. The United States has spent just shy of 20 billion dollars on MFE research in the past sixty years, with tokamaks the dominating force since the 1970's. In the intervening years, the fusion triple product from MFE experiments has increased roughly 1000-fold, though the total money spent on research has only increased be a factor of ten or so. Estimates place the current triple product record at only a factor of ten or so below the necessary levels for a commercial power plant [35]. It seems reasonable that this could be achieved with another 50-80 billion dollars of investment, a large, but not astronomical, sum. For comparison, the Apollo Program is estimated to have cost roughly 170 billion year-2005 dollars [36]. The plasma conditions necessary for a commercial fusion power plant seem to be in reach.

The next major step in magnetic fusion research is a tokamak designed to operate above break-even. Originally conceived in 1985 as a venture in Cold War cooperation, ITER (Latin for "the way") is presently under construction in the south of France [37]. It is an international collaboration involving the European Union, Russia, Japan, the United States, China, India and the Republic of Korea. Operations are scheduled to begin in 2019, with the eventual goal of producing 500 megawatts of fusion power from only 50 megawatts of input power. At present, the estimated construction cost is roughly 18 billion dollars, spread amongst the different ITER member-states.

ITER, while a colossal undertaking, is not a commercial power plant. Many practical issues, such as power extraction, material testing, and plant operations will be largely ignored. ITER is very large, very expensive and may not be the most economical approach to fusion energy. However, the experiment is an important step in the realization of magnetic fusion energy. Net energy production cannot be looked upon lightly. It will be a historic scientific and political achievement.

Research in controlled nuclear fusion has progressed steadily in the past sixty years. ITER is poised to be the first tokamak with self-sustaining fusion reactions, showing that energy gain from controlled fusion is possible with magnetically confined plasmas. NIF aims to demonstrate the same with inertial confinement. Each represents a colossal step towards a demonstration fusion

power plant. With humanity's continued thirst for energy, such a commercial fusion power plant cannot come too soon.

1.6   Scope of Dissertation

This dissertation explores energy confinement on the National Spherical Torus Experiment (NSTX), specifically focusing on gyrokinetic turbulent transport as driven by electron temperature gradients in NSTX plasmas. Chapter 2 introduces the concepts of tokamak plasma confinement, turbulent transport and gyrokinetics, addressing why understanding electron transport is important not only for present-day experimental devices, like NSTX, but also why such an understanding is significant to the development of practical fusion energy. Chapter 3 demonstrates why NSTX is a good laboratory for the study of gyrokinetic electron turbulent transport. Through nonlinear gyrokinetic simulations of NSTX experimental discharges, Chapter 4 aims to answer the degree to which electron temperature gradient driven turbulence can account for thermal losses in NSTX, and how to control such losses. Chapter 5 integrates these turbulence simulations into a transport framework to make predictions of NSTX plasma performance. The conclusions in Chapter 6 discuss how the key findings of this work relate to the ultimate goal of practical fusion energy.

Some of the work of this dissertation, particularly in Chapter 4, contributed to Refs. [38, 39], has been presented at several recent scientific meetings and is greatly expanded herein.

Chapter 2

Tokamaks, Transport and Turbulence

Magnetic fusion reactors work best when they can keep the plasma hot for a long period of time. The longer the plasma stays hot, the more fusion reactions can occur, and the more power one gets out of the reactor. This amounts to maximizing the energy confinement time of a plasma τ_E, defined as the energy content of the plasma, W divided by the rate of energy loss, P_{loss}:

$$\tau_E = \frac{W}{P_{loss}}. \tag{2.1}$$

In a tokamak, particles stream along field lines in the toroidal direction, so their parallel confinement time is very large. However, it is also possible for particles to diffuse outward, in the direction perpendicular to the magnetic field. This perpendicular diffusion rate defines the confinement time of the plasma. The larger the diffusion rate, the quicker hot particles leave the plasma, the smaller the confinement time and the lower the fusion power output. Determining the rate of perpendicular particle and heat diffusion amounts to solving the problem of plasma transport.

The plasma diffusion problem was first thought to be dominated by collisional processes; however, these "classical" arguments were found to greatly underpredict the amount of transport seen in tokamaks. Even considering enhancements due to plasma geometry (so called "neoclassical"

36

transport) cannot make up the difference. Instead, since plasma turbulence can cause diffusion, tokamak plasma confinement is thought to be dominated by turbulent processes.

This chapter begins with some basic properties of tokamaks, such as particle motion in a toroidal geometry, and continues with an introduction to collisional plasma transport. After showing that such collisional processes cannot robustly account for observed levels of transport in tokamaks, we move on to discuss turbulence, how it can cause transport, and how to model it with gyrokinetics.

2.1 The Tokamak

The most-studied magnetic fusion device is the tokamak, of which spherical tori, like the National Spherical Torus Experiment (NSTX), is a subset. The tokamak consists of plasma in an apllied toroidal magnetic field and an induced poloidal field. The net spiral field is meant to counteract particle drifts. An understanding of the confinement properties of NSTX must begin with the behavior of charged particles in a tokamak, which includes gyromotion, mirroring and particle drifts in a toroidal geometry.

2.1.1 Particle Motion in Magnetic Field

The key idea behind MFE is that charged particles, like those in plasma, follow magnetic field lines. Consider a single particle with a charge q moving at velocity $\mathbf{v} = v_x \hat{x} + v_y \hat{y} + v_z \hat{z}$ through a uniform magnetic field: $\mathbf{B} = B\hat{z}$. The force on this particle is given by the Lorentz Force, written in cgs units as:

$$\mathbf{F} = q \left[\mathbf{E} + \frac{1}{c} \mathbf{v} \times \mathbf{B} \right].$$ (2.2)

In the absence of an electric field, $\mathbf{E}$, this force becomes:

$$\mathbf{F} = \frac{qB}{c} \left[v_y \hat{x} - v_x \hat{y} \right].$$

(2.3)

This force is entirely perpendicular to the magnetic field, and would impart an acceleration, a, on the particle based upon its mass, m. The equations of motion for this particle can be written in vector form:

$$m\mathbf{a} = \mathbf{F},$$

$$m \begin{bmatrix} a_x \\ a_y \\ a_z \end{bmatrix} = \frac{qB}{c} \begin{bmatrix} v_y \\ -v_x \\ 0 \end{bmatrix},$$

$$\begin{bmatrix} \ddot{x} \\ \ddot{y} \\ \ddot{z} \end{bmatrix} = \frac{qB}{mc} \begin{bmatrix} \dot{y} \\ -\dot{x} \\ 0 \end{bmatrix}.$$

(2.4)

Dotted notation indicates derivatives with respect to time: $\dot{x} = v_x = \partial_t x$, $\ddot{x} = a_x = \dot{v}_x = \partial_{tt} x$. As there is no acceleration in the $\hat{z}$ direction, the particle's velocity in the direction parallel to the magnetic field remains fixed at its initial $\hat{z}$ velocity, v_{z0}. In other words, parallel to the magnetic field, the particle merely coasts with a constant velocity:

$$z\left(t\right) = z_0 + v_{z0}t.$$

(2.5)

This has an important physical interpretation: a uniform magnetic field will only affect the dynamics of a particle in directions perpendicular to that field. The particle's parallel trajectory remains unchanged.

Ignoring the $\hat{z}$ direction and taking another time derivative, Eqns. 2.4 become:

$$\begin{bmatrix} \dddot{x} \\ \dddot{y} \end{bmatrix} = \frac{qB}{mc} \begin{bmatrix} \ddot{y} \\ -\ddot{x} \end{bmatrix}$$

$$\begin{bmatrix} \dddot{x} \\ \dddot{y} \end{bmatrix} = -\left(\frac{qB}{mc}\right)^2 \begin{bmatrix} \dot{x} \\ \dot{y} \end{bmatrix}$$

$$\begin{bmatrix} \ddot{v}_x \\ \ddot{v}_y \end{bmatrix} = -\left(\frac{qB}{mc}\right)^2 \begin{bmatrix} v_x \\ v_y \end{bmatrix}. \tag{2.6}$$

These are two decoupled differential equations for the velocity of the particle, each of the same form: $\ddot{\xi} = -A^2 \xi$. This equation has an oscillatory solution: $\xi(t) = \xi_1 \cos(At) + \xi_2 \sin(At)$, for some constants ξ_1 and ξ_2, given by the initial conditions of the system. Defining $\Omega_c = (qB)/(mc)$, the velocity equations can be written as:

$$v_x = v_{x1} \cos(\Omega_c t) + v_{x2} \sin(\Omega_c t), \tag{2.7}$$

$$v_y = v_{y1} \cos(\Omega_c t) + v_{y2} \sin(\Omega_c t). \tag{2.8}$$

Because the velocities are not entirely unrelated, this can be simplified. Recall from Eq. 2.4 that $\dot{v}_x = \Omega_c v_y$. This and Eqs. 2.8 imply:

$$\begin{aligned}
v_y &= \frac{1}{\Omega_c} \dot{v}_x, \\
&= \frac{1}{\Omega_c} \partial_t \left[v_{x1} \cos(\Omega_c t) + v_{x2} \sin(\Omega_c t) \right], \\
&= \frac{1}{\Omega_c} \left[-v_{x1} \Omega_c \sin(\Omega_c t) + v_{x2} \Omega_c \cos(\Omega_c t) \right], \\
&= v_{x2} \cos(\Omega_c t) - v_{x1} \sin(\Omega_c t). \tag{2.9}
\end{aligned}$$

Comparing Eqs. 2.8 and 2.9, $v_{y1} = v_{x2}$ and $v_{y2} = -v_{x1}$.

Integrating with respect to time gives equations for the particle's position:

$$x = \frac{v_{x1}}{\Omega_c} \sin\left(\Omega_c t\right) - \frac{v_{x2}}{\Omega_c} \cos\left(\Omega_c t\right) + \frac{v_{x2}}{\Omega_c} + C_x, \tag{2.10}$$

$$y = \frac{v_{x2}}{\Omega_c} \sin\left(\Omega_c t\right) + \frac{v_{x1}}{\Omega_c} \cos\left(\Omega_c t\right) - \frac{v_{x1}}{\Omega_c} + C_y. \tag{2.11}$$

The constants can be determined by initial conditions: $\mathbf{v}\left(t=0\right) = v_{x0}\hat{x} + v_{y0}\hat{y}$ and $\mathbf{x}\left(t=0\right) = x_0\hat{x} + y_0\hat{y}$. Applying $t=0$ to the equations for position and velocity, the boundary conditions are then:

$$x_0 = C_x, \tag{2.12}$$

$$y_0 = C_y, \tag{2.13}$$

$$v_{x0} = v_{x1}, \tag{2.14}$$

$$v_{y0} = v_{x2}. \tag{2.15}$$

Replacing the constants and simplifying yields the equations for particle's evolution:

$$x(t) = x_0 + \frac{1}{\Omega_c}\left\{v_{x0}\sin\left(\Omega_c t\right) + v_{y0}\left[1 - \cos\left(\Omega_c t\right)\right]\right\}, \tag{2.16}$$

$$y(t) = y_0 + \frac{1}{\Omega_c}\left\{v_{y0}\sin\left(\Omega_c t\right) - v_{x0}\left[1 - \cos\left(\Omega_c t\right)\right]\right\}, \tag{2.17}$$

$$z(t) = z_0 + v_{z0}t. \tag{2.18}$$

These equations describe a particle moving in a helix, as depicted in Fig. 1.10. The $\hat{z}$ velocity remains fixed in time. However, in the perpendicular $x - y$ plane, the particle's position moves in a circle. Every $t = 2\pi\Omega_c$, the particle returns to x_0 and y_0. At $t = \pi\Omega$, the particle's x position has increased by a distance of $2v_{y0}/\Omega_c$, while it's y displacement is $-2v_{x0}/\Omega_c$. This implies that the

radius of this circle, ρ, is half the total displacement at $t = \pi\Omega_c$, or:

$$\rho = \frac{1}{2}\sqrt{\left(\frac{2v_{x0}}{\Omega_c}\right)^2 + \left(\frac{2v_{y0}}{\Omega_c}\right)^2} = \frac{\sqrt{v_{x0}^2 + v_{y0}^2}}{\Omega_c} = \frac{v_\perp}{\Omega_c}. \qquad (2.19)$$

For convenience, $v_\perp$ is the particle's speed in the $x - y$ plane. The helical gyration of charged particles in magnetic fields has led to calling ρ the particle's gyro-radius and Ω_c it's gyro-frequency. Since Ω_c contains the charge of the particle, q, positive and negative charges spiral in opposite directions: positive charges with a "left-handed" spiral, and negative charges with a "right-handed" spiral. The frequency of this spiral depends upon the particle's mass, charge and the strength of the magnetic field. The radius of the spiral also depends upon the particle's energy. Faster moving and more massive particles have larger gyro-radii. Increasing the magnetic field decreases the gyro-radius.

2.1.2   The Mirror Effect

As mentioned in Section 1.4.2, particles in non-uniform magnetic fields are subject to the mirror effect, in which conservation of momentum and magnetic moment can cause the particles to bounce away from regions of stronger magnetic field. This is the fundamental principle behind the Mirror Machine; however, non-uniform magnetic fields exist in tokamaks too, making the mirror effect an important arbiter of tokamak dynamics.

To demonstrate the mirror effect, consider a charged particle moving in a cylindrical magnetic field. Its motion is that of a helix, spiraling around the magnetic field lines. Its parallel velocity is given by $v_\parallel = v_{z0}$, while its perpendicular speed is $v_\perp = \sqrt{v_{x0}^2 + v_{y0}^2}$. Since the particle's gyro-frequency, Ω_c, can be very high, on slow enough time scales the particle's motion in the perpendicular plane appears as a current-carrying loop. Its current would be $I = q\Omega_c/(2\pi)$, and its radius $\rho = v_\perp/\Omega_c$. This loop would have a magnetic moment, $\mu = \frac{I}{c}(\pi\rho^2) = \frac{c}{cB}\left(\frac{1}{2}mv_\perp^2\right) = \frac{W_\perp}{B}$.

In this case, $W_\perp$ is the particle's kinetic energy in the perpendicular plane. The magnetic moment μ is known as an adiabatic invariant, that is to say that on slow enough time scales, it is a conserved quantity. In other words, one has the following constant of the particle's motion:

$$\mu = \frac{W_\perp}{B}. \tag{2.20}$$

As the particle moves in a magnetic field, its perpendicular energy will change with the strength of the magnetic field. Allow the magnetic field in the center of the solenoid to be less than that at the ends: $B^{mid} < B^{end}$. Conservation of magnetic moment implies that $\mu^{mid} = \mu^{end}$, while conservation of total energy says that $W^{mid} = W^{end}$. This sets up the following conditions on the particle:

$$W_\perp^{mid} + W_\parallel^{mid} = W_\perp^{end} + W_\parallel^{end}, \tag{2.21}$$

$$\frac{W_\perp^{mid}}{B_{mid}} = \frac{W_\perp^{end}}{B_{end}}. \tag{2.22}$$

Simplifying, one can write some equivalent expressions for the particle's parallel velocity at the end of the solenoid:

$$W_\parallel^{end} = W_\parallel^{mid} + W_\perp^{mid}\left(1 - \frac{B^{end}}{B^{mid}}\right), \tag{2.23}$$

$$= W - W_\perp^{mid}\frac{B^{end}}{B^{mid}}, \tag{2.24}$$

$$= W - \mu B^{end}. \tag{2.25}$$

Since the magnetic field at the end of the solenoid is stronger than in the middle, $B^{end} > B^{mid}$, $W_\parallel^{end} < W_\parallel^{mid}$: the particle slows down in the parallel direction as it approaches the end of the solenoid. As it does so, it gains perpendicular velocity to conserve total energy. If the field is strong enough, the particle can lose all of its parallel energy, such that $W_\parallel^{end} = 0$, effectively stopping

the particle in its tracks. This is the mirror effect: as particles approach an increasing magnetic field, they gyrate faster and faster, slowing down in the direction parallel to the magnetic field and eventually reflecting backwards.

Marginally trapped particles $\left(W_{\parallel}^{end} = 0\right)$ will have $v_{\parallel}^{mid}/v_{\perp}^{mid} = \sqrt{B^{end}/B^{mid} - 1}$. If they have more parallel velocity than this at the middle of the device, they will be moving too quickly in the parallel direction to be trapped. So, the condition for a particle with initial velocities $v_{\parallel}$ and $v_{\perp}$ to be trapped by a magnetic field that varies in strength from B^{min} to B^{max} is:

$$\frac{v_{\parallel}}{v_{\perp}} < \sqrt{\frac{B^{max}}{B^{min}} - 1}. \tag{2.26}$$

This ratio separates plasma into populations of "passing" and "trapped" particles.

2.1.3 Particle Drifts

The center of the particle's spiral, known as the guiding center, will move under the influence of an external force, $\mathbf{F}$, according to:

$$\mathbf{v}_d = \frac{\mathbf{F} \times \hat{b}}{\Omega_c m}. \tag{2.27}$$

The drift of the guiding center is in a direction perpendicular to the magnetic field, $\mathbf{B} = B\hat{b}$. The particle in a torus of major radius R will experience an outward (the $\hat{R}$ direction) force of magnitude:

$$\mathbf{F} = \frac{mv_{\parallel}^2}{R}\hat{R}. \tag{2.28}$$

So, a particle will experience a guiding center drift, either up or down (the $\hat{z}$ direction in toroidal

coordinates), depending upon the sign of its charge:

$$
\begin{aligned}
\mathbf{v}_d &= \frac{\mathbf{F} \times \hat{b}}{\Omega_c m}, \\
&= \frac{m v_\parallel^2}{R \Omega_c m} \hat{R} \times \hat{b}, \\
&= \frac{v_\parallel^2}{R \Omega_c} \hat{z} = \frac{v_\parallel^2}{R} \frac{mc}{qB} \hat{z}.
\end{aligned}
\tag{2.29}
$$

This drift velocity is rather larger. For a fusion plasma, $m v_\parallel^2 \sim 10$ keV, $B \sim 5$ T, $R \sim 500$ cm.

So, $v_D \sim 400$ m/s. Needless to say, any particle would immediately drift out of the torus. Particle

drifts like this play a significant role in toroidal plasma confinement.

2.1.4 Toroidal Geometry

The tokamak attempts to cancel out particle drifts by driving an axial (toroidal) electric current in

the plasma. This toroidal current induces a poloidal magnetic field, so that the total magnetic field

in a tokamak, $\mathbf{B}$, is a sum of an externally applied toroidal field, B_φ, and the induced poloidal field,

B_θ:

$$
\mathbf{B} = B_\varphi \hat{\varphi} + B_\theta \hat{\theta}.
\tag{2.30}
$$

Since the total magnetic field spirals, every time a magnetic field line circles around the toka-

mak in the toroidal direction, it moves a certain amount in the poloidal direction. Within a tokamak

with major radius R_0, the spiraling at a minor radius of r can be defined in terms of the inverse of

the rotational transform, known as the "safety factor" q:

$$
q \doteq \frac{r}{R_0} \frac{B_\varphi}{B_\theta}.
\tag{2.31}
$$

R runs from zero in the center of the torus to R_0 at the center of the plasma's cross section, where $r = 0$. At the plasma boundary, $r = a$, the minor radius. The vertical coordinate is Z. Together, the coordinate systems $(R, Z, -\varphi)$ and (r, θ, φ) are positively oriented.
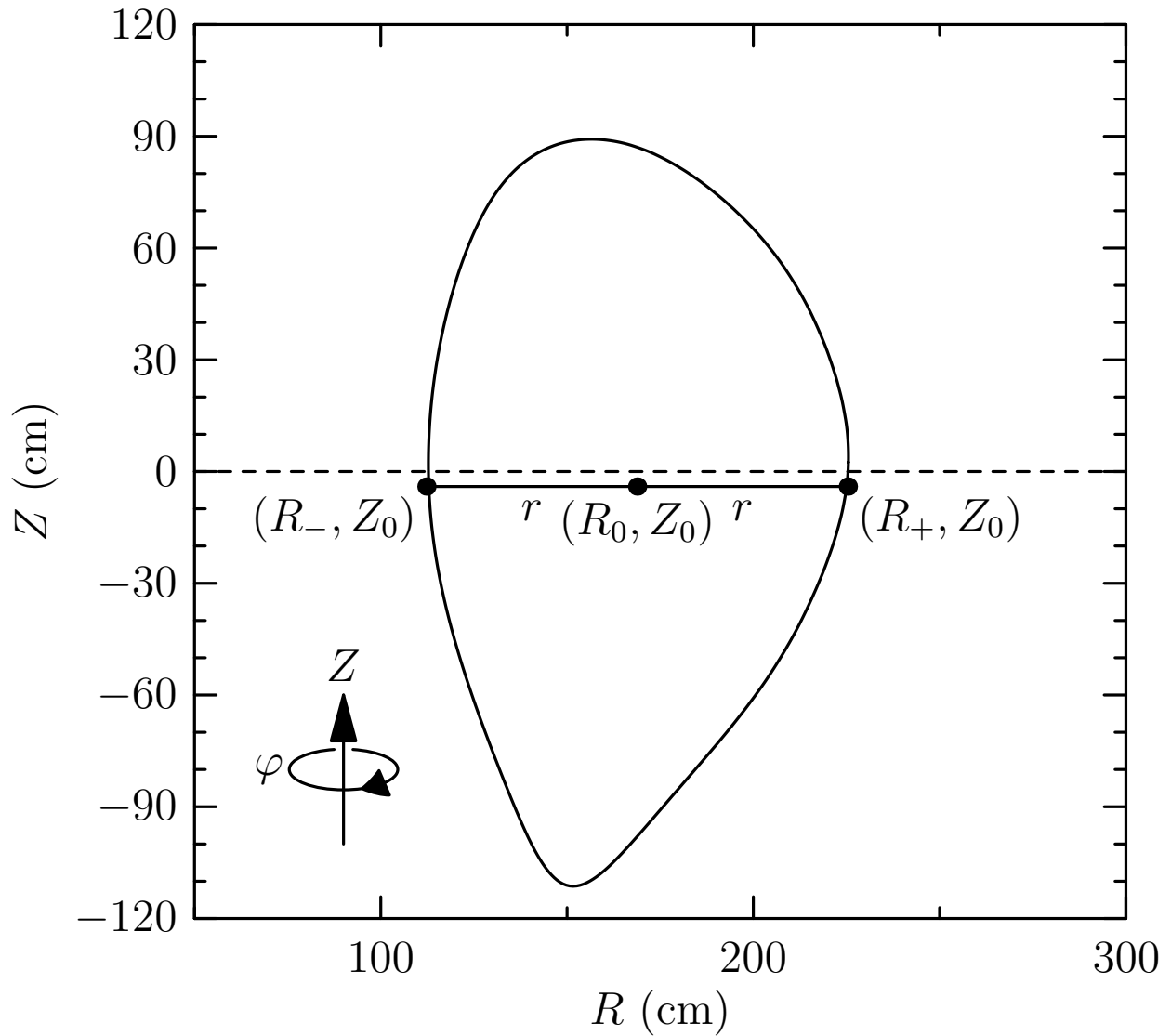
Figure 2.1: An example of a flux surface in toroidal geometry from the DIII-D tokamak, reproduced from Ref. [40].

The magnetic field can be written in terms of fluxes in a field-aligned coordinate system (r, θ, α):

$$\mathbf{B} = \nabla \alpha \times \nabla \psi \left(r \right) \text{ such that } \mathbf{B} \cdot \nabla \alpha = \mathbf{B} \cdot \nabla \psi = 0 \tag{2.32}$$

where ψ is the poloidal flux divided by 2π and

$$\alpha = \varphi + \nu \left(r, \theta \right) \tag{2.33}$$

is the Clebsch angle [41]. α parameterizes both the toroidal and poloidal angles, being a representation of the distance along a magnetic field line. If the plasma's poloidal cross-section is circular, the coordinates are related to one another by:

$$
\begin{aligned}
R \left(r, \theta \right) &= R_0 + r \cos \theta \\
Z \left(r, \theta \right) &= r \sin \theta \\
\nu \left(r, \theta \right) &= -q \left(r \right) \theta
\end{aligned}
\tag{2.34}
$$

Another model, which approximates deformations of the local surfaces of constant flux ("flux surfaces") is the Miller equilibrium model [42], in which the coordinate systems have the following relation:

$$
\begin{aligned}
R \left(r, \theta \right) &= R_0(r) + r \cos \left(\theta + \arcsin \left[\delta(r) \right] \sin \theta \right) \\
Z \left(r, \theta \right) &= Z_0(r) + \kappa(r) r \sin \left(\theta + \zeta(r) \sin 2\theta \right)
\end{aligned}
\tag{2.35}
$$

δ, κ and ζ are known as the flux surface's triangularity, elongation and squareness, respectively. In this case, ν can be calculated numerically (see, for instance, Ref. [40]). An example flux surface in toroidal geometry from the DIII-D tokamak can be seen in Fig. 2.1, reproduced from Ref. [40].

2.2 Plasma Transport

The collective motion of charged particles determines the confinement properties of the magnetic fusion device. Higher levels of confinement correspond to lower levels of particle and heat transport. The success of an MFE system depends then on an understanding of the transport properties of magnetically confined plasmas. Tokamaks are good at confining particles along the field line. The limiting factor, therefore, becomes cross-field transport. This section makes some simple estimates of cross-field diffusive transport in tokamaks.

2.2.1 Random Walk Diffusion

1905 was a very productive year for Albert Einstein. During that year, he published four very important papers. He won the Nobel Prize for his first paper [43], which gave an explanation of the photoelectric effect, the process behind solar panels. He is most famous, perhaps, for his last two [44, 45], which presented the special theory of relativity and the mass-energy equivalence, $E = mc^2$, the principle behind nuclear fusion. But it is his second paper [46] that offers insight into the problem of plasma transport.

In this work, Einstein tackles the problem of Brownian Motion, a curious phenomenon whereby particles of dust suspended in a liquid under a microscope appear to move of their own free will. However, Einstein's explanation discounts the supernatural. Instead, the movement of the dust is attributed to random collisions with atoms in the fluid. Einstein assumed that each atom kicks the dust particle some distance every once in a while. Under this assumption, it turns out that the density of particles, n, evolves under a diffusion equation, of the form:

$$\frac{\partial n}{\partial t} = D \frac{\partial^2 n}{\partial x^2}, \qquad (2.36)$$

which has a solution:

$$n(x, t) = \frac{1}{\sqrt{4\pi Dt}} e^{-x^2/4Dt}. \tag{2.37}$$

From the diffusion coefficient, D, Einstein was able to estimate how quickly particles would move due to these random collisions. He found that the mean squared displacement, $\langle x^2 \rangle$, scales as the time elapsed. Mathematically, this is related to the diffusion coefficient by:

$$\langle x^2 \rangle = 2Dt. \tag{2.38}$$

Alternatively, one can estimate the diffusion coefficient from random motion of an average length, Δx, occurring once in a time interval of Δt by:

$$D = \frac{1}{2} \frac{(\Delta x)^2}{\Delta t}. \tag{2.39}$$

This "random walk" argument proved to be strong evidence to the existence of atoms, which was, at this point, still controversial. Since they agreed with observations of Brownian Motion, Einstein's arguments helped usher in the acceptance of statistical mechanics.

Similar arguments can help estimate diffusion rates in magnetically confined plasmas, a key ingredient in solving the transport problem. The trick is then to find good estimates for Δx and Δt. With knowledge of diffusion in hand, designing a reactor to minimize plasma transport, and maximize fusion gain, becomes a little easier.

2.2.2 Classical Transport

The simplest estimate of cross-field diffusion comes from inter-particle collisions. This process is known as *classical transport*. Consider a plasma in a magnetic field **B**, made up of ions and electrons, with gyro-radii of ρ_i and ρ_e, respectively. Every so often, an electron will collide with an ion, with a collision frequency ν_{ei}. Like two billiard balls, each collision causes the particles'

velocities to change, which manifests as a change in gyro-phase angle. Because of this change of phase, the center of gyration (or the "guiding center") of the particles also changes. This implies that each time particles collide, they will move about one gyro-radius. This allows for a simple estimate of particle diffusion due to collisions, with the random walk step size being the gyro-radius and the time interval the inverse of the collision frequency, namely:

$$D_e \sim \frac{(\Delta x)^2}{\Delta t} \sim \frac{(\rho_e)^2}{1/\nu_{ei}} \sim \nu_{ei}\rho_e^2. \tag{2.40}$$

For ions colliding off electrons, we can exchange e and i and get $D_i \sim \nu_{ie}\rho_i^2$. However, having no net current in a plasma, $\nabla \cdot \mathbf{j} = 0$, implies that as electrons move, ions must move with them to compensate. If the ions were stationary, the displaced electrons would create an electric field that serves to pull the ions towards the electrons. So, electrons and ions must diffuse at the same rate, in this ambipolar fashion. (Additionally, momentum conservation from electron-ion collisions implies that both classical and neoclassical diffusion are in fact automatically ambipolar, even without generating an electric field.) Therefore, $D_e = D_i$. A rough estimate of particle diffusion becomes:

$$D_{classical} \sim \nu_{ei}\rho_e^2 \sim \nu_{ie}\rho_i^2. \tag{2.41}$$

While this estimate only works if the collision frequency is smaller than the gyrofrequency, Ω_c, else it's difficult to argue that the particle maintains gyromotion under collisions, Eq. 2.41 serves a good baseline model for cross-field particle diffusion in a plasma, due entirely to collisions.

The estimate for $D_{classical}$ comes from interactions between ions and electrons. Yet to lowest order one can ignore contributions from electron-electron and ion-ion collisions. Due to conservation of momentum, collisions between like-particles do not cause a net particle diffusion; the sum of the changes in the particles' velocities is zero if they each have the same mass, so their guiding

centers have no net separation after a collision. In this sense, classical particle diffusion arises only from electron-ion collisions.

How large then, typically, is this particle diffusion? For temperatures given in eV, and using cgs units, expressions for the average electron collision frequency and gyroradius are [20]:

$$\nu_{ei} = 2.91 \times 10^{-6} n_e \ln \Lambda T_e^{-3/2} \text{ sec}^{-1} \tag{2.42}$$

and

$$\rho_e = 2.38 T_e^{1/2} B^{-1} \text{ cm}. \tag{2.43}$$

The Coulomb logarithm, $\ln \Lambda$, accounts for the fact that collisions are usually a sum of small-angle collisions instead of large-angle scattering events and has typical values of around 10-20. So an estimate of a classical diffusion coefficient is given by Eq. 2.41. Combining this with Eqs. 2.42 and 2.43 yields:

$$D_{classical} \sim \nu_{ei} \rho_e^2 \sim 2 \times 10^{-4} \frac{n_e \ [\text{cm}^{-3}]}{\left(T_e \ [\text{eV}]\right)^{1/2} \left(B \ [\text{gauss}]\right)^2} \frac{\text{cm}^2}{\text{sec}}. \tag{2.44}$$

Taking the magnetic field strength to be about 10^4 gauss, temperatures of 1 keV and densities of 10^{13} cm^{-3}, this classical diffusion rate is approximately 0.63 cm^2/sec. By considering this as a random walk process that follows a diffusion equation, we can estimate the root mean squared displacement of particles in a plasma by $x_{rms} = \sqrt{2Dt}$. In one second then, on average one could expect a particle to move $\sqrt{2 \cdot 0.63}$ cm ≈ 1.1 cm. Should the tokamak plasma have a minor radius of meters, this estimate would expect particles to remain in the plasma for minutes before diffusing outward due to collisions. This is, unfortunately, not the case at all. Experimentally speaking, particle confinement times may be milliseconds, not seconds. Therefore, classical particle diffusion is a large over-estimate of tokamak confinement.

What about heat flow, which is, after all, very important for fusion? Ignoring sources of heating, one can write a conduction equation based on heat flux, $\mathbf{Q}$, and thermal diffusivities, χ, of the form [47]:

$$\frac{3}{2}\frac{\partial T}{\partial t} = -\nabla \cdot \mathbf{Q} = \nabla_\perp \cdot (\chi_\perp \nabla_\perp T) + \nabla_\parallel \cdot \left(\chi_\parallel \nabla_\parallel T\right). \tag{2.45}$$

This is, again, a diffusion equation. Like particle diffusion, parallel motion is much faster than perpendicular motion, so each field line can be viewed at roughly the same temperature. The perpendicular heat diffusivity, $\chi_\perp$ is much smaller. One can use classic collisional arguments to estimate this perpendicular heat diffusivity. Unlike the particle argument, however, like-particle collisions can lead to a net flux of energy. In this case, ion-ion collisions dominate the thermal flux, since they have large gyro-radii. Taking the random walk step size as the ion gyro-radius and the characteristic time as the inverse of the ion-ion collision frequency, an estimate for the thermal diffusivity becomes:

$$\chi_\perp \sim \nu_{ii}\rho_i^2. \tag{2.46}$$

For a plasma where $T_e \approx T_i$, $\nu_{ii} \approx \sqrt{m_e/m_i}\nu_{ei}$ and $\rho_i = \sqrt{m_i/m_e}\rho_e$ [20]. So the thermal diffusivity can be rewritten as:

$$\chi_\perp \sim \sqrt{\frac{m_i}{m_e}}\nu_{ei}\rho_e^2 \sim \mu_e D_{classical}. \tag{2.47}$$

For convenience, $\mu_e \doteq \sqrt{m_i/m_e}$. It's clear from Eq. 2.47 that the thermal heat diffusivity is greater than the particle diffusivity by a factor of the square root of the ion-to-electron mass ratio. For a deuterium plasma, $\mu_e \approx 60$. However, even with this enhancement, χ as predicted by these classical arguments is still much lower than values seen in experiments.

Energy confinement times, like particle confinement times, are tens of milliseconds in fusion experiments, yet classical transport theory predicts confinement times of seconds, a significant overshoot. These estimates, however, are only rough, and could be greatly improved. A better

calculation would take into account the anisotropic plasma geometry present in a tokamak. This is known as neoclassical transport.

2.2.3 Neoclassical Transport

Toroidal geometries, such as those of tokamaks, enhance the effects of collisions on transport. Collisional transport that considers the device's magnetic geometry is called *neoclassical transport*. Recall from Section 1.4.2 that particles in magnetic fields experience drifts and magnetic trapping. Bending a plasma in a torus breaks the system's symmetry. This manifests itself as anisotropies in the plasma, which in turn create particle drifts and traps. These drifts and traps can enhance the transport due to collisions. An estimate of this enhancement comes from looking at toroidal geometry.

In toroidal geometry with the poloidal magnetic field much weaker than the toroidal, the length increment along a field line can be characterized by the connection length, $\Delta x_\parallel \sim qR_0$. A particle will move along this parallel length segment at its thermal velocity, v_T, until knocked off trajectory by a collision. When this occurs, it will diffuse, both in the parallel and perpendicular directions. An estimate of the parallel diffusion coefficient from this motion is then:

$$D_\parallel \sim \frac{\Delta x_\parallel^2}{\Delta t} \sim v_\parallel^2 \Delta t \sim \frac{v_T^2}{\nu_{ei}}. \tag{2.48}$$

Combining this with the connection length, $\Delta x_\parallel \sim qR_0$, implies that

$$\Delta t \sim \nu_{ei} \left(\frac{qR_0}{v_T} \right)^2. \tag{2.49}$$

Under this motion, the particle experiences a change in the magnetic field strength. The gradient of the magnetic field leads to a guiding-center drift:

$$\mathbf{v}_{\nabla B} = \frac{1}{\Omega_c B}\mathbf{B} \times \mu \nabla B. \tag{2.50}$$

The radial component of this drift can be estimated in the large-aspect ratio limit ($\epsilon \doteq r/R_0 \ll 1$) as:

$$(v_{\nabla B})_r \sim \frac{\rho v_T}{R_0}. \tag{2.51}$$

This radial velocity defines a perpendicular diffusion, according to:

$$D_\perp \sim \frac{\Delta x_\perp^2}{\Delta t} \sim \frac{\left[(v_{\nabla B})_r \Delta t\right]^2}{\Delta t} \sim (v_{\nabla B})_r^2 \Delta t. \tag{2.52}$$

Adding to this estimate Eqs. 2.51 and 2.49 gives an estimate of this drift-corrected diffusion coefficient:

$$D_\perp \sim \nu_{ei}\rho_e^2 q^2 \sim q^2 D_{classical}. \tag{2.53}$$

Typical values of q in a tokamak range from 1-10, implying that neoclassical rates of diffusion are no greater than 10-100 times the classical value, which was estimated from Eq. 2.44 to correspond to a diffusion rate of ≈ 0.6 cm^2/sec. Increasing this by a factor of 100 implies that in one second one could expect a particle to travel $\sqrt{2 \cdot 6} \approx 3.5$ cm. Particles would still be confined in a meter-thick plasma for several seconds, instead of the observed milliseconds.

Neoclassical transport, while a better estimate of collisional diffusion in a tokamak, still grossly over-estimates plasma confinement. The process presently thought to be governing tokamak transport is much more complex, namely plasma turbulence.

2.3 Plasma Turbulence

Historically, as the discrepancies between neoclassical and measured fluxes continued to mount, a growing effort emerged to determine the cause of this "anomalous" transport. Eventually, correlations were found that linked high levels of transport with a marked increase in the intensity of measured plasma fluctuations, thereby suggesting that plasma transport was linked with plasma turbulence [48]. This section touches on some important features of turbulent-driven transport, including profile stiffness, gyrokinetic turbulence and electron-temperature-gradient-driven (ETG) turbulence, one of the prime candidates thought to be governing the performance of some NSTX discharges.

2.3.1 Turbulent Transport

Small-scale fluctuations in plasma density and potential significantly enhance cross-field diffusion. Even 1% perturbations can account for the difference in observed levels and neoclassical estimates of transport. Once thought to be "anomalous," tokamak plasma confinement is now considered to be nearly entirely governed by this *turbulent transport*.

An estimate of the magnitude of transport caused by turbulence can again come from a random-walk diffusion argument, using turbulent eddies' sizes and turnover times for space and time scales. In this case the step size is given by the ion sound radius:

$$\rho_s = \frac{c_s}{\Omega_{c,i}}, \tag{2.54}$$

where $\Omega_{c,i}$ is the gyrofrequency of the ion, and the ion sound speed, c_s is given as:

$$c_s = \sqrt{\frac{T_e}{m_i}}. \tag{2.55}$$

A characteristic time can also be determined from c_s, if normalized to some length, such as the major radius R. Therefore the diffusivity becomes:

$$D_{turb} \sim \frac{(\Delta x)^2}{\Delta t} \sim \rho_s^2 \frac{c_s}{R}. \tag{2.56}$$

Assuming an electron temperature of 1 keV and deuterium, which has a mass of 1875.6 MeV$/c^2$, $c_s \approx 7 \times 10^{-4} c$. Taking $B = 10^4$ gauss, $\rho_s \approx 0.3$ cm. This estimates D_{turb} at over 60 m^2/s for a device with a major radius of 3 m. Since typical experimental values are in the range of several m^2/s, turbulent diffusion could easily account for observed levels of transport. The scaling in Eq. 2.56 is commonly known as gyroBohm diffusion. It suggests that higher magnetic fields and larger machines will have reduced levels of transport. The inverse B and R scalings in particular are one of the major motivators to building a large machine with a strong magnetic field, such as ITER. Transport driven by turbulence is presently considered the primary arbiter plasma confinement. Understanding and controlling turbulent diffusion is, therefore, key to improving confinement times.

In particular, diffusion arises from cross-correlations of fluctuating quantities [49]. As an example, fluctuations in a particle's velocity can lead to its long-time diffusion. Given a two-time correlation function that is the average of the particle's fluctuating velocity

$$C(t, t') = \langle \delta v\,(t)\,\delta v\,(t') \rangle, \tag{2.57}$$

and statistically stationary fluctuations, then $C\,(t, t') = C\,(t - t') = C\,(\tau)$. Asymptotically then the particle will have a diffusion coefficient given by the integral

$$D = \int_0^\infty d\tau C\,(\tau). \tag{2.58}$$

This is a single-particle picture of diffusion as arising from the cross-correlations of that particle's fluctuating velocity. From a fluid point of view, consider a macroscopic quantity A which evolves according to an advection equation of the form:

$$\frac{\partial A}{\partial t} + \mathbf{v} \cdot \nabla A + \cdots = 0. \tag{2.59}$$

$\mathbf{v}$ is a velocity. If $\langle \mathbf{v} \rangle = 0$ and $\nabla \cdot \mathbf{v} = 0$, then averaging this equation yields a diffusion equation

$$\frac{\partial \langle A \rangle}{\partial t} + \frac{\partial \Gamma_A}{\partial x} + \cdots = 0. \tag{2.60}$$

Γ_A is the turbulent flux for the field A:

$$\Gamma_A \doteq \langle \delta v_x \delta A \rangle, \tag{2.61}$$

which involves a cross-correlation between the velocity and the advected field A. (Often in plasma tokamak turbulence, $\mathbf{v} = \mathbf{v}_E$, that arising from $\mathbf{E} \times \mathbf{B}$ drift motion. In this case the correlation involves the electrostatic potential.)

In turbulence it is often useful to think of the system in terms of individual Fourier modes (of wavenumber $\mathbf{k}$: $A_{\mathbf{k}} = |A_{\mathbf{k}}| e^{i\theta_{\mathbf{k}}}$), so that Eq. 2.61 involves not only two modes' rms fluctuation levels but also their phase difference $\Delta\theta$:

$$\Gamma_A = \sum_{\mathbf{k}} \left\langle |V_{\mathbf{k}}| \, |A_{\mathbf{k}}| \, e^{i\Delta\theta_{\mathbf{k}}} \right\rangle. \tag{2.62}$$

The macroscopic diffusion of a quantity undergoing microscopic fluctuations involves the cross-correlations of that quantity and its velocity. Individual oscillating Fourier modes thus contribute to turbulent diffusion through not only their magnitude but also their cross-phase.

Plasma turbulence is fairly ubiquitous. It arises from free-energy sources, such as pressure gradients. (Pressure gradients in the atmosphere, for instance, can drive wind.) Since $\nabla P = \nabla(nT) = T\nabla n + n\nabla T$, both temperature and density gradients can drive turbulence. As the plasma in a tokamak is both hotter and denser in its core than at its edge, experimental plasmas are often inherently unstable. While a cup of water will not become turbulent unless stirred, a ball of plasma can stir itself. These naturally occurring unstable modes lead, through their cross-correlations, to turbulent diffusive transport.

Typically, gradient-driven turbulence has a threshold before it turns on: some finite amount of free energy is necessary to trigger the instability. Plasma transport then involves understanding not only the linear threshold for instability, where individual Fourier harmonics become unstable, but also the nonlinear interaction of these modes, since it is the time-averaged cross-correlations of fluctuating quantities that govern macroscopic transport.

Microscopic plasma turbulence can drive macroscopic plasma transport at experimentally relevant levels. Naturally occurring pressure gradients can trigger instabilities, which nonlinearly interact to diffuse fluctuating quantities. Understanding the interaction of plasma profiles and the turbulent diffusion they can trigger is an important step in improving MFE confinement.

2.3.2 Stiff Profiles

Since plasma gradients can drive large amounts of turbulent transport, it follows that many plasmas will exhibit a *stiff profile phenomenon*, whereby all plasma parameters hover near the marginal stability threshold for turbulent transport. Once plasma parameters exceed the triggering level for instability, the plasma becomes turbulent, and large levels of turbulence-induced diffusion relax the plasma back below that critical threshold.

Figure 2.2 illustrates the effect of a stiff electron temperature profile. Under an external heat source, such as radiofrequency heating, the electron temperature (black dashed) can heat up until its
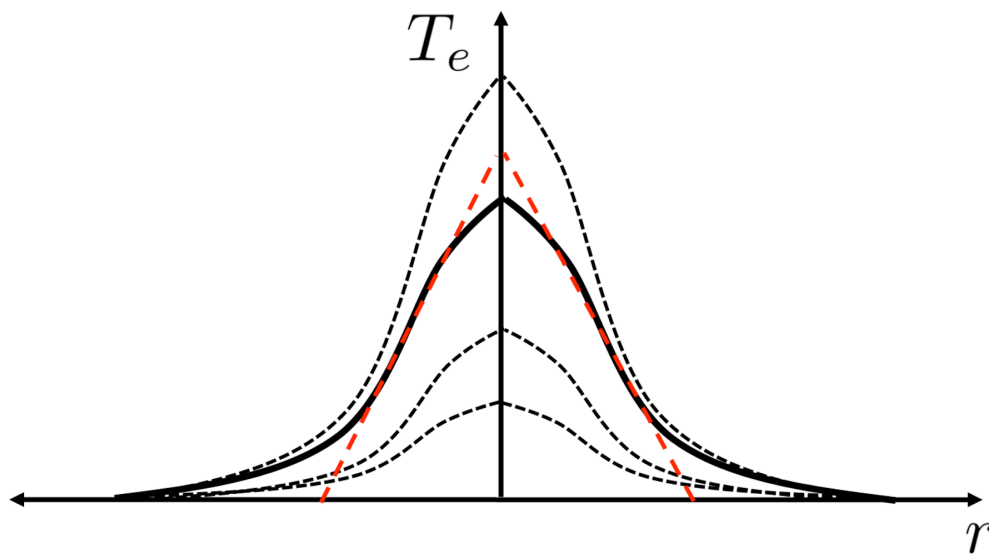
Figure 2.2: The stiff profile phenomenon, in which small changes in gradients can lead to large levels of flux. Electron temperatures (black dashed) can heat up until they exceed a critical gradient threshold for transport (red), at which time the plasma becomes unstable to a temperature-gradient-driven mode and transitions to a turbulent state. Turbulent fluctuations then drive strong levels of heat flux, which relaxes the temperature profile. The result is a plasma profile that hovers near marginality (black solid).

gradients exceed a critical gradient for turbulence (red). At this point, the plasma becomes linearly unstable to an electron-temperature-gradient mode (the plasma can sustain an oscillation with a finite growth rate). This mode grows in amplitude and interacts with other Fourier harmonics, until the plasma reaches a turbulent state. The turbulent oscillations then drive large heat fluxes, which serve to quickly expel energy from the core of the plasma. This sudden cooling relaxes the temperature back towards the critical gradient. The result is a plasma profile that hovers near marginal stability (black solid), usually either slightly above ("supercritical") or slightly below ("subcritical") the critical gradient, depending on the exact nature of the turbulence.

Many plasma profiles hover near marginality. As such, their profiles are "stiff." Since about this point small changes in gradients lead to large fluxes, it is very difficult to heat plasmas much beyond marginality. Many plasmas, both terrestrial and extraterrestrial, exhibit stiff profiles. For an example of stiff turbulent heat flux in the solar convection zone, see Ref. [50]. Because of the stiff profile phenomenon, plasma turbulence directly affects the achievable temperatures and densities in tokamaks.

2.3.3   From Kinetics to Gyrokinetics

Plasma turbulence in the core of tokamaks is best described by a kinetic picture, which casts a plasma species' dynamics in terms of the advection of a distribution of particles throughout phase space:

$$\frac{\partial f\left(\mathbf{x}, \mathbf{v}, t\right)}{\partial t} + \mathbf{v} \cdot \nabla f + \mathbf{a} \cdot \nabla_{\mathbf{v}} f = C\left[f\right]. \tag{2.63}$$

$f\left(\mathbf{x}, \mathbf{v}, t\right)$ is a distribution function for the species and depends upon the six-demensional phase space of position $\mathbf{x}$ and velocity $\mathbf{v}$. $\nabla_{\mathbf{v}} = \partial/\partial \mathbf{v}$ and the acceleration $\mathbf{a}$ is given by the motion of a particle in an electric field, $\mathbf{E}$, and a magnetic field, $\mathbf{B}$:

$$\mathbf{a} = \frac{q}{m}\left(\mathbf{E} + \frac{1}{c}\mathbf{v} \times \mathbf{B}\right). \tag{2.64}$$

The operator on the right hand side of Eq. 2.63 accounts for inter-particle collisions. If it is zero, the kinetic evolution equation is known the Vlasov equation. Outright evolving Eq. 2.63 is, however, challenging, as it represents a partial differential equation of seven variables (3 space, 3 velocity and time) with a vast range of time and space scales, from the very fast electron gyrofrequency and plasma frequency of $\sim 10^{11}$ Hz to the slower electron turbulence scales of $\sim 10^6 - 10^7$ Hz to the very slow transport evolution of the plasma, which can evolve on seconds. To grossly understate, analytically capturing the dynamics of this equation is challenging, so one turns often to numerics. Solving Eq. 2.63 on a computer with a very coarse 10 grid points in each dimension still results in one million grid points. Increasing each dimensions to 100 would involve a total computational mesh of one trillion grid points. For drift-wave types of problems, which are driven largely by spatial gradients, one might be able to use a coarser mesh in velocity space than in real space, thereby alleviating some of these requirements, but the large space and time scales that have to be resolved in a fully kinetic code would remain. This is extremely difficult, even on modern supercomputers.

Instead of working directly with the full kinetic picture, one can use physical insight to transform Eq. 2.63 into a more tractable version. Specifically, particles rapidly gyrate around magnetic field lines. For fluctuation frequencies much lower than Ω_c, one can average out the particles' gyromotion, thereby reducing the dimensionality of the problem and the eliminating the need to resolve particle gyromotion, and still capture the interesting turbulent dynamics. This is the fundamental principle behind gyrokinetics.

Gyrokinetics is a kinetic plasma description with a physically-motivated coordinate transformation to reduce the dimensionality of particle phase space and rigorously average over the fast gyromotion. The key picture is that in the presence of magnetic fields, like those found in tokamaks, particles gyrate around magnetic field lines at very high frequencies. On slower time scales, the evolution of particles appears closer to that of charged rings, whose centers move along field

lines and experience perpendicular drifts. The idea is to evolve then a distribution of gyrocenters, H, instead of the particles themselves.

A simple gyrokinetic equation, which ignores magnetic drifts and finite gyroradius effects, is

$$\frac{\partial H}{\partial t} + v_\parallel \nabla_\parallel H + \mathbf{v}_E \cdot \nabla H + \frac{q}{m} E_\parallel \frac{\partial H}{\partial v_\parallel} = 0, \tag{2.65}$$

where $\parallel$ represents the direction parallel to the magnetic field, $\mathbf{b} = \mathbf{B}/B$, and $\mathbf{v}_E$ is the aforementioned $\mathbf{E} \times \mathbf{B}$ drift velocity:

$$\mathbf{v}_E \doteq \frac{c\mathbf{E} \times \mathbf{B}}{B^2}. \tag{2.66}$$

Equation 2.65 must be coupled to a "gyrokinetic Poisson equation," the Maxwell equation that calculates the electrostatic potential in terms of gyrocenters.

Originally, gyrokinetic equations were derived in two steps (such as the approach in Ref. [51]). First, one transforms coordinate space from a particle-centered system to a gyrocenter-oriented one. Then, one averages over the gyromotion of the particles. The result is an equation for charged rings that experience perpendicular drifts, with their parallel and perpendicular dynamics separated. The magnetic moment, from this perspective, is conserved, thereby eliminating another dimension to differentiate (Eq. 2.65 has only four derivates, of 3 spatial dimensions and $v_\parallel$. The perpendicular velocity dimension, $v_\perp$, does not require differentiation, because terms can be cast in terms of the magnetic moment, μ, which is conserved for each particle.) The first derivation of a nonlinear gyrokinetic theory was by Frieman and Chen [52], which has since been derived with various techniques and extensions, such as in Refs. [53, 54] The "modern" method of deriving gyrokinetics involves Lie transforms and perturbation theory [55–59], which casts the problem in terms of an approximate Hamiltonian transformed into a coordinate system where the magnetic moment is an exact invariant. Both methods derive an equation that captures the dynamics of oscillations slower than the gyrofrequency.

Gyrokinetics is a kinetic description of plasmas that takes advantage of the gyromotion of individual particles to reduce the difficulties of the fully kinetic problem, by not only reducing the problem dimensionality, but also, and more importantly, negating the need to resolve the very fast particle gyromotion. By transforming the Vlasov equation to evolve a distribution of guiding centers, one can more easily capture the dynamics of turbulent oscillations of frequencies $\omega \ll \Omega_c$, thereby making the simulation of plasma turbulent transport much more tractable.

2.3.4   The Plasma Microturbulence Code GYRO

The simulation code `GYRO` solves the electromagnetic gyrokinetic-Maxwell equations in toroidal geometry on a fixed (Eulerian) grid using finite-difference, finite-element and spectral techniques [40, 60]. `GYRO` also aligns its grid along magnetic field lines, so that coarse grid spacing along the field lines can still capture the streaming dynamics of particles, an advantage for microturbulence emphasized by Refs. [61, 62]. Some key features of `GYRO` include the ability to capture electrostatic and electromagnetic fluctuations, and the ability to run in either a global mode, which allows for the radial variation of plasma profiles, or a local (flux-tube) approximation, in which the turbulent dynamics on a specific flux surface only depend upon the plasma properties at that surface. In the limit where $\rho_\star = \rho_s/a \to 0$ the global and local solutions are equal, and plasma transport becomes purely gyroBohm [63].

Furthermore, `GYRO` is designed to simulate real tokamaks. As such, a variety of tools exist for the translation of experimental data into simulation space, including `transp2gyro`[1], a python code built as part of this dissertation to pull experimental data from a `TRANSP MDS+` server and automatically create the input files necessary for gyrokinetic simulation.

The equations solved and the algorithms used by `GYRO` are described in full detail in Ref. [40] and online[2]. For concreteness, we summarize the gyrokinetic equations as solved by `GYRO`, using

---

[1]https://fusion.gat.com/theory/Profiles_gen#Interaction_with_TRANSP
[2]https://fusion.gat.com/theory/Gyro

the notation of Ref. [40], which follows the gyrokinetic equations as derived in Ref. [51]. For a species a with mass m_a and charge $e_a = ez_a$ is:

$$\frac{\partial h_a}{\partial t} + \left(v_\| \mathbf{b} + \mathbf{v}_d\right) \cdot \nabla H_a + \mathbf{v}_{E0} \cdot \nabla h_a + \delta \mathbf{v}_a \cdot \nabla h_a \ +$$
$$\delta \mathbf{v}_a \cdot \left(\nabla f_{a0} + \frac{m_a v_\| f_{a0}}{T_a} \frac{I}{B} \nabla \omega_0 \right) \ = \ C_a^{GL}\left[H_a\right]. \tag{2.67}$$

$C_a^{GL}\left[H_a\right]$ is a collision operator. The velocities include the $\mathbf{E} \times \mathbf{B}$ and drift velocities:

$$\mathbf{v}_d \ \dot{=} \ \frac{v_\|^2 + \mu B}{\Omega_{ca} B} \mathbf{b} \times \nabla B + \frac{2 v_\| \omega_0}{\Omega_{ca}} \mathbf{b} \times \mathbf{s} + \frac{4\pi v_\|^2}{\Omega_{ca} B^2} \mathbf{b} \times \nabla p, \tag{2.68}$$
$$\mathbf{v}_{E0} \ \dot{=} \ \frac{c}{B} \mathbf{b} \times \nabla \phi_{-1}, \tag{2.69}$$
$$\delta \mathbf{v}_a \ \dot{=} \ \frac{c}{B} \mathbf{b} \times \nabla \Psi_a. \tag{2.70}$$

I and $\mathbf{s}$ are geometric quantites (for a full description see Ref. [40]). The perturbed distribution function of guiding centers $H_a(\mathbf{R})$ is broken into two components:

$$H_a(\mathbf{R}) = \frac{e_a f_{a0}}{T_a} \Psi_a(\mathbf{R}) + h_a(\mathbf{R}). \tag{2.71}$$

$\Psi_a(\mathbf{R})$ is a gyrophase average involving the fluctuating potentials $\delta \phi$ and $\delta \mathbf{A}$ ($\mathbf{B} = \nabla \times \mathbf{A}$):

$$\Psi_a(\mathbf{R}) \dot{=} \left\langle \delta \phi(\mathbf{R} + \rho) - \frac{1}{c}(\mathbf{V_0} + \mathbf{v}) \cdot \delta \mathbf{A}(\mathbf{R} + \rho) \right\rangle. \tag{2.72}$$

The gyrophase average of a function $z(\mathbf{r}) = z\left(\mathbf{R} + \rho(\xi)\right) = z(\mathbf{R}, \xi)$ is formally defined as the ξ average at a fixed guiding center position:

$$\langle z \rangle \dot{=} \oint \frac{d\xi}{2\pi} z(\mathbf{R}, \xi). \tag{2.73}$$

$\mathbf{V_0} = V_0\hat{\varphi} = R\omega_0(\psi)\hat{\varphi} = -Rc\partial_\psi\phi_{-1}\hat{\varphi}$ is the lowest-order toroidal flow velocity of the plasma. f_{a0} is a Maxwellian distribution in this rotating frame:

$$f_{a0} = \frac{n_a(\psi,\theta)}{(2\pi T_a/m_a)^{3/2}} \exp\left(-\frac{m_a(\mathbf{v}-\mathbf{V_0})^2}{2T_a}\right), \tag{2.74}$$

which is the zeroth-order solution of kinetic equation. Given the first-order fluctuating distribution function

$$\hat{f}_{a1}(\mathbf{x}=\mathbf{R}+\rho) = -\frac{e_a\delta\phi(\mathbf{x})}{T_a}f_{a0} + H_a(\mathbf{R}), \tag{2.75}$$

one can write the necessary Maxwell equations that complete the system:

Poisson equation

$$-\nabla_\perp^2\delta\phi(\mathbf{x}) = 4\pi\sum_a ez_a\delta n_a = 4\pi\sum_a e_a\int d^3v\,\hat{f}_{a1}(\mathbf{x}). \tag{2.76}$$

Parallel Ampère's Law

$$-\nabla_\perp^2\delta A_\|(\mathbf{x}) = \frac{4\pi}{c}\sum_a \delta j_{\|,a} = \frac{4\pi}{c}\sum_a e_a\int d^3v v_\|\hat{f}_{a1}(\mathbf{x}). \tag{2.77}$$

Perpendicular Ampère's Law

$$\nabla_\perp\delta B_\|(\mathbf{x})\times\mathbf{b} = \frac{4\pi}{c}\sum_a \delta\mathbf{j}_{\perp,a} = \frac{4\pi}{c}\sum_a e_a\int d^3v\mathbf{v}_\perp\hat{f}_{a1}(\mathbf{x}). \tag{2.78}$$

The important fluctuating scalar fields are the electrostatic potential $\delta\phi$ and the electromagnetic fields $\delta A_\| \doteq \mathbf{b}\cdot\delta\mathbf{A}$ and $\delta B_\| \doteq \mathbf{b}\cdot\nabla\times\delta\mathbf{A}$.

A final note on the mathematics behind GYRO is that if one expands a field $z(\mathbf{R})$ in terms of a Fourier basis

$$z(\mathbf{R}) \doteq \sum_{\mathbf{k}_\perp} e^{iS(\mathbf{R})}\tilde{z}(\mathbf{k}_\perp), \tag{2.79}$$

then the gyroaverage operator reduces to

$$\langle z \left(\mathbf{R} + \rho \right) \rangle = \sum_{\mathbf{k}_\perp} e^{iS(\mathbf{R})} J_0 \left(k_\perp \rho_a \right) \tilde{z} \left(\mathbf{k}_\perp \right), \tag{2.80}$$

where $\mathbf{k}_\perp \doteq -i\nabla_\perp$, $\rho_a \doteq v_\perp / \Omega_{ca}$ and J_0 is the Bessel function of the first kind:

$$J_0(x) = \frac{1}{2\pi} \int_{-\pi}^{\pi} e^{ix \sin \tau} d\tau. \tag{2.81}$$

This property, and with their high accuracy and efficiency, is one of the motivating factors for using spectral methods to numerically simulate the gyrokinetic equation.

In summation, GYRO solves the nonlinear electromagnetic gyrokinetic-Maxwell system of equations in toroidal geometry. As it was designed from the outset to compare against experiment, and as the goal of this thesis is to investigate NSTX, GYRO will be the primary tool to probe gyrokinetic electron turbulent transport for the remainder of this work.

2.3.5   Gyrokinetic Turbulence

The gyrokinetic equations of magnetized plasmas contain many unstable roots, each of which represents a different linear mode. The free energy for these instabilities comes from gradients in the background plasma. As such, they are both numerous in type and ubiquitous in nature. Once a single linear mode becomes unstable, the plasma has the potential to become turbulent. Herein, we touch upon a few different kinds of gyrokinetic turbulence.

One of the most prominent drift wave instabilities is the ion temperature gradient (ITG) mode. Driven by gradients in the ion temperature, it was of the first to be studied in depth [64–66]. As the goal of fusion research is fuse ions, the ion temperature in a reactor must be hot. With the central ion temperature greater than that of the edge, the ITG mode's presence seems likely. It exists on "ion scales" of characteristic wavenumbers of $k_\perp \rho_s \sim 1$; the ITG mode grows with

oscillation wavelengths of roughly the ion sound radius. A plasma state based on ITG-driven turbulence should exhibit potential eddies with widths of roughly ρ_s in the perpendicular direction. ITG transport with a simple adiabatic electron response produces no net particle flux, but it can produce significant heat flux. However, when including a more realistic electron treatment, it can produce significant particle flux as well. Furthermore, the mode does not exist in isolation, but nonlinearly interacts with other modes, and while energy may enter the plasma on the ion-scale, it can cascade to other scales. In particular, the ITG mode couples very well to "zonal flows," which are symmetric plasma flows within a flux surface, so named after their counterparts in atmospheric turbulence.

Zonal flows have poloidal wavenumber n and toroidal wavenumber m both equal to zero [67]. Physically, zonal flows appear as poloidal and/or toroidal plasma rotations. In general, these flows are any $m = n = 0$ component of a flow that stays within a flux surface. Since radially elongated eddies produce more radial transport, zonal flows are important, because without finite binormal wavenumber they do not produce radial transport themselves and simultaneously shear apart eddies that do. Zonal flows serve as energy sinks for the plasma, pulling energy out of ITG (or other) turbulence and producing no net radial transport in the process. Because zonal flows are driven by nonlinear energy cascades from other modes, a balancing act emerges: the ITG mode becomes unstable and drives zonal flows, which grow up in amplitude and shear apart the ITG eddies. Eventually the system reaches a steady-state, as the zonal flows themselves cannot grow indefinitely (for instance, they could lose their energy through dissipative processes or by coupling to another plasma oscillation) [68].

The importance of zonal flow dynamics appeared in early simulations of gyrofluid and gyrokinetic turbulence (gyrofluid equations are moments of the gyrokinetic equation, much as fluid equations are moments of the kinetic equation) [69–74]. Of particular interest is the effect they have on the stiff profile phenomenon. An early cross-code benchmarking exercise [75, 76], known as the Cyclone comparison, demonstrated that when the zonal flow effects are taken into account,

one can actually push a temperature gradient beyond the threshold for linear ITG instability before producing significant transport. This nonlinear upshift of the critical gradient (the "Dimits Shift," after the first author of Cyclone benchmark paper) holds the prospect of breaking the boundaries imposed by stiff transport. In this case the ITG mode, though unstable at temperature gradients larger than $R/L_{T_i} \doteq -(R/T)dT_i/dr$ of approximately 4, produced negligible thermal transport below $R/L_{T_i} \approx 6$. The ITG mode could be tamed, up to a point. A 50% increase in achievable local temperature gradient could lead to a significant improvement in achievable core plasma temperature. However, the exact magnitude of the Dimits shift depends upon specific problem parameters, such as plasma shaping [77] and is often smaller than this for actual experimental parameters and when including a non-adiabatic electron treatment [78].

Another method of mitigating the effects of ITG turbulence is from equilibrium $\mathbf{E} \times \mathbf{B}$ flow shear, which can be driven by neutral beam injection, neoclassical effects and even spontaneously by plasma turbulence itself, the mechanisms for which are still an active area of research [79–82]. A strong radial electric field could interact with the magnetic field to produce large scale flows as well. If the electric field has a shear in it, so too would $\mathbf{v}_E$, which could serve to shear apart turbulent eddies. Although still an active area of research, $\mathbf{E} \times \mathbf{B}$ flow shears in general suppress turbulence whose growth rate γ is less than the shearing rate γ_E [71, 72]. By cranking up the shearing rate, one could, in theory, cut off the turbulence before it has a chance to grow. In present machines, one method to do this is with neutral beam injection; however, the scalability of this mechanism to a reactor is unclear. Yet, if plasma turbulence itself can spontaneously drive these equilibrium-scale flows, then perhaps this mechanism for turbulence suppression can exist in a reactor. Presently, the existence of flow shear is thought to be a major contributor to high-confinement operating regimes (known as "H-modes" in contrast to "L-modes"). Achieving similar enhanced performance in a reactor would be desirable. As such, exploring the mechanisms for flow shear generation is a very important and active area of research.

Ion turbulence is much better understood than electron turbulence, which grows up on much smaller time and space scales. Furthermore, a number of possible electron modes could exist in a plasma. These include the trapped electron mode (TEM), which can be driven by either density or temperature gradients and comes from the motions of trapped particles, the microtearing mode, an electro-magnetic mode related to the small-scale breaking of magnetic field lines, and the electron temperature gradient (ETG) mode, which is the electron version of the ITG mode. Understanding electron turbulence is important for the future of MFE systems. In particular, researchers would like to know whether or not electron modes can drive significant heat and particle flux in a reactor, where electrons are bound to be hot (perhaps even hotter than the ions since alpha particles preferentially heat electrons over ions).

A simple estimate of the transport due to ETG turbulence grossly underestimates observed levels of electron heat flux. Since the ITG ion heat diffusivity χ_i should show gyroBohm scaling, so should χ_e, with $i \to e$:

$$\frac{\chi_e}{\chi_i} \sim \frac{\rho_e^2 v_e}{\rho_s^2 c_s} \sim \frac{m_e}{m_i} \sqrt{\frac{m_i}{m_e}} \sim \mu_e^{-1}. \tag{2.82}$$

The square root of the ion-electron mass ratio, $\mu_e \doteq \sqrt{m_i/m_e}$, is roughly 60 for deuterium, thereby suggesting that electron thermal transport should be 60 times smaller than ion heat transport. Yet one of the great experimental mysteries is that frequently $\chi_e \gtrsim \chi_i$. Observations show that electron thermal transport is often as high as ion thermal transport. It is not, as this estimate would have it, much smaller. This contradiction is one of the great reasons why the study of electron turbulence in MFE plasmas is particularly interesting.

Electron Temperature Gradient Turbulence

As mentioned, the isomorphism between ion temperature gradient (ITG) driven and electron temperature gradient (ETG) driven turbulence suggests that ETG turbulence should be very weak. That is, since the original simulations of ITG turbulence for the Cyclone parameters found $\chi_i \sim$

$0.7\rho_i^2 v_{T_i}/L_{T_i} = 0.7\chi_{GBi}$, ETG turbulence with similar parameters, exchanging ions and electrons, should give $\chi_e \sim 0.7\rho_e^2 v_{T_e}/L_{T_e} = 0.7\chi_{GBe}$, which is smaller than χ_i by a factor of $\mu_e \approx 60$ for deuterium. If $\chi_i \approx \chi_e$ in an experiment, this argument would imply that the ETG mode cannot account for observed levels of large electron transport. However, numerical simulations have shown that ETG driven turbulence can be much larger than this estimate, large enough in some cases to be experimentally relevant.

Some important questions regarding ETG transport are

1. How much transport can it produce?

2. How can we control that transport?

The earliest simulations of ETG turbulence found the saturated state as containing radially elongated eddies, or "streamers" [83–85]. This state was characterized by larger levels of transport than one would expect from the ITG-isomorphism argument. Ref. [85] found that for Cyclone-like parameters $\chi_{ETG} \approx 13\chi_{GBe}$, instead of $0.7\chi_{GBe}$, an enhancement of nearly 18.6. Instead of being $\mu_e = 60$ times smaller than χ_i, χ_{ETG} was only about a third of χ_i. These streamers, characteristic of the nonlinear saturated state for ETG turbulence, offer insight into the saturation mechanisms of ETG turbulence. As discussed in Ref. [85], ETG turbulence is thought to be regulated by Kelvin-Helmoholtz-like (K-H) instabilities, which are driven by flow shears. At modest values of magnetic shear the ETG mode saturates by driving a zonal flow secondary ("Rogers" [68]) instability, from shears in perpendicular velocities. However, the ions' motion shields the electrons from the zonal flows, allowing a larger saturation level than ITG turbulence. The result in this situation is elongated streamers that can drive large amounts of transport. At negative magnetic shear, the ETG mode becomes highly localized along a field line and has a strong parallel velocity. Shears in this parallel velocity drive another K-H-like mode, known as the "Cowley" secondary instability [61]. The Cowley instability is very strong in this case and ETG saturates at low levels of transport. The

magnitude of saturated ETG turbulence depends on whether the relative weak Rogers or relatively strong Cowley instability balances the ETG mode.

This mechanism allows ETG streamers to grow to very high amplitudes before they saturate, bringing with them large levels of transport that correspond to electron heat diffusivities of several gyroBohms. Furthermore, the magnitude of transport depends largely on the driving gradient, and how far it is above criticality:

$$\chi_e = C_e \chi_{GBe} \left[\left(\frac{R}{L_{T_e}} \right) - \left(\frac{R}{L_{T_e}} \right)_{\text{crit}} \right], \tag{2.83}$$

$$\chi_i = C_i \chi_{GBi} \left[\left(\frac{R}{L_{T_i}} \right) - \left(\frac{R}{L_{T_i}} \right)_{\text{crit}} \right]. \tag{2.84}$$

$$\tag{2.85}$$

The precise value of C_i depends on the strength of the nonlinearly-upshifted $(R/L_{T_i})_{\text{crit}}$, which falls in the range of $5.3 - 6$ in Ref. [75]. But as an example, if as found in Refs. [83–85], $C_e \approx 10 C_i$, the difference in magnitude between χ_e and χ_i could potentially be made up in plasmas with $[(R/L_{T_e}) - (R/L_{T_e})_{\text{crit}}] > 6 [(R/L_{T_i}) - (R/L_{T_i})_{\text{crit}}]$. A formula for the ETG linear critical gradient was found for large-aspect ratio tokamaks as [86]:

$$\left(\frac{R}{L_{T_e}} \right)_{\text{crit}} = \max \left\{ (1 + \tau) \left(1.33 + 1.91 \frac{\hat{s}}{q} \right) (1 - 1.5\epsilon) \left(1 + 0.3\epsilon \frac{d\kappa}{d\epsilon} \right), 0.8 \frac{R}{L_n} \right\} \tag{2.86}$$

$L_n = -(1/n_e)(dn_e/dr)$ is the inverse density gradient length. Many of the key parameters are geometric, which include the elongation κ, $\epsilon = r/R_0$, q and $\hat{s} \doteq (r/q)(dq/dr)$, the magnetic shear. The other major parameter in this formula is τ:

$$\tau = \frac{T_e}{n_e} \sum_i \frac{n_i Z_i^2}{T_i} \approx Z_{eff} \frac{T_e}{T_i}. \tag{2.87}$$

If all ions i have comparable temperatures, equation 2.87 can be reduced to include Z_{eff}, the effective charge state of the ions. If the plasma is purely hydrogenic, $Z_{eff} = 1$. It is defined as [87]:

$$Z_{eff} = \frac{\sum_i n_i Z_i^2}{\sum_i n_i Z_i} = \sum_i \frac{n_i Z_i^2}{n_e}, \qquad (2.88)$$

according to the plasma quasineutrality condition $n_e = \sum n_i Z_i$. Z_i is each ion's charge state: $e_i = e Z_i$. Although calibrated to only a selected parameter range ($\hat{s} > 0.2$ and low normalized pressure gradient $\alpha < 0.1$), the critical gradient formula in Eq. 2.86 still gives clues about how to affect ETG transport. Clearly the magnetic geometry, as characterized by q and $\hat{s}$, is important. The particular theoretical importance of $\hat{s}$ in determining the nonlinear saturated state was discovered early on [83]. For $\hat{s} > 0.5$, ETG could produce high levels of thermal transport. For $\hat{s} = -1$, electron thermal transport was found drop an order of magnitude relative to positive shear, though it could still be significant if strongly driven above the linear critical gradient, $R/L_{T_e} \sim 2(R/L_{T_e})_{\text{crit}}$ [85]. Changing the magnetic shear thus has a large influence on both the transport level and the achievable temperature gradient. This picture is consistent with the Rogers-Cowley secondary instability saturation mechanism.

A major assumption made in these first generation ETG simulations is that of an adiabatic ion response. Namely the perturbed ion distribution function f_i (in particle coordinates) evolves according to [88]

$$\frac{\delta f_i}{n_i F_M} = -\frac{Z_i e \delta \phi}{T_i}. \qquad (2.89)$$

F_M is the Maxwellian distribution. In other words $n_i \sim \exp\{-Z_i e \delta \phi / T_i\}$. Formally the adiabatic approximation arises in the limit where the ion gyroaverage operator tends to zero. A major cross-code comparison (with parameters like the Cyclone case, but for ETG instead of ITG) concluded that this assumption, however, was invalid for certain parameters [89]. Specifically, when $\hat{s} > 0.5$ and trapped electrons are included, simulations with adiabatic ions (ETG-ai) over-estimated transport levels when compared with kinetic ion (ETG-ki) simulations. Sometimes, ETG-ai runs

failed to saturate at all, reaching fluxes that were orders of magnitude larger than those found with the more expensive ETG-ki runs. Yet, these ETG-ki simulations could still produce experimentally relevant values of $\chi_e \sim 10\rho_e^2 v_e/L_{T_e}$. Again, magnetic shear could alter the saturated transport levels. But the general view is that ETG can potentially produce transport that is much larger than from a simple ITG-ETG isomorphic argument. The physical mechanism for this difference is that for ITG turbulence adiabatic electrons can only move along parallel field lines, so they cannot shield a radial (zonal) electric field. This enhances zonal flows and reduces ITG turbulence. For ETG turbulence, however, the ions are adiabatic not because of quick parallel motion but because of large perpendicular wavenumbers, $k_\perp \rho_i \gg 1$, making them able to effectively shield a radial electric field. This reduces zonal flows and enhances the saturated level of turbulence.

Simulations involving ETG turbulence are challenging, and the absolute levels of flux depend largely on the parameters of the system. Because of their poloidally thin and radially elongated eddies, simulations need to have relatively large box sizes. The growth of large wavelength modes appears to be another challenge, as it makes saturation difficult. Ref. [90] found that for certain parameters, saturation was not simply a kinetic-adiabatic ion mechanism, as even ETG-ki simulations could fail to saturate. However, turning on electron collisions or $\mathbf{E} \times \mathbf{B}$ flow shear could stabilize the simulations. Both of these mechanisms stabilize long-wavelength modes, such as the trapped electron mode. This is also consistent with the mechanism for poor ETG-ai saturation in Ref. [89]. Unlike the simulations of Refs. [83–85], these simulations included the effects of trapped particles. This turns on the longer wavelength trapped electron mode. Using kinetic ions reduces the zonal flow shielding, enhancing the zonal flows, which helps stabilize long wavelength modes. Collisions, equilibrium flow shear and kinetic ions can all help ETG simulations saturate by stabilizing the growth of long wavelength modes. But in general, despite their difficulty, simulations of ETG turbulence tend to saturate at large levels, which may be experimentally relevant.

The absolute magnitude of ETG driven turbulence appears to depend on the specific problem parameters. In one situation involving both ion and electron scales, it was found that ITG tur-

bulence could swamp out the smaller-scale ETG turbulence [88, 91]. However, these simulations were run with very large ion temperature gradients, and reducing the ion drive closer to marginality could allow the electrons to grow up to higher amplitudes [92]. When ions and electrons are both driven at experimental gradients, ETG and ITG again could compete. Additionally, $\mathbf{E} \times \mathbf{B}$ flow shear affects ions more readily than electrons, because of slower ion growth rates. In situations like this, should the flow shear quench ITG turbulence, perhaps the ETG mode could be more important.

Revisiting the outstanding questions for ETG turbulence, how much transport it can produce and how it can be controlled, the universal answer appears to be "it depends." The magnitude of ETG thermal transport appears to depend on the problem parameters and the models used, sometimes lying near experimental levels, other times too high, or too low. In terms of controlling ETG, certainly magnetic shear is an important parameter. Presumably so is $\mathbf{E} \times \mathbf{B}$ flow shear, although ETG has growth rates that are μ_e times greater than ITG, so γ_E would need to be very large to suppress ETG growth. Because Z_{eff} and T_e/T_i affect the linear ETG drive, they could also affect the nonlinear turbulent state. Finally, the interaction of ETG with longer-wavelength modes, such as ITG and TEM, may also alter saturated thermal transport.

Ion turbulent transport is thought to govern the performance of many MFE devices; however, when electron turbulent transport is experimentally relevant remains much more of an open question. Yet in one machine, electron transport is considered especially important, making it an excellent laboratory for the study of ETG turbulence. Housed at the Princeton Plasma Physics Laboratory, that machine is the National Spherical Torus Experiment, NSTX.

Chapter 3

Turbulent Transport in the National Spherical Torus Experiment (NSTX)

A few reasons make the National Spherical Torus Experiment (NSTX) [93] at the Princeton Plasma Physics Laboratory an excellent laboratory for the study of electron turbulence and transport. First of all, electrons can be the dominant loss mechanism in NSTX: ion transport in NSTX often approaches neoclassical levels, especially in H-mode plasmas, while electron losses are highly "anomalous." Secondly, NSTX is equipped with a coherent microwave scattering diagnostic, designed to study electron-scale (high-k) density fluctuations. Combined with its abilities to heat electrons to very high temperatures and reach extreme values of magnetic shear, these features of NSTX make the machine aptly suited for the study of electron transport in general, and ETG turbulent transport in particular.

3.1   The National Spherical Torus Experiment

The National Spherical Torus Experiment (Fig. 3.1) at the Princeton Plasma Physics Laboratory is the flagship spherical torus in the United States. A spherical torus (or ST, also sometimes called a
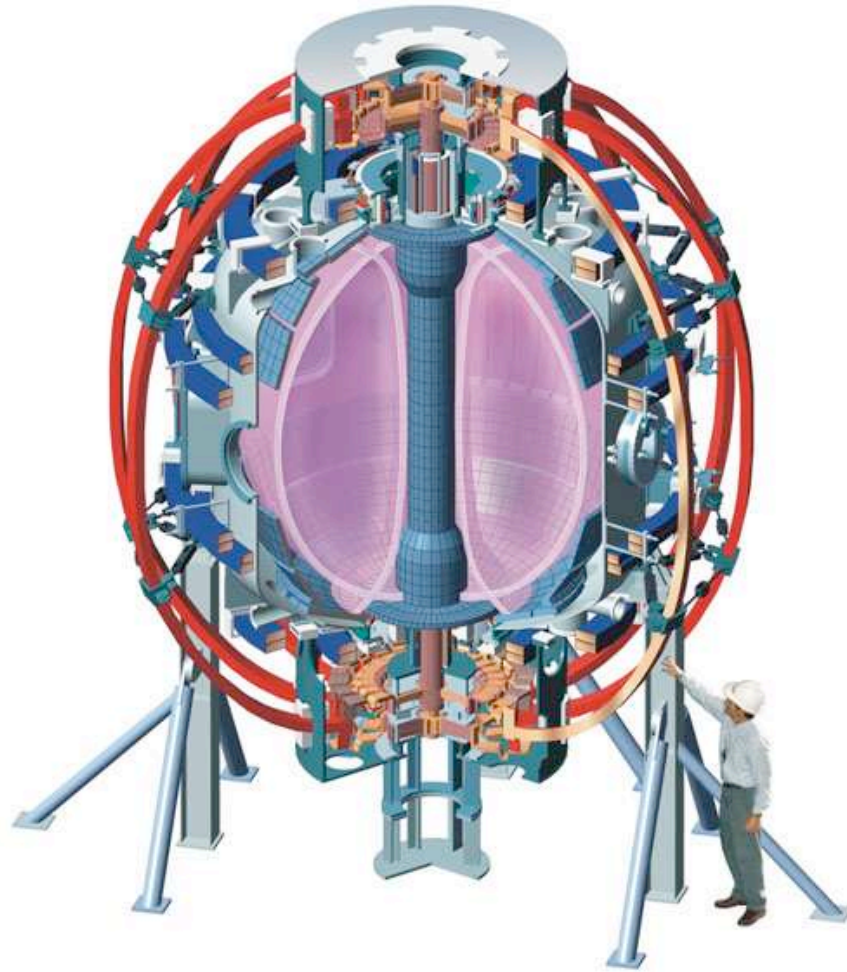
Figure 3.1: An artist's rendition of the National Spherical Torus Experiment (NSTX), shown with an engineer for scale. Image: Princeton Plasma Physics Laboratory.

Table 3.1: Typical NSTX Plasma Parameters, data from Ref. [94].

Parameter	Value
Major radius R_0	85 cm
Minor radius a	67 cm
Plasma current I_p	≤ 1500 kA
Pulse length	≤ 1 s
Toroidal field	≤ 0.55 T
Neutral beam (NB) power	≤ 7 MW
Radio-frequency (RF) power	≤ 6 MW
Peak electron temperature	1.5 keV (NB); 5 keV (RF)
Peak ion temperature	$1 - 1.5$ keV
Core electron density	$10^{19} - 10^{20}$ m^{-3}
Toroidal β	$\leq 35\%$

"spherical tokamak") is a tokamak with a low aspect ratio R_0/a. In this low-aspect ratio magnetic geometry, with the major radius R_0 not much larger than minor radius a, particles spend more time on the inboard side of the plasma ($R < R_0$) then on the outboard side ($R > R_0$). This could improve some of the stability properties of the plasma, because a centrifugal force would tend to push a toroidally moving particle radially outward. If that particle were on the inboard side of the plasma, that force would serve to push the particle back into the center of the plasma, whereas an outboard-oriented particle would be pushed away from the plasma. Minimizing the time a particle spends on the outboard side of the plasma could improve its confinement.

Other interesting features of the ST concept include a more compact design, which may positive have economic implications for a fusion power plant, and the ability to achieve high values of magnetic pressure, β. Since β is a measure of the plasma pressure to the magnetic pressure, a higher β means that a larger density and temperature can be sustained with a lower magnetic field. Additionally, NSTX can have very large values of $\mathbf{E} \times \mathbf{B}$ flow shear, which is beneficial for controlling the effects of turbulence. Some typical plasma parameters for NSTX can be found in Table 3.1.

3.1.1 Global Energy Confinement

Energy confinement in NSTX is not like that of typical large-aspect-ratio tokamaks. Unlike other devices, ion thermal transport is not extremely anomalous, often dipping to neoclassical levels in H-modes [95]. This is thought to occur for a few reasons. For one, neoclassical transport in NSTX is actually very high, so having neoclassical levels of ion transport isn't really that great anyway. But, in H-mode, NSTX can also have very high levels of $\mathbf{E} \times \mathbf{B}$ flow shear, which can exceed the growth rates of ion-scale turbulence [96]. The logic in these cases is that large flow shears suppress ion turbulence and, therefore, reduce ion thermal transport.

Electron transport in NSTX is, however, extremely large. χ_e can approach or exceed χ_i, even though the neoclassical electron diffusivity is 60 times smaller than that of the ion, indicating anomalous electrons. Additionally, electron transport tends to dictate the global scaling of energy confinement, which is, without lithium wall conditioning [95]:

$$\tau_E \sim B_\varphi^{0.9} I_p^{0.4}.$$
(3.1)

The toroidal field scaling, $B_\varphi^{0.9}$, is stronger than both the plasma current scaling, $I_p^{0.4}$, and that found in the ITER98PB(y,2) scaling of other tokamaks [97]. Furthermore, analysis has found that electrons play a major role in determining the B_φ part of the total energy scaling [95]. The logic is that the electron contribution to energy transport is higher in NSTX than in other devices and is the dominant loss mechanism in NSTX.

The highly anomalous electron confinement in NSTX makes it an excellent laboratory for the study of electron turbulent transport. As the ions in NSTX can display non-turbulent levels of transport, electron turbulent transport may be better isolated in NSTX, simplifying the analysis of electron-scale turbulence, which can be muddled when one must consider ion-electron interactions.

3.1.2   High-k Scattering Diagnostic

One of the most important experimental tools for studying electron turbulence on NSTX is the high-k microwave scattering system [98]. This diagnostic uses the scattering of coherent electromagnetic waves to achieve localized measurements of electron density fluctuations. Microwaves launch into the plasma from a probe beam and Thomson scatter off electrons and into collecting optics, whose geometric relationships to the probe beam determine the specific wavenumber k of the measured fluctuations [99]. Specifically, the angle θ between the incident and scattered waves must satisfy a Bragg condition:

$$k = 2k_i \sin\left(\frac{\theta}{2}\right).$$

(3.2)

k_i is the incident wave number. Therefore, by adjusting the geometric angle between the launching and collecting optics, one can fine-tune a system to search for fluctuations around very specific values of k. The exact resolution depends upon the beam spectrum, which doesn't emit a single wavenumber but rather some spread. As such, the diagnostic is sensitive to fluctuations around k, with a spread Δk that is set by the physical width of the probe beam. The additional parameter that determines the measured fluctuations is set by the turbulence itself, with its perpendicular wavenumber $k_\perp$ much larger than its parallel wavenumber $k_\parallel$ (corresponding to greater variation perpendicular to the magnetic field than along the magnetic field):

$$k_\parallel \ll k_\perp.$$

(3.3)

The scattering volume is defined as that part of probe-scatter intersection volume that satisfies both Eqs. 3.2 and 3.3. Since the latter condition is determined in part by magnetic geometry, NSTX's magnetic field allows its scattering system to have an extremely localized measurement volume.

The NSTX collective scattering system measures electron-gyroradius-scale density fluctuations up to $k_\perp \lesssim 20 \text{ cm}^{-1}$, corresponding to typically $k_\perp \rho_e \lesssim 0.6$. It has five detection channels, with each one measuring around a distinct value of k at a resolution of $\Delta k \approx 0.7 \text{ cm}^{-1}$.

Being sensitive to these small scales, the NSTX system was designed to specifically measure ETG-like fluctuations. ETG turbulence, being the electron counterpart to ITG turbulence, has typical fluctuation spectra peaking near $k_\theta \rho_e \approx 0.3$. The NSTX scattering volume is sensitive to wavenumbers this high. Furthermore, the frequency of the observed spectra can allow one to distinguish between density fluctuations moving in the ion and electron directions. With sensitivity to small-scale oscillations and the ability to distinguish between electron and ion modes, the NSTX high-k scattering system is well-posed to probe the existence of ETG-induced density fluctuations.

However, one subtlety is that the high-k system observes $k_\perp \rho_e \lesssim 0.6$ and not $k_\theta \rho_e \lesssim 0.6$. Radially elongated streamers, like those found in early ETG simulations, correspond to high k_θ and low k_r (greater variation in the poloidal direction than the radial). Both of these directions are perpendicular to the magnetic field. So while it's true that ETG streamers are small-scale perpendicular oscillations with large values of $k_\perp$, they preferentially have $k_\theta > k_r$. The high-k measurement system, on the other hand, preferentially measures $k_r > k_\theta$ [98]. Plans do exist to change the configuration in the upcoming years to measure $k_\theta > k_r$ [100], and one expects some degree of nonlinear turbulent scattering to a variety of wavenumbers, but the difference between high values of k_θ and high values of $k_\perp$ is an important one to keep in mind, especially when investigating ETG turbulence.

To sum up, the high-k collective scattering diagnostic is uniquely suited to study electron turbulence, because it can observe fluctuations as small as $k_\perp \rho_e \sim 0.6$ and it can distinguish between ion- and electron-directed motion. However, given the unique geometry of the system, measurements from the high-k system must be carefully interpreted when applying them to the study of ETG turbulence.

3.2 ETG Experiments on NSTX

A number of experiments have been conducted on NSTX to investigate ETG turbulence. A few can be grouped into two categories. The first involve driving ETG turbulent transport while observing high-k fluctuations. The second set of experiments attempts just the opposite: suppressing ETG. While an impressive body of work, these ETG experiments offer just as many new questions as they do answers.

3.2.1 Electron-Scale Fluctuations

Experimental investigations of ETG turbulence in NSTX have found a connection between high-k density fluctuations and gradients in the electron temperature. This work supports the idea that ETG could be one of the energy loss mechanisms in NSTX.

The earliest use of the high-k system involved using RF power to push the core electron temperature, and the temperature gradient, to very high values, exceeding the critical threshold for ETG instability [101, 102]. As the local electron temperature gradient surpassed this value, high-k activity increased. These density fluctuations were not only in the electron diamagnetic direction, indicative of an electron mode, but were also at very small scales, with $k_\perp \rho_e \sim 0.1 - 0.2$. An example discharge, 124948 is shown in Fig. 3.2. At $r/a \approx 0.38$, the ETG mode is unstable at 0.3 s but stable at 0.43 s. High-k power spectra at this radial location are relatively two orders of magnitude stronger when the mode is unstable than when it is stable. This, combined with the fact that these oscillations appear in the electron diamagnetic direction, suggests that these fluctuations measure ETG-driven turbulence.

High-k fluctuations can also appear during neutral beam-heated discharges on NSTX. In these situations, NSTX can have large values of $\mathbf{E} \times \mathbf{B}$ flow shear. High-k activity coincides with an $\mathbf{E} \times \mathbf{B}$ shearing rate that is comparable to or lower than the linear ETG growth rate. When the
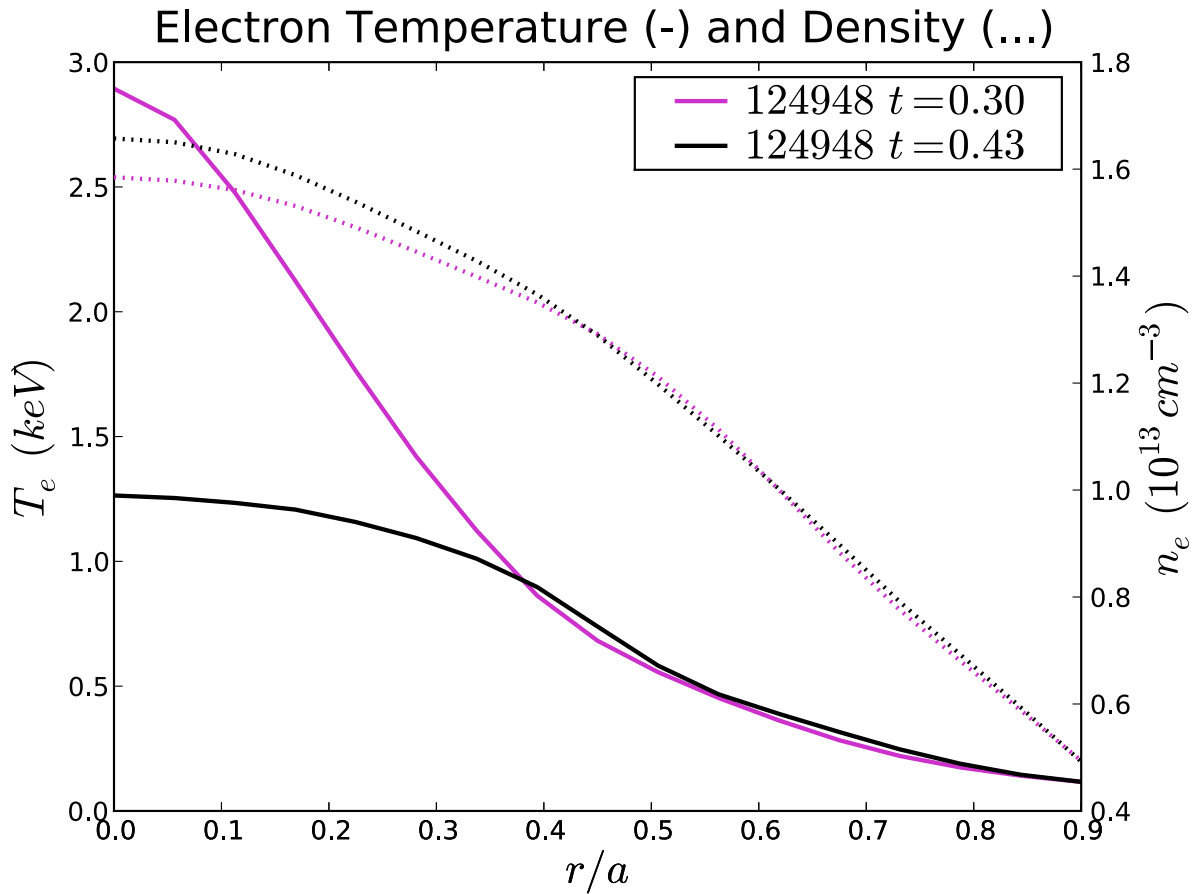
Figure 3.2: Electron temperature and density profiles, NSTX shot 124948 at two different times, 0.3 s (purple) and 0.43 s (black). At $r/a \approx 0.38$, the ETG mode is linearly unstable at 0.3 s and high-k measurements indicate electron-scale density fluctuations, which disappear as the mode stabilizes at 0.43 s.

$\mathbf{E} \times \mathbf{B}$ shearing rate exceeds the linear growth rate of the ETG mode, the observed fluctuations disappear [103].

Yet the link between high-k fluctuations and thermal transport levels is less clear. For instance, fluctuations can exist where ETG is linearly stable or when electron thermal transport is low [104]. Since turbulence is an inherently nonlinear process, fully understanding these fluctuations in the context of linear gyrokinetics has its limitations.

These experiments, while providing important evidence of the existence of ETG turbulence in NSTX, have left a few questions unanswered:

1. Are high-k fluctuations indicative of ETG turbulence?

   In some cases, ETG appears to be at least linearly unstable during high-k activity. However, the saturated turbulent state involves the interaction of many linear eigenmodes. If another mode is simultaneously unstable, the high-k diagnostic may not be solely measuring ETG-driven turbulence. Since the diagnostic measures $k_r > k_\theta$, it may in fact only be picking up the tail end of a turbulent power spectrum, even when ETG turbulence is present.

2. If so, how much thermal transport does ETG cause?

   In NSTX situations where ETG is thought to exist, for how much of the measured electron thermal transport can it account? This aims at the heart of the matter: does ETG produce experimentally-relevant levels of transport? If ETG exists, it either limits the performance of the machine (through a large ETG-created turbulent flux), or is more benign than other instabilities.

In essence, experimental evidence exists that ETG turbulence may be causing electron-scale density fluctuations in NSTX; however, the relationship between these fluctuations and the device's confinement properties is less firm. The questions raised by these experiments cannot be answered from a purely linear gyrokinetic analysis. Nonlinear gyrokinetic simulations of realistic NSTX

experimental parameters are necessary to elucidate the link between turbulent fluctuations and electron thermal transport.

3.2.2   Internal Transport Barriers

Often NSTX exhibits stiff electron temperature profiles, whereby the plasma's temperature gradients cannot significantly exceed the linear threshold for turbulent instability, even under strong external heating. However, in certain cases, NSTX has *electron internal transport barriers* (or e-ITBs), which are plasmas with very steep electron temperature profiles, the gradients of which often greatly exceed the linear critical gradient for the onset of the ETG mode. In these cases, some mechanism appears to suppress transport from ETG turbulence. Experimental evidence suggests that this mechanism is reversed magnetic shear.

An example of an electron internal transport barrier is shown in Fig. 3.3. Shot number 129354 displays a very steep electron temperature gradient at $r/a \approx 0.3$, while the gradients in shot 129347 are much less intense. The steeper gradients of the e-ITB allow its core temperature be over 50 percent greater than those of a non-e-ITB. The puzzle with e-ITBs is that at such steep electron temperature gradients, they should be unstable to ETG turbulence. They should be *extremely* unstable to ETG turbulence, often exceeding the linear critical gradient by 200-300 percent [38].

e-ITBs can be found in a variety of plasma conditions. They can be formed with RF or NB heating, using deuterium or helium. Their location is correlated with neither that of maximum $\mathbf{E} \times \mathbf{B}$ shear nor that of the minimum value of q. Nor does their existence appear to depend upon $\tau = Z_{eff}T_e/T_i$ [38].

Instead, the single parameter that experimentally dictates the formation of NSTX e-ITBs is the magnetic shear, $\hat{s}$. No e-ITB has been found on NSTX without reversed magnetic shear. Every NSTX e-ITB has $\hat{s} < 0$ [38, 39]. The difference between the discharges in Fig. 3.3 comes down to their q-profiles. The "standard" non-e-ITB discharge has a monotonic q-profile. The e-ITB
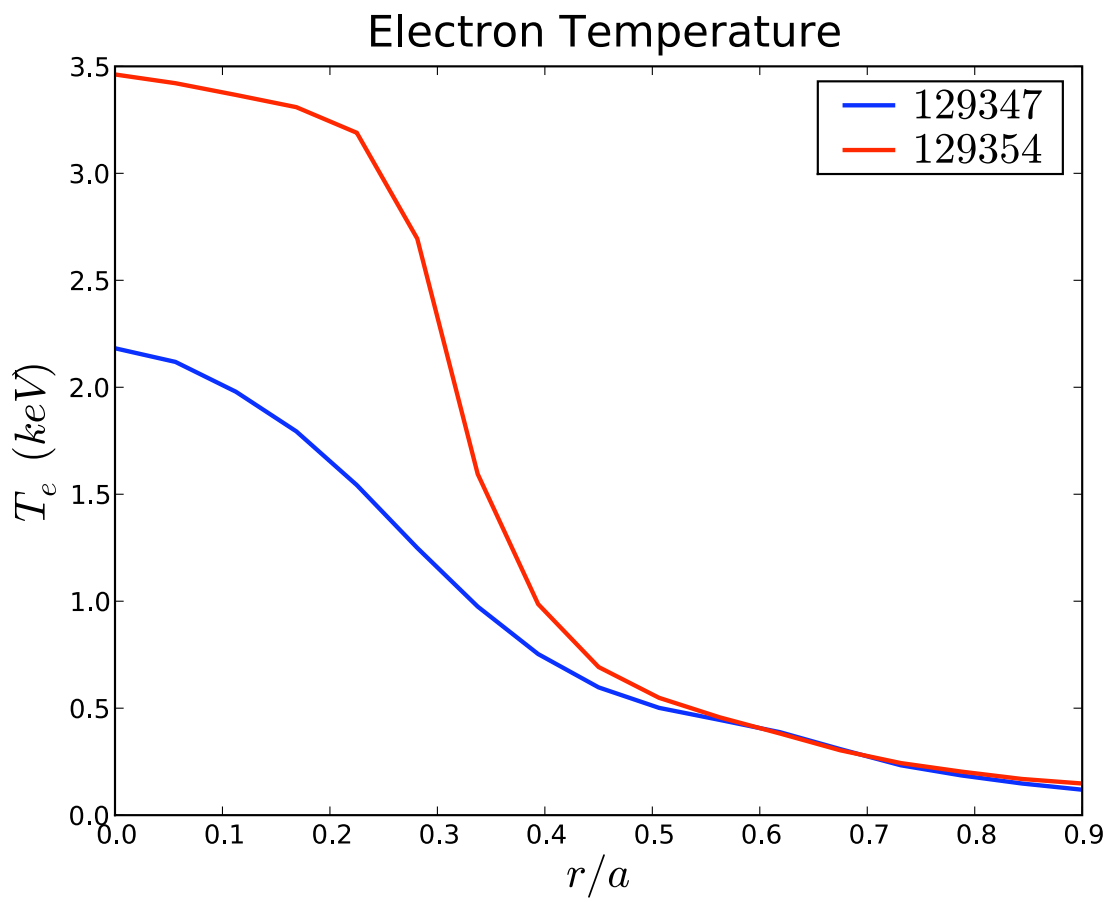
Figure 3.3: Electron temperature profiles of NSTX with (shot 129354 @ 240 ms, red) and without (shot 129347 @ 400 ms, blue) an electron internal transport barrier.
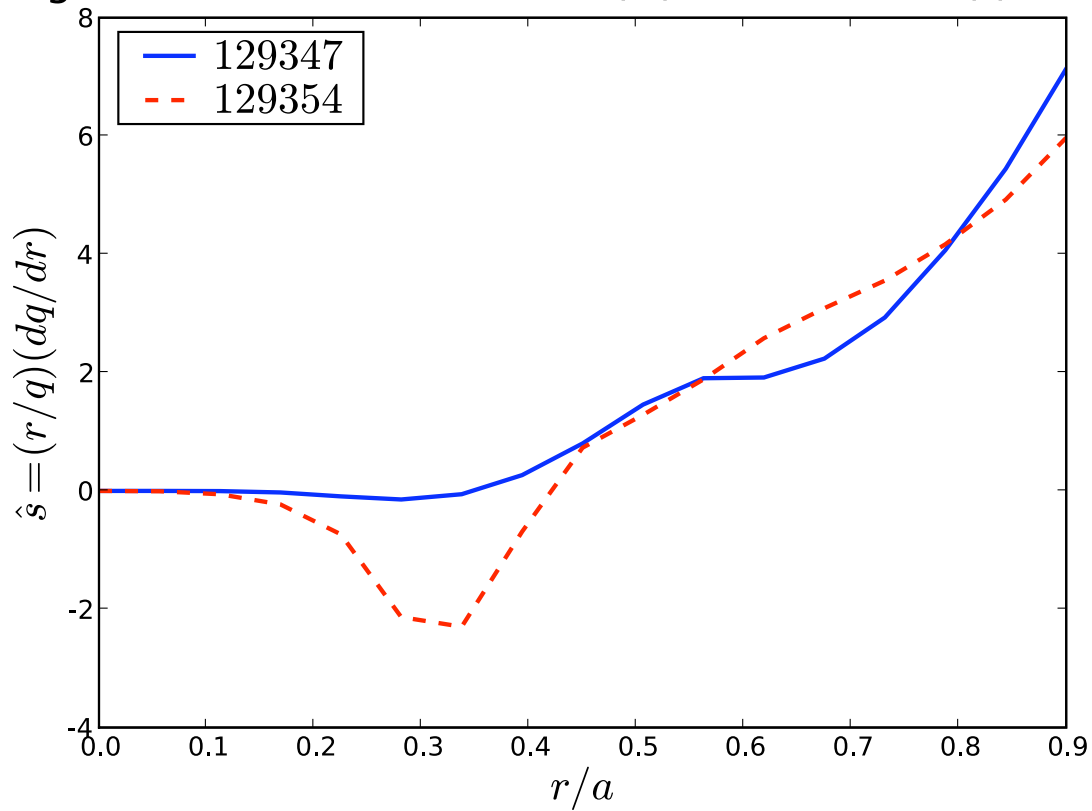
Figure 3.4: Magnetic shear profiles for discharges with (dashed) and without (solid) an e-ITB. The NSTX discharges are those of Fig. 3.3.

does not. Figure 3.4 shows the magnetic shear profiles $\hat{s} = (r/q)(dq/dr)$ for the discharges in Fig. 3.3. $\hat{s}$ is sharply negative for the e-ITB, but stays mostly positive for the other discharge (a slight dip may exist near $r/a = 0.3$, but it is much more modest than the e-ITB's). This region of negative $\hat{s}$ coincides with the location of the e-ITB, where the electron temperature profile steepens. Reversed magnetic shear, corresponding to negative values of $\hat{s}$, triggers high-electron confinement discharges in NSTX. These electron internal transport barriers violate the stiff-profile phenomenon, reaching temperature gradients that exceed the local threshold for ETG turbulence by factors of two or three.

e-ITBs also coincide with a reduction in high-k turbulence [39]. Within the transport barrier, high-k amplitudes generally decrease to low levels. However, in some cases and especially during strong heating, the diagnostic measures bursts of activity. These intermittent "bursts" have growth rates comparable to ETG linear growth rates and reach very high amplitudes, before crashing down and disappearing. The growth rates and frequencies of these signals serve as further evidence that the high-k system is measuring ETG turbulence. That the ETG-like bursts quickly die, combined with the general low level of high-k activity, suggests that reversed magnetic shear is reducing ETG turbulence, thereby allowing NSTX to exceed the linear ETG threshold and form an e-ITB.

Despite this experimental evidence of the suppression of ETG turbulence by reversed-shear, a few questions remain.

1. Is reversed shear the single important parameter?

   Recall from Eq. 2.86 that $\hat{s}$ is only one of many factors that affects the linear growth rate of the ETG mode. Perhaps e-ITBs are not triggered by $\hat{s}$, but by one of these other factors instead, like Z_{eff} and T_e/T_i. Experimentally, reversed shear seems to be the key. Can the same be found numerically?

2. What limits the maximum achievable temperature gradient of an e-ITB?

If ETG controls the temperature profile, and reversed shear suppresses ETG transport, what prevents the plasma from heating up indefinitely?

3. What causes the high-k bursts?

Are they signatures of ETG turbulence? If so, why are they intermittent and what causes their decay?

Electron internal transport barriers are high-confinement operational modes in NSTX that display electron temperature gradients well above the threshold for local linear ETG instability. Experimentally, they appear to be triggered by a reversal in NSTX's magnetic shear and coincide with a reduction in electron-scale density fluctuations, but the effects of magnetic shear alone cannot be simply determined during a dynamic plasma experiment with many constantly changing parameters. Nonlinear gyrokinetic simulations of e-ITB plasmas, in which the effects of magnetic shear can be more easily isolated, could help answer some of the remaining questions regarding e-ITBs.

ETG turbulent transport appears to be at work in some NSTX plasmas. Excellent experimental evidence, supported by linear gyrokinetic analysis, suggests not only that ETG can exist, but that it can also be controlled, with both $\mathbf{E} \times \mathbf{B}$ flow shear and magnetic shear. In the latter case, the suppression of ETG appears to be so great as to trigger high-confinement electron internal transport barriers. However, the link between density fluctuation measurements and ETG-driven thermal transport remains less clear. Hopefully, nonlinear gyrokinetic simulations of realistic NSTX experiments can cut through some of the fog, by showing if ETG turbulence exists, the degree to which it causes thermal transport and how best to overcome it.

Chapter 4

Gyrokinetic Simulations of Electron Turbulence in NSTX

With experimental evidence for the existence of ETG turbulence in NSTX growing, we turn toward gyrokinetic simulations for further insight. The question remains to what extent can such simulations support (or refute!) the experimental observations of ETG modes driving significant thermal transport in NSTX.

In essence, we hope that nonlinear gyrokinetic simulations of NSTX discharges can elucidate the role of ETG turbulence in determining electron confinement. Some key questions are:

- Does ETG turbulence exist on NSTX?

- If so, how much electron energy transport does it produce?

- How can we know if ETG turbulence is active in the experiment?

- Does the high-k diagnostic measure ETG-driven fluctuations?

- How can we control electron turbulence in NSTX?

To answer some of these questions, we turn now to two discharges from NSTX, discussed in Chapter 3. The first, 124948, whose electron temperature and density profiles are in Fig. 3.2, is an radio-frequency (RF) heated L-mode. At 0.3 s, the plasma at $r/a = 0.35$ becomes linearly unstable to the ETG mode, at which point the high-k diagnostic measures enhanced fluctuations [101]. After the RF is turned off, the profile relaxes and by 0.43 s, ETG is linearly stable, and the enhanced fluctuations disappear. Taken as a whole, this discharge is thought to present strong evidence that ETG turbulence causes the high-k fluctuations. In other words, ETG-driven turbulence can exist in NSTX, and the high-k system can measure it. In this chapter, we use global nonlinear gyrokinetic simulations to investigate 124948 at 0.3 s, during the peak in high-k activity, with the goal to provide numerical evidence of the existence of ETG turbulence in this case.

The second discharge, 129354, is an example of an electron internal transport barrier (or e-ITB). At 0.23 s, the magnetic shear displays a strong reversal at $r/a \approx 0.3$, at which point the electron temperature profile, shown in Fig. 3.3, becomes extremely steep, increasing by a factor of 3 when moving inward from $r/a = 0.4$ to 0.2. With an e-ITB, like that of 129354, high-k activity generally decreases, although occasionally signal bursts with ETG mode growth rates and frequencies appear. Experimentally, e-ITBs require a magnetic shear reversal [38, 39]. Numerically, the goal is to pin down the cause of their formation, separating the effects of $\hat{s}$ from other parameters, such as Z_{eff}. Through a series of local and global gyrokinetic simulations of 129354, we aim to do just that, to see if ETG suppression by magnetic shear alone can trigger e-ITBs.

But before trying to suppress ETG turbulence in NSTX, we first determine its strength, by verifying the linear gyrokinetic predictions with nonlinear simulations.

4.1 Driving ETG Turbulence

In an attempt to quantify the degree to which ETG can account for observed levels of electron transport, we use gyrokinetics to simulate an experimental discharge thought to give strong evidence of ETG activity in NSTX. 124948 at 0.3 s is linearly unstable to the ETG mode.

4.1.1 Linear Analysis
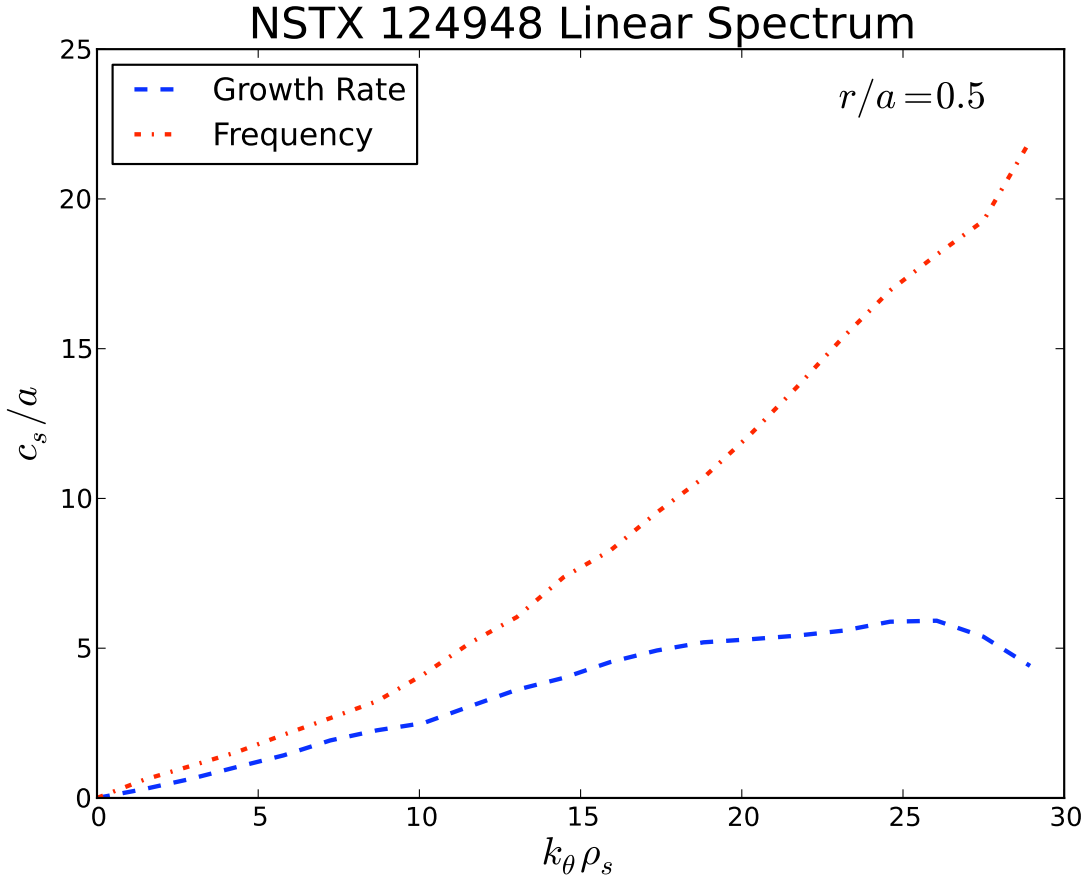
Figure 4.1: GYRO-calculated linear spectrum of unstable high-k modes for NSTX shot 124948 @ 300 ms, at $r/a = 0.5$. For reference, the $\mathbf{E} \times \mathbf{B}$ shearing rate γ_E at this time is $0.1\ (c_s/a)$.

The ETG mode is linearly unstable during this discharge. Figure 4.1 shows the fastest growing linear mode at $r/a = 0.5$. The mode is in the electron direction and has a peak growth rate in the electron range, $k_\theta \rho_s \sim 25$. The $\mathbf{E} \times \mathbf{B}$ shearing rate γ_E at this time is 0.1 (c_s/a), so its effect on these modes, with much larger growth rates, is unlikely.

TGLF also shows the ETG mode to be unstable, as shown in Figure 4.2, a plot of ion and electron growth rates and frequencies for $r/a = 0.3, 0.4, 0.5$ and 0.6. At all radii the ETG mode is the fastest growing mode. However, it does not appear to be the only unstable mode in this discharge. Changes in the real frequency spectrum, such as that at $k_\theta \rho_s = 10$ at $r/a = 0.3$ suggest changes in the mode's dispersion relation. Also at larger radii modes in the ion diamagnetic direction (red) compete with those in the electron direction. But, the salient point is that the ETG mode is the most unstable during shot 124948 between r/a of 0.3 and 0.5, when and where the high-k diagnostic measures fluctuation activity on the electron-scale.

4.1.2 TGLF-NEO flux calculations

As a rough sketch of transport properties of this plasma, we can use TGLF [105, 106] and NEO [107] to calculate turbulent and neoclassical thermal diffusivities for this shot. TGLF is a reduced model that calculates quasilinear-based estimates of turbulent fluxes. TGLF has specific models for nonlinear saturation mechanisms, such as zonal flows, and is calibrated to nonlinear GYRO simulations. While TGLF itself is deterministic (given a set of input parameters, the calculated fluxes will be accurate to machine precision), the calculations are sensitive to input parameters. An in-depth discussion of this effect and its implications to experimental comparisons appear in Section 4.3. But in what follows we show only error bars for GYRO calculations, which represent a standard deviation in the fluctuating turbulent quantities, and save the discussion on input sensitivity for Section 4.3.
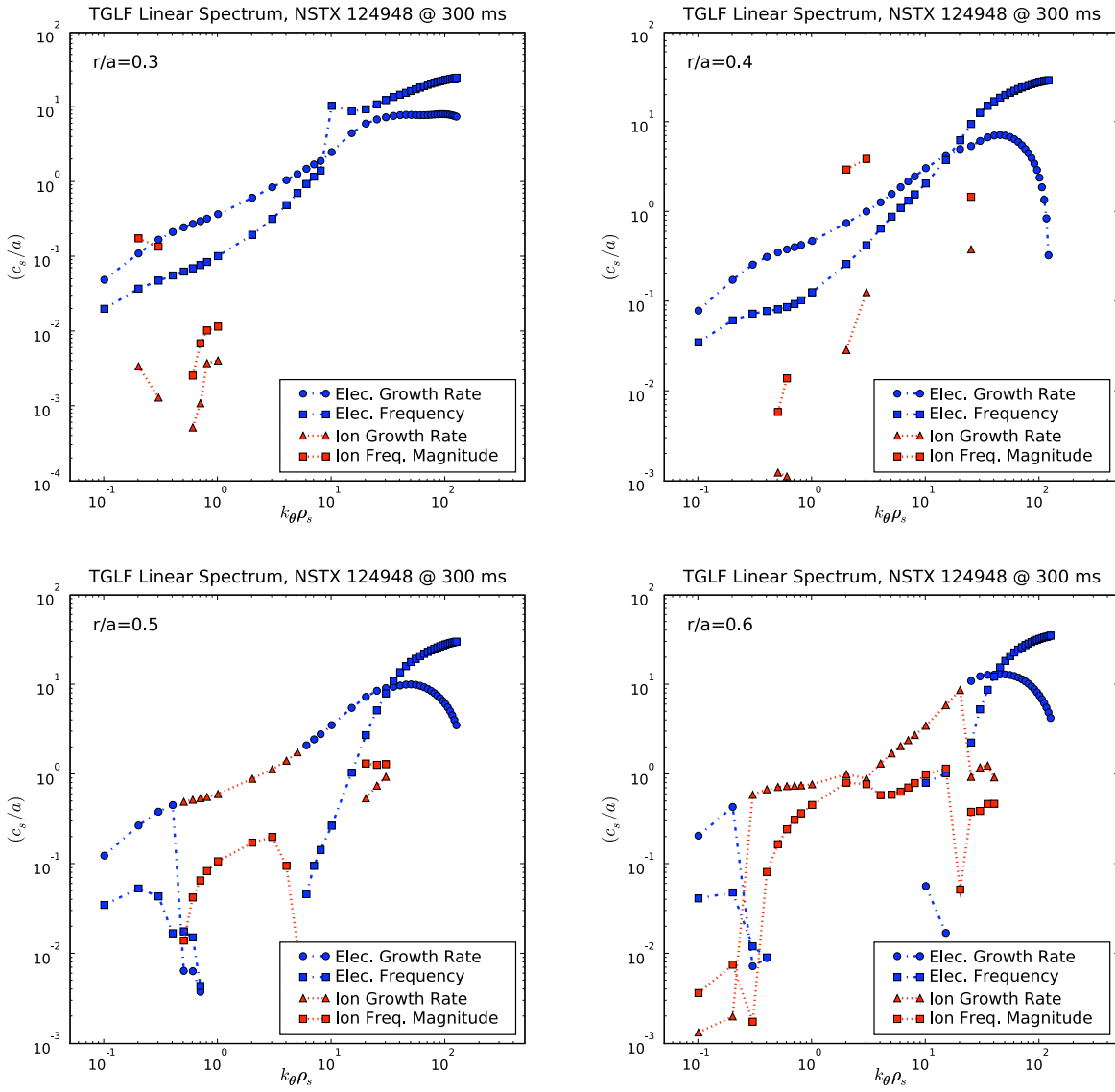
Figure 4.2: `TGLF`-calculated linear spectrums of unstable modes for NSTX shot 124948 @ 300 ms, at $r/a = 0.3 - 0.6$. In these units, the $\mathbf{E} \times \mathbf{B}$ shearing rate γ_E is approximately 0.1.
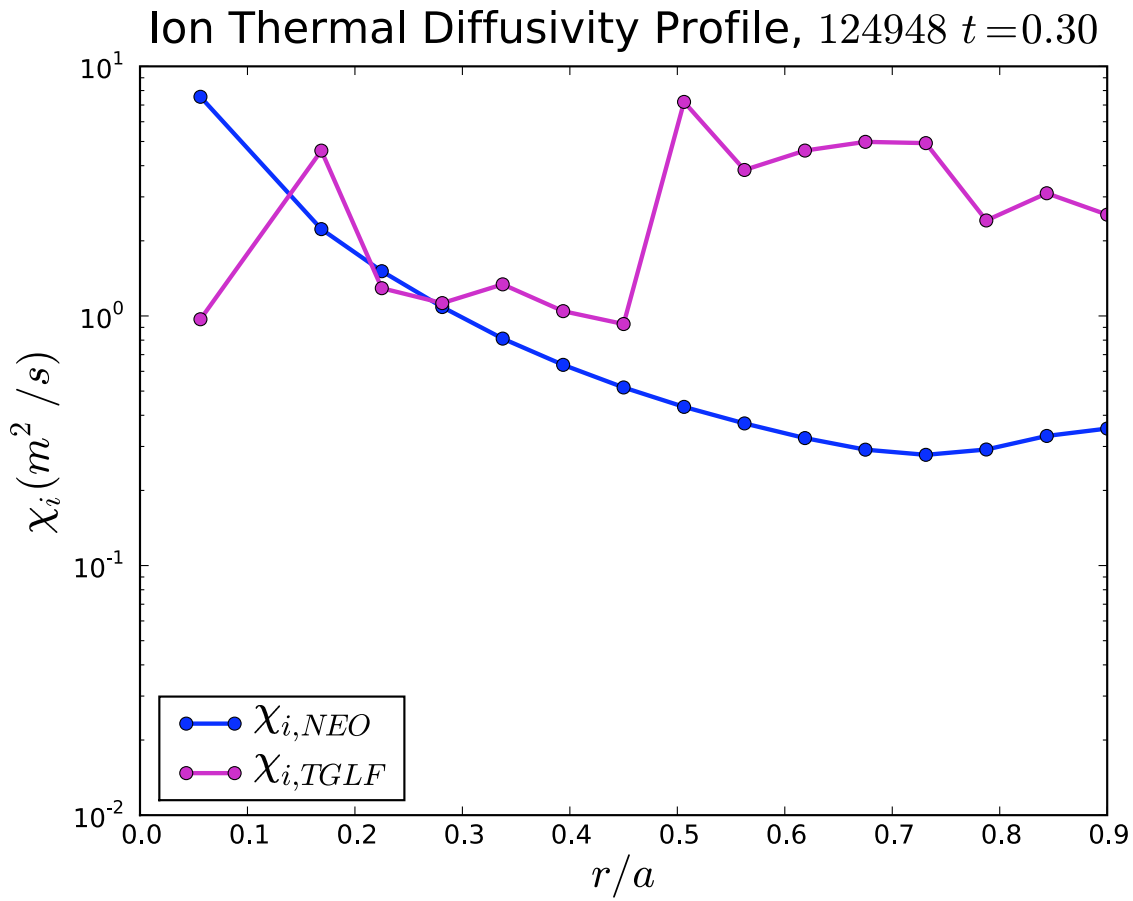
Figure 4.3: Quasilinear-based turbulent and neoclassical ion thermal diffusivities, NSTX 124948, 300 ms. Calculated by `TGLF` and `NEO`, respectively.

Beginning with the ions, Figure 4.3 shows a radial profile of quasilinear and neoclassical heat fluxes. Inside $r/a \approx 0.45$, the turbulent flux is comparable to the neoclassical value. At the inner most radial point, the neoclassical flux is actually greater. In the outer half of the plasma, χ_i is anomalous, with values in the range of $2 - 7$ m^2/s. The ions' turbulent flux dominates in the outer half of the plasma, but inside $r/a = 0.5$, the neoclassical and turbulent fluxes compete.
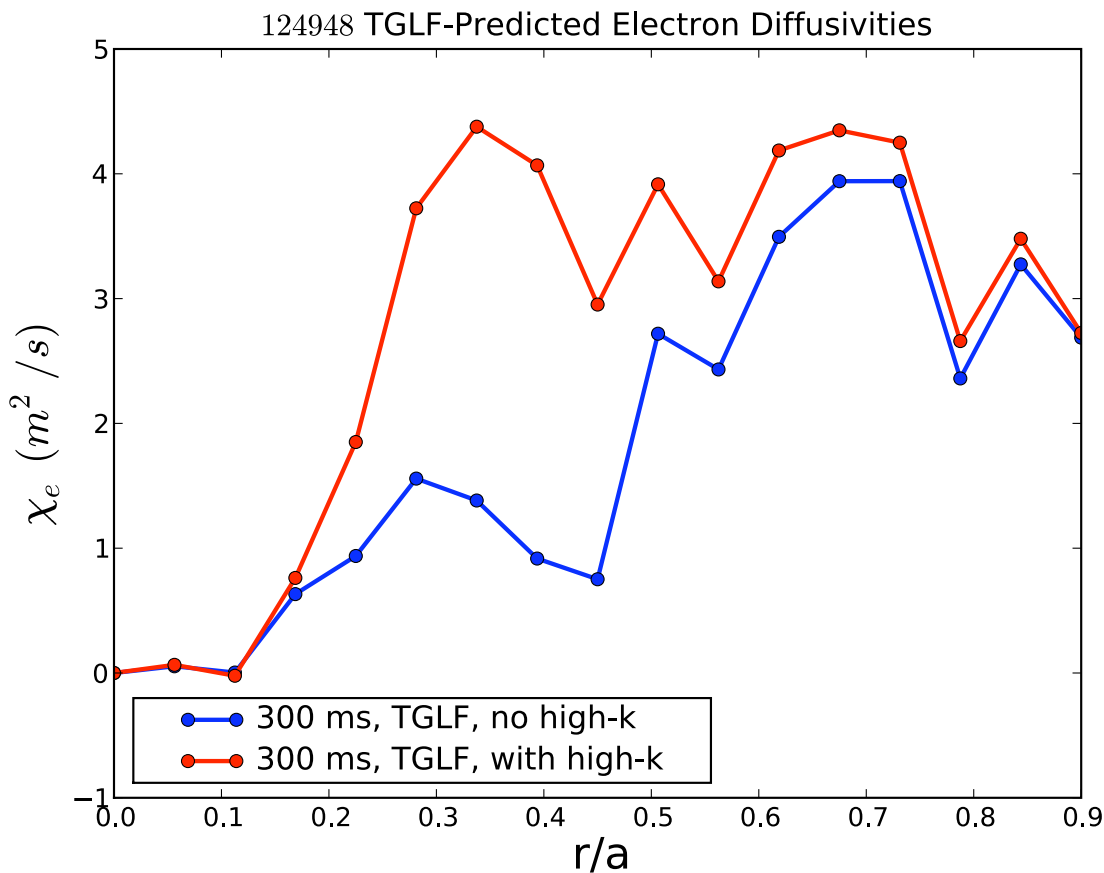
Figure 4.4: Electron thermal diffusivities, NSTX 124948, 300 ms. Calculated by TGLF using a model without high-k ETG modes (blue) and with ETG modes (red). The experimental value at $r/a = 0.5 = 3 \pm 1.5$ m^2/s.

While the ions may be largely neoclassical, the electrons are not. Figure 4.4 shows the TGLF-predicted χ_e profiles for two different models. The first, in blue, is a turbulent flux from low-k

modes only. The red includes a model for high-k ETG turbulence. The key difference between the two lies at $r/a \approx 0.3$. Including ETG modes in the calculation raises the thermal diffusivity from ~ 1.5 m^2/s to ~ 4 m^2/s. For comparison, the experimentally measured value at $r/a = 0.5$ is 3 ± 1.5 m^2/s. From this point of view, the ETG mode is not only unstable, but also substantial, accounting for $\sim$50-75% of the electron thermal transport. The thermal fluxes associated with the
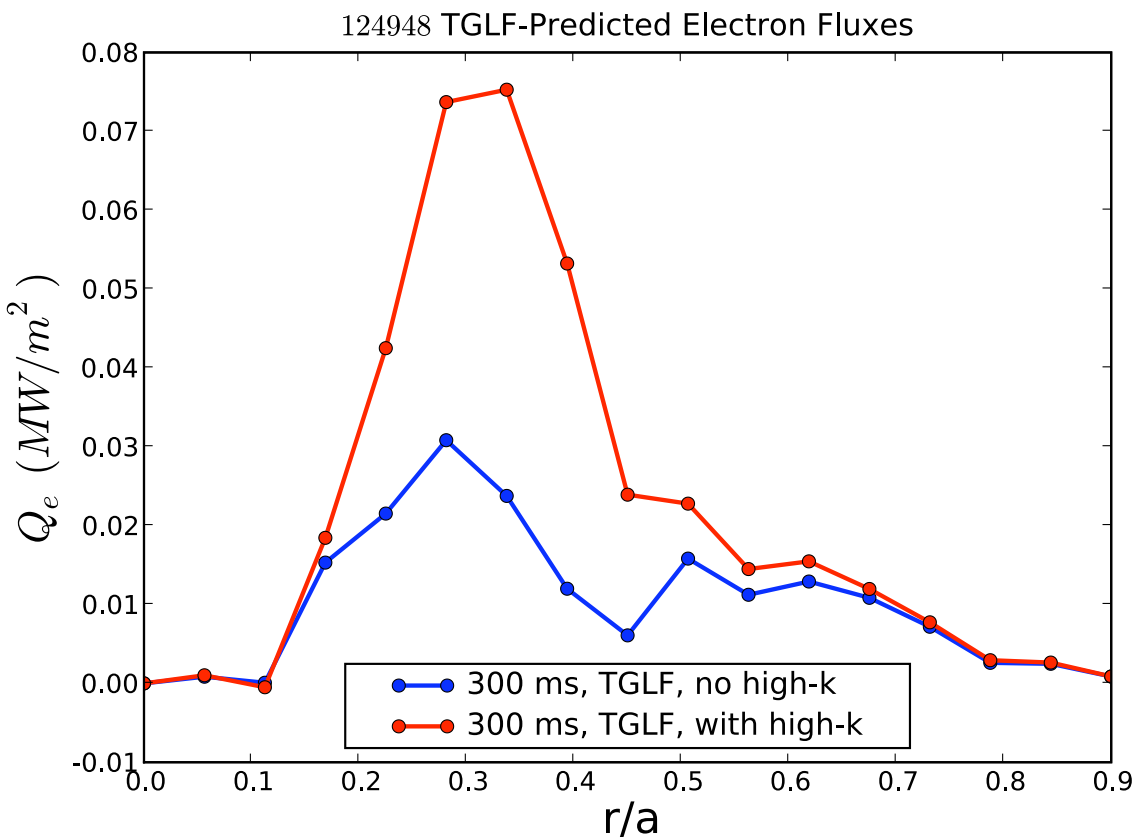
Figure 4.5: Electron thermal flux, NSTX 124948, 300 ms. Calculated by `TGLF` using a model without high-k ETG modes (blue) and with ETG modes (red).

`TGLF`-calculated χ_es appear in Fig. 4.5. Linearly including ETG turbulence substantially increases the integrated electron heat flux for $0.2 \leq r/a \leq 0.5$. This suggests that the ETG mode could be contributing significant flux to the system. However, a few caveats exist. Firstly, `TGLF` is a reduced turbulent model, calibrated to a finite set of `GYRO` simulations, and the accuracy of its calibration

to these discharges is unknown. Additionally, the calculated fluxes from both `TGLF` and `GYRO` are inherently sensitive to variations in input parameters. A full discussion is saved for Section 4.3, but briefly, the effects of this sensitivity on calculations can be quite large, with rms uncertainties approaching order unity.

4.1.3 Nonlinear Gyrokinetic Flux Tube Simulations at $r/a = 0.5$

While the `TGLF` results suggest that ETG may be actively driving thermal flux, the bridge between turbulent fluctuations and transport cannot be formed solely from a quasilinear-based analysis. Nonlinear gyrokinetic simulations can help fill the gap. In particular, we are interested in using `GYRO` to model the turbulent flux in an electron-scale annulus centered around $r/a \sim 0.37$, near the location of high-k measurements.

Resolution Requirements

Before diving in with global simulations at $r/a \sim 0.37$, we begin with convergence tests in flux tubes centered at $r/a = 0.52$ (the outer most location of the global simulation, where plasma shape is the least circular and the resolution requirements thought to be most stringent). For the convergence studies, we follow 16 toroidal modes up to $(k_\theta \rho_e)_{\text{max}} = 1.18$ in box sizes of $L_x \times L_y = 78.5\rho_e \times 79.7\rho_e$, using the ETG-ai model and $\mu_e = 20$. At this location $\hat{s} = 0.14$, a shear value for which the ETG-ki and ETG-ai models were found to agree in cross-code benchmarking tests [89, 91]. (As the mass ratio is lower than the physical value, we report turbulent quantities in electron units, which are invariant for different mass ratios above $k_\theta \rho_e > 0.1$ [91].) Baseline values for the number of poloidal gridpoints per passing particle and number of radial grid points are respectively $n_\theta = 10$ and $n_r = 96$. $n_\theta = 10$ corresponds to setting the input parameters `ORBIT_GRID` and `BLEND_GRID` each to 6. ($n_\theta = 2 \times$ `ORBIT_GRID` $- 2$.) In all scans we keep the default velocity space grid resolutions (`ENERGY_GRID` $= 8$, `PASS_GRID` $=$ `TRAP_GRID` $= 4$,

corresponding to 8 energy grid points, and 16 pitch angles for a total 128 velocity grid points per cell) [40] and hold $dt = 5 \times 10^{-4} \, (c_s/a)$ to ensure numerical stability.
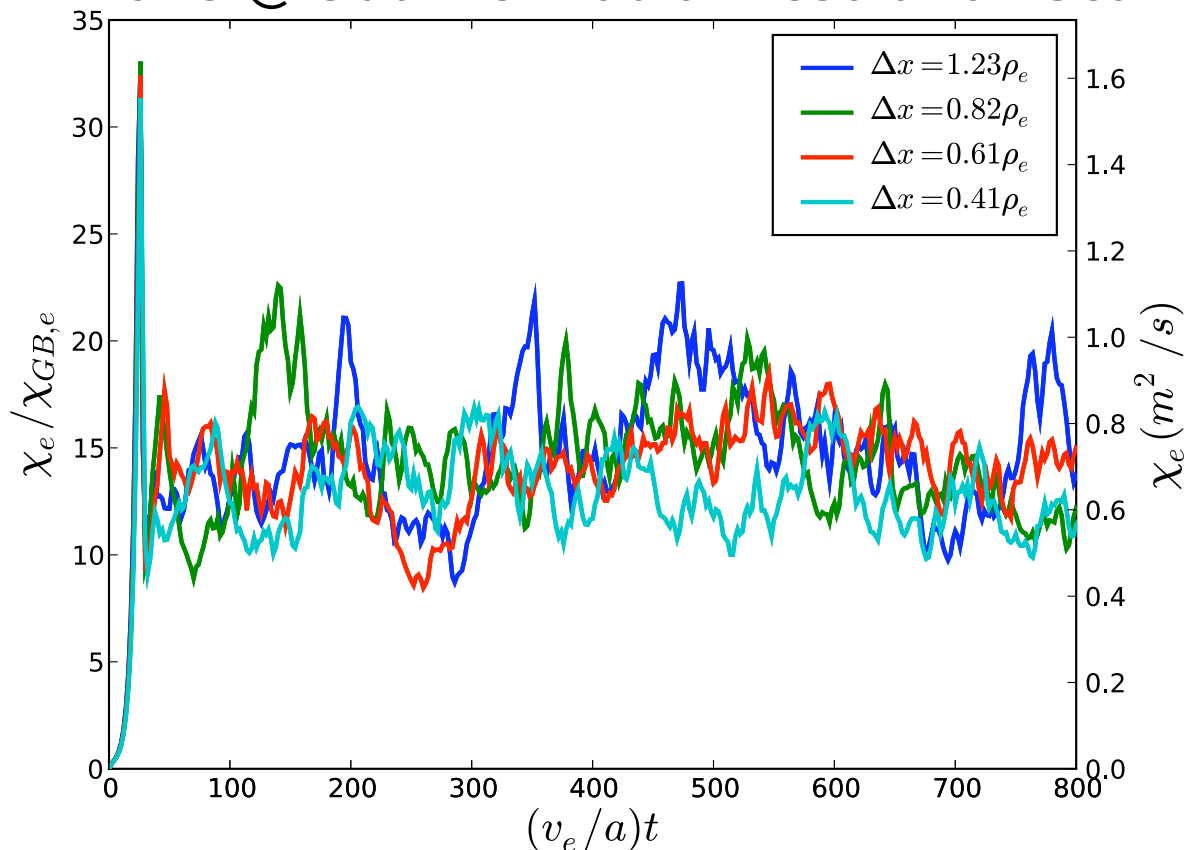
Figure 4.6: Radial resolution convergence test, 124948. ETG-ai flux tube centered at $r/a = 0.52$. The number of poloidal grid points per passing particle is held fixed at 10.

Time histories of χ_e for the radial and poloidal resolution scans can be found in Figs. 4.6 and 4.7, respectively, reported in both electron and mks units. Greater variation in the poloidal resolution scan exists than in the radial scan. Radial grid resolutions of less than ρ_e all seem sufficient, while $n_\theta \geq 14$ is necessary for convergence.

A summary of the flux tube resolution scans comparing time-averaged diffusivities, shown in Fig. 4.8 clearly demonstrates the need for higher-than-standard poloidal resolution. While these
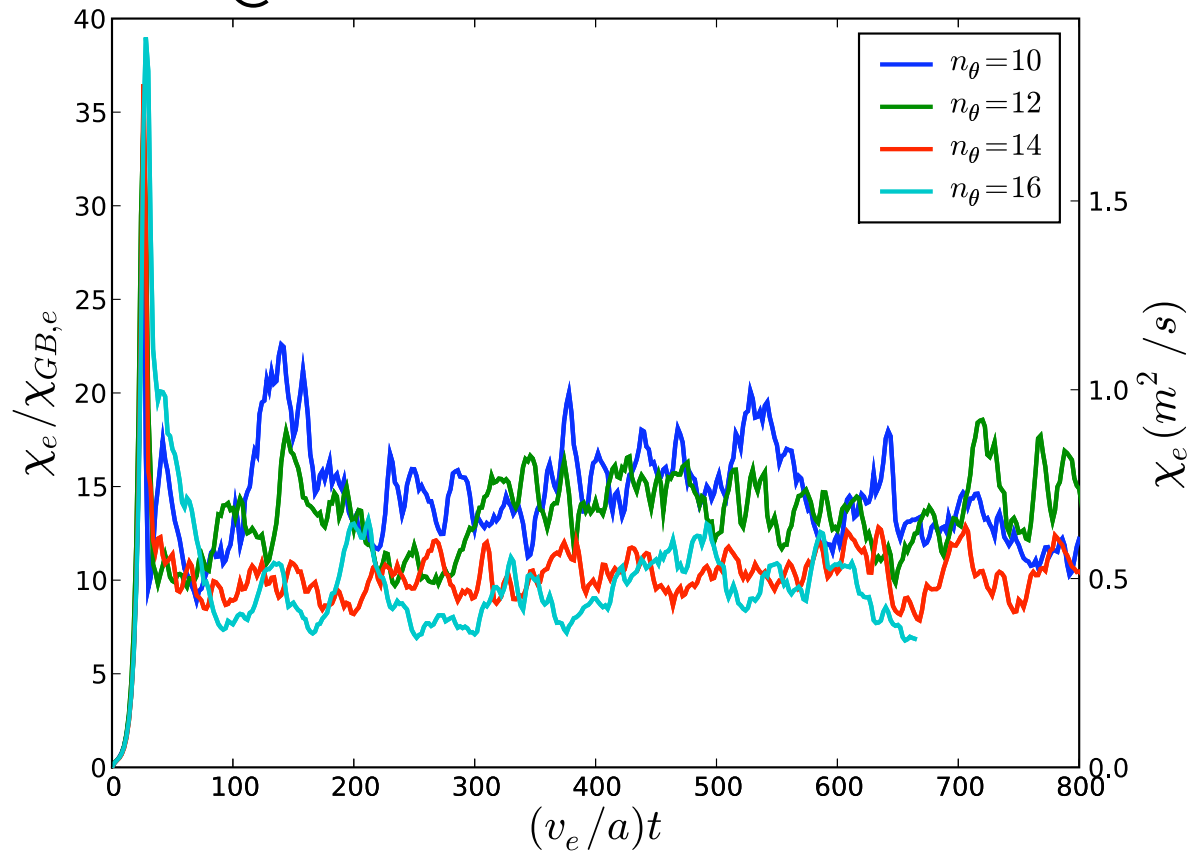
Figure 4.7: Poloidal resolution convergence test, 124948. n_r is held fixed at 96.
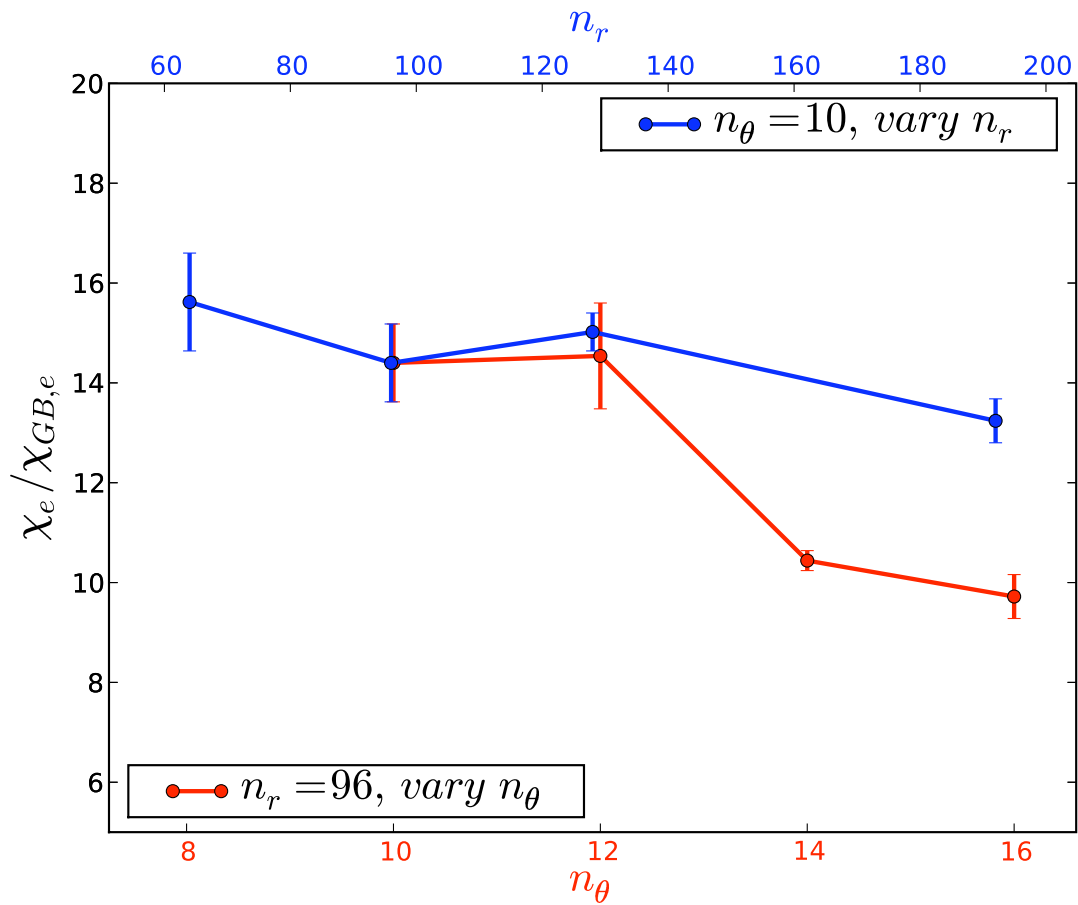
Figure 4.8: Summary of convergence tests for 124948. The error bars correspond to statistical uncertainties in the fluctuating diffusivities, specifically rms fluctuations about the mean.

time-averaged quantities should be taken with a grain of salt (since shifting the time-averaging window can account for much of the variation), some trends are clear. Increasing the number of radial grid points above 96 (corresponding to $\Delta x = 0.82\rho_e$) does not statistically alter the solution; however, increasing n_θ from 12 to 14 causes the thermal diffusivity to drop by roughly 30%. This need for higher poloidal resolution agrees with existing linear eigenmode analysis of NSTX plasmas [108].

Comparison to `TGLF`, `NEO` and Experiment

Again, saving a discussion on sensitivities to inputs for Section 4.3, we briefly compare these `GYRO`-calculated fluxes to those calculated by `TGLF` and `TRANSP` to be present in the experiment. The flux-tube values of χ_e, at $\sim 10 - 20\chi_{GB,e}$ are roughly one third of the `TRANSP`-inferred experimental value. Figure 4.9 shows that the experimental value at $r/a = 0.52$ agrees with the calculation from `TGLF`. (Neoclassical flux, as calculated by `NEO` is much smaller.) The `GYRO` flux-tube convergence tests estimate a somewhat lower value of χ_e from ETG than estimated by `TGLF` and `TRANSP`.

Although these diffusivities are lower than the experiment, they are still many gyroBohm units, an enhancement that comes from radially extended streamers (like those commonly seen in ETG simulations). An example of said streamers appears in snapshot of midplane potential fluctuations in Fig. 4.10. Since the radial domain is roughly $80\rho_e$ across, these streamers can extend for $> 50\rho_e$.

The nonlinear flux-tube simulations at $r/a = 0.52$ not only dictate resolution requirements for NSTX-ETG simulations, but also calculate that high-k ETG turbulence can account for roughly one third to one half of the experimentally measured thermal diffusivity.
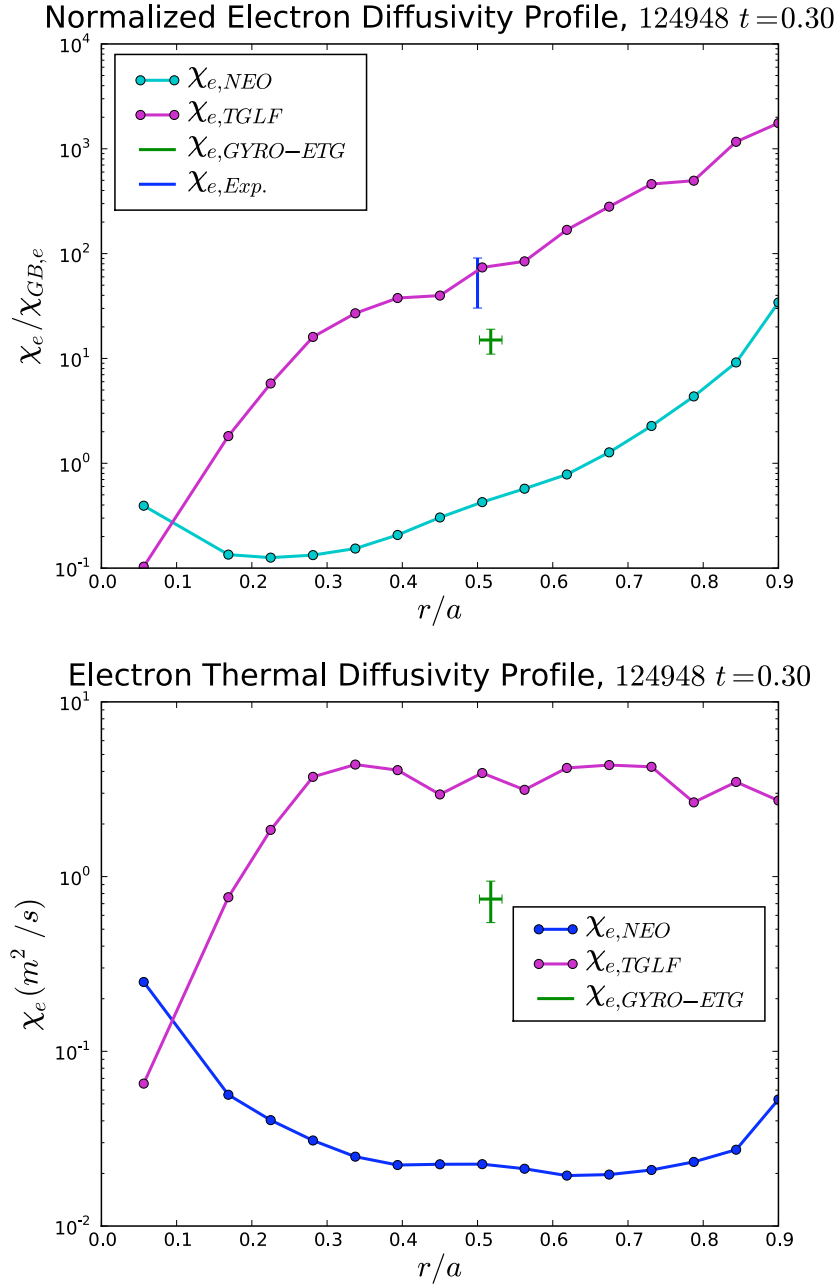
Figure 4.9: Comparison of GYRO electron-scale flux tube, TGLF, NEO and experimental measurements of χ_e, in both normalized and mks units.
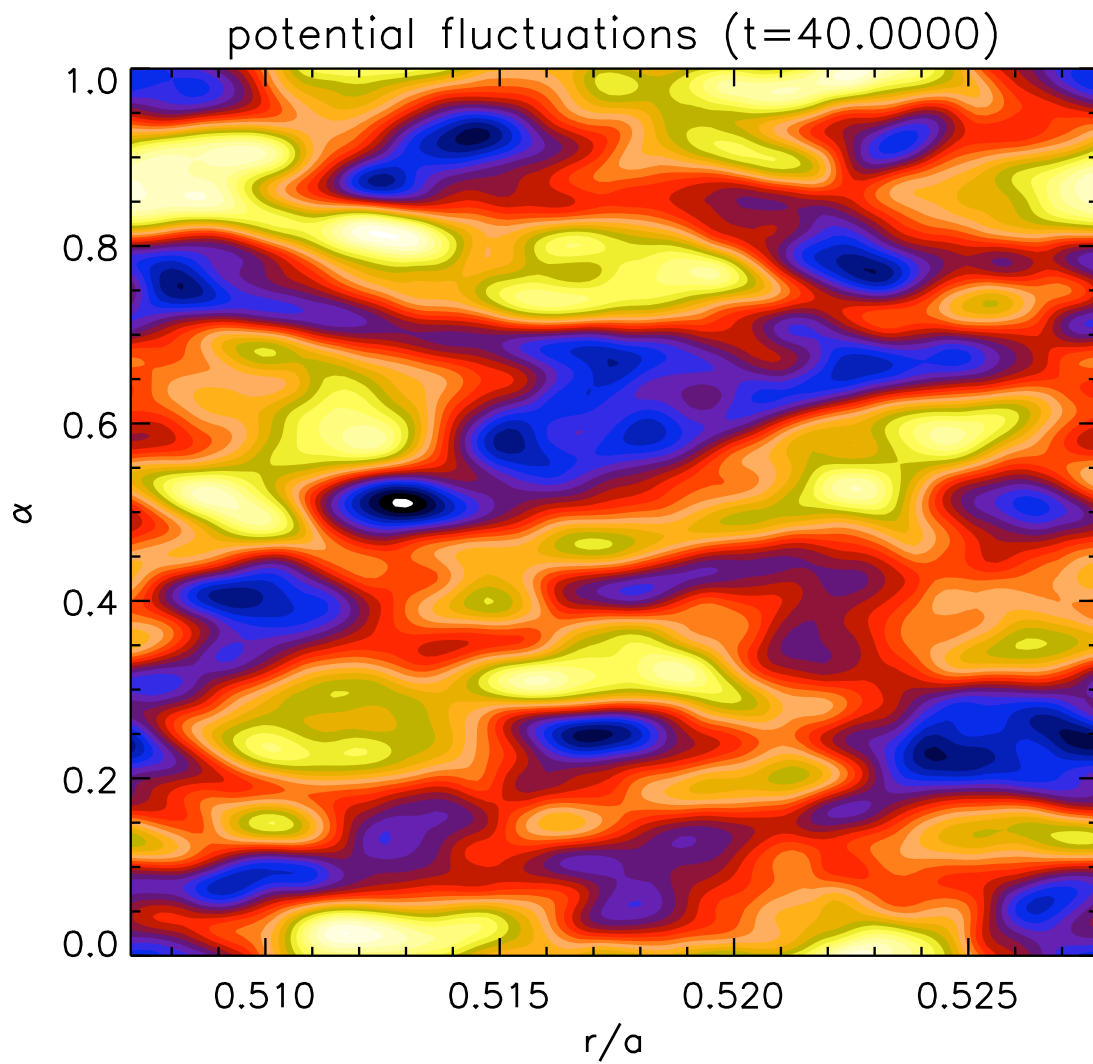
Figure 4.10: Example snapshot of the potential fluctuations from one of the flux tube simulations at $r/a \approx 0.5$, showing radially elongated streamers. The radial domain is approximately $80\rho_e$ across.

4.1.4 Nonlinear Global Simulations around $r/a = 0.37$

Armed with an understanding of the resolution requirements for these NSTX ETG turbulence calculations, we turn now to global simulations at the location of the high-k measurements, $r/a = 0.37$, parameters for which appear in Table 4.1. To relax the resolution requirements for the

Table 4.1: Parameters for global gyrokinetic simulation of NSTX 124948 at 300 ms.

Simulation Box Parameters			
L_x/ρ_e	635.2	L_y/ρ_e	102.6
$\Delta\left(k_\theta\rho_e\right)$	0.061	$\left(k_\theta\rho_e\right)_{\max}$	0.92
μ_e	20	Buffer Widths	$8\rho_s$
Plasma Parameters at Box Center			
r_0/a	0.373	Z_{eff}	2.5
R_0/a	1.502	$\gamma_E\left(a/c_s\right)$	-5.6×10^{-3}
κ	1.859	λ_D/a	9.4×10^{-5}
δ	0.129	ζ	-0.010
q	3.113	$\hat{s}$	-0.127
s_δ	0.050	s_κ	-0.731
$\nu_{ei}\left(a/c_s\right)$	0.087	s_ζ	-0.016
$\nu_{ii}\left(a/c_s\right)$	0.000	a/L_n	0.628
$\rho_\star$	0.007	a/L_{T_i}	1.302
n_i/n_e	1.000	a/L_{T_e}	4.71
T_i/T_e	0.833	$\beta_{e,unit}$	6.1×10^{-3}

$635\times103\rho_e$ box, the ion-electron mass ratio is reduced, $\mu_e = \sqrt{m_D/m_e} = 20$. We also neglect ion-ion collisions, but will test the effects of including electron-ion collisions, $\mathbf{E}\times\mathbf{B}$ flow shear and electromagnetic fluctuations. We will also test the ETG-ai and ETG-ki models. As these simulations are global, in a thin annulus that allows for radial profile variation, they require buffer regions for the imposed Dirichlet boundary conditions [40], whose width and damping rate strength are respectively set to $8\rho_s = 160\rho_e$ (defined by ρ_s at the box center) and $1.0\ (c_s/a)$ for

both ions and electrons. When considering the buffers widths, the central box is roughly $315\rho_e$ wide.

We use 640 radial grid points ($\Delta x = 0.99\rho_e$) and set $n_\theta = 16$. We also increase the velocity space resolutions above those of the flux tubes, setting PASS_GRID and TRAP_GRID equal to 5, while holding ENERGY_GRID at 8. Temporal convergence can be achieved with $dt = 1 \times 10^{-3}(c_s/a)$ and $t_{max} = 100\,(a/c_s) = 2000\,(a/v_e)$.
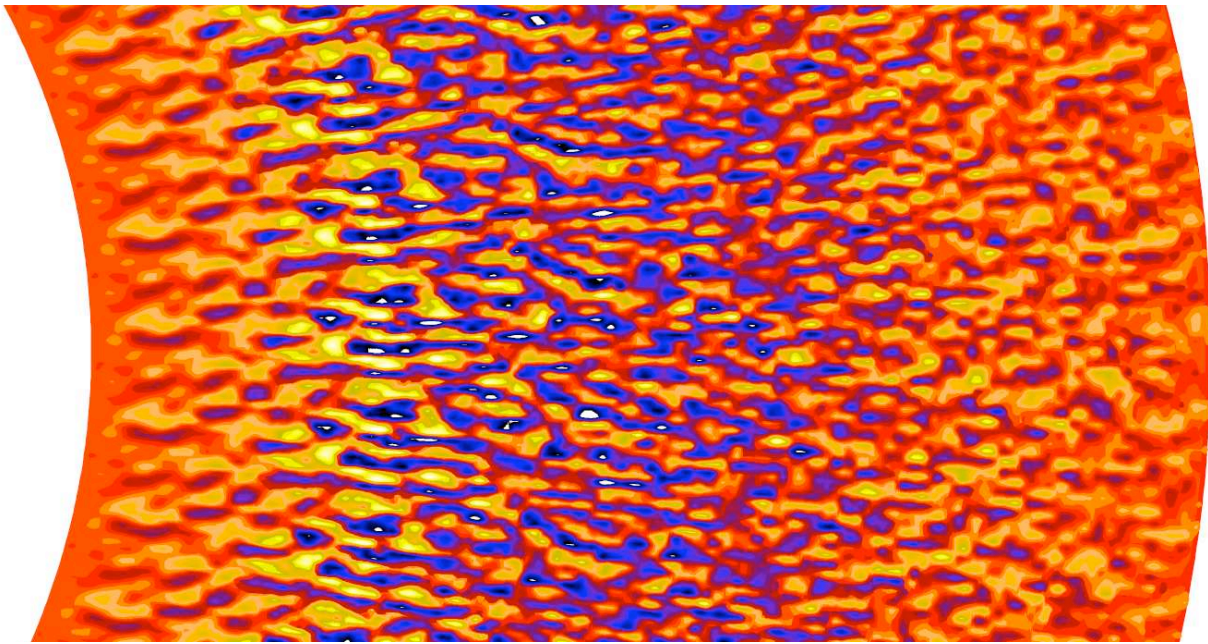
Figure 4.11: Part of a poloidal cross section of density fluctuations from a global electrostatic simulation, with the radial direction horizontal and the poloidal direction curving vertically. The entire domain is $\sim 635\rho_e \sim 32\rho_s$ across, spanning from r/a of 0.22 to 0.52.

Like the flux tube simulations, global simulations at $r/a = 0.37$ show significant ETG turbulence, characterized by radially elongated eddies. A cross-section of electron density fluctuations for an electrostatic ETG-ki global simulation appears in Fig. 4.11. The radial direction expands horizontally and the torus' poloidal curve can be seen on both low r/a (left) and high r/a (right) domain edges. Since the entire domain is $\sim 635\rho_e$ across, eddies extend into streamers of

$\sim 50 - 75\rho_e$, like those of the flux tube simulations. The decreased fluctuation amplitude in the buffer zones is also visible.

Comparisons with `TGLF` and Experiment
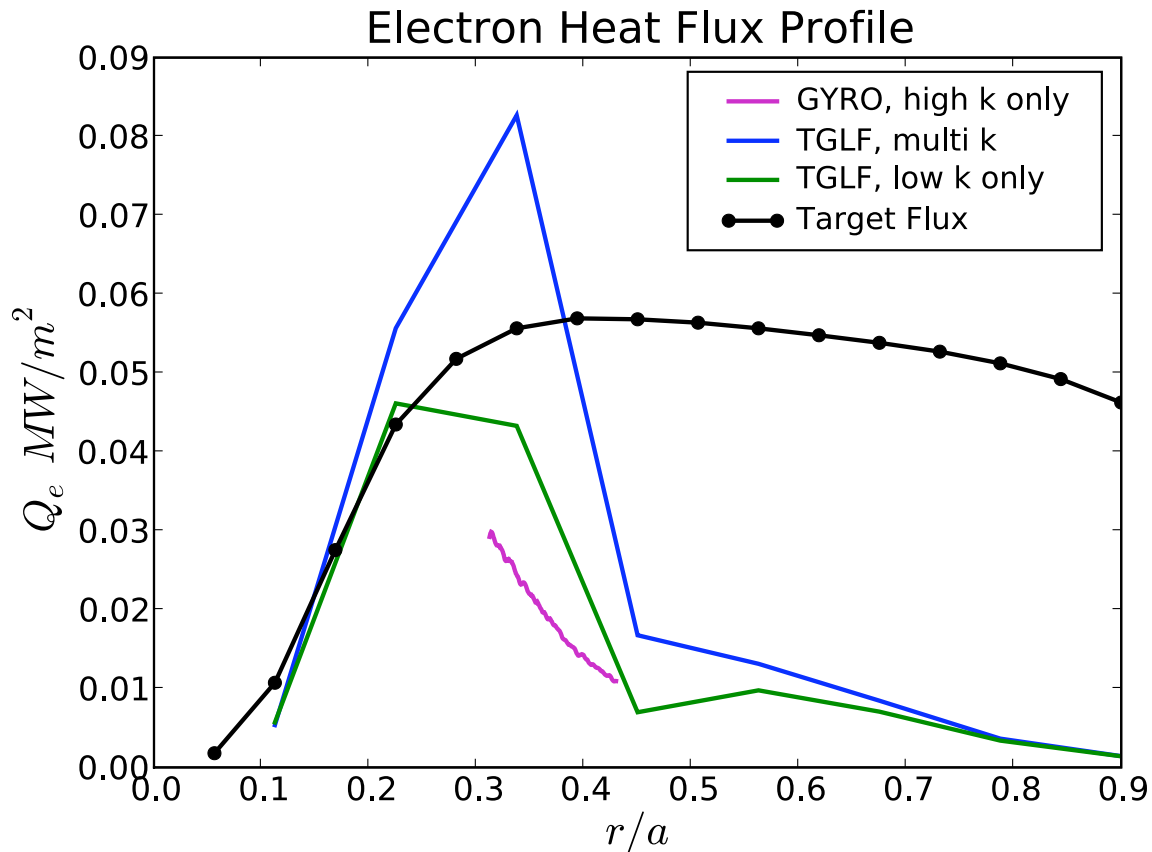
Figure 4.12: Radial electron heat flux profiles as calculated by `GYRO` (purple) and `TGLF` with (blue) and without (green) ETG turbulence for NSTX shot 124948. The experimental flux is marked in black, and `GYRO`'s buffer zone fluxes have been masked.

Another interesting feature of this electron-scale turbulence is that the intensity of the streamers is greatest on the inboard side of the plasma, corresponding to roughly a 50% change in electron heat flux across the radial domain, from $\sim 60 - 30Q_{GB,e}$. Incidentally, this variation is mirrored by `TGLF` simulations, as shown in Fig. 4.12. `TGLF` both with and without its ETG model show

a large radial variation in heat flux around $r/a = 0.4$. Not surprisingly, this is where the RF heating makes the electron temperature gradient the largest. Like the flux tube simulations at $r/a = 0.5$, GYRO ETG simulations can account for perhaps one third to one half of the measured heat flux in this region. It also seems plausible that adding the low-k contribution, as represented by the TGLF results, to the GYRO high-k contribution could make up the difference between the experimental and numeric fluxes, especially at $r/a \sim 0.3$, where $Q_{\text{TGLF, low}} = 0.04$ MW/m^2 and $Q_{\text{GYRO}} = 0.03$ MW/m^2. Here, $Q_{exp} = 0.055$ and $Q_{\text{TGLF, multi-k}} = 0.07$, suggesting not only that the ETG-contribution from GYRO is relevant, but also that the total heat flux may have a significant low-k contribution; however, given the profile stiffness to the electron temperature gradient at this location, such comparisons should be made carefully: a ten percent change in local gradient can lead to a factor of 2 change in heat flux, as mentioned in Section 4.3. The stiff-profile phenomenon motivates comparisons of plasma temperature profiles, and not heat flux profiles, as discussed in the following Chapter. In any case, GYRO predicts a large electron heat flux, which is both at the location of the high-k fluctuation measurements and perhaps one half of the total experimentally inferred heat flux.

Sensitivity to some input parameters

Treating the ions adiabatically (ETG-ai) instead of gyrokinetically (ETG-ki) does not significantly affect the calculated turbulent flux. Figure 4.13 shows that over a range of $\mathbf{E} \times \mathbf{B}$ shear values, the turbulent heat flux for both models statistically agree. Both models calculate the simulated flux to be roughly one half of the experimental value, as calculated by TRANSP. While in some cases it is important to calculate ETG turbulence with kinetic ions [91, 92], in this situation the ETG-ai model appears adequate, likely due to the low value of magnetic shear. As such, the computational savings from using the simpler ETG-ai model allows for the addition of more complex physics models to this ETG turbulence, beginning with collisions. The fact that the flux from neither
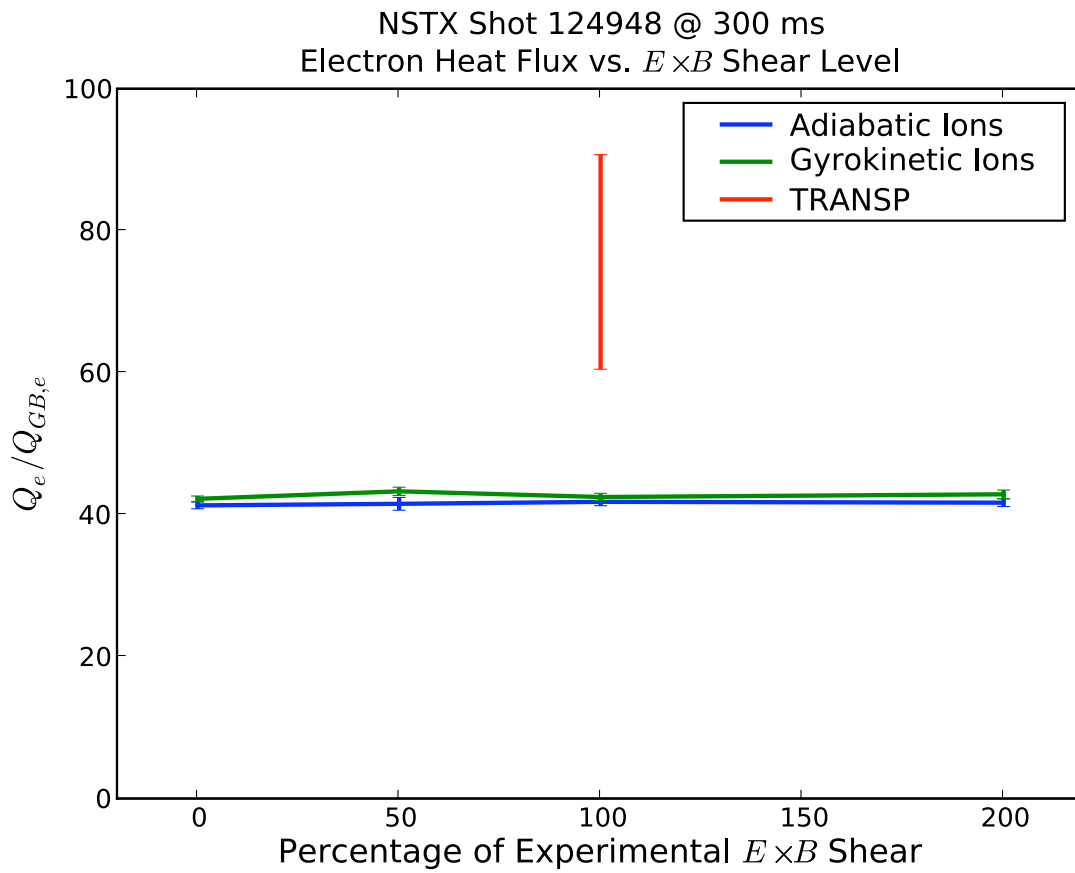
Figure 4.13: A comparison of global ETG-ki (green) and ETG-ai (blue) simulations over a range of flow shears. The TRANSP experimental calculation is in red.

model changes when altering the $\mathbf{E} \times \mathbf{B}$ shear is not terribly surprising, because shearing rate is very low to begin with during this RF-heated discharge.
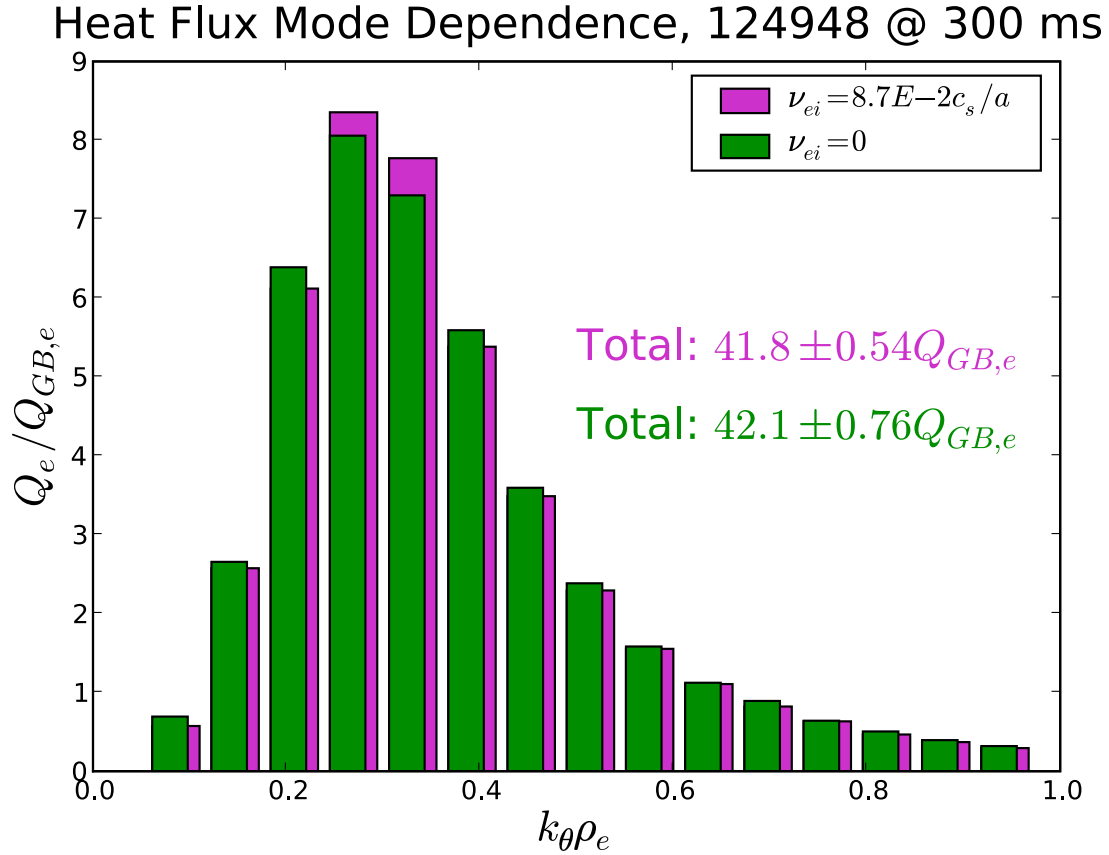
Figure 4.14: Integrated heat flux spectra for 124948 global simulations with (purple) and without (green) electron-ion collisions.

Electron-ion collisions have no statistically significant effect on the integrated heat flux, as shown in Fig. 4.14. The spectra both roll off at low and high k and peak at $k_\theta \rho_e \sim 0.3$, consistent with ETG turbulence.

Electromagnetic Effects

Including magnetic fluctuations, $\delta A_\parallel$ specifically, increases the integrated heat flux by roughly 10%. Figure 4.15 shows the integrated toroidal heat flux spectra from an electromagnetic global
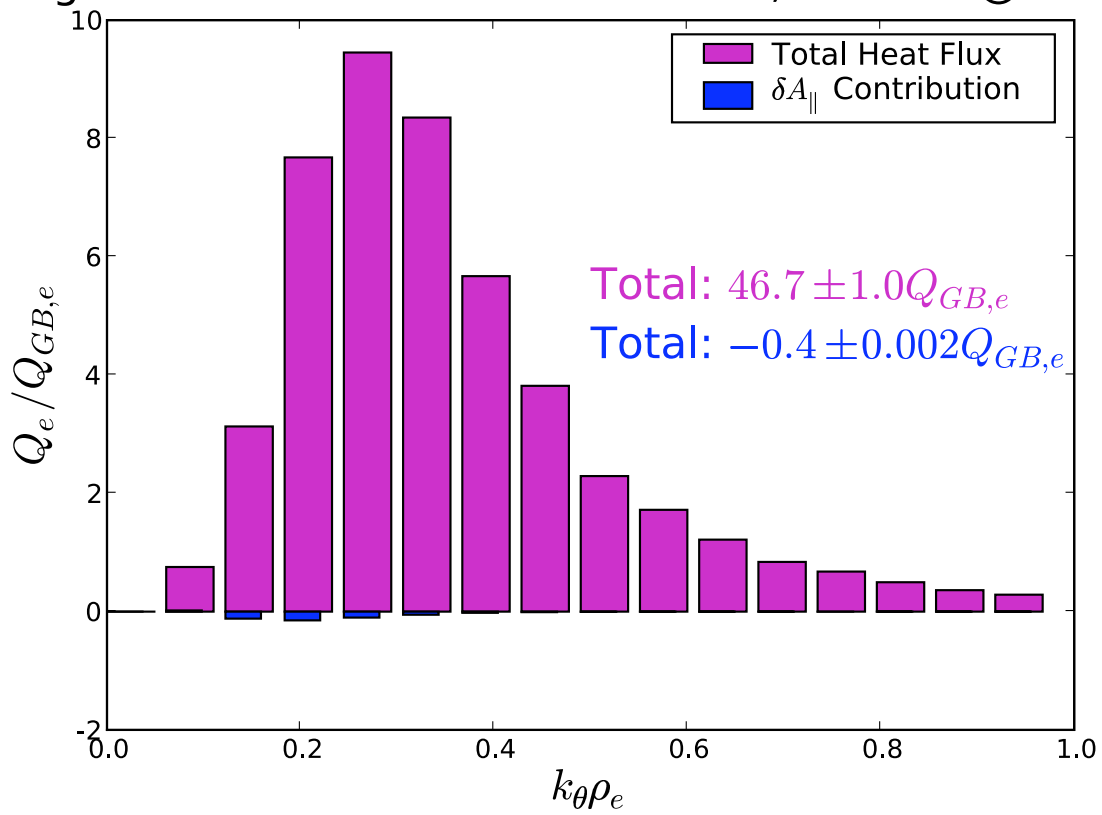
Figure 4.15: Integrated heat flux spectra for electromagnetic global simulations. The total heat flux is in purple, while the contribution from $\delta A_\parallel$ is in blue.

simulation. The total heat flux is in purple, while the contribution from $\delta A_\parallel$ is in blue. Although the absolute contribution from $\delta A_\parallel$ is relatively small and in the opposite direction (a negative heat flux), the total heat flux is 10 percent greater than both the collisional and collisionless electrostatic cases of Fig. 4.14. The $\delta A_\parallel$ spectra also peaks at slightly lower $k_\theta \rho_e$ (0.2 vs. 0.3), but adding electromagnetic fluctuations does not move the peak of the electrostatic heat flux.
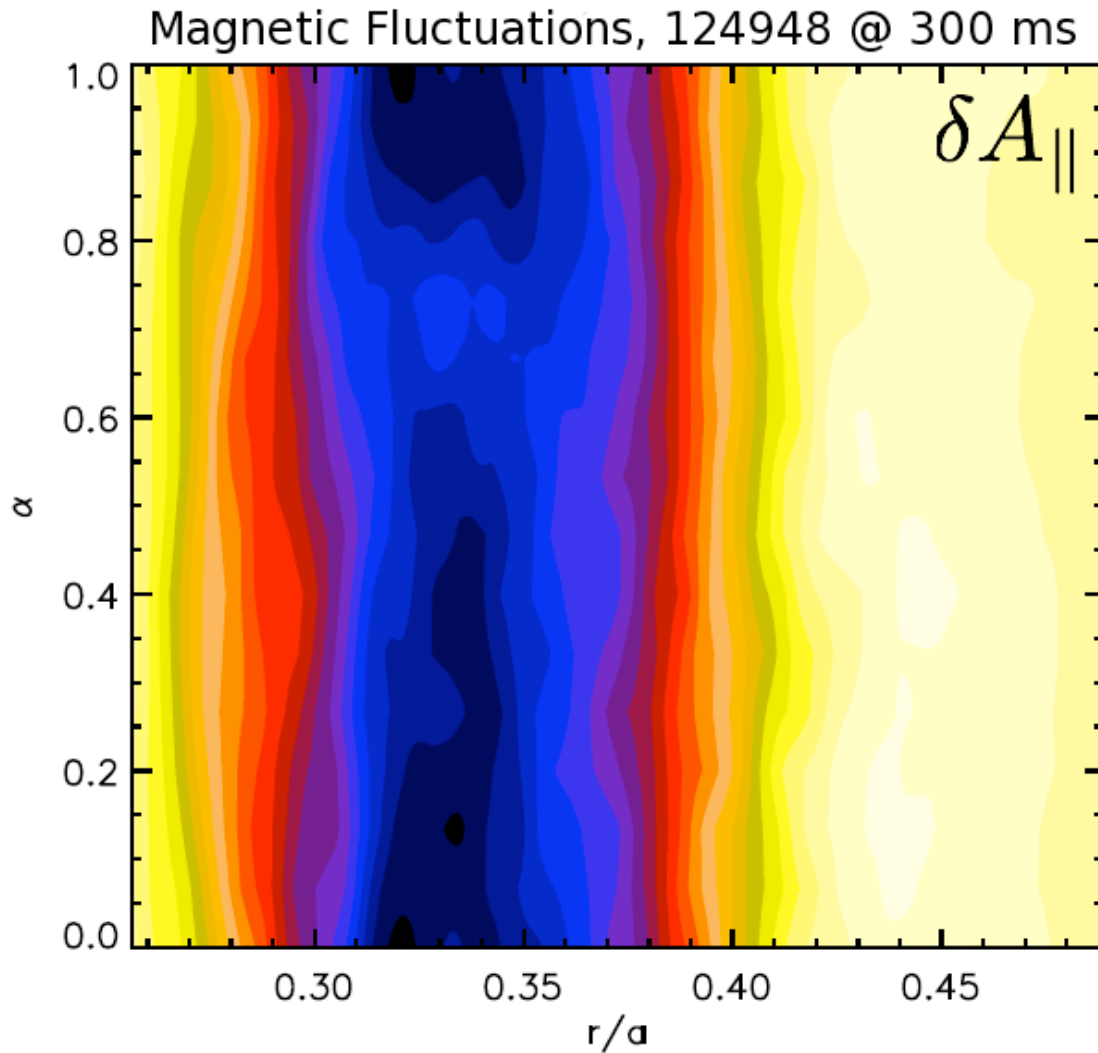
Figure 4.16: Snapshot of midplane $\delta A_\parallel$ perturbations for the global electromagnetic simulation.

Like the electrostatic and density fluctuations, $\delta A_\parallel$ also has its largest amplitude on the inner side of the plasma, as shown in Fig. 4.16, contours of $\delta A_\parallel$ on the midplane. Unlike δn and $\delta\phi$, however, $\delta A_\parallel$'s eddies are very large, filling much of the box and likely too large for the domain. Interestingly enough, large $\delta A_\parallel$ and small δn eddies have been observed in simulations of microtearing modes on NSTX [109]. Furthermore, this shot has been found to be linearly unstable to small-scale tearing modes, what the authors of Ref. [110] refer to as "high-k microtearing modes." They conclude that this microtearing mode linearly dominates over ETG at $r/a \lesssim 0.33$ and exists at $k_\theta\rho_s \lesssim 3$, corresponding to a smaller scale than the traditional microtearing modes' $k_\theta\rho_s < 1$. Despite the analysis in Ref. [110] being at a slightly different time (315 vs 300 ms), a high-k microtearing mode may be unstable on the inboard side of the nonlinear electromagnetic simulation. Since our measured $\delta A_\parallel$ fluctuations peak both at $r/a \sim 0.33$ and $k_\theta\rho_s \sim 4$, this may be nonlinear evidence of the so-called high-k microtearing mode, although without convergence studies (particularly in box size), this cannot be determined for sure. In any case, however, adding electromagnetic fluctuations has only a modest 10% effect on the integrated heat flux.

Implications for the High-k Density Fluctuations

Taken as a whole, these nonlinear simulations show that indeed ETG could exist during this discharge and produce significant electron thermal flux, which can account for perhaps 30-50% of the experimentally measured value. We now turn to the question of the high-k measurements. As mentioned, the high-k system measures large $k_\perp$, not large k_θ. Since the eddies seen in the NSTX simulations are, like other ETG eddies, radially elongated, they would tend to drive fluctuations with high values of k_θ and low values of k_r. Table 4.2 lists the spectral measurement locations of the three active channels during this shot. In all cases $k_\theta\rho_e < k_r\rho_e$. Even though the diagnostic channels measure high values of $k_\perp$, most of it comes from high values of k_r, thereby making the diagnostic less sensitive to the radially elongated (low k_r) streamers in the nonlinear simulations.

Table 4.2: High-k Measurement Locations, NSTX shot 124948, 300 ms.

Measurement Channel	$k_r\rho_e$	$k_\theta\rho_e$
3	0.21	0.07
4	0.31	0.09
5	0.40	0.12
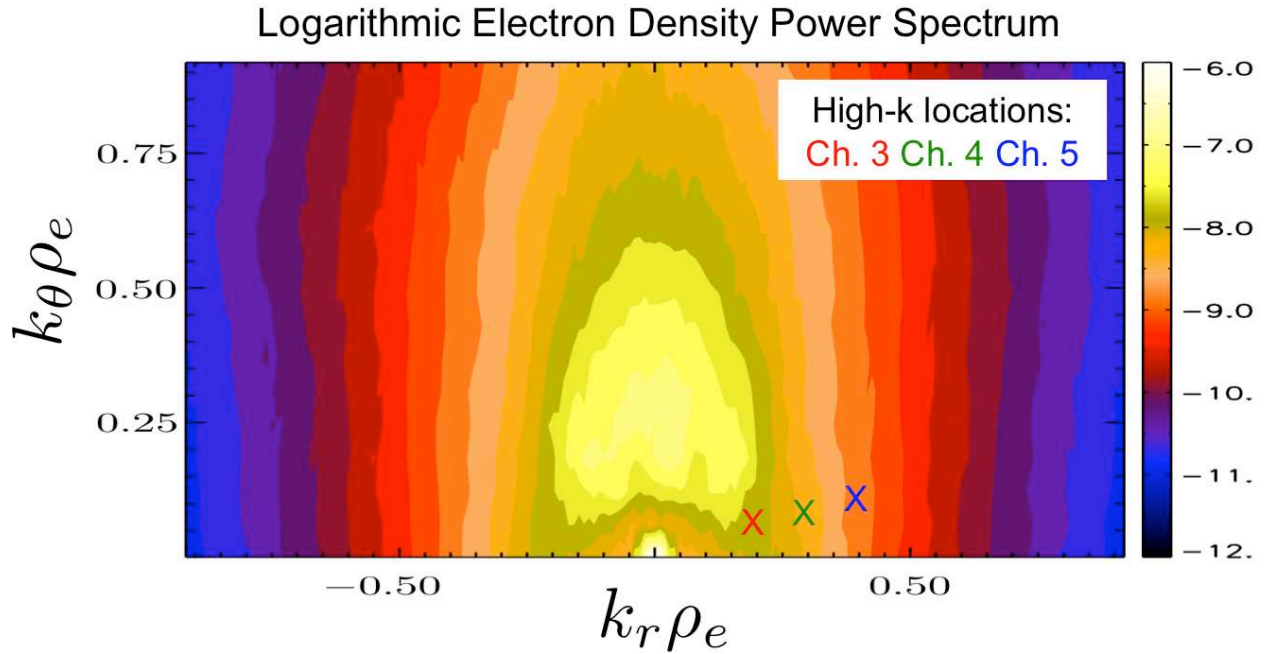
Figure 4.17: Power spectrum of midplane electron density fluctuations in k_r and k_θ. The measurement locations of the three high-k diagnostic channels active during the experiment are also plotted.

The midplane density fluctuation power spectra from an electrostatic ETG-ki simulation, shown in Fig. 4.17, confirms that the three active measurement channels during this discharge miss the peak of the ETG spectrum. This power spectrum is logarithmic. Although the power at Channel 3 is more than one order of magnitude greater than at Channel 5, it is still over two orders of magnitude below the peak of the spectrum at $k_r = 0$. Obviously a more-thourough analysis of measured high-k power would employ a synthetic diagnostic (such as that of Ref. [111]); however, the picture painted by Fig. 4.17 shows that the measured high-k power comes not from the peak of the ETG fluctuations, but rather from its spectral tail.

ETG turbulence exists in this NSTX simulation at the location of the high-k measurements. Furthermore, it can drive experimentally relevant levels of thermal flux. However, it's not clear that the high-k diagnostic itself is actually measuring this ETG turbulence, as the diagnostic windows center on the fluctuations' spectral tail and not its peak. When combined with the evidence from TGLF that a large amount of thermal flux can be produced *without* including ETG modes, the link between the high-k measurements and ETG-driven fluctuations is tenuous.

Were the high-k system not only measuring ETG-driven fluctuations, what else might the diagnostic see? A possible answer is the spectral tail of a longer-wavelength instability, not included in the nonlinear simulations, which have a minimum $k_\theta \rho_s$ of $0.81 - 1.98$, depending on the radial location (since the profile varies radially, so does $k_\theta \rho_s$). One candidate is microtearing, although the density spectrum in the electromagnetic simulation doesn't noticeably differ from the electrostatic case. Another possibility is the trapped electron mode (TEM). It is also driven by the electron temperature gradient. The RF heating meant to drive ETG may have driven TEM as well.

Figure 4.18 shows that a variety of unstable long-wavelength modes exist with growth rates above the $\mathbf{E} \times \mathbf{B}$ shearing rate, γ_E, making their existence possible. Also recall that Fig. 4.2 shows many other unstable modes in this plasma with growth frequencies above γ_E. These modes have longer wavelengths than captured by the nonlinear ETG simulations, so their contributions to the fluctuating spectrum are missing from Fig. 4.17. It may be that as energy cascades from these
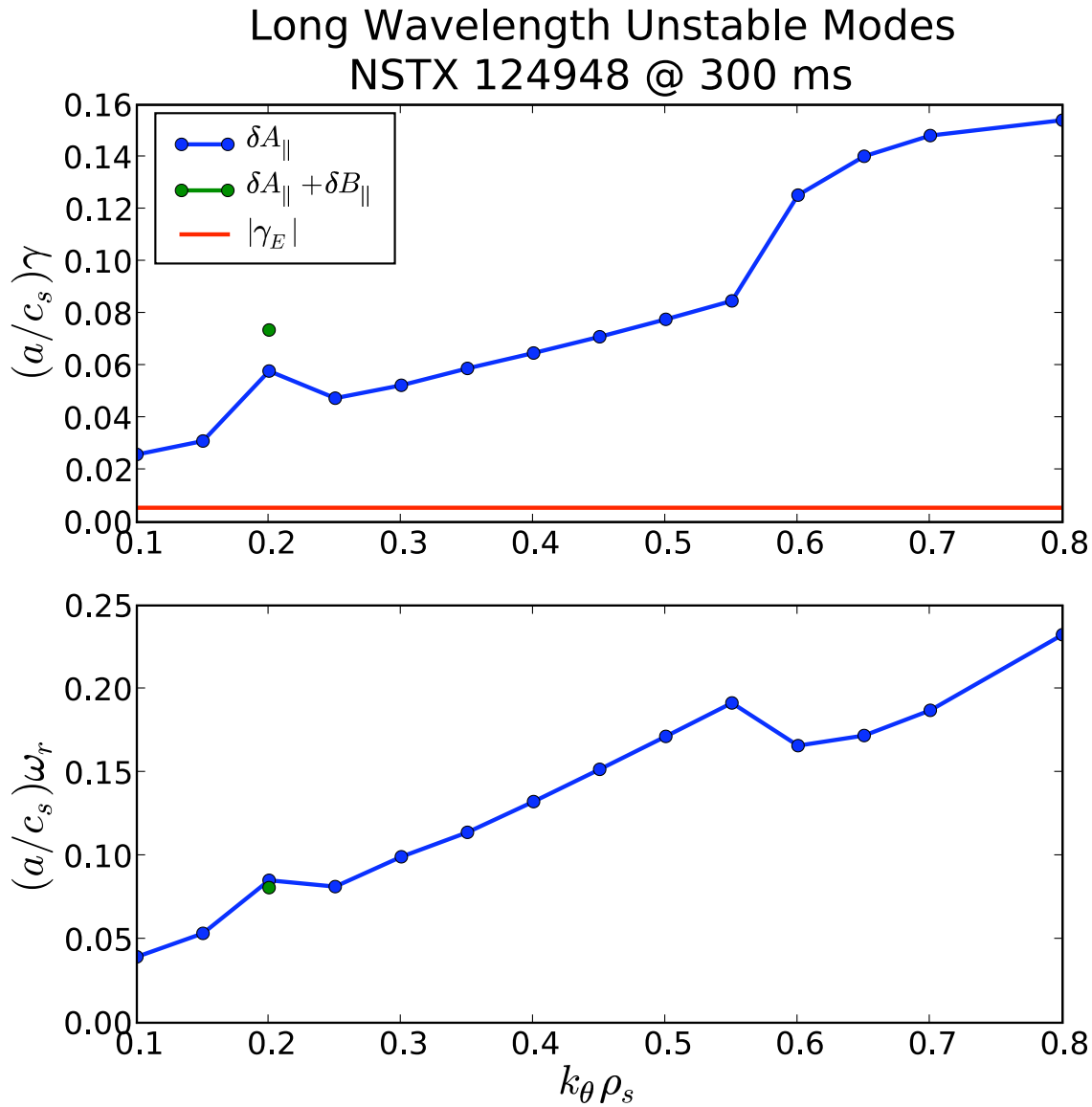
Figure 4.18: Growth rates and frequencies of long wavelength instabilities at $r/a = 0.37$, including electromagnetic fluctuations. The unstable modes are both in the electron diamagnetic direction and have growth rates above the $\mathbf{E} \times \mathbf{B}$ shearing rate.

modes, it combines with the ETG's spectrum, so that the high-k system is measuring not only ETG-driven oscillations, but also TEM or microtearing-driven oscillations.

In summary, at the given experimental parameters the ETG mode is unstable in shot 124948. The resultant turbulent fluctuations can account for roughly half of NSTX's electron thermal flux; however, this comparison comes with a number of caveats. Firstly, the transport may be sensitive to input parameters, such as the driving gradient. A complete discussion of these effects appears in Section 4.3. Secondly, ETG is not the only unstable mode in this plasma: a number exist at longer wavelengths. TGLF suggests that these longer wavelength modes can make up the other half of the experiment's heat flux. Since the high-k system does not measure the peak of the ETG-driven power spectrum, it is likely measuring a tail. This tail could be the nonlinear cascade of the ETG mode, or that of a longer-wavelength instability, or, most likely, some combination thereof. Without a computationally expensive multiscale simulation, the question of whether the source of high-k fluctuations is ETG-driven oscillations must remain unanswered.

Although determining the origin of high-k fluctuations is nuanced, in part because the plasma exists in a turbulent state as defined by the nonlinear interactions of many linear modes, NSTX's small-scale fluctuations can still drive significant electron thermal flux. The important question is, given this flux, how can we control it?

4.2 Suppressing ETG Turbulence

A method to reduce electron transport in NSTX is the introduction of reversed magnetic shear. This effect can be so strong as to trigger the formation of electron internal transport barriers, or e-ITBs. Through nonlinear gyrokinetic simulations, we now attempt to explain the formation of e-ITBs by reversed magnetic shear.

NSTX shot 129354 is a prime example of an e-ITB. The electron temperature, Fig. 3.3, is above 3 keV in the inner-most quarter of the plasma. Outside of this zone, it drops significantly; in the

outer half of the plasma $T_e < 0.5$ keV. The transition occurs over a very small region, from r/a of $\sim 0.25 - 0.5$. As the minor radius is only 67 cm, this "barrier" is less than 20 cm across. The other feature of 129354 is that its magnetic shear, Fig. 3.4, is very negative, dipping below -2 for $0.25 < r/a < 0.35$. $\hat{s} < 0$ at the location of the barrier is characteristic of an NSTX e-ITB plasma. Experimentally, the only way to trigger an e-ITB is to reverse the magnetic shear.

The puzzle about plasmas like 129354 is that they have gradients that are well-above the linear critical gradient for ETG transport. If ETG can drive significant heat flux, as shown in the previous section, why then doesn't it during an e-ITB? Some mechanism must be at work, preventing ETG-driven flux from relaxing the temperature gradient. Since magnetic shear is the experimentally important knob (e-ITBs can be formed over a range of Z_{eff} and q), it seems to be a good candidate for the ETG-suppression occurring during an e-ITB.

In this section we aim to determine to what degree $\hat{s}$ is responsible for suppressing ETG turbulence and triggering e-ITBs in NSTX. A key goal is to separate the effects of linear and non-linear physics. $\hat{s}$, $\tau = Z_{eff}T_e/T_i$ and q all affect the linear critical gradient for ETG instability, $z_c = (R/L_{T_e})^{\text{linear}}_{\text{critical}}$. In particular, Jenko and Told have pointed out that if Z_{eff} could potentially be strongly stabilizing for this NSTX discharge [112]. Perhaps $\hat{s}$ shuts off the ETG mode by raising z_c. This would indicate linear physics as the driving mechanism for e-ITB formation. An alternative would be an enhanced critical gradient, due to nonlinear physics, z_c^{NL}, whose effects would only emerge in a nonlinear turbulent system. Turbulent plasma profiles would be stiff around z_c^{NL}, which may or may not be close to z_c. The Dimits shift discussed in Chapter 2 occurs when the nonlinear interaction of zonal flows and ITG turbulence causes z_c^{NL} to be greater than z_c by about 50%: $z_c \sim 4\ R/L_{T_i}$, but $z_c^{NL} \sim 6\ R/L_{T_i}$, for the Cyclone case [76]. The strength of this upshift for ITG turbulence depends on the specific problem parameters: the shift is reduced at higher q or when including the effects of trapped electrons [78], but can be enhanced by plasma shaping [77]. A similar effect may also occur with ETG turbulence, so a possible explanation for the e-ITBs is a magnetic shear-induced nonlinear upshift of the critical gradient for ETG transport, with $z_c^{NL} > z_c$.
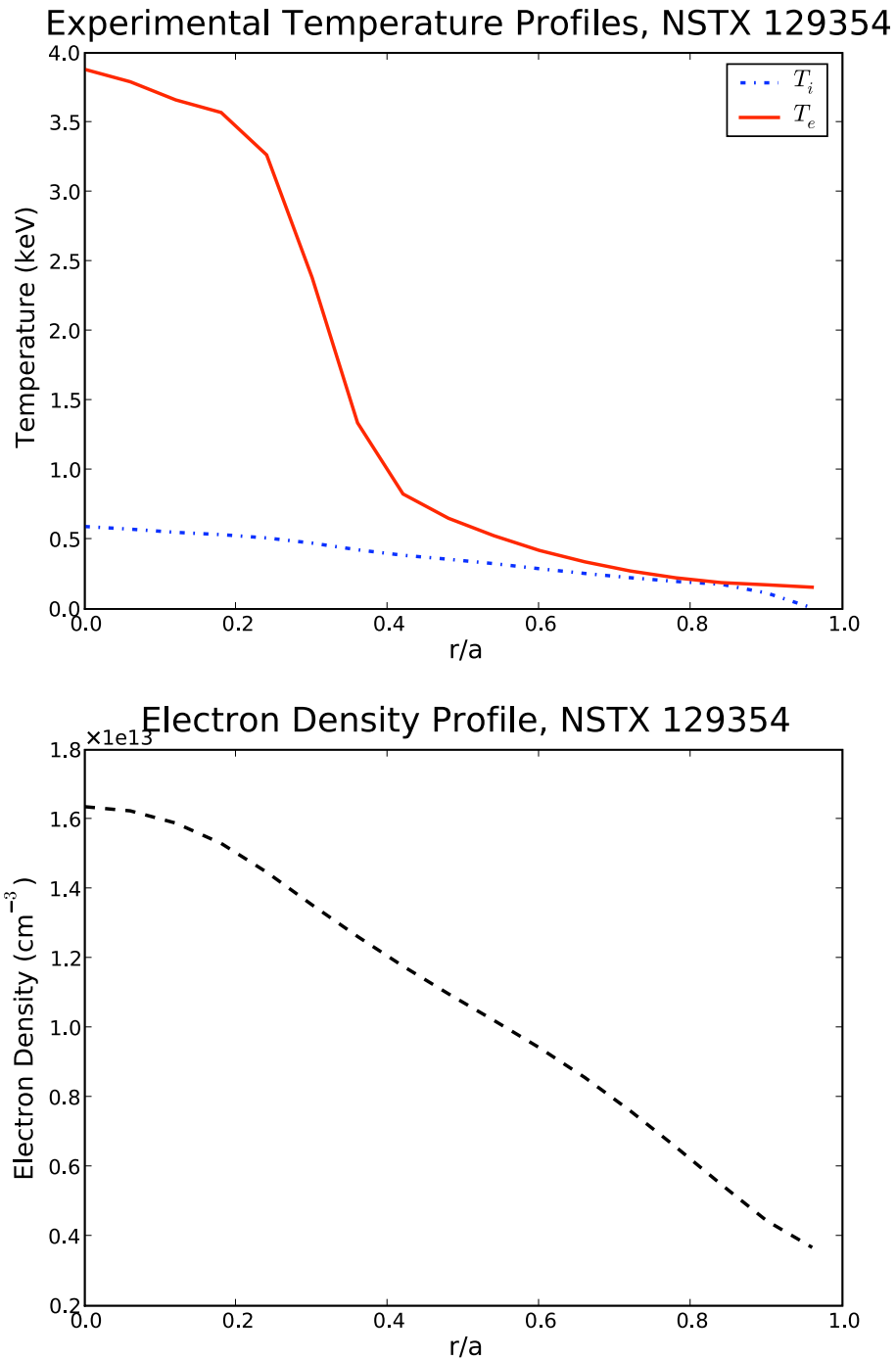
Figure 4.19: Temperature and density profiles for NSTX shot 129354 at 232 ms during an electron internal transport barrier, e-ITB.

Table 4.3: Parameters for 129354 e-ITB flux tube simulations.

Geometric					
r_0/a	0.300	R_0/a	1.547	$\rho_\star$	0.046
Δ	-0.268	κ	1.765	s_κ	-0.349
δ	0.105	s_δ	-0.073	ζ	-0.002
s_ζ	0.127	q	2.395	$\hat{s}$	-2.401
Baseline Plasma					
T_D/T_e	0.22	R/L_{T_e}	11.6	R/L_{n_e}	1.79

To investigate the barrier formation we pick NSTX shot 129354 at 232 ms, during its RF-heated e-ITB phase, using GYRO to simulate a series of flux tubes with different parameters, but each centered on the plasma at $r/a = 0.3$. Figure 4.19 shows the temperature and density profiles at this time, and Table 4.3 lists the baseline experimental parameters at $r/a = 0.3$. The electrons are much hotter than the deuterium ions. The TRANSP-calculated baseline temperature gradient, $R/L_{T_e} = 11.6$, is an under-estimate of the observed gradients in the barrier due to spline smoothing of the plasma profiles. The un-splined value lies between 20 and 30 [39].

A major uncertainty in the profile comes from the plasma's impurities, and therefore Z_{eff}. Deuterium is the main ion. Some amount of carbon does exist during this shot; however, from a combination of disagreeing diagnostics and stray-light from the RF antenna, the exact concentrations of impurities are not known to a high precision. Due to experimental uncertainties, τ could vary from roughly 3 to 17, although the most likely value lies between 7 and 9. This measurement uncertainty is problematic, especially since the linear critical gradient for ETG is thought to be sensitive to this parameter. Figure 4.20 shows the effect of τ on z_c over the range of possible experimental values.

Primarily, increasing τ increases z_c, for both the ETG-ki and ETG-ai models. It is possible for this effect to explain the observed gradients ($R/L_{T_e} > 20$), but it is unlikely, not only because it
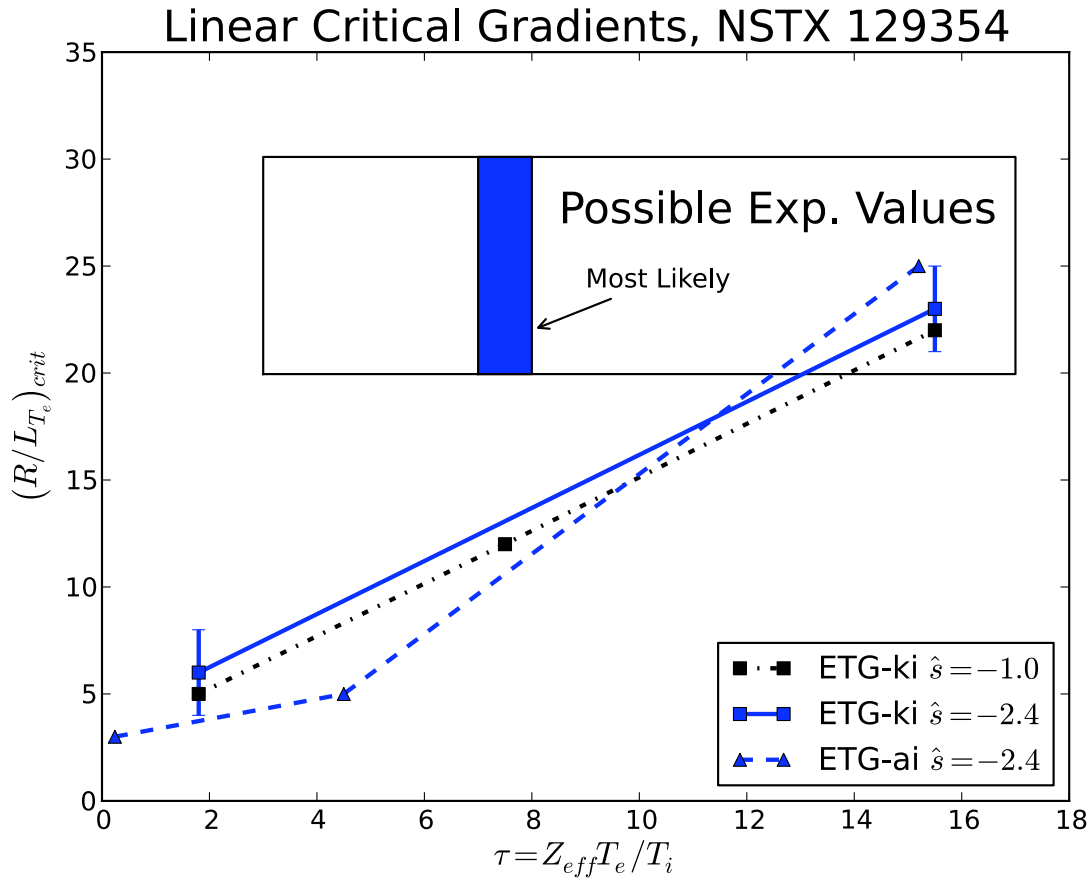
Figure 4.20: Linear critical electron temperature gradients, NSTX 129354 during an e-ITB, testing the effects of τ, $\hat{s}$ and ion model. Although only shown for the ETG-ki $\hat{s} = -2.4$ case, the uncertainty in each point is the same (which comes from extrapolating linear growth rates at large gradients downward to the threshold for positive growth). The boxes represent possible and mostly likely experimental values of τ and R/L_{T_e} within the e-ITB, where $\hat{s} = -2.4$.

would require values of τ on the extremes of the experimental uncertainty, but also because Z_{eff} is not the observed trigger of e-ITBs. The important mechanism is $\hat{s}$, which evolves during the course of the shot. At some point during the e-ITB, the current profile relaxes and $\hat{s}$ becomes positive. When this occurs, τ doesn't change. T_e/T_i is still very large, and so is τ. However, the e-ITB collapses. The linear effect of τ increasing the critical gradient is not likely the cause of the e-ITBs.

Another observation is the effect of $\hat{s}$ on z_c. The ETG-ki curves in Fig. 4.20 show that decreasing $\hat{s}$ from -1 to -2.4 does indeed increase z_c, but the effect is too small to explain the experimental temperature gradients. At the most likely value of τ, $z_c = 12 \pm 2$, far below the observed 25 ± 5 R/L_{T_e}. The linear stabilization of the ETG mode by $\hat{s}$ cannot explain the e-ITBs.

According to Fig. 4.20, τ has the greatest effect on the linear critical gradient for the ETG mode. The trend is linear and roughly follows the equation

$$\left(\frac{R}{L_{T_e}}\right)_{\text{crit.}} = 3.5 + 1.25\tau. \tag{4.1}$$

We can use this estimate to approximate the linear critical gradient as a function of plasma radius, due only to τ, taking into account the variability of T_e/T_i and the uncertainty on Z_{eff}, which though most likely near 2, could range from 1.5 to 3.5 and not disagree with experimental measurements. Figure 4.21 shows a profile of experimental and estimated critical gradients using Eq. 4.1. The lower bound uses $Z_{eff} = 1.5$, the dashed line $Z_{eff} = 2$ and the upper bound $Z_{eff} = 3.5$. A few features stand out. Firstly, outside of $r/a = 0.4$, the foot of the barrier, the experimental and linear critical gradients agree fairly well. Between $r/a = 0.3$ and $r/a = 0.4$, the measured gradients are above the linear critical gradient, even considering the uncertainties in Z_{eff} and R/L_{T_e}. Inside of $r/a = 0.3$, however, the linear critical gradient is very high, much larger than the experimental value, due to the large value of T_e/T_i in the core. This analysis breaks the plasma into three distinct regions: inside the barrier ($r/a < 0.3$), a barrier ($0.3 < r/a < 0.4$), and outside of the barrier
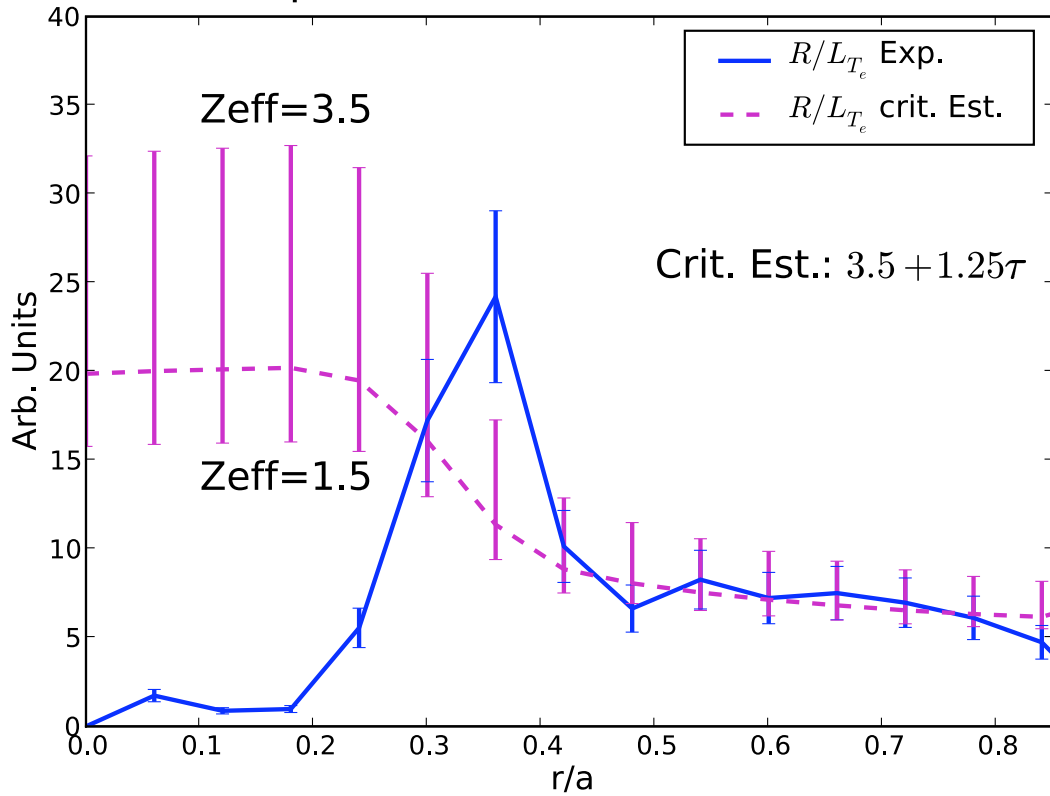
Figure 4.21: Profile of experimental and ETG linear critical gradients, NSTX 129354, using Eq. 4.1 to estimate the linear critical gradients. The lower bound represents $Z_{eff} = 1.5$, the dashed profile $Z_{eff} = 2$ and the upper bound $Z_{eff} = 3$.

$(0.4 < r/a)$. The gradients in the outer region are consistent with the limits of linear ETG physics. Within the barrier, the experimental gradients are larger than the linear critical gradient. And the inner region does not appear to be limited by the ETG mode: something else must be constraining the gradients inside of the barrier, causing the temperature profiles to be flat. Determining the mechanism that limits the gradients inside the barrier is beyond the scope of this work. For now, the salient point is that the barrier exists, with measured experimental gradients well above the threshold for the linear ETG mode's instability. Outside of the barrier, the plasma may indeed be limited by the ETG mode. That is, we expect ETG-driven transport to be low for $r/a < 0.4$ and high for $r/a > 0.4$. But as it stands, the linear ETG critical gradient cannot explain the observed e-ITB gradients.

Since linear physics does not seem to explain gradients above $R/L_{T_e} = 20$, perhaps nonlinear physics does. The goal is to investigate the existence of a strong z_c^{NL} up-shift from z_c, using a series of flux-tube simulations at different values of τ and $\hat{s}$, comparing the heat flux as a function of driving gradient.

4.2.1   Resolution Requirements

The ETG simulations of the previous section inform the resolution requirements for the nonlinear e-ITB experiments. We pick a realistic mass ratio, using $\mu_e = 60$. Δx should be less than ρ_e. The bounce-orbit grid will likely need to be higher than the value for large aspect ratio tokamaks. We choose to vary some numerical resolutions by the parameter X, which defines not only the poloidal grid, but also the passing and trapped particle pitch angles: `PASS_GRID = TRAP_GRID = X`, `ORBIT_GRID = BLEND_GRID = 2X`. Keeping this relationship between the grid parameters helps insure uniform convergence in the different dimensions' resolutions [113]. These input parameters correspond to $n_\theta = 4X - 2$. For reference, the earlier convergence studies found that $n_\theta \geq 14$ was necessary for convergence, corresponding to $X \geq 4$.

Since we will vary the shear and driving gradients, our baseline resolution test will involve median parameters: $\hat{s} = -1, \tau = 1.8, R/L_{T_e} = 15.5$ and the ETG-ki model, at the most unstable end of Fig. 4.20. The flux tube measures $2.22 \times 2.33\ \rho_s$ $(133 \times 140\ \rho_e)$, containing 24 modes ranging from $k_\theta \rho_s$ $(k_\theta \rho_e)$ of 2.70 (0.045) up to 62.03 (1.03). $\Delta x = 0.89 \rho_e$.

Energy Grid Convergence
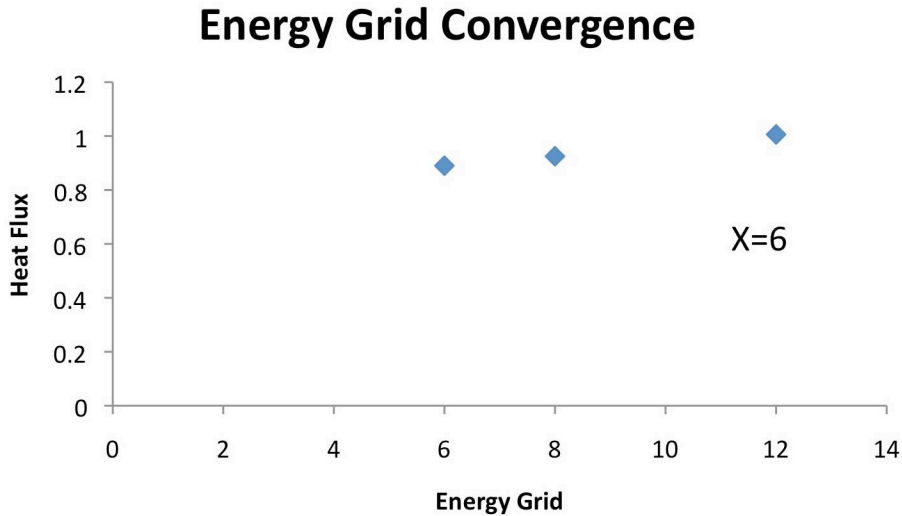
Figure 4.22: e-ITB resolution tests varying the energy grid. The bounce-orbit parameter $X = 6$ and $dt = 3.3 \times 10^{-4}$. Fluxes are electron heat fluxes in ion gyroBohm units.

Figure 4.22, a scan in energy grid resolution at fixed $dt = 3.3 \times 10^{-4}$ and $X = 6$, shows little sensitivity in the electron heat flux above $n_\epsilon = 6$. Doubling the energy-grid resolution increases the heat flux by only about 10 percent. Considering the magnitude of the fluctuating values of the nonlinear chaotic system, such as demonstrated by the $X = 6$ time trace in Fig. 4.23, this change is not very significant.

The effects of bounce-orbit resolution are more pronounced, as demonstrated in Fig. 4.24. This test shows heat fluxes for a number of values of X and δt at fixed $n_\epsilon = 6$. In agreement with the earlier ETG convergence studies, $X = 3$ is under-resolved. Statistical convergence doesn't arrive
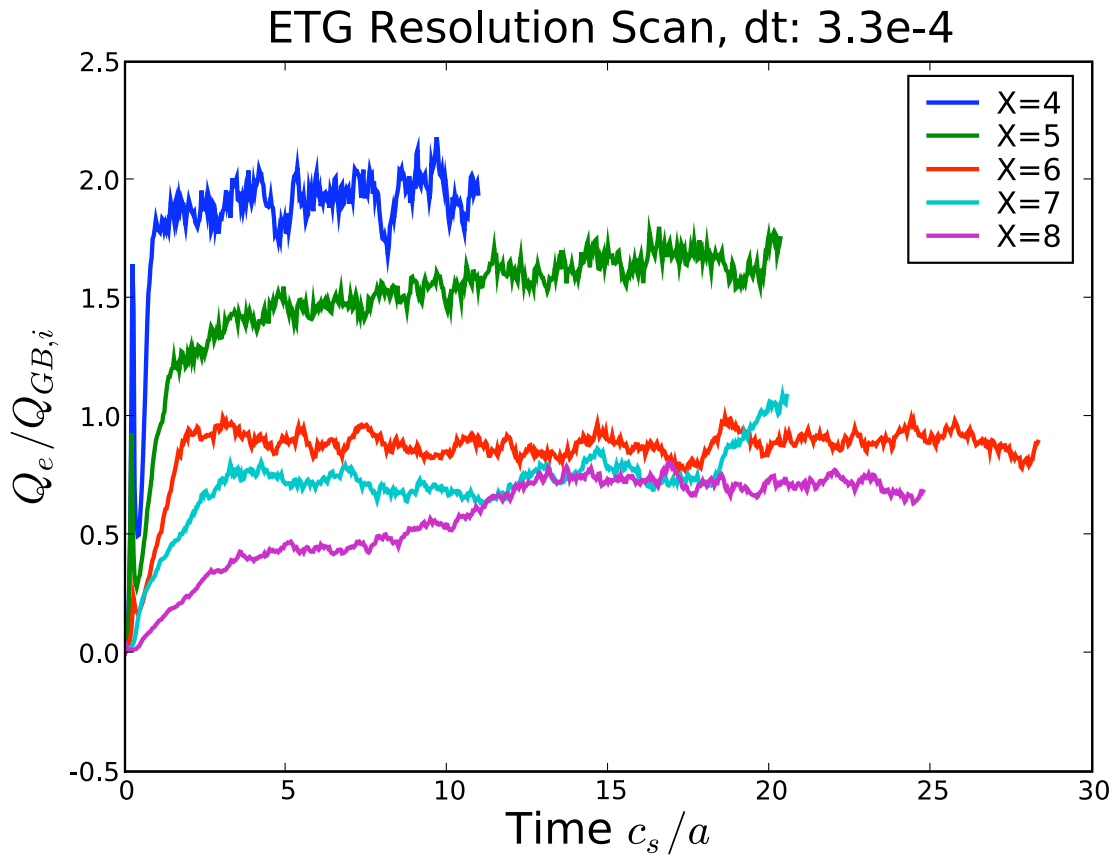
Figure 4.23: Time traces of the e-ITB resolution tests varying the bounce-orbit grid (as defined by X) at a fixed time step $dt = 3.3 \times 10^{-4}$. The energy grid resolution is held at $n_\epsilon = 6$.
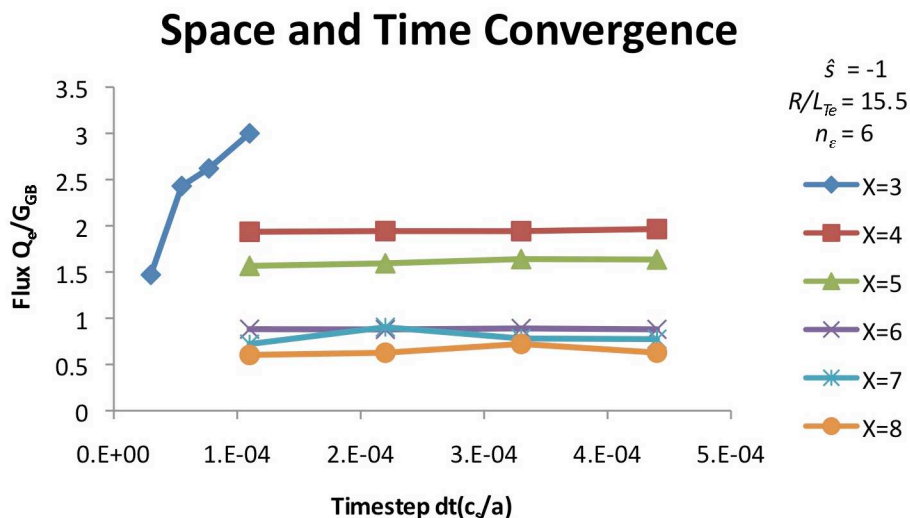
Figure 4.24: e-ITB resolution tests varying the bounce-orbit grid (as defined by X) and time step. The energy grid resolution is held at $n_\epsilon = 6$.

until $X = 6$, above which the differences in fluxes depend on the location of time-averaging windows.

At these high resolutions, even flux tube computations become very expensive, costing upwards of $100,000$ CPU-hours a piece. Balancing accuracy with feasibility, the $\hat{s}$ and R/L_{T_e} parameter scans proceed with $X = 6$, $n_\epsilon = 6$ and $dt(c_s/a) = 3.3 \times 10^{-4}$.

4.2.2 $\tau = 7.5$

We start the parameter scan in the most likely range of τ, simulating ions, electrons and carbon simultaneously. $n_D/n_e = 0.867$ and $n_c/n_e = 0.022$ and $\hat{s} = -1$. The flux tube, however, remains electron-sized, with a default size of $L_x \times L_y = 178 \times 140\rho_e$, and $k_\theta\rho_e < 1.03$. Figure 4.25 compares the electron heat fluxes as a function of driving gradient. The ETG-ki and ETG-ai models at the default box size agree fairly well up to very large gradients (although the ETG-ai runs consistently calculate less flux). The similarity between ETG-ki and ETG-ai runs shows that
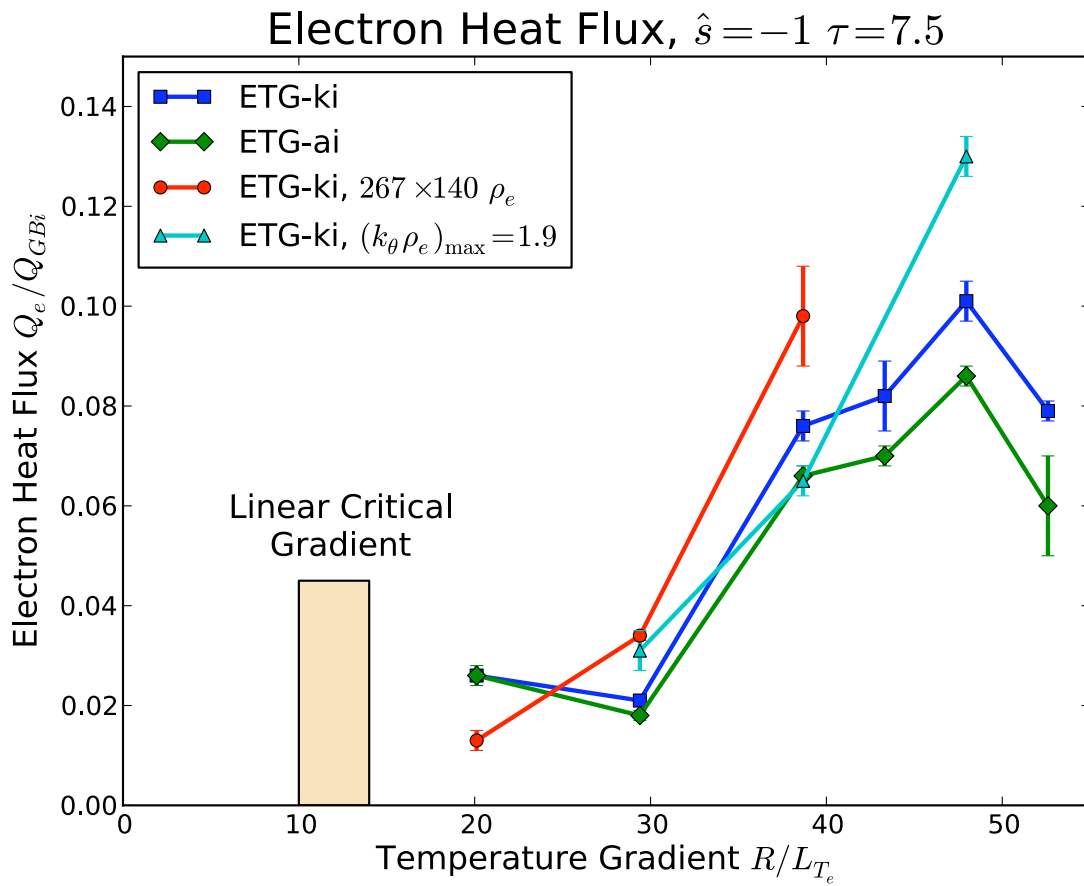
Figure 4.25: Electron heat flux as a function of driving gradient for $\tau = 7.5$, $\hat{s} = -1$.

the ion response in this region is nearly adiabatic. This is encouraging from the impurity point of view, because altering the concentrations of ions has the exact same effect as using an effective charge. The important parameter is thus τ, and not n_D, n_c or n_{Fe}.

Overall, Fig 4.25 displays remarkably little heat flux, even at temperature gradients that are not only well-above the linear critical gradient, but that are also well-above the experimental parameters. 0.1 ion gyroBohms of electron heat flux corresponds to 9×10^{-3} MW/m^2, which is only 18% of the typical 5×10^{-2} MW/m^2 seen in the normal shear RF experiment (see Fig. 4.12). Furthermore, in order to achieve this level of flux, one must drive the experiment above the experimental range of $20 - 30$ R/L_{T_e}. Only above this point does the heat flux start to increase significantly with the gradient. As such, $z_c^{NL} \sim 30 - 40$. The nonlinear critical gradient for transport is much higher than the linear critical gradient. While the ITG Dimits shift saw $z_c^{NL} - z_c \approx 2$, for the ETG $\hat{s} = -1$ shift, $z_c^{NL} - z_c \gtrsim 15 - 25$. This is very strong. In some sense, though, it is too strong, because even at $R/L_{T_e} = 40$, the flux much smaller than experimentally inferred levels. While a more complete comparison to experimental levels should contain a discussion of measurement uncertainties, which we save for Section 4.3, generally speaking in order to drive the heat flux to experimentally-relevant levels (of $Q_e \sim 0.1 - 0.2 Q_{GBi}$ for this shot), one needs gradients that are well above the experimental parameters.

Keeping in mind that typical experimental heat fluxes correspond to $Q_e \sim 0.1 - 0.2 Q_{GBi}$, in absolute units increasing the box size on the ETG-ki model has a modest effect on the flux for $R/L_{T_e} \approx 40$, but less so at lower gradients. Including very high-k modes, up to $k_\theta \rho_e$ of 1.9 does increase the integrated flux at $R/L_{T_e} \approx 48$ by about 25% over the baseline case, but at more modest gradients the effect is negligible. This is due to the fact that the linear growth spectrum moves to higher-k as the temperature gradient increases; however, this is not the case below $R/L_{T_e} \approx 40$. While both the default box size and maximum mode number seem adequate in the range of experimentally relevant parameters, $R/L_{T_e} \lesssim 30$, neither increasing the box size

nor including additional modes can push the calculated flux to experimentally relevant levels, even at gradients much larger than those observed in the experiment.

Flux tube simulations at $\tau = 7.5$ show that electron transport remains low for driving gradients that are much higher than the linear critical gradient. However, the nonlinear critical gradient implied by this transport rests well-above observations of e-ITB plasmas. Furthermore, the effects of τ and $\hat{s}$ cannot at this point be separated: the upshifted critical gradient could be due to either, or both, of these parameters. To identify $\hat{s}$ as the crucial ingredient in NSTX e-ITBs requires simulations at a different value of τ.

4.2.3 $\tau = 1.8$

This low value of τ corresponds to a plasma that is the most linearly unstable to ETG. In this particular discharge, it is a value that is lower than seen in the barrier and more similar to parameters just outside the barrier, where T_e and T_i are closer to each other. It is also likely that the transport properties at the foot of the e-ITB play a role in determining the properties of the barrier. That is, transport should be stiff outside of the e-ITB. If it were not, under applied heating the plasma gradients would climb, pushing the foot of the barrier outward. Logically, then the barrier foot would exist at the stiff-transport threshold, near z_c^{NL}.

The search for z_c^{NL} at $\tau = 1.8$ involves a series of flux tube simulations at different values of $\hat{s}$: -0.2, -1.0 and -2.4, the most negative found during the e-ITB. This spans the range of negative magnetic shears found in NSTX. Experimentally, $\hat{s} = -0.2$ is not associated with an e-ITB, but the other two values are. The numeric resolutions are: $X = 6$, $L_x \times L_y = 255.6 \times 144\rho_e$, $\Delta x = 0.998\rho_e$, $(k_\theta \rho_e)_{max} = 1.004$, $n_\epsilon = 12$, $dt = 3.3 \times 10^{-4}$. The simulations retain electron-ion collisions, with $\nu_{ei} = 0.016(a/c_s)$, but include neither $\mathbf{E} \times \mathbf{B}$ flow shear nor finite Debye length. They are all electrostatic. Even at these parameters, each flux tube simulation is again very expensive, costing $80,000 - 100,000$ CPU-hours a piece.
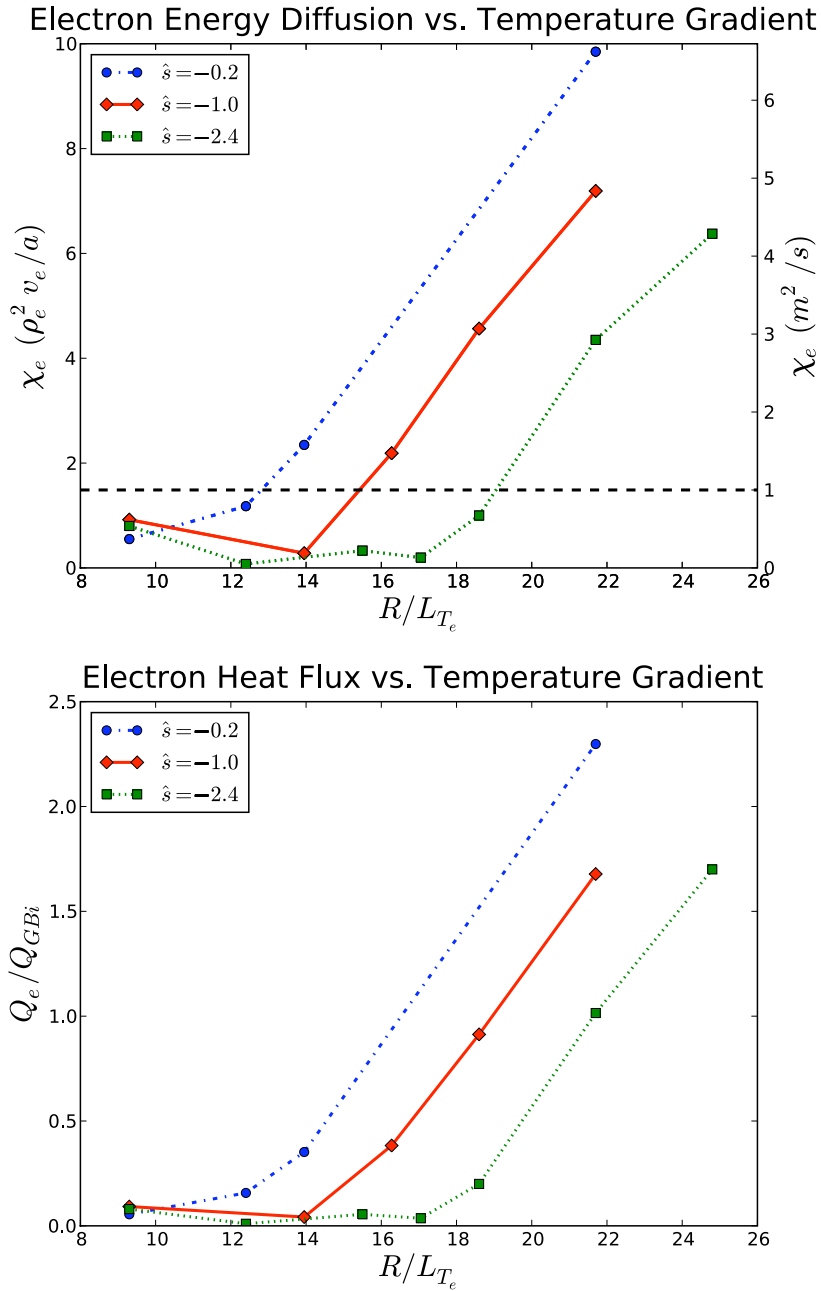
Figure 4.26: Electron thermal diffusivity (top) and heat flux (bottom) as functions of driving gradient and magnetic shear for $\tau = 1.8$. The horizontal dashed line marks typical experimental values of χ_e.

Primarily we find a large upshift in the critical gradient for transport, due to magnetic shear. Figure 4.26 shows both electron heat flux and thermal diffusivities for a number of gradients and shear values. The horizontal dashed line marks experimentally relevant thermal diffusivities at $1 \text{ m}^2/\text{s}$. This serves as just a guide for typical levels. See Section 4.3 for a complete discussion on the comparisons against experiment. In any case, at the lowest gradients, the thermal transport is low, but raising the gradient does not immediately increase the flux, even though all of these are linearly unstable to ETG turbulence. Figure 4.27 shows the linear and nonlinear critical gradients for the different values of shear, where z_c^{NL} is defined as the point above which the thermal diffusivity exceeds $1 \text{ m}^2/\text{s}$. For all tested values of shear, the upshift in the critical gradient $\Delta z = z_c^{NL} - z_c$ is very strong and gets stronger as the magnetic shear gets more negative, ranging from 9 at $\hat{s} = -0.2$ to 13 at $\hat{s} = -2.4$. As a comparison, the Dimits shift represents an increase of the critical ITG gradient from $R/L_{T_i} = 4$ to 6 for the Cyclone parameters [76]. The effect of magnetic shear on ETG turbulence is much stronger.

Additionally, the location of z_c^{NL} is consistent with observed gradients during an e-ITB. $z_c^{NL}(\hat{s} = -2.4) = 19$, which approaches the experimental range of 20-30. Although this value still lies below the experimental value, increasing τ to within the experimental range is likely to boost z_c^{NL}.

Another interesting feature of z_c^{NL} is that above this value ETG drives large amounts of electron heat flux. The pioneering work by Jenko and Dorland on ETG turbulence with reversed shear found that electron transport stayed low at $\hat{s} = -1$ for $z - z_c \lesssim 11$ [85]. This is right near the threshold for our calculations at $\hat{s} = -1$, for which $\Delta z \approx 11$. Perhaps had this early work included even higher temperature gradients, it would have also found that electron transport becomes stiff again.

Above this threshold, the nature of the turbulence also changes, in some cases identified by radial streamers that lie not on the midplane, but at a finite poloidal elevation. Figure 4.28 shows a poloidal cross-section of electron density fluctuations above the linear critical gradient, but below the nonlinear critical gradient. While the location of the central flux surface is correct, the radial
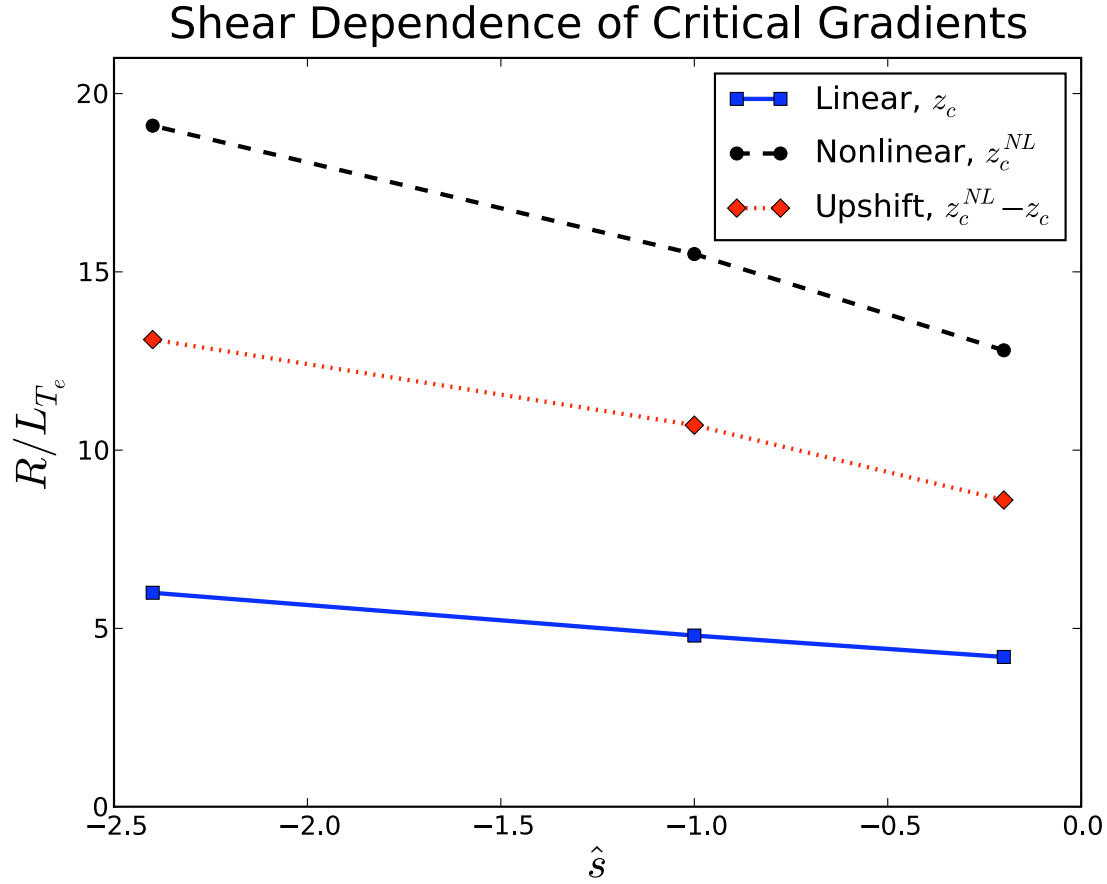
Figure 4.27: Critical gradients as a function of magnetic shear, $\tau = 1.8$. ETG becomes linearly unstable at gradients above z_c (solid with square). Above z_c^{NL} (dashed with circles), turbulent χ_e exceeds experimental values, $1 \text{ m}^2/\text{s}$. The dotted line with diamonds represents the nonlinear upshift of the critical gradient, $\Delta z = z_c^{NL} - z_c$. For comparison, the original cyclone ITG test case found an upshift in the critical gradient for transport that extended R/L_{T_i} by 2, from $z_c = 4$ to $z_c^{NL} = 6$ at $\hat{s} = 0.78$ [76].

$$\tilde{n}_e \quad \hat{s} = -2.4 \quad R/L_{T_e} = 9.3$$
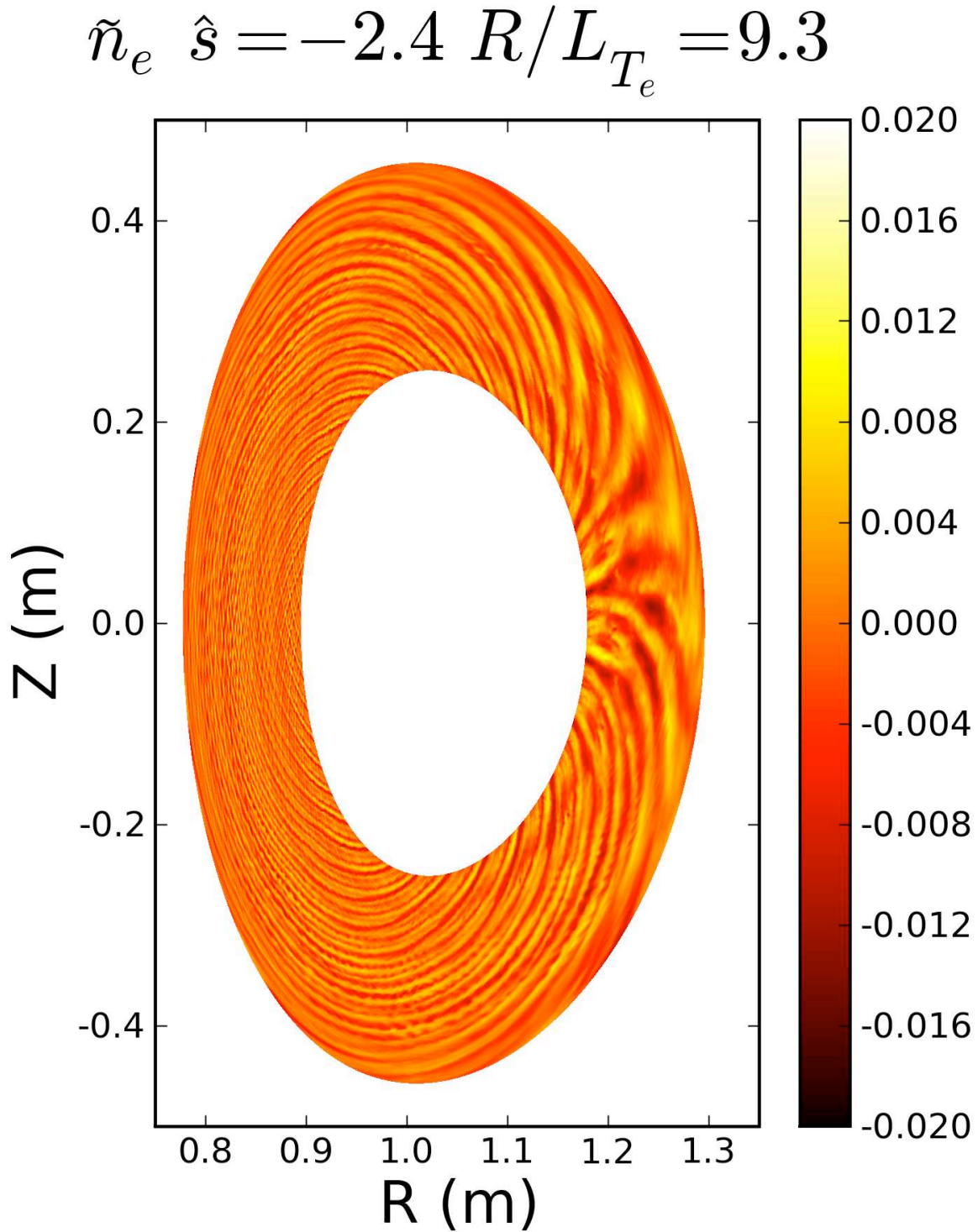
Figure 4.28: A cross-section of density fluctuations for $\hat{s} = -2.4$, with z above z_c but below z_c^{NL}. The location of the flux surface's center correct, but its width has been enhanced to show the fluctuations. The magnetic shear rotates eddies away from the midplane.

width of the computational domain has been enhanced for visibility. (The flux tubes were run with $\rho_\star = 4.6 \times 10^{-2}$, a factor of 4 above the physical value. $\rho_\star$ itself doesn't enter the local flux tube equations.) In Fig. 4.28 the eddies rotate away from the midplane, consistent with theories on how magnetic shear can reduce transport [114]. More radially elongated streamers produce larger amounts of radial flux, such as seen in the non-e-ITB ETG simulation of Fig. 4.11. The magnetic shear works by rotating these streamers away from the midplane, so while the ETG mode is unstable and active, its effect on transport is mitigated.

While $\hat{s}$ serves to rotate eddies and reduce transport when z is below the nonlinear critical gradient, a different picture emerges when z is above z_c^{NL}. Figure 4.29 shows the density fluctuations at $R/L_{T_e} = 21.8$, where ETG again produces large amounts of electron flux $Q_e \approx 1Q_{GBi}$ (four times the experimentally relevant levels). The midplane is populated with small-scale broadband tubulence, while off the midplane, $\theta = \pm\pi/2$, large-scale structures appear. These elongated eddies point in the minor radial direction, which at these poloidal locations corresponds to aligning in the Z direction, out of the top and bottom of the annulus.

These "off-midplane" streamers drive a significant amount of heat flux, accounting for roughly one quarter of the integrated total. They also are localized in a narrow toroidal spectral band. Figure 4.30 shows fluctuation powers as a function of poloidal angle and toroidal mode number. The strongest peak exists at $\theta \approx \pm\pi/2$, the location of the off-midplane streamers. These peaks are not only very strong and poloidally localized, but also center around $k_\theta \rho_s = 13$. Furthermore, the midplane fluctuations exist in a broadband spectrum at higher mode numbers. Figure 4.31 shows the integrated heat flux from these fluctuations as a function of the maximum $k_\theta \rho_s$. The heat-flux signatures of both the midplane broadband turbulence and the off-midplane streamers are visible, as is the linear growth rate spectrum. The turbulent flux has a broad spectrum and a sharp narrow peak, at the location of the off-midplane streamers, whose integrated flux ($0.25\, Q_{GB,i}$) is roughly one quarter of the total. The off-midplane streamers drive a significant amount of thermal flux.

$$\tilde{n}_e \quad \hat{s} = -2.4 \quad R/L_{T_e} = 21.8$$
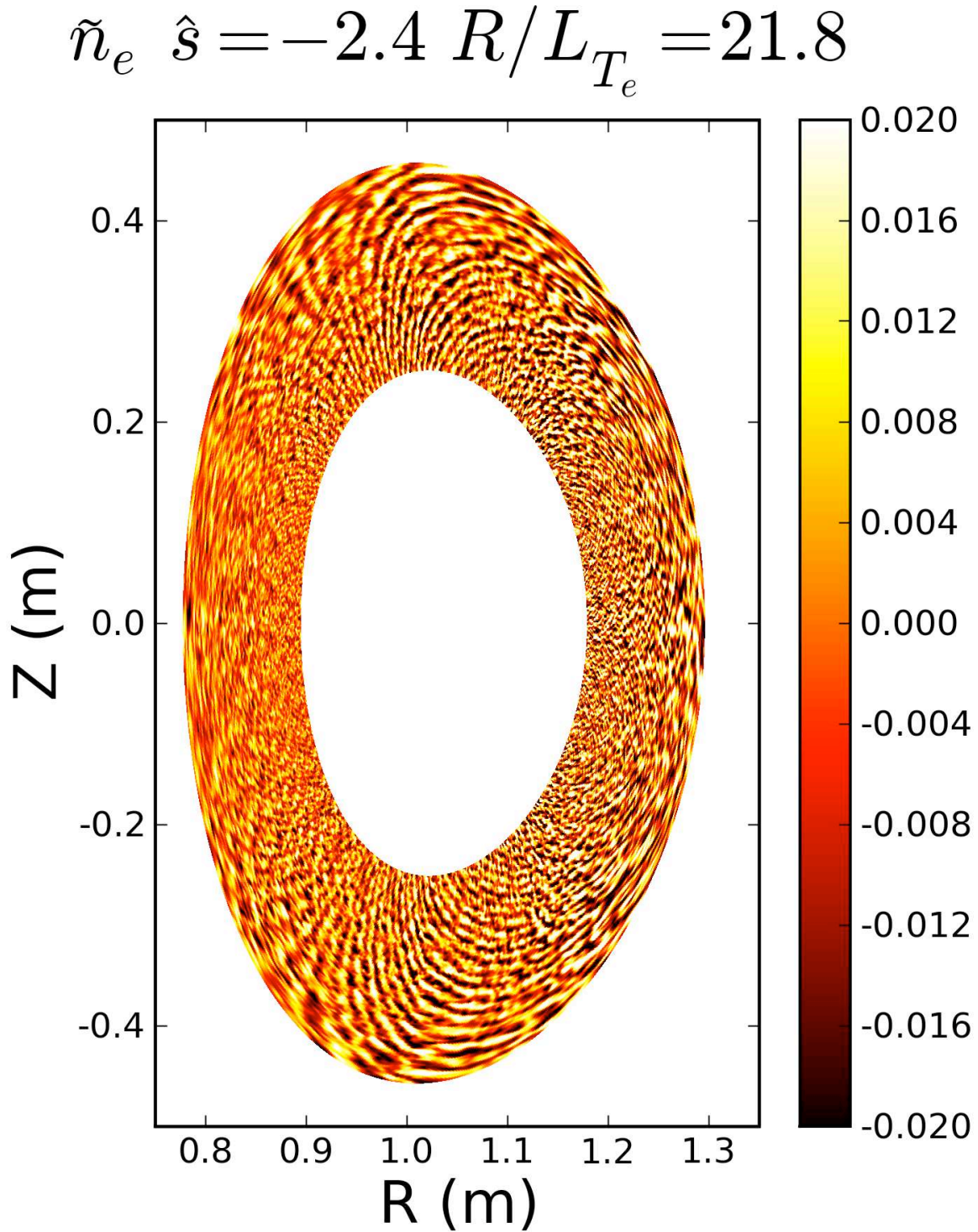
Figure 4.29: A cross-section of density fluctuations for $\hat{s} = -2.4$, with z above z_c^{NL}. The location of the flux surface's center correct, but its width has been enhanced to show the fluctuations. Streamers exist not on the midplane, but rather at $\theta \approx \pm\pi/2$.
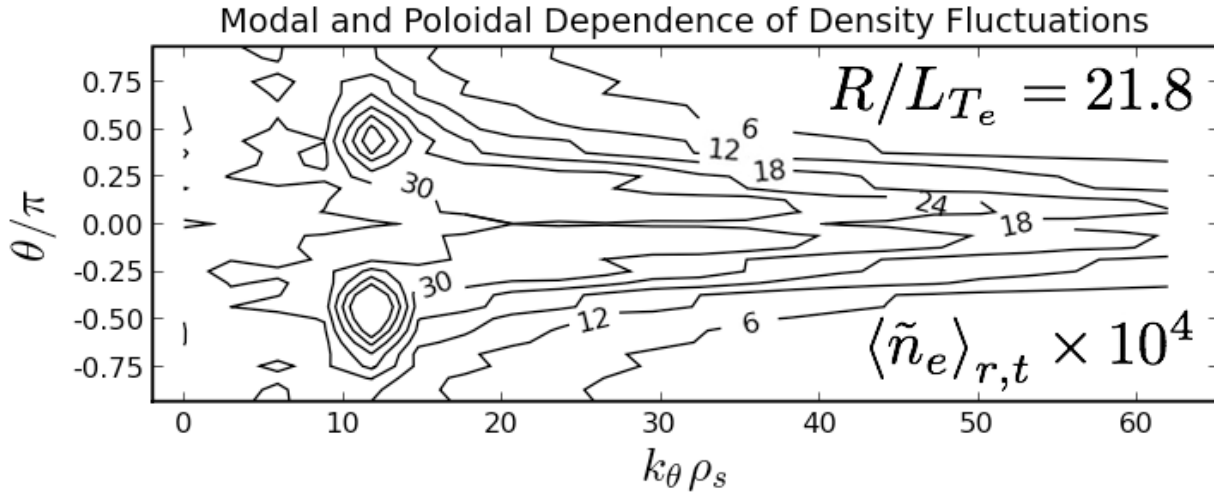
Figure 4.30: Density fluctuations as a function of poloidal angle θ and k_θ, showing off-midplane peaking at $k_\theta \rho_s \approx 13$.

Additionally, the off-midplane streamers evolve on a slower time-scale than the broadband turbulence. Figure 4.32, the time-evolution of the heat flux spectrum, shows the growth at $k_\theta \rho_s \sim$ 40 at early times, $t(c_s/a) < 0.5$. This cascades to lower k and becomes the broadband flux at $k_\theta \rho_s \sim 25$. The streamers' flux, however, doesn't saturate until much later times, $t(c_s/a) \sim 8$. (Only the first half of the simulation is shown, but the spectrum doesn't change at later times).

The sharp spectral peak is actually the signature of narrow band of fluctuations, constrained to finite Fourier modes. Figure 4.33 demonstrates this by overlaying the heat flux spectra from a number of simulations with different values of $k_{\max}$ and δk. The interesting spectrum is the purple, which shows two peaks and not one. In this case δk is such that the power in the red spectral peak is split into the two closest purple modes, suggesting that the continuous spectrum represented by the streamers' peak has a spectral band that is more narrow than the discrete mode spacing δk.

The streamers are not purely a linear feature. The linear growth rate spectrum has three main regions of instability: small peaks centered at $k_\theta \rho_s$ of 12 and 20, and a much larger one around 40. While an instability exists near $k_\theta \rho_s = 13$, failing to include the peak ETG drive at $k_\theta \rho_s \sim$
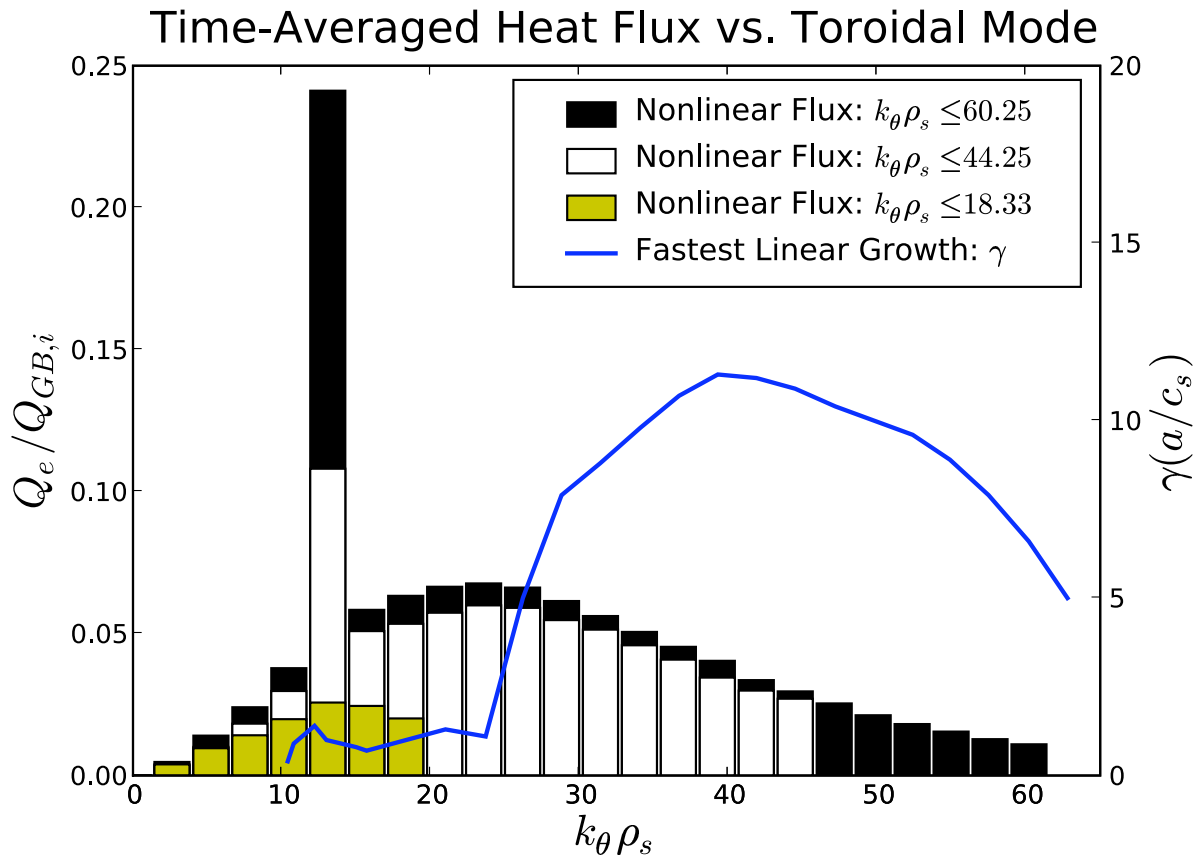
Figure 4.31: Time averaged heat flux spectra for different values of $(k_\theta \rho_s)_{\max}$, $\hat{s} = -2.4$, $z = 21.8$, and the spectrum of the fastest growing linear mode.
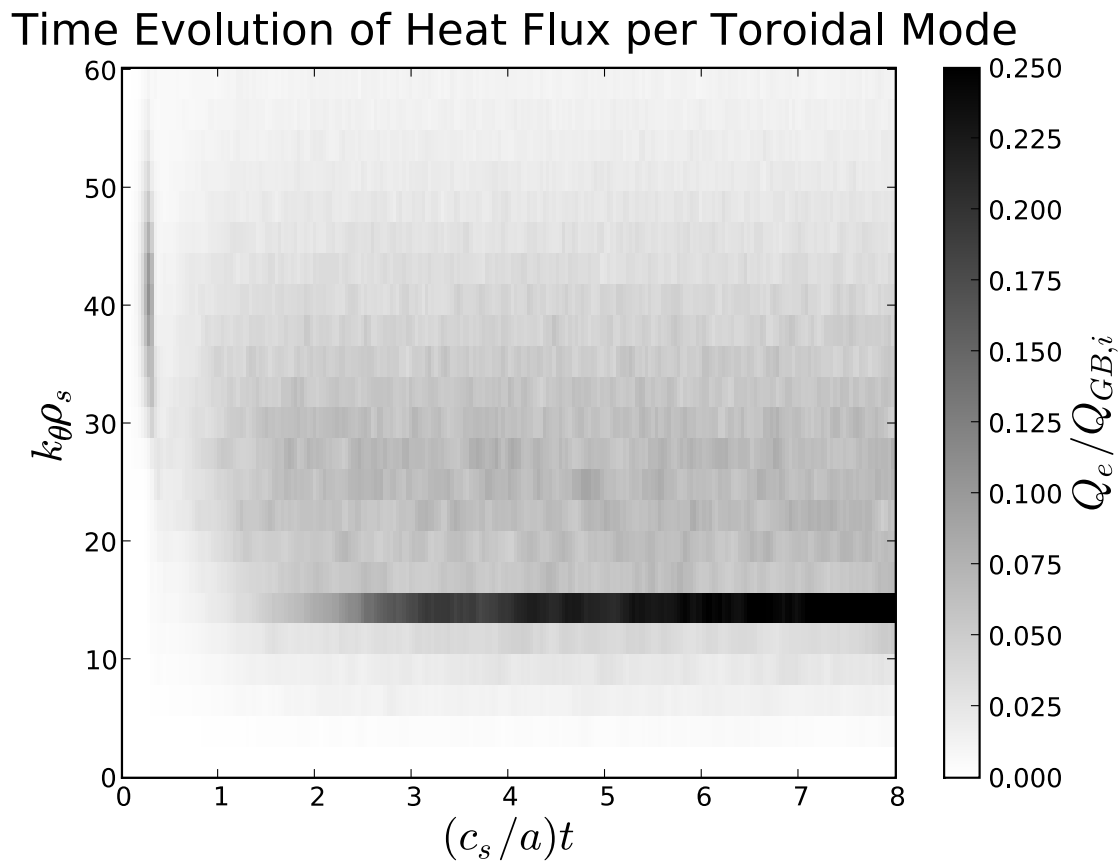
Figure 4.32: Time evolution of heat flux spectrum, $\hat{s} = -2.4$, $z = 21.8$.
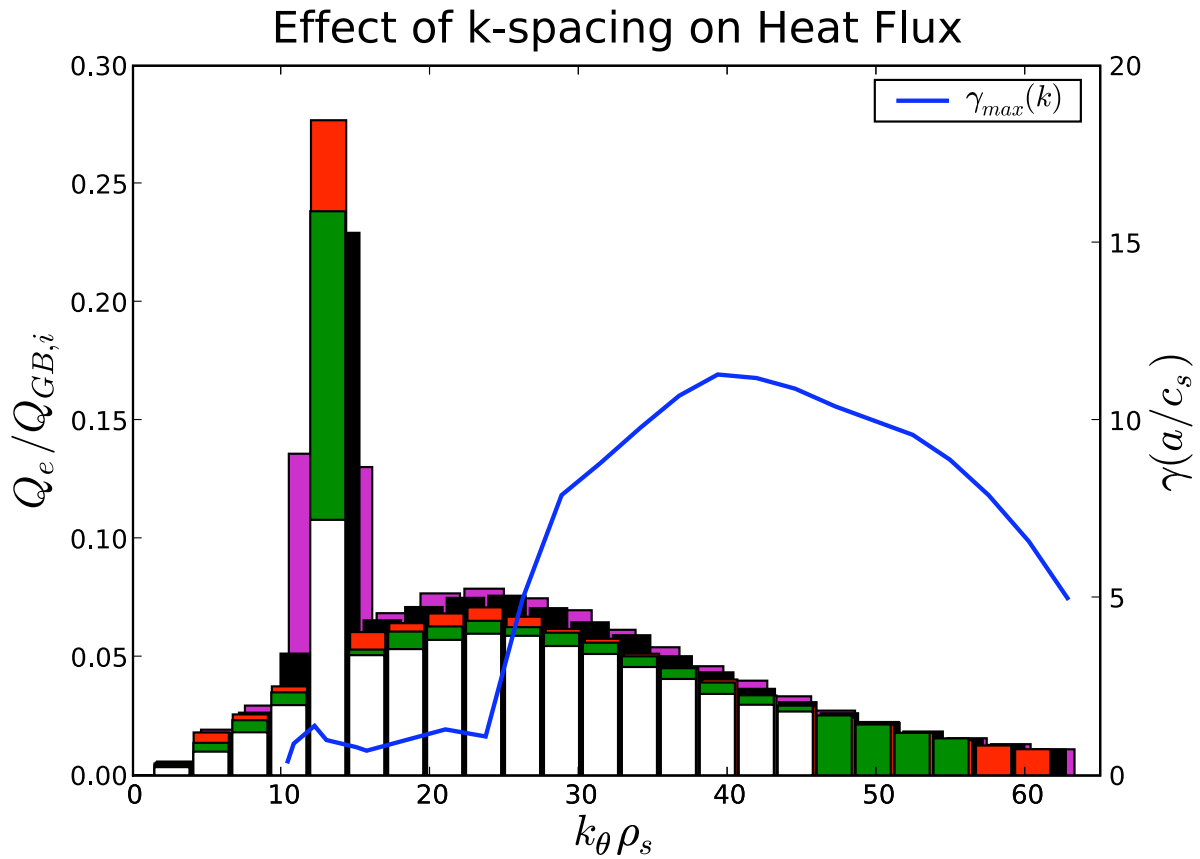
Figure 4.33: Time averaged heat flux spectra for different box sizes and resolutions. The single peak can split its spectral power, depending on the spacing of k_θ.

40 causes the streamers to disappear. Such behavior suggests that the ETG modes growing at $k_\theta \rho_s = 40$ are nonlinearly driving the off-midplane streamers. Put another way, if the streamers were a linear phenomenon, their growth should be independent of the other modes in the system. Since their amplitude depends on the existence of other Fourier modes, a linear explanation for the formation of these streamers is unlikely. The instability growing linearly at $k_\theta \rho_s = 40$ appears to nonlinearly drive both broadband midplane turbulence and off-midplane streamers.

What could these streamers possibly be? Since the evidence suggests they are nonlinearly driven by the ETG mode, the streamers may be the signature of a secondary instability. This was the proposed mechanism for ETG saturation presented early on by Jenko and Dorland [83–85]. Secondary instability theory says that a primary mode (ETG) is linearly unstable in the plasma. As it grows in amplitude, it couples to a second mode, driving it unstable. The secondary mode sucks energy from the primary mode at the secondary's growth rate. Saturation occurs when the growth rates of the two modes balance. The off-midplane streamers may be a signature of an ETG-coupled secondary.

In summation, the flux tube scans at $\tau = 1.8$ have found not only a very strong nonlinear critical gradient, caused by reversed magnetic shear, but also off-midplane streamers, large-scale structures that are nonlinearly driven by ETG turbulence. However, their appearance is not ubiquitous. They only appear at very large gradients and strong reversed shear, and while this condition is necessary, it's not sufficient. In this sense, the streamers may or may not be important to this discharge, since the heat fluxes associated with them are many times the experimentally measured levels, and since they are found at values of τ lower than in the e-ITB. Yet, regardless of the applicability to this particular discharge, their existence is an interesting example of nonlinear turbulent interactions, energy cascades, secondary instabilities and coherent structures.

Taken as a whole, the first-of-a-kind flux tube simulations of NSTX e-ITBs suggest that their formation is caused by reversed magnetic shear, which suppresses ETG-driven thermal transport, thereby allowing the plasma to sustain gradients that are well above the linear threshold for in-

stability. However, experimental uncertainties in τ limit the interpretation. Around an e-ITB, $\hat{s}$ and T_e vary rapidly. Adjusting these parameters independently within a local flux tube simulation allows for the effects of each parameter to be isolated; however, it is their interaction that controls the performance of the experiment. To effectively capture this dynamic, one must allow for plasma profile variation. In other words, we proceed with global simulations of an electron internal transport barrier.

Global Simulations of an e-ITB

To capture the structure of the e-ITB, the global ETG simulation domain spans the foot of the barrier, from $r/a = 0.27$ to $r/a = 0.43$, where T_e drops from ≈ 2.7 to ≈ 0.7 keV, corresponding to $T_e/T_i \approx 5.2$ at the inner radius and ≈ 1.7 at the outer radius, as shown in Fig. 4.19. The goal will be to test two values of Z_{eff}: 2.0 and 3.5, which span the experimental range. τ for $Z_{eff} = 2.0(3.5)$ ranges from $10.4 - 3.4(18.2 - 6.0)$.

With a realistic deuterium-electron mass ratio, $\mu_e = 60$, the domain is $862.2\ \rho_e$ in width, requiring 864 radial grid points. To maximize the useful radial domain, and based on the ETG simulations of Ref. [115], we chose a buffer that is 16 grid points wide, but employ strong electron damping, $\nu_e^{\text{buffer}} = 60(c_s/a)$, and turn on the adaptive source. Such a large radial domain is only feasible with lower-resolutions elsewhere. Since the convergence studies found little sensitivity to the energy grid, $n_\epsilon = 6$. $dt = 2 \times 10^{-4}$ and $X = 6$. Furthermore, as the ETG-ki and ETG-ai models show little difference in the flux tube simulations of Fig. 4.25, we'll treat the ions adiabatically. At these resolutions, each run costs over $150,000$ CPU-hours.

Figure 4.34 shows the radial domain and variation of q and $\hat{s}$. The minimum value of $\hat{s}$, occurring at $r/a = 0.296$ is -2.408. The minimum value of q is 1.466, at $r/a = 0.428$. Inside of this radial location $\hat{s} < 0$. With this setup, we can distinguish between the effects of $\hat{s}_{\text{min}}$ and q_{min} on ETG turbulence and e-ITB formation. The flux tube simulations in this chapter suggest that a
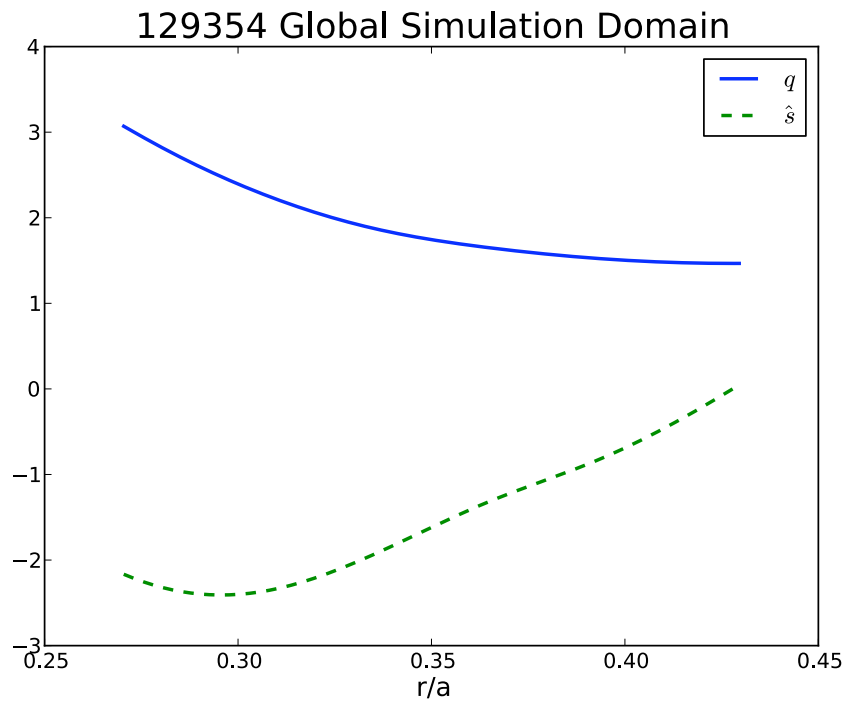
Figure 4.34: q and $\hat{s}$ profiles, 129354 global simulation domain

barrier would exist closer to $\hat{s}_{min}$, where the shear is most negative, than q_{min}, where the shear is zero.
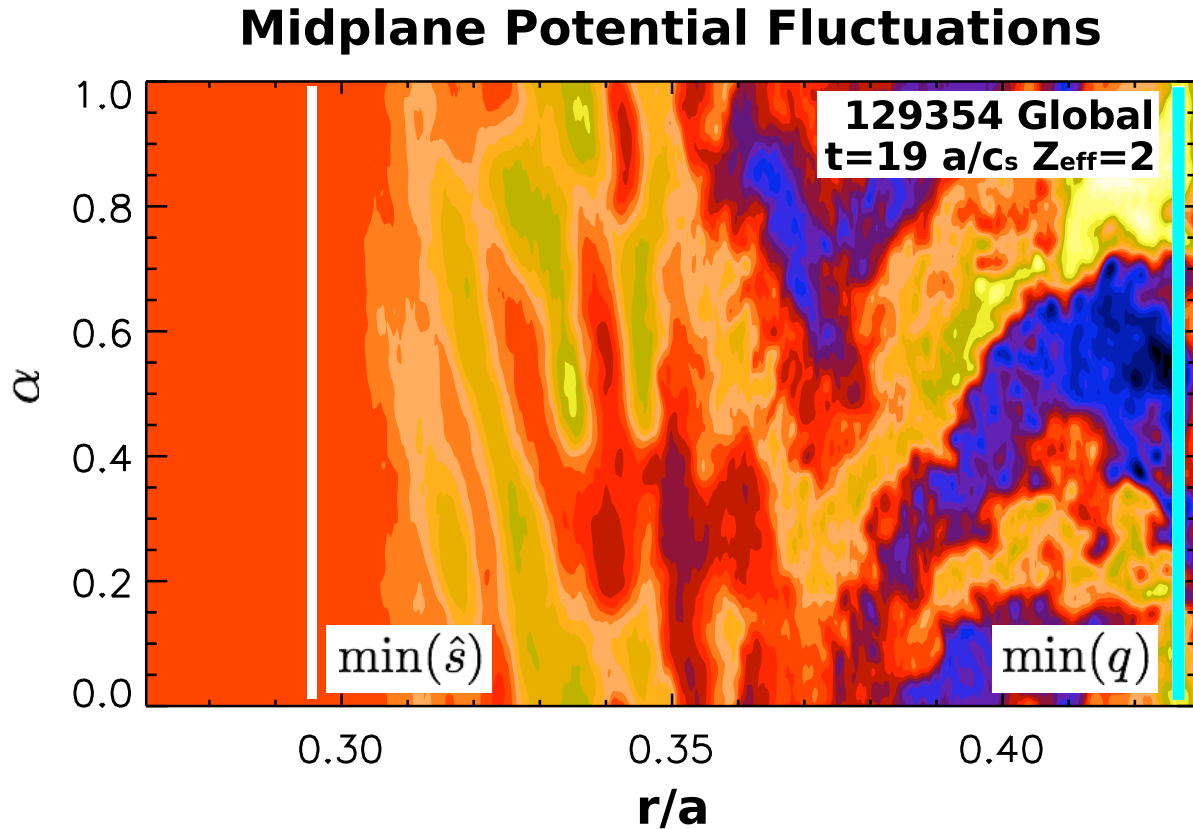
Figure 4.35: Midplane fluctuation snapshot, 129354 global simulation. The white and cyan lines mark the locations of minimum $\hat{s}$ (-2.408) and minimum q (1.466), respectively. The radial width is roughly $860\rho_e$.

Beginning with the simulation of $Z_{eff} = 2$, the importance of $\hat{s}_{min}$ becomes clear. Figure 4.35 shows a snapshot of midplane potential fluctuations, along with the locations of minimum shear and minimum safety factor. Two distinct regions emerge. Far outside of $\hat{s}_{min}$, large-scale steamer-like eddies exist. Their magnitude is greatest near q_{min}. Yet as they move radially inward, they begin to rotate, aligning themselves not radially but in the binormal direction instead. Put another way their radial wavenumber k_r increases as the eddies approach $\hat{s}_{min}$, consistent with the flux tube simulations of reversed magnetic shear that show eddies rotating away from the midplane. The most striking feature, however, is not the streamers in the outer part of the domain, but rather

the lack of turbulence in the inner. No eddies exist inside of $\hat{s}_{min}$. A barrier appears to exist, which coincides with regions of strong negative shear, nearer to $\hat{s}_{min}$ than q_{min}.

The existence of an ETG barrier is clear in the poloidal cross section of electron density fluctuations of Fig. 4.36. Strong ETG streamers exist at large values of r/a. Moving radially inward, the eddies rotate away from the midplane. As they rotate, the eddies decrease in amplitude and eventually disappear entirely inside $r/a \sim 0.3$. A zoomed in view of the outboard side, Fig. 4.37, shows fine structures embedded in larger eddies, which rotate toward the vertical as they approach the barrier at $R = 1.24$ m. The barrier itself is made up of very fine low-amplitude structures, inside of which no fluctuations exist.

The inner region of the plasma is not only devoid of turbulence, but also of transport. Figure 4.38 shows the time-evolution of the radial electron heat flux profile, along with the location of $\hat{s}_{min}$. The heat flux increases first outside of $\hat{s}_{min}$ and spreads throughout the radial domain. A transient burst at $r/a = 0.35$ grows up at a rate similar to that of the flux tube simulations' off-midplane streamers, but dies at later times. In all, the flux never reaches significant levels inside $r/a \approx 0.31$ and by $t \approx 11(a/c_s)$ a steady-state appears, with large heat flux at large r and negligible at small r. In short, Fig. 4.38 shows an electron internal transport barrier due to the magnetic shearing of ETG eddies. Inside of the barrier, turbulent transport is negligible. Outside of this location, however, electron thermal transport can reach experimentally relevant levels of $> 0.1\, Q_{GBi}$. Strong reversed magnetic shear prevents ETG turbulent eddies from propagating radially inwards, forming a transport barrier. This e-ITB coincides with $\hat{s}_{min}$ (or, more precisely, very negative $\hat{s}$) and not q_{min}, where $\hat{s} = 0$.

Altering Z_{eff} does not negate the important role of $\hat{s}$. The radial heat flux profiles of the two simulations, shown in Fig. 4.39, follow similar patterns. Overall, lowering Z_{eff} increases the transport, which is to be expected, since it coincides with stronger ETG drive. For reference, electron heat fluxes as calculated by `TRANSP` increase as one moves radially from $\sim 0.16\, Q_{GBi}$ ($r/a = 0.35$) to $0.19\, Q_{GBi}$ ($r/a = 0.40$). The $Z_{eff} = 3.5$ case seems to under-predict experimental

Density Fluctuations
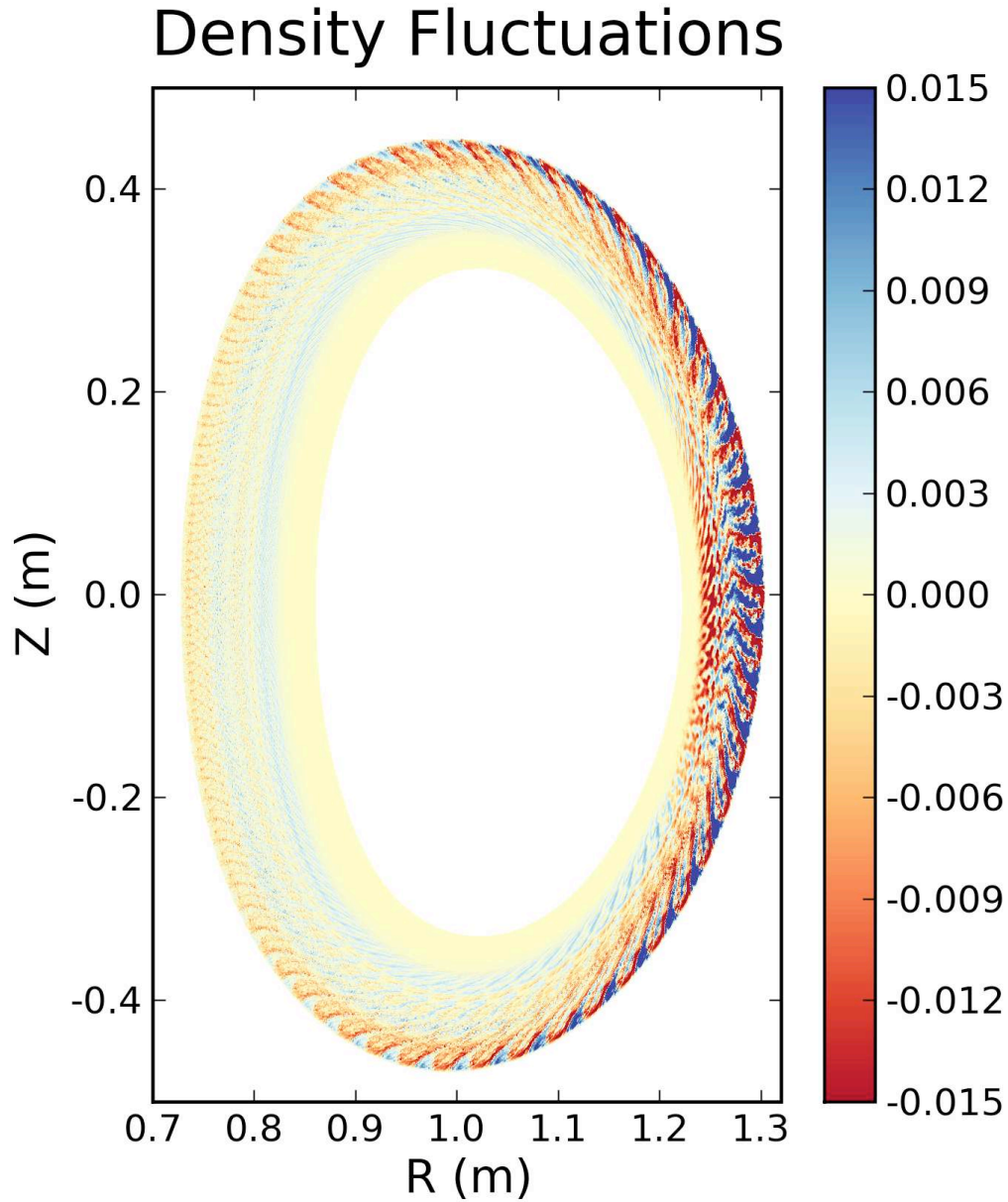
Figure 4.36: Cross-section of electron density fluctuations, 129354 global simulation, showing an electron internal transport barrier. $Z_{eff} = 2.0$ $t = 19.18$ (a/c_s). Although peak amplitudes of $\pm 5\%$ exist, for clarity only $\tilde{n}_e \le \pm 1.5\%$ are shown.
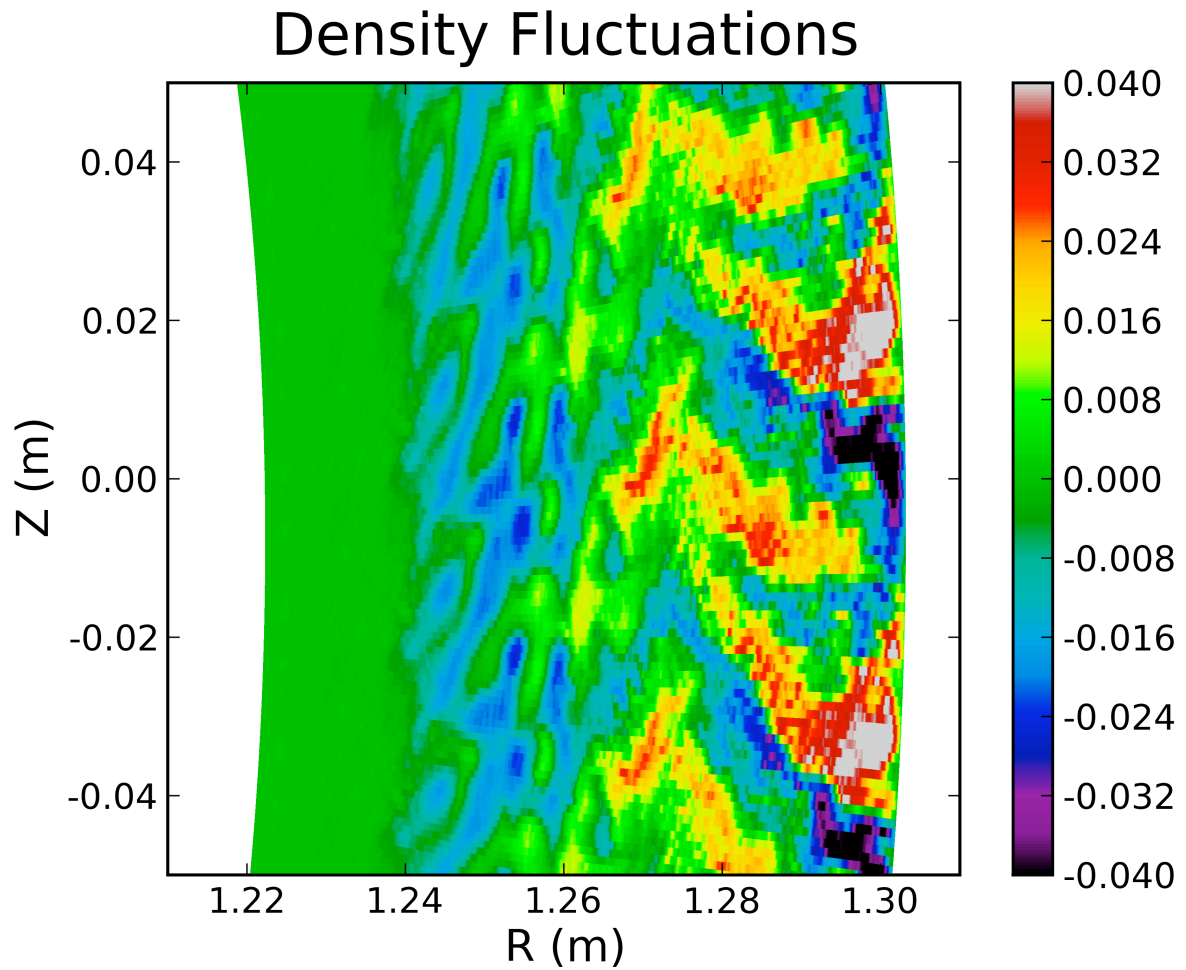
Figure 4.37: Zoomed-in snapshot of electron density fluctuations, 129354 global simulation. $Z_{eff} = 2.0\ t = 19.18\ (a/c_s)$, showing $\tilde{n}_e \leq \pm 4\%$.
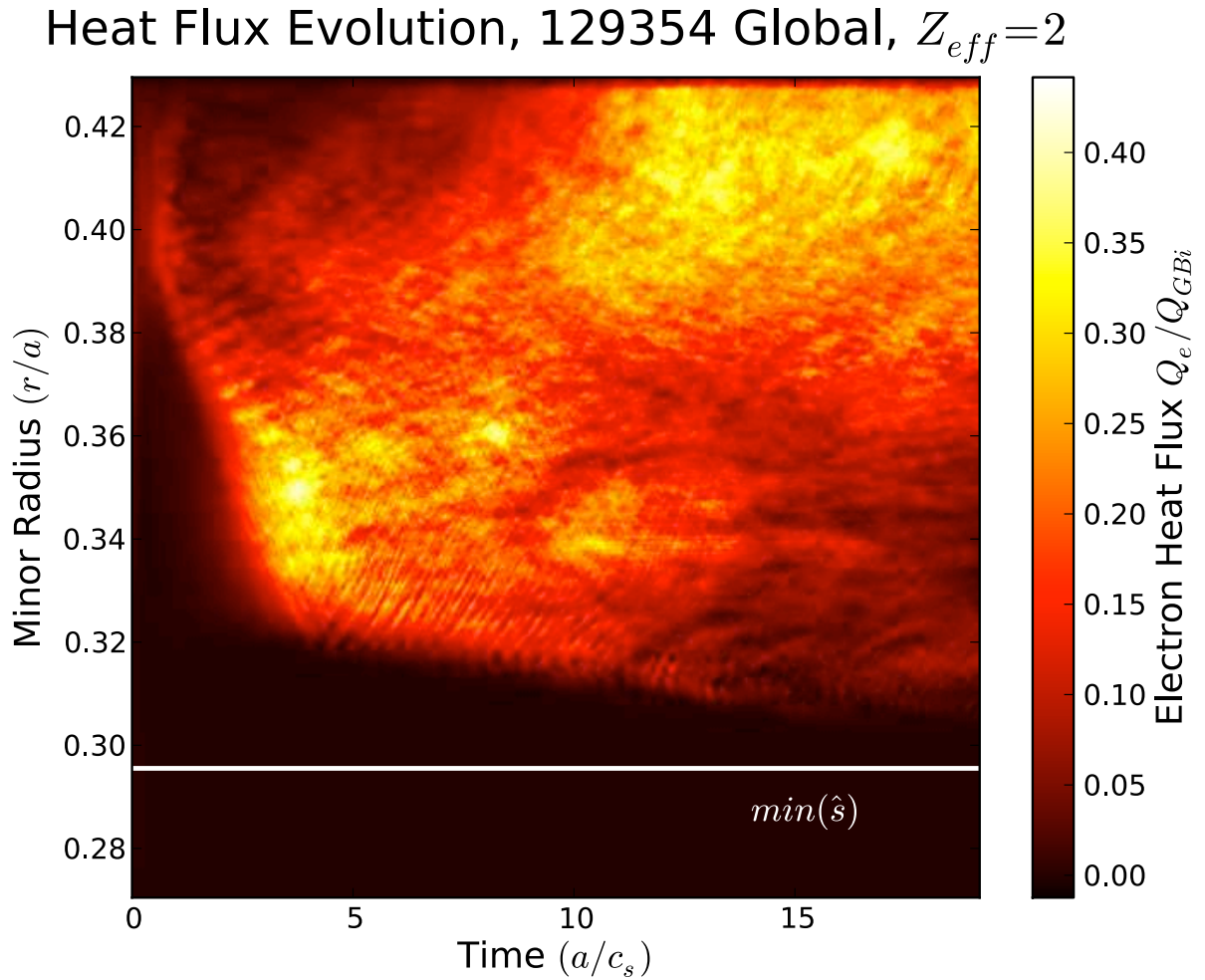
Figure 4.38: Time evolution of radial heat flux profile, 129354 global simulation, $Z_{eff} = 2$. The white line marks the location of minimum $\hat{s}$. Heat fluxes as calculated by TRANSP increase as one moves radially from $\sim 0.16\ Q_{GBi},\ (r/a = 0.35)$ to $0.19\ Q_{GBi}\ (r/a = 0.40)$.
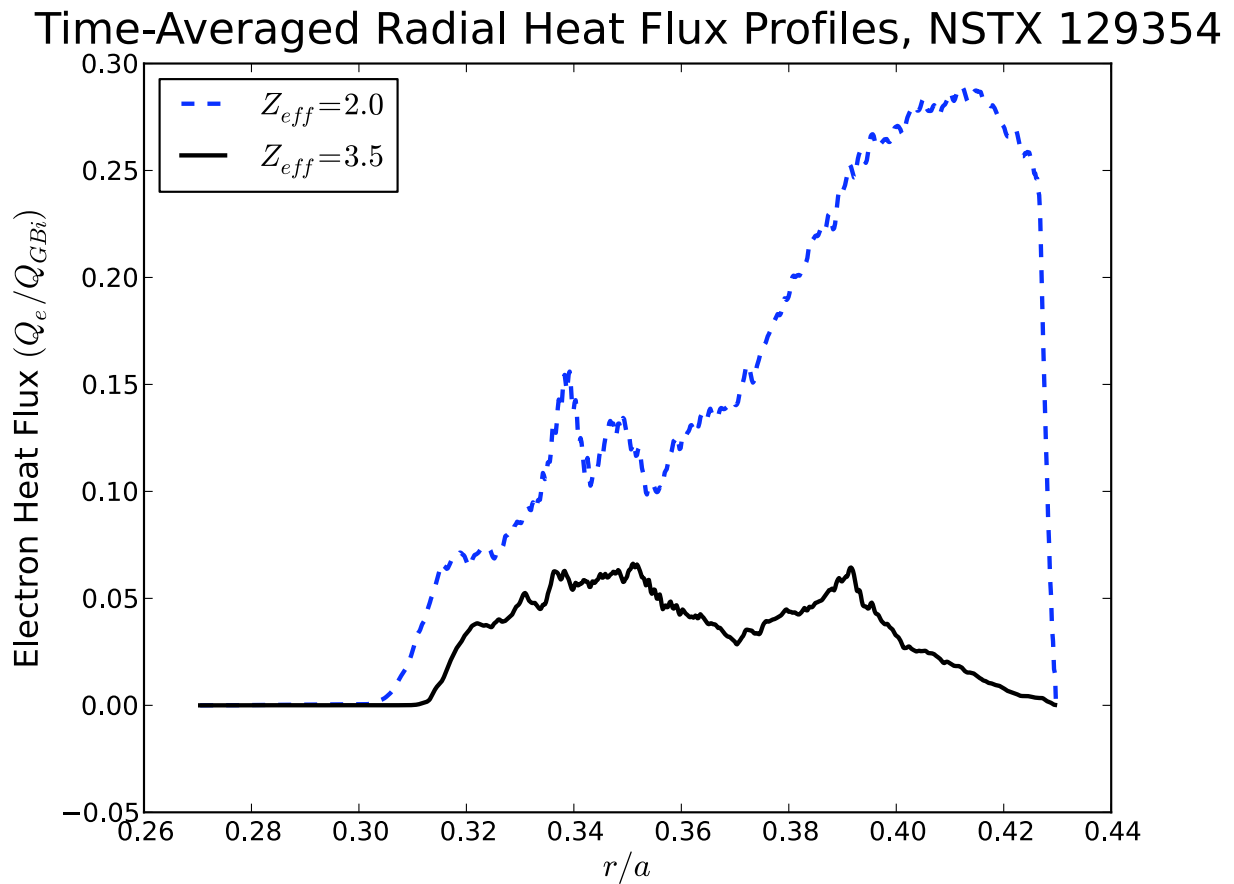
Figure 4.39: Time-averaged heat flux profiles for global simulations with different values of Z_{eff}. For reference, experimentally inferred levels range from $0.16\ Q_{GBi}$, $(r/a\ =\ 0.35)$ to $0.19\ Q_{GBi}$ $(r/a = 0.40)$.

levels of heat flux. While such a high value of Z_{eff} cannot be ruled out *a priori*, the most likely experimental value is closer to 2 [116]. At this level, ETG can drive enough flux to account for experimentally measured levels, although a more complete comparison to experimental fluxes appears in Section 4.3. The key point is that both profiles show a barrier that separates regions of negligible and significant flux. Like the experimental observations on NSTX, $\hat{s}$ causes the e-ITB, not τ.

In essence, reversed magnetic shear triggers e-ITBs in NSTX by suppressing nonlinear ETG turbulence. The importance of $\hat{s}$ alluded to in the local parameter scans is confirmed by global ETG simulations. In regions of strong reversed shear, turbulent eddies are twisted away and cannot penetrate into the inner regions of the plasma. These barriers exist near the location of minimum $\hat{s}$, where $\hat{s}$ is most negative. In areas of more modest shear, closer to $q_{\min}$, ETG turbulence, characterized by radially extended streamers, is strong enough to drive experimentally relevant levels of heat flux. In short, outside of an e-ITB, the electron temperature gradient is stiff. But thanks to reversed magnetic shear, inside the barrier, the plasma can break the bonds of stiff turbulent transport.

4.3 The Limitations of Comparing Fluxes

The strength of ETG-driven turbulence is highly sensitive to input parameters. The critical threshold phenomenon makes comparisons to experiments particularly difficult. Indeed this applies to other drift waves as well. Thus far, we've seen certain cases where ETG can drive fluxes that are not inconsistent with inferred experimental levels. But, the absolute value of the turbulent flux comes with an uncertainty. Here, we try to aggregate the results from these NSTX ETG scans and attempt to quantify the degree of uncertainty that stems from attempting to compare experimentally inferred and numerically simulated levels of ETG-driven flux.

First of all, the input parameters to an ETG simulation, as measured or inferred from experimental analysis, come with a finite level of uncertainty. For instance, electron temperatures as calculated from Thomson scattering measurements are known to within roughly 5 percent [117]. But Z_{eff} may vary between 1.6 (as measured by CHERS for 129354) and 3.5 (from VB for the same discharge) during these RF-heated shots [116]. Table 4.4 lists some experimental uncertain-

Table 4.4: Uncertainties on ETG-relevant experimental parameters for typical RF L-mode conditions [38, 116, 117].

Quantity y	$y \pm \delta y$	$|\delta y/y|$	$(\delta y/y)^2$
T_e	2 ± 0.1 keV	0.05	0.0025
T_i	550 ± 40 eV	0.07	0.0052
R/L_{T_e} : e-ITB	25 ± 5	0.20	0.04
R/L_{T_e} : non e-ITB	8 ± 1.5	0.19	0.035
$\hat{s}$	-1 ± 0.1	0.10	0.01
q	2 ± 0.1	0.05	0.0025
Z_{eff}	2.5 ± 0.9	0.36	0.1296

ties in parameters that may affect ETG-driven transport in the discharges examined in this chapter. The largest uncertainties come from R/L_{T_e}, which for both e-ITB and non-e-ITB cases is roughly 20 percent, and from Z_{eff}, which is about 35 percent. We can roughly estimate an uncertainty from a flux calculation depending only upon these parameters by summing up the square uncertainties in the last column of Table 4.4:

$$\left(\frac{\delta Q}{Q}\right)_{\text{exp.}} \approx \sqrt{\sum_i \left(\frac{\delta y_i}{y_i}\right)^2} \tag{4.2}$$

$$= 0.42 \tag{4.3}$$

This serves as a general estimate of the uncertainty on the experimentally inferred flux, because in the strictest sense Eq. 4.3 is only exact if the flux is only a product and/or quotient of those measurements and if those measurements are independent and random, which may not be the case

at all. A more complete estimate of the uncertainties in a `TRANSP` calculation involves many other parameters, such as R-F deposition strengths and electron-ion coupling terms. These fuller calculations estimate that experimentally inferred heat flux is only known to within 40 to 50 percent. As an example, NSTX shot 124948, has `TRANSP` calculations of χ_e at $r/a = 0.5$ of 3 ± 1.5 m^2/s [118].

The larger question when comparing fluxes between simulations and experiments is the sensitivity of the simulation's results to variations in input parameters. For any function f that depends upon independent parameters y_i each known to within a standard deviation δy_i, the uncertainty in f is [119]:

$$\delta f = \sqrt{\sum_i \left(\frac{\partial f}{\partial y_i}\delta y_i\right)^2}. \tag{4.4}$$

Eq. 4.4 allows for an estimate of the sensitivity of the calculated electron heat flux to input parameters y_i, even though their functional dependence is not known *a priori*, by approximating

$$\frac{\partial f}{\partial y_i} \approx \frac{\Delta f}{\Delta y_i}, \tag{4.5}$$

where Δf is an observed change in the output function given a change in the input parameter Δy_i. Table 4.5 aggregates the sensitivies of calculated electron heat fluxes in ion gyroBohm units

Table 4.5: Aggregated sensitivies of calculated fluxes to some input parameters from the e-ITB simulations, gathered from Figures 4.25 and 4.26. The experimental uncertainties δy come from Table 4.4.

Parameter	y	Q_e (Q_{GBi} units)	δy	Δy	ΔQ_e	$\left(\frac{\Delta Q_e}{\Delta y}\delta y\right)^2$
R/L_{T_e}	17.5	1.2	5	3	0.7	1.32
$\hat{s}$	-1.0	1.0	0.1	0.8	0.6	5.6×10^{-3}
τ	7.5	1.2	2.8	5.7	1.17	0.33

from the e-ITB simulations of Figures 4.25 and 4.26. The last column serves as an estimate of the individual terms in Eq. 4.4. Clearly the largest source of uncertainty comes from the input gradient, as defined by R/L_{T_e}. This phenomenon is due to the very stiff nature of the transport, combined with the large uncertainty in the measured gradient. The next largest source of uncertainty is from τ. We can estimate $\delta\tau$ from a true square propagation of errors (since $\tau = Z_{eff}T_e/T_i$, $(\delta\tau/\tau)^2 = (\delta Z_{eff}/Z_{eff})^2 + (\delta T_e/T_e)^2 + (\delta T_i/T_i)^2$). But interestingly enough, even though Z_{eff} (and consequently τ) have large relative uncertainties, their effect on the flux's uncertainty is much less than that from R/L_{T_e}. Being much larger than the errors from the other terms, the uncertainty in input gradients dominates the total uncertainty in the calculated heat flux. In other words,

$$\delta Q_e \quad \approx \quad \left|\frac{\Delta Q_e}{\Delta\left(R/L_{T_e}\right)}\right| \delta\left(R/L_{T_e}\right), \tag{4.6}$$

$$= \quad 0.23\,\delta\left(R/L_{T_e}\right). \tag{4.7}$$

To quantify this further, for the e-ITB case, $\delta\left(R/L_{T_e}\right) = 5$, so the uncertainty on Q_e is roughly $0.23 \times 5.0 = 1.15\,Q_{GBi}$. Since Q_e itself is calculated as $1.2\,Q_{GBi}$,

$$\left(\frac{\delta Q_e}{Q_e}\right)_{\text{calc. e-ITB}} = 0.96. \tag{4.8}$$

For the e-ITB calculations, the uncertainty in the calculated heat flux is of order unity. For the non-e-ITB case with a lower gradient (and hence, lower uncertainty on the gradient), the uncertainty in Q_e is a little less, but still large. Specifically, Eq. 4.7 estimates an uncertainty of $0.35\,Q_{GBi} = 21\,Q_{GBe}$. Comparing with the results of Fig. 4.13, which calculates $Q_e \approx 41\,Q_{GBe}$,

$$\left(\frac{\delta Q_e}{Q_e}\right)_{\text{calc. non-eITB}} = 0.51. \tag{4.9}$$

The uncertainties in input gradients dominate the uncertainties in GYRO-calculated fluxes. Due to the highly stiff nature of this transport, Q_e as calculated via simulation is highly sensitive to changes in local gradient, resulting in a standard error of roughly 50 to 100 percent.

Admittedly this uncertainty analysis serves as merely an estimate of the sensitivities of the fluxes to input parameters, and other parameters could also be important, such as q. However, even though the uncertainties on other quantities may be large, their effect on the magnitude of calculated heat flux is much less than that of the gradient. The stiff nature of turbulent transport implies that experimental uncertainties of 20 percent can translate into order unity uncertainties in calculated fluxes. Even the experimentally inferred fluxes themselves are only known to 45 percent or so. This illustrates the limitations of comparing turbulent fluxes between simulations and experiments. In any case, Table 4.6 summarizes the experimentally inferred and numerically

Table 4.6: Summary of heat fluxes from global GYRO simulations and TRANSP.

Flux (MW/m^2)	124948 ($r/a = 0.3$)	129354 ($r/a = 0.4$)	129354 ($r/a = 0.35$)
from GYRO	0.030 ± 0.015	0.027 ± 0.014	0.012 ± 0.012
from TRANSP	0.055 ± 0.023	0.017 ± 0.007	0.015 ± 0.006

calculated heat fluxes for the global ETG simulations of the two discharges in this chapter, from Figs. 4.12 and 4.39, using Eqs. 4.3, 4.8 and 4.9 to estimate the uncertainties. From this point of view, the calculated fluxes from the experiments and simulations are in qualitative agreement. However, given the large uncertainties, this conclusion must be taken with a grain of salt. Just because the ranges of values overlap does not necessarily imply agreement.

As an example to quantify the degree to which the GYRO simulation's calculation of Q_e for shot 124948 agrees with the experimentally inferred value, we can calculate the probability that GYRO's ETG-driven heat flux lies within one standard deviation of the TRANSP value, namely that $Q_e^{\text{TRANSP}} - \delta Q_e^{\text{TRANSP}} < Q_e^{\text{GYRO}} < Q_e^{\text{TRANSP}} + \delta Q_e^{\text{TRANSP}}$. The probability of Q_e lying on the
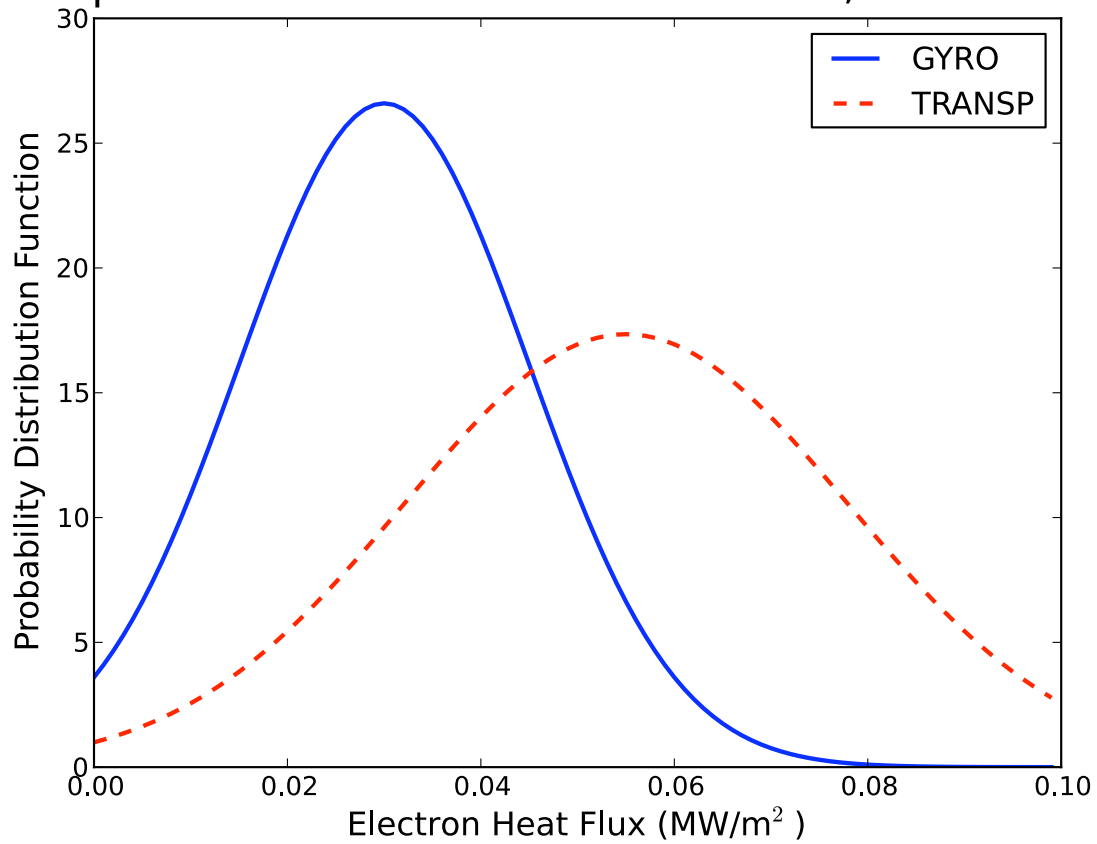
Figure 4.40: Probability distribution functions of GYRO and TRANSP calculations of electron heat fluxes, assuming normal distributions with means and deviations from Table 4.6.

interval is

$$P(Q_e{}^{\text{TRANSP}} - \delta Q_e{}^{\text{TRANSP}} \quad < \quad Q_e{}^{\text{GYRO}} < Q_e{}^{\text{TRANSP}} + \delta Q_e{}^{\text{TRANSP}})$$

$$= \quad P(0.032 < Q_e^{\text{GYRO}} < 0.078)$$

$$= \quad P(Q_e^{\text{GYRO}} < 0.078) - P(Q_e^{\text{GYRO}} < 0.032). \qquad (4.10)$$

Under the assumption that Q_e is a normally distributed random variable with a mean of 0.03 and a standard deviation of 0.015 (see Fig. 4.40), these probabilities can be calculated with the error function [119]:

$$P(x) = P(Q_e^{\text{GYRO}} < Q) = \frac{1}{2} \left[1 + \text{erf} \left(\frac{Q - 0.03}{0.015\sqrt{2}} \right) \right]. \qquad (4.11)$$

So it follows from Eqs. 4.10 and 4.11 that the probability that the simulated heat flux lies within the experimental range of uncertainties is

$$P(0.032 < Q_e^{\text{GYRO}} < 0.078) \quad = \quad P(0.078) - P(0.032)$$

$$= \quad 0.999 - 0.553$$

$$= \quad 0.446. \qquad (4.12)$$

In essence, there's a 45 percent chance that the GYRO ETG calculation lies within one standard deviation of the experimentally inferred value. One could also quantify this in terms of the cross-correlation of the two measurements; in this case, the convolution of the GYRO and TRANSP Q_e distributions is another normal distribution with mean 0.085 and standard deviation of 0.027. In either case, the large uncertainties in both the GYRO and TRANSP calculations of Q_e highlight the difficulties inherent in comparing fluxes.

In summation, this section's uncertainty analysis attempts to answer the degree to which experimentally inferred and numerically simulated electron heat fluxes agree. In both the standard

and reversed shear simulations, the ETG-driven fluxes are near the experimental ones. However, each of these calculations comes with a very large uncertainty: the experimental value of Q_e is only known to within 40 percent or so, while the GYRO-calculated fluxes' uncertainties lie in the 50-100 percent range. The distribution of likely values is broad, but there is some overlap in the distributions. The single largest driver of uncertainty is from temperature gradients, due to the highly stiff nature of the transport. A 20 percent uncertainty in input gradient can translate to a 96 percent uncertainty in calculated fluxes. This large variation makes the comparison of fluxes from gradients nuanced.

What can this say about ETG's role in NSTX? Put one way, the odds are roughly 45 percent that the GYRO-calculated ETG-driven flux for NSTX shot 124948 lies within one standard deviation of the inferred experimental value. Put another way, there's a 55 percent chance that it does not. The best one can say is that the ETG-driven heat fluxes can reach experimentally relevant levels.

4.4   Summary

This chapter has shown that electron temperature gradient driven turbulence can exist in NSTX plasmas. When present, the ETG mode can drive both experimentally relevant levels of heat flux and density fluctuations that can be measured by the high-k scattering system. However, interpreting high-k measurements universally as ETG-driven fluctuations is difficult, because the diagnostic views the tail-end of the ETG spectrum. Furthermore, the ETG mode may not be the only instability in these plasmas: microtearing and TEM modes could also contribute to the high-k signal. Isolating the contributions from individual instabilities is challenging. Additionally, the large uncertainties both in fluxes simulated with GYRO and inferred from TRANSP make the quantification of the amount of ETG-driven thermal transport difficult. In any case, ETG turbulence can potentially limit the performance of NSTX plasmas.

Reversing the magnetic shear is an effective method at suppressing ETG-driven transport. Plasmas with large negative values of $\hat{s}$ can support gradients that are linearly unstable to the ETG mode, but drive negligible amounts of turbulent flux. The important role of $\hat{s}$ alluded to by local simulations is reinforced by global simulations of an NSTX electron internal transport barrier. Barriers form where $\hat{s}$ is strongly negative, and not at minimum q, where $\hat{s} = 0$, regardless of τ. Outside of the e-ITB, the electron heat flux again becomes experimentally relevant.

Nonlinear gyrokinetic simulations of electron turbulence show that the ETG mode potentially limits the performance of some NSTX discharges. It's possible to suppress this turbulence with magnetic shear. Doing so could allow the plasma to sustain very steep gradients, well above the linear threshold for instability. However, firmly establishing the effect of turbulent flux on steady-state plasma profiles is a difficult problem. Such a feat involves not only a knowledge of plasma turbulence, but also of plasma transport.

Chapter 5

Integrating Turbulence Models to Predict Plasma Performance

Plasma turbulence is important because it can drive plasma transport. The fluxes created by electron turbulence in NSTX lead to heat and particle losses. These losses alter the plasma's profile, which in turn affects the strength of the turbulence. The resulting system is thus highly nonlinear, with plasma profiles driving turbulence and turbulence altering profiles.

A major challenge is that these two processes work on vastly different time and space scales. Turbulent dynamics are governed by particle motions, as characterized by gyroradii and guiding center drifts. Transport, however, occurs across the entire plasma over (hopefully) long enough times to get sufficient fusion power output. Because of the disparate temporal and spatial scales, simultaneously modeling these two processes, turbulence and transport, is very difficult. However, advanced numerical techniques can make the problem more tractable.

In this chapter, we examine the steady-state transport problem, whereby fluxes out of the plasma exactly balance sources into the plasma. Finding self-consistent solutions to these equations is the purpose of TGYRO [120], a transport equilibrium solver designed originally to interface with GYRO, and later extended to use TGLF. After an introduction to the problem, we devise a

novel simple example to illustrate some of the challenges this system possesses. From there, we develop some new numerical techniques for TGYRO that can help overcome some of these obstacles and use a few test cases to gauge their effectiveness. Finally, we apply these methods to predict some self-consistent plasma profiles for one of the ETG NSTX discharges examined in the previous chapter.

5.1   The Steady-State Transport Problem

The flux created by electron turbulence, like all plasma turbulence, can transport plasma radially outward. Sources of heat and/or particles can eventually balance this loss. These sources can be external, such as RF-heating or neutral beam injection, or internal, such as heat from fusion alpha particles. Indeed this could be the case for a reactor during steady-state operation: the heat leaving the plasma would be replaced by that generated from fusion reactions. The balance of plasma sources and sinks is known as the transport problem.

The turbulence problem asks whether or not fluxes calculated from a given profile match measured fluxes. Traditionally, as in the previous chapter, one compares the calculated heat flux from a turbulence (and/or neoclassical) code with experimentally measured heat fluxes, as calculated from a power balance of sources. This problem takes as input plasma profiles, such as temperature and density, and outputs fluxes. Yet this makes for not necessarily a straightforward comparison. Since turbulent transport in particular is stiff, a slight uncertainty in driving gradient can lead to large differences in heat fluxes. Furthermore, the heat fluxes against which one is comparing can be only known in some cases to within a factor of two or so. Making a judgement call as to whether or not plasma turbulence can account for measured levels transport becomes at this point nuanced.

The transport problem, on the other hand, asks the reverse question. Instead of taking a temperature profile and calculating a heat flux, a transport solver takes a heat flux and calculates a temperature profile. This is done by iterating on the plasma profile until calculated heat fluxes

match experimental sources. The resulting calculated temperature and density profiles can then be compared against measured profiles. This is attractive for a few reasons. Firstly, typical uncertainties on temperature and density profiles are much smaller than uncertainties on sources. While the sources (such as the RF power absorbed by the plasma) may only be known to within a factor of two, electron temperature can be measured to within five percent.

The second reason transport calculations are attractive is that turbulent transport is very stiff, particularly near marginal stability, so a slight uncertainty in driving gradient can lead to a large uncertainty in calculated flux. The reverse is also true: if changing the gradient by ten percent alters the heat flux by a factor of two, changing the heat flux by a factor of two only alters the gradient by ten percent. In this sense, since the experimental and numerical uncertainties in plasma profiles are much smaller than the uncertainties in experimental and numerical fluxes, it makes more sense to compare profiles than fluxes. By taking as input fluxes and calculating self-consistent temperature and density profiles, a transport solver makes such a comparison possible.

The final reason that the steady-state transport problem is an important one to solve is that a reactor's performance will ultimately depend on how hot it can get. We care less about values of heat diffusivity than core ion temperatures when trying to maximize fusion gain. ITER's success depends largely on its maximum attainable temperature. Instantaneous values of heat flux only become meaningful when placed in the context of plasma confinement, which is governed by the transport equations. In a reactor, the power generated by alpha particles will be transported throughout the plasma. These dynamics depend on the transport equations, so a meaningful transport calculation becomes extremely important in the broader context of fusion.

Despite its importance and attractiveness, this steady-state problem is not easy to solve. Some of the characteristics of turbulence flux, such as nonlinear stiff transport, make the steady-state transport problem challenging to solve, even with modern computational power. Simultaneously modeling multiple temporal and spatial scales in a meaningful and tractable way is no small feat.

5.1.1 Equations

Slowly-evolving radial plasma transport equations, under proper spatial and temporal separation assumptions in a tokamak, can be written for a species a as [51, 120]:

$$\frac{\partial \langle n_{0a} \rangle}{\partial t} + \frac{1}{V'} \frac{\partial}{\partial r} (V'\Gamma_{2a}) = \left\langle \int d^3 v S_{2a} \right\rangle, \tag{5.1}$$

$$\frac{\partial \langle W_a \rangle}{\partial t} + \frac{1}{V'} \frac{\partial}{\partial r} (V'Q_{2a}) = \left\langle \int d^3 v \frac{m_a v^2}{2} S_{2a} \right\rangle. \tag{5.2}$$

Here n_{0a} is the equilibrium number density, Γ_{2a} and Q_{2a} are the second-order particle and heat fluxes, respectively. $W_{0a} = (3/2)n_{0a}T_{0a}$, the equilibrium energy density, is defined in terms of the equilibrium temperature T_{0a}, while V' is the radial derivative of the flux surface volume $V(r)$. S_{2a} includes the sources of plasma particles, from fueling or beams, for instance. Like Ref. [120] we've explicitly ignored turbulent energy exchange [121], which is formally of the same order in $\rho_\star$ but sub-dominant in practice.

In steady-state, $\partial/\partial t = 0$. The transport equations have the same form, which for the heat flux is:

$$\frac{1}{V'} \frac{\partial}{\partial r} (V'Q_{2a}) = s_{2a}(r). \tag{5.3}$$

In this case, the integrated sources, s_{2a}, have units of power/volume and can include contributions from auxiliary heating, thermonuclear reactions, radiation losses and classical temperature equilibration, which is finite for $T_{0e} \neq T_{0i}$.

Equation 5.3 can be written in a volume-integrated form, which is (omitting the ordering subscripts):

$$Q_a(r) = \frac{1}{V'(r)} \int_0^r dx V'(x) s_a(x) \doteq Q_a^T(r). \tag{5.4}$$

Q_a^T is called the *target flux* and contains the known integrated sources that must be matched by the calculated fluxes. The flux, Q_a, contains both neoclassical and turbulent components: $Q_a = Q_a^{neo} + Q_a^{turb}$.

Since neoclassical and turbulent codes require profile gradients as inputs, the transport equations can be defined in terms of the logarithmic gradient:

$$z_a \doteq -\frac{1}{T_a}\frac{\partial T_a}{\partial r}. \tag{5.5}$$

Then, by specifying a *matching radius* $r_\star$ at which to keep the temperature fixed (say at the edge of the plasma), with $T_{a\star} \doteq T_a(r_\star)$, the gradients uniquely determine the plasma profiles, T_a:

$$T_a(r) = T_{a\star} \exp\left(\int_r^{r_\star} dx z_a(x)\right). \tag{5.6}$$

A trapezoidal integration rule can approximate the temperature profile on a discrete grid $\{r_j\}$:

$$T_a(r_{j-1}) = T_a(r_j) \exp\left(\left[\frac{z_a(r_j) + z_a(r_{j-1})}{2}\right][r_j - r_{j-1}]\right). \tag{5.7}$$

Putting the transport fluxes, target fluxes and gradients on the discrete grid completes the problem: $Q_{a,j} = Q_a(r_j)$, $Q_{a,j}^T = Q_a^T(r_j)$, and $z_{a,j} = z_a(r_j)$. The steady-state transport problem can be written in vector form:

$$\mathbf{Q}_a(\mathbf{z}) = \mathbf{Q}_a^T. \tag{5.8}$$

If the equations are solved using gyroBohm normalizations, or if the sources depend on the temperature and density profiles, the target fluxes can also depend upon the gradients; that is let $\hat{Q} = Q/Q_{GB}$ with $Q_{GB}(r) = n_e T_e c_s (\rho_s/a)^2$. The gyroradius $\rho_s = c_s m_D c/(eB)$ depends on the deuterium mass, m_D, the magnetic field B, the speed of light c, the electron charge e and the ion sound speed c_s, which also depends upon the local temperature: $c_s = \sqrt{T_e/m_D}$. Since in this

formulation (which is the one used by TGYRO) the temperature and densities are defined by local gradients, both the transport fluxes and target fluxes depend on $\mathbf{z}$. The transport equations then reduce to:

$$\hat{\mathbf{Q}}_a\left(\mathbf{z}\right) = \hat{\mathbf{Q}}_a^T\left(\mathbf{z}\right). \tag{5.9}$$

$\hat{\mathbf{Q}}$ is a vector containing heat fluxes at a number of discrete radial points. $\hat{\mathbf{Q}}_a^T$ contains corresponding sources, as inferred usually by an experimental transport analysis. Solving the steady-state transport problem amounts to balancing the sources, $\hat{\mathbf{Q}}_a^T$, with the transported fluxes, $\hat{\mathbf{Q}}_a$, as in Eq. 5.9. While Eq. 5.9 is explicitly for energy transport, equations of the same form exist for particle and momentum transport.

5.1.2 An illustrative example transport problem

A simple problem using equations like Eq. 5.9 can yield valuable insight into how best to approach transport calculations.

Consider a problem involving two radial locations with one a fixed matching radius, respectively r_1 and $r_2 = r_\star$, and only consider electron heat flux ($Q_a = Q_e = Q$). Eq. 5.8 becomes in this case:

$$\begin{bmatrix} Q_1 \\ Q_2 \end{bmatrix} = \begin{bmatrix} Q_1^T \\ Q_2^T \end{bmatrix}. \tag{5.10}$$

For Q, consider a model of stiff heat transport. Namely let

$$Q_j = C_j T_j^{5/2} \hat{z}_j \left\{ \hat{z}_j - \hat{z}_j^{crit} \right\} H\left[\hat{z}_j - \hat{z}_j^{crit} \right]. \tag{5.11}$$

In this model, the heat flux depends upon the local gradient $\hat{z}_j \doteq z_j a = \frac{a}{T_j}\frac{\partial T_j}{\partial r}$, some critical gradient $\hat{z}_j^{crit}$, the local electron temperature $T_j \doteq T_{e,j}$, some constant factor C_j and the heaviside function, $H[x]$, which is one for positive values of x and zero otherwise. While crude, this model

says that above a critical local gradient, turbulence turns on a heat flux which scales as the five-halves power of the local temperature and quadratically with the driving gradient. In gyroBohm units, we can divide both sides of Eq. 5.11 by $Q_{GB,j} = n_{e,j} T_j c_{s,j} (\rho_{s,j}/a)^2$:

$$
\begin{aligned}
\frac{Q_j}{Q_{GB,j}} &= \frac{C_j T_j^{5/2}}{Q_{GB,j}} \hat{z}_j \left\{ \hat{z}_j - \hat{z}_j^{crit} \right\} H \left[\hat{z}_j - \hat{z}_j^{crit} \right], \\
\hat{Q}_j &= \frac{a^2 e^2 B_j^2}{m^{1/2} c^2 n_{e,j}} C_j \hat{z}_j \left\{ \hat{z}_j - \hat{z}_j^{crit} \right\} H \left[\hat{z}_j - \hat{z}_j^{crit} \right], \\
\hat{Q}_j &= A_j \hat{z}_j \left\{ \hat{z}_j - \hat{z}_j^{crit} \right\} H \left[\hat{z}_j - \hat{z}_j^{crit} \right].
\end{aligned}
\tag{5.12}
$$

$A_j = C_j T_j^{5/2}/Q_{GB,j}$ is a dimensionless factor that takes into account the local density and magnetic field, neither of which we are evolving in this model. The gyroBohm normalization in Eq. 5.12 eliminates the factor of $T_j^{5/2}$ and says that above a critical gradient, the gyroBohm heat flux increases quadratically with driving gradient. This model is in qualitative agreement with the turbulence calculations made in the previous chapter.

Assume a model for the critical gradient at each location as governed by local linear ETG physics:

$$
\hat{z}_j^{crit} = 1 + Z_{eff,j} \frac{T_{e,j}}{T_{i,j}} \doteq 1 + Z_{eff,j} \hat{T}_j,
\tag{5.13}
$$

which depends upon the local ion temperature, $T_{i,j}$ and Z_{eff}. For simplicity, let $Z_{eff,j} = 1$. The local heat flux in this model becomes:

$$
\hat{Q}_j = A_j \hat{z}_j \left\{ \hat{z}_j - \left(1 + \hat{T}_j \right) \right\} H \left[\hat{z}_j - \left(1 + \hat{T}_j \right) \right]
\tag{5.14}
$$

The local gyroBohm normalized target fluxes are:

$$
\begin{aligned}
\hat{Q}_j^T &= Q_j^T/Q_{GB,j} \tag{5.15} \\
&= \frac{A_j}{C_j} \frac{Q_j^T}{T_j^{5/2}}. \tag{5.16}
\end{aligned}
$$

It's clear from this formulation that the heat fluxes $\hat{Q}_j$ and the target fluxes $\hat{Q}_j^T$ depend upon the temperature and gradients: $\hat{Q}_j \left(\hat{z}_j, T_j \right)$ and $\hat{Q}_j^T \left(T_j \right)$. One point, r_2, is a matching boundary, so T_2 is a constant. However, Eq. 5.7 shows that T_1 depends on T_2 and the gradients at both r_1 and r_2:

$$T_1 = T_2 \exp \left(\left[\frac{\hat{z}_2 + \hat{z}_1}{2a} \right] [r_2 - r_1] \right). \tag{5.17}$$

Functionally, the entire system depends upon the boundary condition T_2, the constants $A_{1,2}$, $C_{1,2}$, $\Delta r = \left(r_2 - r_1 \right) / a$ and the gradients $\hat{z}_1$ and $\hat{z}_2$:

$$\hat{Q}_1 \left(\hat{z}_1, \hat{z}_2 \right) = A_1 \hat{z}_1 \left\{ \hat{z}_1 - \left(1 + \hat{T}_1 \left(\hat{z}_1, \hat{z}_2 \right) \right) \right\} H \left[\hat{z}_1 - \left(1 + \hat{T}_1 \left(\hat{z}_1, \hat{z}_2 \right) \right) \right], \tag{5.18}$$

$$\hat{Q}_2 \left(\hat{z}_2 \right) = A_2 \hat{z}_2 \left\{ \hat{z}_2 - \left(1 + \hat{T}_2 \right) \right\} H \left[\hat{z}_2 - \left(1 + \hat{T}_2 \right) \right], \tag{5.19}$$

$$\hat{Q}_1^T \left(\hat{z}_1, \hat{z}_2 \right) = A_1 Q_1^T / \left(C_1 T_1 \left(\hat{z}_1, \hat{z}_2 \right)^{5/2} \right), \tag{5.20}$$

$$\hat{Q}_2^T = A_2 Q_2^T / \left(C_2 T_2^{5/2} \right). \tag{5.21}$$

$\hat{Q}_2^T$ is a constant, while the other fluxes depend upon the two gradients. The solution comes down to balancing the local heat fluxes with the target fluxes.

$$\hat{Q}_1 - \hat{Q}_1^T = 0, \tag{5.22}$$

$$\hat{Q}_2 - \hat{Q}_2^T = 0. \tag{5.23}$$

Explicitly this condition becomes $F_1 = F_2 = 0$, where:

$$F_1 = \hat{z}_1 \left\{ \hat{z}_1 - \left(1 + \hat{T}_1 \right) \right\} H \left[\hat{z}_1 - \left(1 + \hat{T}_1 \right) \right] - Q_1^T / \left(C_1 T_1^{5/2} \right), \tag{5.24}$$

$$F_2 = \hat{z}_2 \left\{ \hat{z}_2 - \left(1 + \hat{T}_2 \right) \right\} H \left[\hat{z}_2 - \left(1 + \hat{T}_2 \right) \right] - Q_2^T / \left(C_2 T_2^{5/2} \right). \tag{5.25}$$

The constants $A_{1,2}$ cancel out. Other constants include T_2, $Q_{1,2}^T$ and $C_{1,2}$. The functional dependence is on $\hat{z}_1$ and $\hat{z}_2$, since $T_1(\hat{z}_1, \hat{z}_2)$, as in Eq. 5.17.

Alternatively, one could ignore the gyroBohm normalizations and use Eq. 5.11 directly, in which case the solution amounts to $G_1 = G_2 = 0$, with

$$G_1 = C_1 T_1^{5/2} \hat{z}_1 \left\{ \hat{z}_1 - \left(1 + \hat{T}_1\right) \right\} H \left[\hat{z}_1 - \left(1 + \hat{T}_1\right) \right] - Q_1^T, \tag{5.26}$$

$$G_2 = C_2 T_2^{5/2} \hat{z}_2 \left\{ \hat{z}_2 - \left(1 + \hat{T}_2\right) \right\} H \left[\hat{z}_2 - \left(1 + \hat{T}_2\right) \right] - Q_2^T. \tag{5.27}$$

An important figure of merit for the solution are the square residuals, $G_1^2 + G_2^2$ and $F_1^2 + F_2^2$. At the solution, all of these will be zero.

For illustrative purposes consider this problem with $C_{1,2} = T_2 = T_{i,1,2} = 1.0$, $r_1/a = 0.5$ and $r_2/a = 1.0$, so $\Delta r = 0.5$. Figure 5.1 shows F_1, F_2, G_1 and G_2 for the model transport problem for $\hat{z}_{1,2} : [0, 10]$. The location of the zero for each function is highlighted in magenta. Note firstly that F_1 and G_1 have the same zero, as do F_2 and G_2. However, the magnitudes of F_1 and G_1 in particular are quite different. G_1, that is the problem without the gyroBohm normalizations, varies much more than does F_1. Secondly, both F_2 and G_2 are independent of $\hat{z}_1$, as to be expected. The most interesting feature of this problem, however, is that neither F_1 nor G_1 is a monotonic solution of $\hat{z}_1$. Specifically, the zero contour turns over on itself, indicating that for $\hat{z}_2 = 0$, F_1 and G_1 increase until $z_1 \approx 6$ and then decrease again, becoming negative for $\hat{z}_1 \geq 8$. Both F_1 and G_1 are strong functions of $\hat{z}_2$. The flux at the inner radius, r_1 depends greatly on the gradient at r_2.

The non-monotonic behavior of F_1 has serious implications for the problem. A solution exists when $F_1 = 0$ and when $F_2 = 0$. This is represented by an intersection of the two magenta lines. Figure 5.2, the square residuals for $F_{1,2}$ and $G_{1,2}$ as a function of $\hat{z}_1$ and $\hat{z}_2$, clearly shows that no solution exists, since the magenta lines do not intersect. While for these parameters, there exists no solution, if the solution line for $F_2 = 0$ were to intersect the line for $F_1 = 0$, one could conceivably have two possible solutions, each mathematically satisfying the system of equations. This is shown
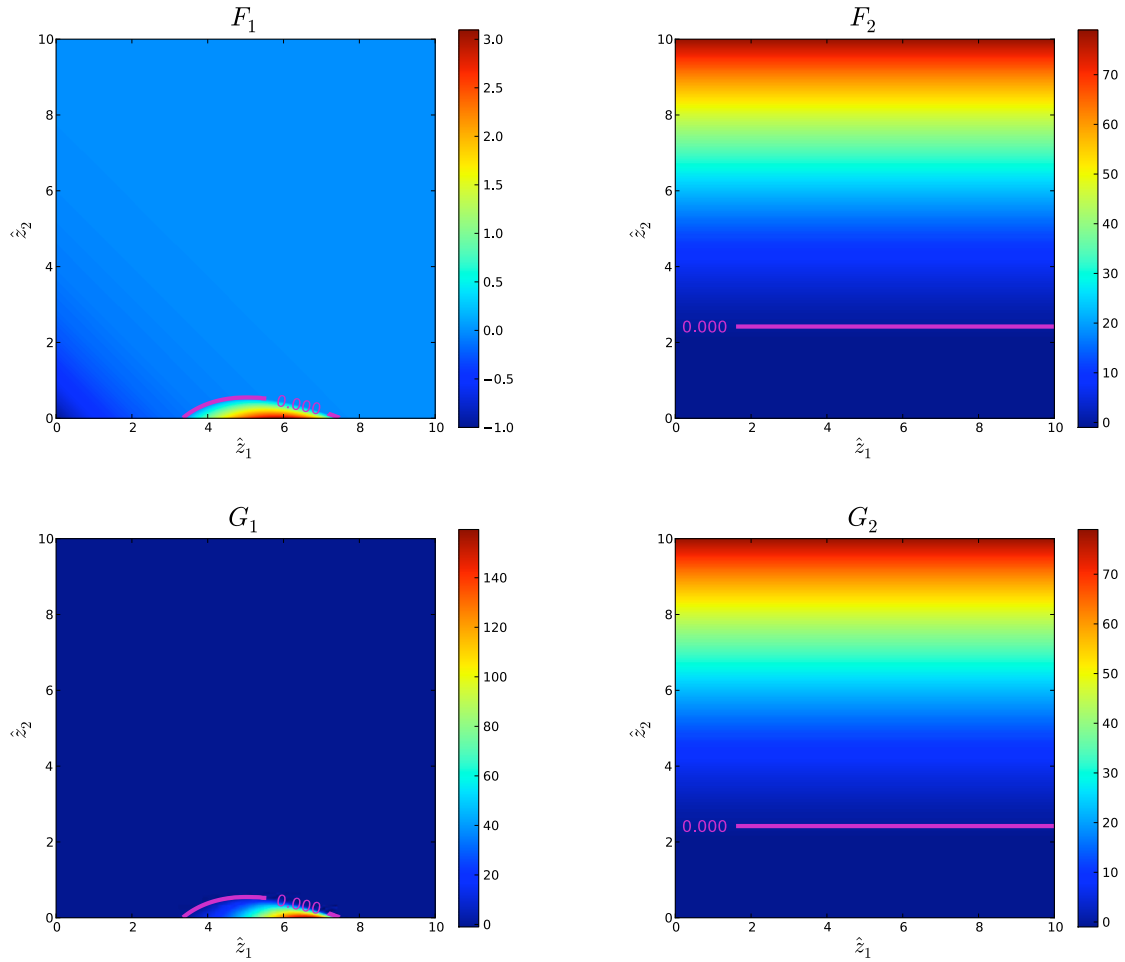
Figure 5.1: F_1, F_2, G_1 and G_2 for the model transport problem with $C_{1,2} = T_2 = 1.0$; $\Delta r = r_2 - r_1 = 0.5$. Despite the color scales, both functions go negative, as indicated by the zero contour for each function, the solid magenta line.
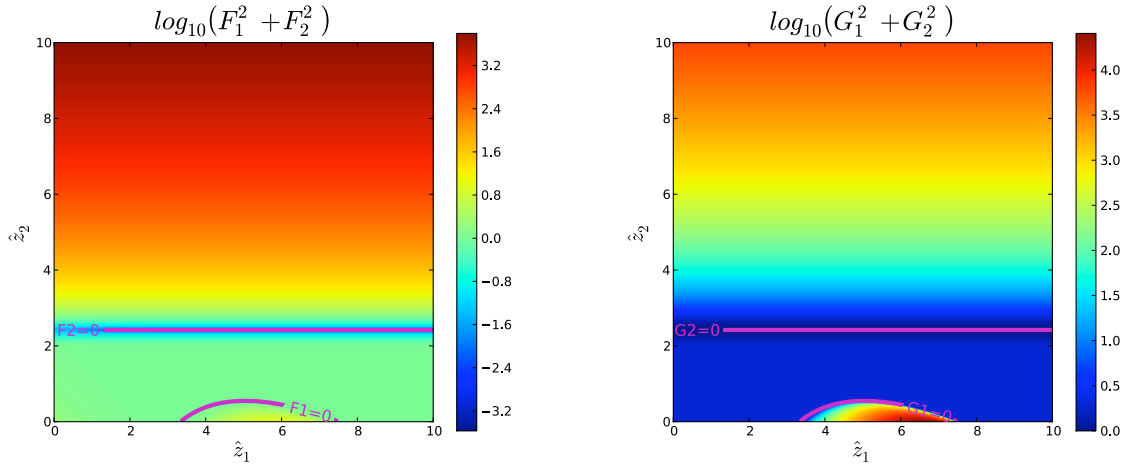
Figure 5.2: Square residuals for the model transport problem with $C_{1,2} = T_2 = 1.0$; $\Delta r = (r_2 - r_1)/a = 0.5$. The zero contours for $F_{1,2}$ and $G_{1,2}$ are indicated by the solid magenta lines.
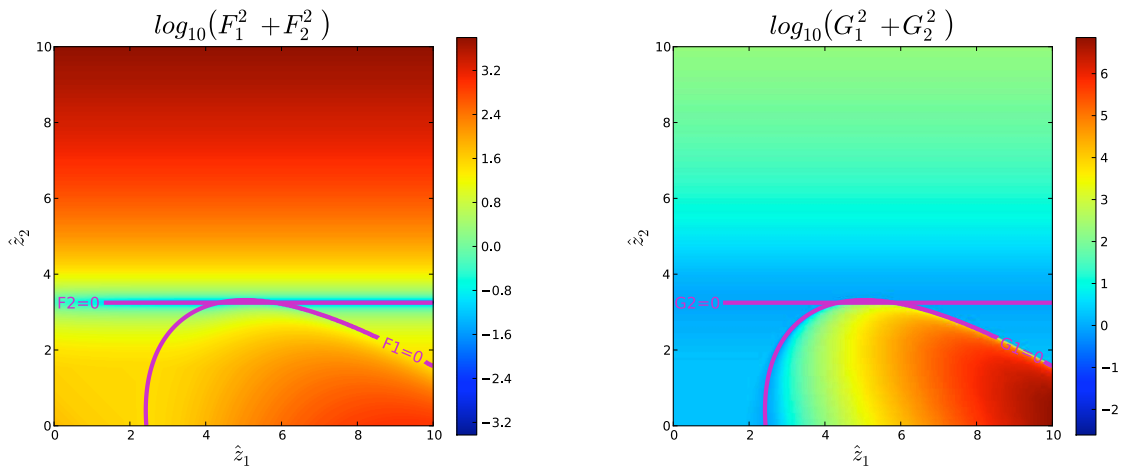
Figure 5.3: Square residuals for the model transport problem with $C_{1,2} = 1.0$; $T_2 = 0.5$; $\Delta r = (r_2 - r_1)/a = 0.5$. The zero contours for $F_{1,2}$ and $G_{1,2}$ are indicated by the solid magenta lines.
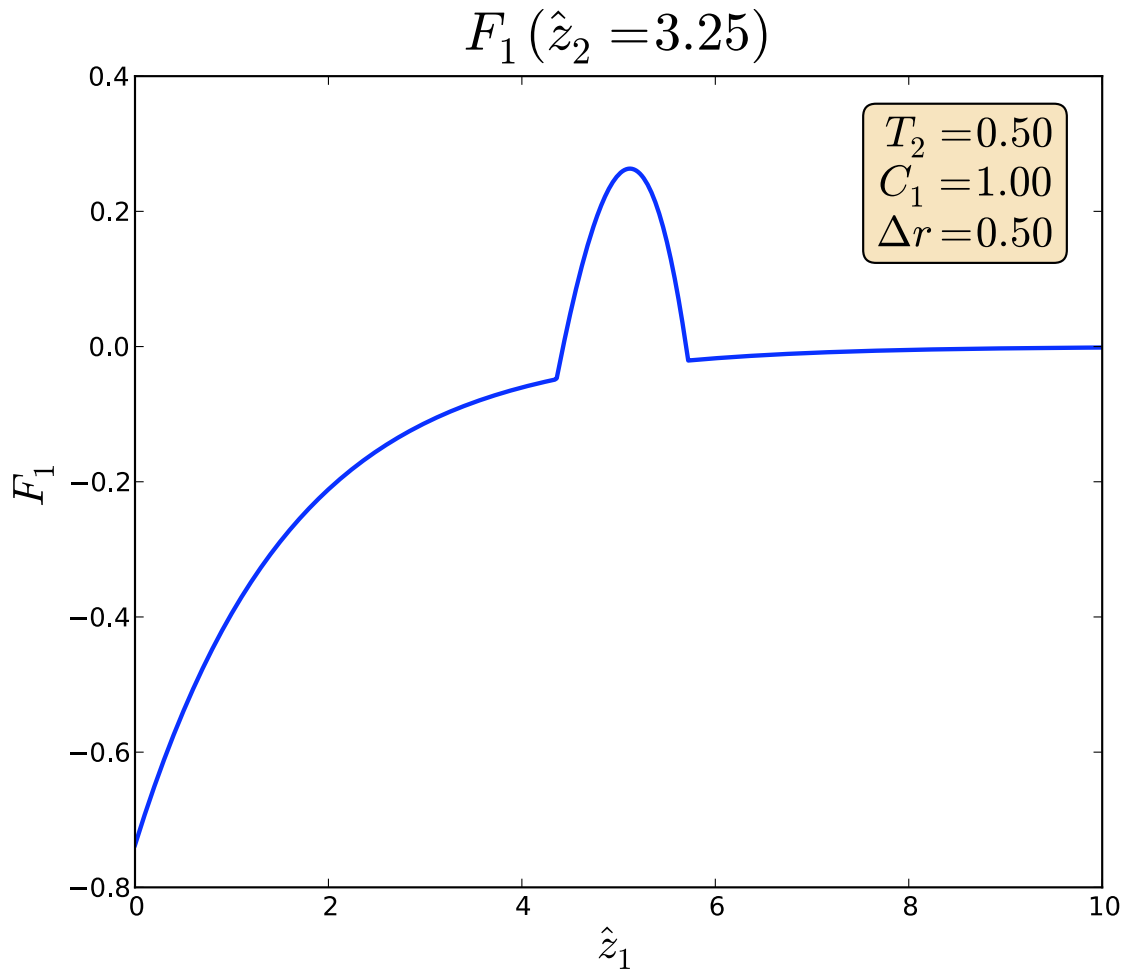
Figure 5.4: $F_1(F_2 = 0)$ for $C_{1,2} = 1.0$; $T_2 = 0.5$, $\Delta r = 0.5$, showing two solutions for $F_1 = F_2 = 0$.

in Fig. 5.3, in which we've lowered T_2 to 0.5. The model problem in this case has two solutions. $F_2 = 0$ when $\hat{z}_2 \approx 3.25$. A slice of F_1 at this location, as in Figure 5.4, demonstrates two solutions for $F_1 = 0$. The non-monotonic behavior of $F_1(\hat{z}_1)$ can cause the steady-state transport problem to have either no solution, or multiple solutions.
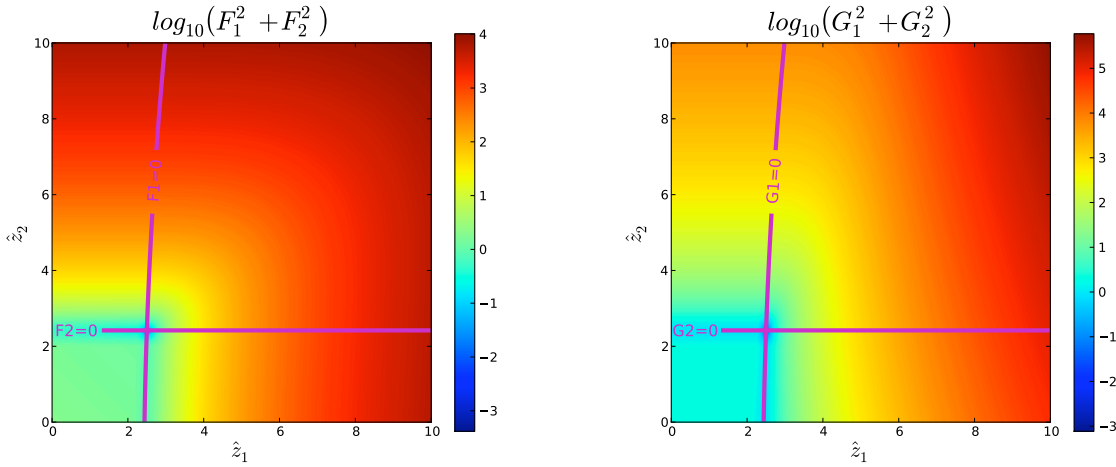
Figure 5.5: Square residuals for the model transport problem with $C_{1,2} = T_2 = 1.0$; $\Delta r = 0.1$. The zero contours for $F_{1,2}$ and $G_{1,2}$ are indicated by the solid magenta lines.

Yet, the lack of solution to the model transport problem is due to the problem discretization, instead of the problem itself. Figure 5.5 shows the same case as in Fig. 5.2, for which there is no solution, but with $\Delta r = 0.1$ instead of 0.5. Both the $F_1 = F_2 = 0$ and $G_1 = G_2 = 0$ have unique solutions at $\hat{z}_1 \approx \hat{z}_2 \approx 2.5$. Since both F and G exhibit the same behavior, the gyroBohm normalization does not cause multiple solutions to exist.

The actual reason behind the non-monotonicity of F_1 is Δr. Figure 5.6 shows the contour for $F_1 = 0$ for different values of Δr. As Δr decreases from 0.4 to 0.01, the zero contour unfolds to the vertical, making F_1 more monotonic in $\hat{z}_1$ as it converges towards the actual solution. Large values of Δr allow for the possibility of not one, but either two or zero solutions, depending on the specific problem parameters. Consider a horizontal line at $\hat{z}_2 = 8$. If this represented the solution to $F_2 = 0$, it would intersect the $\Delta r = 0.01$ and 0.1 contours once on this domain, the 0.2 contour
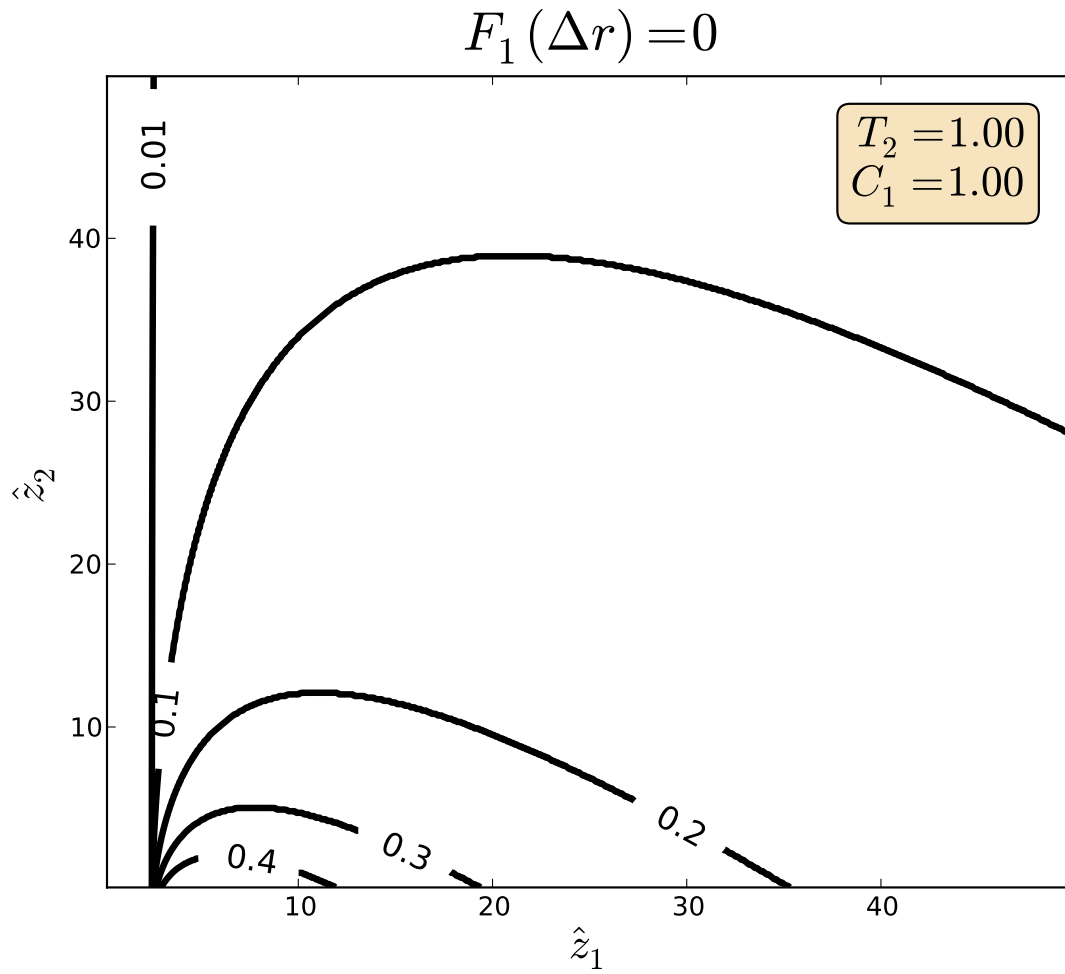
Figure 5.6: Zeros for F_1 for different values of radial separation $\Delta r = [0.01, 0.1, 0.2, 0.3, 0.4]$, with $T_2 = C_{1,2} = 1.0$.

twice and miss the 0.3 and 0.4 contours entirely. The number of global solutions then depends on the grid spacing Δr.
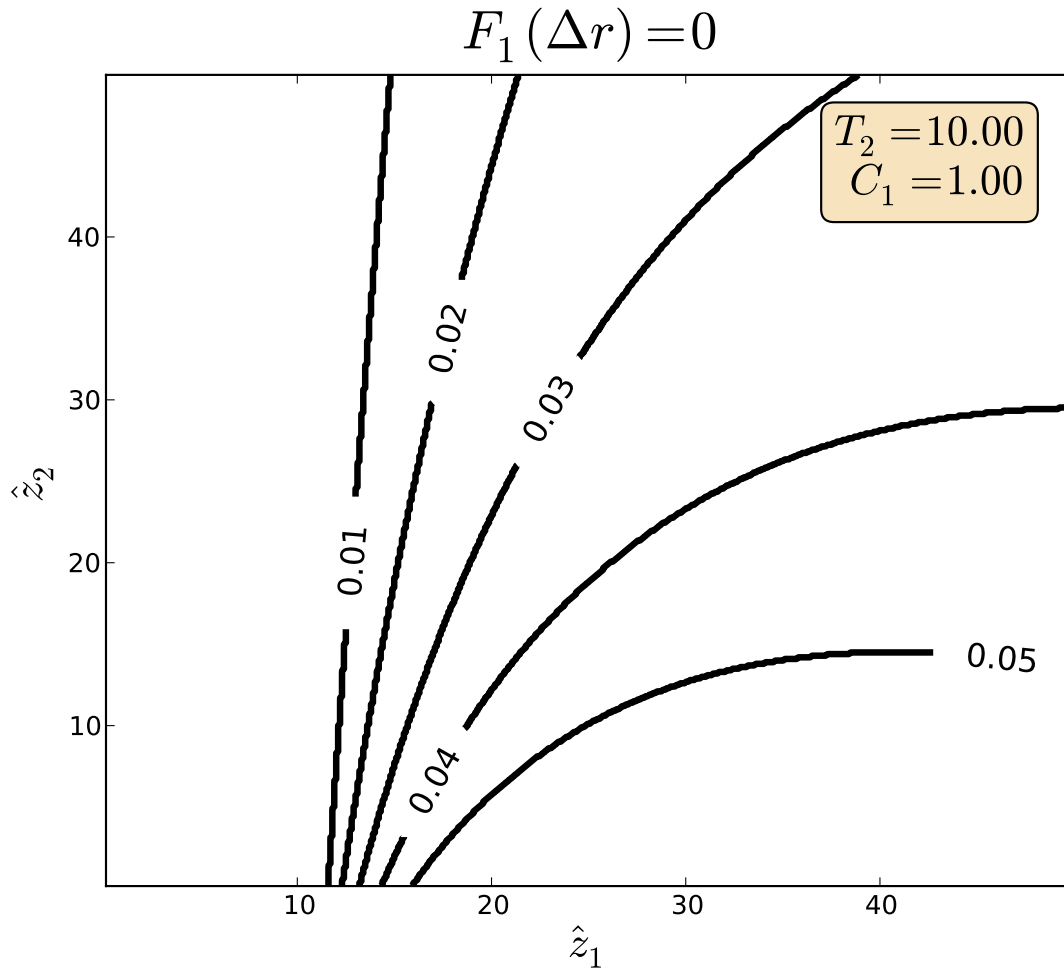
Figure 5.7: Zeros for F_1 for different values of radial separation $\Delta r = [0.01 - 0.05]$, with $T_2 = 10.0$; $C_1 = 1.0$; $C_2 = 1.0$.

Based on Fig. 5.6, an argument could be made that $\Delta r = 0.1$ would be adequate, since values of $\hat{z} > 20$ are rare in plasmas. Even e-ITBs do not reach much beyond $R/L_T \sim 40$. However, *any* finite value of Δr introduces non-monotonicity in $F_1(\hat{z}_1)$. As an example, Fig. 5.7 increases T_2 in the model from 1.0 to 10.0. In this case since its zero-contour bends from the vertical, F_1 is strongly non-monotonic for values of $\Delta r > 0.02$. Even this relatively high radial resolution

has the possibility of displaying multiple global solutions. Finite values of Δr, even if very small, allow for the possibility of multiple global solutions to the steady-state transport problem.

But, even though both solutions solve the equilibrium state-state transport problem, only the one with the lower gradient is stable. About the second solution, reducing the gradient increases the flux above the heating source, cooling the plasma to lower gradients. Increasing the gradient has the opposite effect, lowering the flux, heating the plasma and further increasing the gradient. In a time-dependent formulation, the solution from the turnover of F_1 is unstable.

In cases where multiple solutions exist, the more physical one has the lower gradient. The turnover of F_1 occurs at high values of $\hat{z}_1$. This can be seen by looking at the effects of Δr. The radial grid spacing appears in the calculation of T_1 from T_2:

$$T_1 = T_2 \exp \left(\int_{r_1}^{r_2} z(r) dr \right).$$ (5.28)

A trapezoidal rule approximates the integral in the exponential:

$$\int_{r_1}^{r_2} z(r) dr \approx (r_2 - r_1) \frac{z_2 + z_1}{2} = \frac{\Delta r}{2} \left(\hat{z}_2 + \hat{z}_1 \right).$$ (5.29)

Take $\hat{z}_2$ as a constant and consider the equation for $Q_1 \left(z_1, \ \Delta r \right)$, with $\hat{z} > \hat{z}_1^{crit}$:

$$Q_1 \sim T_1^{5/2} \hat{z}_1 \left\{ \hat{z}_1 - \left(1 + \hat{T}_1 \right) \right\}.$$ (5.30)

If T_1 is constant, the quadratic function in $\hat{z}_1$, $Q_1 - Q_1^T$, has two roots, one (unphysically) below the critical gradient and one other. However, T_1 is a function of $\hat{z}_1$. For small Δr, $\exp \left(\frac{1}{2} \Delta r \hat{z}_1 \right) \sim 1 + \left(\frac{1}{2} \Delta r \hat{z}_1 \right) + \frac{1}{2} \left(\frac{1}{2} \Delta r \hat{z}_1 \right)^2$. Therefore, Q_1 is not actually quadratic when using a finite value of

Δr. Instead, to first order in Δr:

$$Q_1 \sim \left[1 + \frac{5}{4}\Delta r \hat{z}_1\right] \hat{z}_1 \left\{\hat{z}_1 - \left(1 + \left[1 + \frac{1}{2}\Delta r \hat{z}_1\right]\right)\right\}, \tag{5.31}$$

$$\sim \Delta r \left(\frac{5}{4}\hat{z}_1^3 - 3\hat{z}_1^2\right) - \hat{z}_1^2 - 2\hat{z}_1. \tag{5.32}$$

Since $Q_1(z_1, \Delta r)$ is cubic in $\hat{z}_1$, three roots exist, not just two. Furthermore, for large values of $\hat{z}_1$, the exponential terms dominate. Specifically:

$$\lim_{\hat{z}_1 \to \infty} T_1^{5/2} \hat{z}_1 (\hat{z}_1 - (1 + T_1)) = \lim_{\hat{z}_1 \to \infty} \hat{z}_1 - 1 - e^{\frac{\hat{z}_1 \Delta r}{2}} = -\infty. \tag{5.33}$$

This implies that for large enough gradients, Q_1 drops off. In actuality, Q_1 doesn't go negative, because the heaviside function sets it to zero: $Q_1 \sim (\hat{z}_1 - (1 + T_1)) H [\hat{z}_1 - (1 + T_1)]$, with $[\hat{z}_1 - (1 + T_1)] \to -\infty$. Even had we replaced the heaviside function with a more gradual model of stiff transport, Q_1 would still drop off rapidly for high values of $\hat{z}_1$.

This behavior of $Q_1(\hat{z}_1)$ is seen in the graphs of F_1 and G_1. With increasing $\hat{z}_1$, F_1 and G_1 eventually stop increasing and quickly decrease, thereby causing the zero contour to bend towards the $\hat{z}_1$ axis. Even $\Delta r = 0.01$ shows a slight bend in its contour.

The exponential function in the calculation of T_1 causes the non-monotonicity of $Q_1(\hat{z}_1)$. As long as the integral in the exponent is a function of $\hat{z}_1$, Q_1 will turn over, even for very small values of Δr. Physically, Q_1 should not behave like this, because increasing the gradient should increase, not decrease, the flux. By placing the problem on a discrete grid and approximating the temperature integral with a function of $\hat{z}_1$, a single unique solution to the steady-state transport problem no longer exists. Such a single solution may exist on a range of local parameters (for instance, for low enough values of $\hat{z}_1$), but, depending on the problem parameters, its uniqueness cannot be guaranteed.

This model problem also illustrates the kind of residual terrain one can expect to find in the steady-state transport problem. Figure 5.5 shows the global residuals for $\Delta r = 0.1$. For values of $\hat{z}_{1,2} < 2$, the residual function is flat for G_1 and nearly so for F_1. This corresponds to $\hat{z} < \hat{z}^{crit}$. In this region, the plasma is stable and produces no turbulent heat flux. As such, the local gradient is also zero, which shows up as a flat plane in the residual. While a realistic problem may still have some small amount of neoclassical flux in this vicinity of phase space, the gradient will still likely be very small. The terrain is also punctuated by very narrow valleys, which lie along the zero contours for each function. Along these lines, the residual is very small, as the solution is exact for one of fluxes. Slight deviations can lead to very steep rises in heat flux, thanks to the stiff-profile phenomenon. Together, flat planes surrounded by very narrow valleys are some characteristic features of the steady-state transport problem.

The simple two-point model of turbulent heat flux gives some valuable lessons about the transport problem. Firstly, when integrating gradients to get temperatures on a finite grid, the uniqueness of a global solution cannot be guaranteed when the local temperature also depends on the local gradient. Secondly, even if a unique solution exists in the problem domain, the residual terrain is likely to be complex, punctuated with flat planes and narrow valleys. Solving the steady-state transport problem in a computationally efficient manner is certain to be challenging.

5.1.3 Computational Challenges

The lessons learned from the example in the previous section highlight some of the computational challenges that may arise when attempting to solve the steady-state transport problem. These include the possibility of multiple solutions and complex terrain, whose combination can lead to poor convergence and a very expensive calculation.

Firstly, the steady-state transport problem can have multiple solutions. The multiple global solutions can arise from the discrete radial grid and by defining the profiles as functions of their

local gradients. In this case, the discretized equations can actually have multiple solutions, each mathematically correct, even if only one is physical. Once an algorithm has found a solution, it is difficult to know *a priori* whether it is the "correct" physical one. Furthermore, it is impossible to guarantee that a unique solution even exists. In the case in Fig. 5.3 without a solution, an algorithm could wander around indefinitely, trying to find an answer that doesn't exist.

The second major challenge for an algorithm comes from the complex residual terrain presented by the transport problem. Specifically, the local gradients can be either very small or very large. Flat terrain can be particularly challenging for root-finding algorithms, as they often depend upon information from the Jacobian matrix to determine the best direction to search. In these cases the Jacobian becomes ill-conditioned, making it difficult to determine the search direction. Simply put, if the plasma is locally stable and the gradient is nearly zero in every direction, there's no way to tell in which of those directions lies the solution, as they all appear locally to have the same effect on the error. The transport problem is also likely to have steep, narrow valleys, for instance where one radial location is near its solution. In Fig. 5.3 the residual for F changes over three orders of magnitude by varying $\hat{z}_2$ from 2 to 3. Near the bottom of this valley, the gradient in the direction of $\hat{z}_1$ is much less than in the $\hat{z}_2$ direction. The tendency of some algorithms in these situations is to "zig-zag" across the valley, taking larger steps in $\hat{z}_2$ than in $\hat{z}_1$. This is related to the flat-plane problem. As the gradient in the direction of $\hat{z}_1$ approaches zero, the search direction in $\hat{z}_1$ becomes less certain. Instead of traversing directly along the bottom of the valley, an algorithm starts to climb out of the valley. The resulting path is a zig-zag pattern, which is highly inefficient.

The problems presented by the non-uniqueness of solutions and difficult-to-navigate terrain manifest themselves as poor convergence and computational expense. Calculating turbulent fluxes can be expensive, for instance with a flux calculation at a single radial point taking several thousand CPU-hours. Multiply this by the number of radial grid points in the transport calculation and a single evaluation of the flux can easily approach a hundred thousand CPU-hours, or more. The dimensions of the Jacobian matrix are $(N_{radii} \cdot N_{profiles}) \times (N_{radii} \cdot N_{profiles})$, where N_{radii}

represents the number of discrete radial grid points and $N_{profiles}$ represents the number of plasma profiles to evolve. With 10 discrete radial grid points and just evolving T_e, the Jacobian matrix already has 100 elements. Evolving T_i as well increases this to 400. To evaluate the Jacobian with finite differences requires a unique flux calculation for each element of the matrix, at several thousand CPU-hours a piece. Even though one could calculate each element in parallel, the computational cost of calculating the Jacobian matrix can be very large, even if the terrain behaved well enough for quick convergence.

The "ideal" iterative root-finding algorithm would minimize the number of flux calculations by efficiently navigating the residual terrain. Dependent upon at least an evaluation of the flux at each radial location (and a Jacobian evaluation, if using it to determine the search direction), each iteration could easily cost tens or hundreds of thousand of CPU-hours. As such, minimizing the number of iterations directly affects the feasibility of solving the transport problem. Furthermore, the possibility of multiple solutions implies that an algorithm must reliably approach the physical one. Presumably, a good initial guess based on experimentally measured profiles is close to the desired solution. The ideal algorithm will approach this solution and not an alternate.

Essentially, the complex terrain features, multiple zeros and expensive function evaluations of the steady-state transport problem necessitate advanced root-finding algorithms that can quickly and reliably reach the desired physical solution.

5.2 New algorithms for **TGYRO**

TGYRO [120] solves the steady-state transport equations on a discrete radial grid. At each radius, turbulent fluxes can be calculated by either GYRO or TGLF [105, 106], the trapped gyro-Landau fluid transport model, which approximates linear eigenmodes for gyrokinetic drift-waves to calculate quasi-linear heat fluxes. Neoclassical fluxes can be calculated numerically with the NEO

code, [107] or analytically. In its original formulation, TGYRO uses a Newton algorithm to iterate on plasma profiles until the calculated fluxes balance the target fluxes.

After outlining TGYRO's original algorithm, this section uses intuition gained about the steady-state transport problem to develop and implement new root-finding methods for TGYRO. These include Levenberg-Marquardt Minimization, which combines information from the gradient and steepest-descent directions to determine a search direction, and two methods for line backtracking, which determine how far along that search direction the algorithm should move.

5.2.1   Original Algorithm

TGYRO solves the steady-state transport equations in a gyro-Bohm normalization, as in Eq. 5.9:

$$\hat{\mathbf{Q}}_a\left(\mathbf{z}\right) = \hat{\mathbf{Q}}_a^T\left(\mathbf{z}\right). \tag{5.34}$$

The local gradients determine the plasma profiles, which are approximated with trapezoidal integration from a boundary condition, as in Eq. 5.7:

$$T_a(r_{j-1}) = T_a(r_j) \exp\left(\left[\frac{z_a(r_j) + z_a(r_{j-1})}{2}\right][r_j - r_{j-1}]\right). \tag{5.35}$$

The solution to Eq. 5.34 is reached iteratively, by expanding around an initial guess of gradients $\mathbf{z}^0$:

$$\hat{\mathbf{Q}}\left(\mathbf{z}^0\right) + \mathbb{J}\left(\mathbf{z}^0\right)\delta\mathbf{z} - \left[\hat{\mathbf{Q}}^T\left(\mathbf{z}^0\right) + \mathbb{J}^T\left(\mathbf{z}^0\right)\delta\mathbf{z}\right] = 0. \tag{5.36}$$

$\mathbb{J}$ and $\mathbb{J}^T$ are the Jacobian matrices of the transport and target fluxes, respectively:

$$J_{a,b} = \frac{\partial \hat{Q}_a}{\partial z_b}. \tag{5.37}$$

The iterative scheme is based off a single function $\mathbf{F}(\mathbf{z}) = \hat{\mathbf{Q}}(\mathbf{z}) - \hat{\mathbf{Q}}^T(\mathbf{z})$, the difference in the transport and target fluxes, and $\mathbb{J}^F = \mathbb{J} - \mathbb{J}^T$. Solving the transport equations is akin to solving $\mathbf{F}(\mathbf{z}) = \mathbf{0}$.

The Jacobians are all approximated with forward finite differences, such that:

$$J_{a,b}^F \approx \mathcal{J}_{a,b} = \frac{F_a(z_b + \Delta z) - F_a(z_b)}{\Delta z}. \tag{5.38}$$

$\mathcal{J}$ is typically strongly diagonally dominant but not necessarily so. Since $\mathbf{Q}$ and $\mathbf{Q}^T$ depend on plasma profiles, which are calculated by integrating gradients from a fixed boundary point, some off-diagonal components appear in the Jacobian. However, the accuracy of the Jacobian approximation does not affect the solution, but merely the rate of convergence. In terms of the $\mathcal{J}$, the system is defined as:

$$\mathbf{F}(\mathbf{z}^0) + \mathcal{J}(\mathbf{z}^0)\,\delta\mathbf{z} = 0. \tag{5.39}$$

The iterative procedure becomes:

$$\mathbf{z}^{n+1} = \mathbf{z}^n - \mathcal{J}^{-1}(\mathbf{z}^n)\,\mathbf{F}(\mathbf{z}^n), \tag{5.40}$$

which begins with an initial guess of gradients $\mathbf{z}^0$ and iterates until convergence in $\mathbf{z}^n$. $\delta\mathbf{z} = \mathcal{J}^{-1}(\mathbf{z}^n)\,\mathbf{F}(\mathbf{z}^n)$ is the Newton search direction for the algorithm. One has arrived at the solution when $\mathbf{z}^n = \mathbf{z}^{n+1}$, so $\mathbf{F}(\mathbf{z}^n) = 0$.

The original `TGYRO` algorithm combines this pure Newton method with a residual monitoring algorithm. Instead of Eq. 5.40, the algorithm updates according to:

$$z_j^{n+1} = z_j^n + \delta z_j \eta_j^n. \tag{5.41}$$

η^n is a positive relaxation parameter. It is a vector that scales the components of the new step. The logic for this scaling comes from monitoring the residual vector, $\mathbf{R}$, which is some function of $\mathbf{F}$. For concrete purposes, let $\mathbf{R}$ represent the square residuals:

$$R_j = \frac{1}{2}F_j{}^2 = \frac{1}{2}\left(\hat{Q}_j - \hat{Q}_j^T\right)^2. \tag{5.42}$$

The magnitude of $\mathbf{R}$, is a scalar function of $\mathbf{z}$, which we are trying to minimize:

$$R(\mathbf{z}) = \frac{1}{2}\mathbf{F}(\mathbf{z}) \cdot \mathbf{F}(\mathbf{z}). \tag{5.43}$$

Note that for this choice of R, its gradient depends on the transpose of the Jacobian:

$$\nabla R = \mathcal{J}^{\mathbf{T}}\mathbf{F}, \tag{5.44}$$

so that

$$\begin{aligned}
\nabla R \cdot \delta\mathbf{z} &= \left(\mathcal{J}^{\mathbf{T}}\mathbf{F}\right) \cdot \left(-\mathcal{J}^{-1}\mathbf{F}\right) \\
&= -\left(\mathcal{J}^{\mathbf{T}}\mathbf{F}\right)^{\mathbf{T}}\left(\mathcal{J}^{-1}\mathbf{F}\right) \\
&= -\left(\mathbf{F}^{\mathbf{T}}\mathcal{J}\right)\left(\mathcal{J}^{-1}\mathbf{F}\right) \\
&= -\mathbf{F} \cdot \mathbf{F} \\
&= -2R < 0.
\end{aligned} \tag{5.45}$$

The Newton direction, as defined by $\delta\mathbf{z}$, is a descent direction for the square residual of $\mathbf{F}$. This means that a step in this direction *must* decrease R, bringing the solution closer to $\mathbf{F} = 0$, as long as $\mathbf{F}$ is sufficiently smooth and the second derivative term ignored in the expansion around $\mathbf{z}^n$ is negligible.

Algorithm 5.1 Original TGYRO Newton-Relaxation method for calculating new gradients, $\mathbf{z}^1$, from a previous iteration's, $\mathbf{z}^0$.

Input: $\mathbf{z}^0$, η^0, C_η, Δz, $\Delta z_{\max}$
Output: $\mathbf{z}^1$, η^1

1:   $\mathbf{R}^0 \leftarrow R\left(\mathbf{z}^0\right)$ # Current residual
2:   **for all** j, k **do**   # Approximate Jacobian
3:      $\mathcal{J}_{j,k} = \frac{F_j\left(z_k^0 + \Delta z\right) - F_j\left(z_k^0\right)}{\Delta z}$
4:   **end for**
5:   Calculate $\mathcal{J}^{-1}$
6:   $\delta\mathbf{z} \leftarrow \mathcal{J}^{-1} \cdot \mathbf{F}\left(\mathbf{z}^0\right)$ # Newton direction
7:   **for all** j **do**
8:      $\delta z_j' \leftarrow \delta z_j \eta_j^0$ # Relax step
9:      **if** $\left|\delta z_j'\right| > \Delta z_{\max}$ **then**   # Limit step size
10:        $\delta z_j' \leftarrow \text{sign}\left(\delta z_j'\right) \Delta z_{\max}$
11:      **end if**
12:     $z_j^1 \leftarrow z_j^0 + \delta z_j'$ # Take new step
13:   **end for**
14:   $\mathbf{R}^1 \leftarrow R\left(\mathbf{z}^1\right)$
15:   **for all** j **do**
16:      **if** $R_j^1 > R_j^0$ **then**   # Reset step and increase relaxation
17:        $z_j^1 \leftarrow z_j^0$
18:        $\eta_j^1 \leftarrow \eta_j^0 / C_\eta$
19:        **if** $\eta_j^1 < 1/C_\eta^3$ **then**   # Minimum value for relaxation
20:           $\eta_j^1 \leftarrow 0.75 C_\eta$
21:        **end if**
22:      **else**   # Reset relaxation
23:        $\eta_j^1 \leftarrow 1$
24:      **end if**
25:   **end for**
26:   **return** $\mathbf{z}^1$, η^1 # New gradients and relaxation

---

The original `TGYRO` algorithm monitors the individual components of $\mathbf{R}$. If a step would cause a value of R_j to increase, η_j decreases by a factor of $C_\eta > 1$. In this sense, one wouldn't take a full step in that direction, instead trying to relax the length of δz_j until R_j decreases. This procedure, it should be noted, rotates the update vector, so that it no longer points along the Newton direction:

$$\delta\mathbf{z} = \sum_j \delta z_j \mathbf{e_j} \nparallel \delta\mathbf{z}' = \sum_j \delta z_j \eta_j \mathbf{e_j} \text{ if } \exists i, j \mid \eta_i \neq \eta_j. \tag{5.46}$$

Additionally, the iterative algorithm sets a cap on the maximum length of $\delta z_j \eta_j$, $\Delta z_{\max}$. Algorithm 5.1 shows the full procedure, which calculates a new vector of gradients $\mathbf{z}^1$ from an initial vector of gradients $\mathbf{z}^0$, the constants $\Delta z_{\max}$ and C_η and a relaxation vector η (which is initialized to unity, but varies dynamically during the course of iteration).

The Newton-Relaxation method presented in Algorithm 5.1 has a few potential pitfalls. First of all, the relaxation scheme allows for infinite iterative loops without any improvement in the solution. Since line 20 prevents the relaxation parameter from getting too small, while line 17 does not allow any steps that increase R_j, should R_j decrease only for $\eta_j < C_\eta^{-3}$, the algorithm will refuse to take such a step, effectively freezing in place. The algorithm would be stuck trying the following sequence of values for η_j : $\{1, C_\eta^{-1}, C_\eta^{-2}, C_\eta^{-3}, 0.75C_\eta, 0.75, 0.75C_\eta^{-1}, 0.75C_\eta^{-2}, 0.75C_\eta, 0.75, 0.75C_\eta^{-1}...\}$. The iterator would loop in the repeating series $\{0.75C_\eta, 0.75, 0.75C_\eta^{-1}, 0.75C_\eta^{-2}\}$ without updating z_j. Such a situation is not inconceivable, especially near marginal stability, when small changes in gradients can lead to large change in flux. In these cases, a step may need to be smaller than the floor set by C_η^{-3}.

A major pitfall in Algorithm 5.1 is that once it calculates its search direction, it effectively ignores it. Since η is a vector, both the magnitude and direction of $\delta\mathbf{z}$ and $\delta\mathbf{z}'$ are different. A key point is that the magnitude of the square residual $\mathbf{R}$ must initially decrease when traveling in the Newton direction. No such stipulation is made on the components of $\mathbf{R}$. Individual values of

R_j may increase in the Newton direction. Every time a value of R_j increases, TGYRO's original algorithm scales and rotates the search vector. Because $\delta \mathbf{z} \nparallel \delta \mathbf{z}'$, there is no guarantee that R will decrease for any step size in the $\mathbf{z}'$ direction. Furthermore, one could actually now be searching *away* from the desired root. Since multiple roots exist mathematically in this system, rotating off the Newton direction could have serious consequences.

A final difficulty with the present method is that it first searches solely in the Newton direction, $\delta \mathbf{z} = \mathcal{J}^{-1} \mathbf{F} (\mathbf{z}^0)$. As the local gradient decreases, the Newton step size increases. Near well-behaved roots, Newton's method converges quadratically. However, as the Jacobian matrix gets smaller, the second derivative terms ignored in the expansion around $\mathbf{z}^0$ become non-negligible. In cases like these, $\delta \mathbf{z}$ becomes too large. Newton works very well near roots, but becomes unreliable in regions of vanishing gradient. Since areas of flat gradients are characteristic of the transport problem, relying solely on Newton iteration has its limitations.

5.2.2   Levenberg-Marquardt Minimization

In cases where the Newton search direction becomes problematic, it becomes desirable to change search directions. One method that does this is the Levenberg-Marquart method for a sum of squares residual minimization [122, 123]. The idea behind the method is combine the Newton and steepest-descent directions.

Levenberg-Marquardt aims to minimize the least squares residual of $\mathbf{F}$, R. Expanding R around a guess $\mathbf{z}^0$ gives:

$$R \left(\mathbf{z}^0 + \delta \mathbf{z} \right) \approx R \left(\mathbf{z}^0 \right) + \nabla R^{\mathbf{T}} \bigg|_{\mathbf{z}^0} \delta \mathbf{z} + \frac{1}{2} \delta \mathbf{z}^{\mathbf{T}} \mathbb{H} \bigg|_{\mathbf{z}^0} \delta \mathbf{z}. \tag{5.47}$$

$\mathbb{H}$ is the Hessian matrix of second derivatives of R:

$$H_{j,k} = \partial_j \partial_k R \left(\mathbf{z} \right). \tag{5.48}$$

To find a minimum of R, take the derivative of Eq. 5.47 with respect to $\delta\mathbf{z}$ and set it equal to zero. This gives a step of $\delta\mathbf{z}$ as:

$$\delta\mathbf{z} = -\mathbb{H}^{-1}\nabla R\Big|_{\mathbf{z}^0}. \tag{5.49}$$

Recall the least-squares definition of R, written in component form:

$$R = \frac{1}{2}\sum_{i=1}^{n_z} F_i^2. \tag{5.50}$$

n_z is the number of total gradients in $\mathbf{z}$. The components of ∇R can be written as:

$$(\nabla R)_j = \sum_{i=1}^{n_z} F_i \frac{\partial F_i}{\partial z_j}, \tag{5.51}$$

$$= \sum_{i=1}^{n_z} F_i J_{i,j}. \tag{5.52}$$

So the components of $\mathbb{H}$ can be written in terms of F as:

$$H_{j,k} = \sum_{i=1}^{n_z} \left(\frac{\partial F_i}{\partial z_j}\frac{\partial F_i}{\partial z_k} + F_i \frac{\partial^2 F_i}{\partial z_j \partial z_k} \right) \tag{5.53}$$

$$= \sum_{i=1}^{n_z} \left(J_{i,j} J_{i,k} + F_i \frac{\partial^2 F_i}{\partial z_j \partial z_k} \right) \tag{5.54}$$

When neglecting the second term in the sum as small, one can write an approximation of the Hessian matrix of R:

$$\mathbb{H} \approx \mathcal{J}^{\mathbf{T}}\mathcal{J}. \tag{5.55}$$

Under this approximation we can see that Eq. 5.49 is equal to a Newton step for $\mathbf{F}$. Multiplying the Newton formulation, Eq. 5.39, by the transpose of the Jacobian, $\mathcal{J}^{\mathbf{T}}$, yields an equivalent system

to solve, which can be rearranged to determine a new step size:

$$\mathcal{J}^{\mathbf{T}}\mathbf{F}\left(\mathbf{z}^0\right) + \mathcal{J}^{\mathbf{T}}\mathcal{J}\left(\mathbf{z}^0\right)\delta\mathbf{z} \;=\; 0 \tag{5.56}$$

$$\delta\mathbf{z} \;=\; -\left[\mathcal{J}^{\mathbf{T}}\mathcal{J}\right]^{-1}\mathcal{J}^{\mathbf{T}}\mathbf{F}\left(\mathbf{z}^0\right). \tag{5.57}$$

Since R is chosen to be a least squares residual, $\nabla R = \mathcal{J}^{\mathbf{T}}\mathbf{F}$. As long as $\mathbb{H} \approx \mathcal{J}^{\mathbf{T}}\mathcal{J}$, the Newton step for $\mathbf{F}$, Eq. 5.57, aligns with the minimization of R, Eq. 5.49.

The Levenberg-Marquardt method replaces Eq. 5.57 with a damped version.

$$\delta\mathbf{z} = -\left[\mathcal{J}^{\mathbf{T}}\mathcal{J} + \alpha\mathrm{diag}\left(\mathcal{J}^{\mathbf{T}}\mathcal{J}\right)\right]^{-1}\mathcal{J}^{\mathbf{T}}\mathbf{F}\left(\mathbf{z}^0\right). \tag{5.58}$$

The magnitude of the damping parameter α determines the descent direction.

$$\delta\mathbf{z} = \begin{cases} -\left[\mathcal{J}^{\mathbf{T}}\mathcal{J}\right]^{-1}\mathcal{J}^{\mathbf{T}}\mathbf{F}\left(\mathbf{z}^0\right) & \text{as } \alpha \to 0, \\[2ex] -\frac{1}{\alpha}\mathcal{J}^{\mathbf{T}}\mathbf{F}\left(\mathbf{z}^0\right) & \text{as } \alpha \to \infty. \end{cases} \tag{5.59}$$

Equation 5.59 says that for small values of α the step direction $\delta\mathbf{z}$ lies in the Newton direction, as in Eq. 5.57. However, because $\mathcal{J}^{\mathbf{T}}\mathbf{F}\left(\mathbf{z}^0\right) = \nabla R\left(\mathbf{z}^0\right)$, for large values of α the step direction lies along the negative gradient of R. The key to the Levenberg-Marquardt method is to dynamically combine these two directions. Near a root, one preferentially uses the Newton direction, because it converges rapidly. However, away from a root, where the second derivatives ignored in the Hessian approximation become important, one can resort to moving in the direction of the local steepest descent in R.

The algorithm dynamically alters the strength of α by monitoring the change in residual. Each time an iteration lowers the residual, α is lowered by a damping factor $\delta > 1$. Should the residual increase, α is multiplied by a boosting factor $\beta > 1$. The idea is to bring α closer to zero when the residual is decreasing, so one moves more in the Newton direction. Where an iteration would

increase the residual, α increases, to move more along the steepest-descent direction. The implementation also maintains that $\alpha > 0.01$ when it needs to increase or $\alpha < 0.01$ when it needs to decrease. This limits wasted iterations whose sole purpose is to change α.

Additionally, Marquardt [123] solves a scaled version of Eq. 5.58, which has a diagonal of magnitude unity. This allows α to have a similar effect on each dimension. Since TGYRO uses a gyroBohm normalization, the components of $\mathcal{J}$ could vary by orders of magnitude. Solving an equivalent scaled problem becomes desirable in this case. Specifically, define:

$$\mathbb{A} = \mathcal{J}^{\mathbf{T}}\mathcal{J}, \tag{5.60}$$

$$\mathbf{b} = -\mathcal{J}^{\mathbf{T}}\mathbf{F}\left(\mathbf{z}^{0}\right), \tag{5.61}$$

$$\mathbb{A}^{*}: A_{j,k}^{*} = \frac{A_{j,k}}{\sqrt{A_{j,j}A_{k,k}}}\left(1 + \alpha\delta_{j,k}^{Kr}\right), \tag{5.62}$$

$$\mathbf{b}^{*}: b_{j}^{*} = \frac{b_{j}}{\sqrt{A_{j,j}}}. \tag{5.63}$$

$\delta_{j,k}^{Kr}$ is the Kroenecker delta. Then the equivalent scaled equations to solve become $\mathbb{A}^{*}\mathbf{x} = \mathbf{b}^{*}$. Finally, the step size in each direction becomes:

$$\delta z_{j} = \frac{x_{j}}{\sqrt{A_{j,j}}}. \tag{5.64}$$

The implementation in TGYRO also limits the maximum step size, as defined by $\Delta z_{\max}$, but scales each component of the step vector equally:

$$\delta\mathbf{z}' = \delta\mathbf{z}\min\left(1, \Delta z_{\max}/\max_{j}|\delta z_{j}|\right). \tag{5.65}$$

The next iteration is given by $\mathbf{z}^{1} = \mathbf{z}^{0} + \delta\mathbf{z}'$. The full Levenberg-Marquardt minimization method as implemented in TGYRO is given in Algorithm 5.2.

Algorithm 5.2 Levenberg-Marquardt method for calculating new gradients, $\mathbf{z}^1$, and damping parameter α^1 from a previous iteration's, $\mathbf{z}^0$ and α^0.

Input: $\mathbf{z}^0, \alpha^0, \delta, \beta, \Delta z, \Delta z_{\max}$
Output: $\mathbf{z}^1, \alpha^1$
 1: $\mathbf{R}^0 \leftarrow R\left(\mathbf{z}^0\right)$
 2: **for all** j, k **do**
 3: $\quad \mathcal{J}_{j,k} = \frac{F_j\left(z_k^0 + \Delta z\right) - F_j\left(z_k^0\right)}{\Delta z}$
 4: **end for**
 5: $\mathbb{A} \leftarrow \mathcal{J}^{\mathbf{T}} \mathcal{J}$
 6: $\mathbf{b} \leftarrow -\mathcal{J}^{\mathbf{T}} \mathbf{F}\left(\mathbf{z}^0\right)$
 7: **for all** j, k **do**   # Scaled matrices with damping
 8: $\quad A_{j,k}^* \leftarrow \frac{A_{j,k}}{\sqrt{A_{j,j} A_{k,k}}} \left(1 + \alpha \delta_{j,k}^{Kr}\right)$
 9: $\quad b_j^* \leftarrow b_j / \sqrt{A_{j,j}}$
10: **end for**
11: $\mathbf{x} \leftarrow \left[\mathbb{A}^*\right]^{-1} \mathbf{b}^*$
12: **for all j do**
13: $\quad \delta z_j \leftarrow x_j / \sqrt{A_{j,j}}$
14: **end for**
15: $\delta\mathbf{z}' \leftarrow \delta\mathbf{z} \min\left(1, \Delta z_{\max} / \max_j |\delta z_j|\right)$ # Limit step size, but scale equally
16: $\mathbf{z}^1 \leftarrow \mathbf{z}^0 + \delta\mathbf{z}'$ # Take step
17: $\mathbf{R}^1 \leftarrow R\left(\mathbf{z}^1\right)$
18: **if** $\mathbf{R}^1 > \mathbf{R}^0$ **then**   # Reset step, increase damping
19: $\quad \mathbf{z}^1 \leftarrow \mathbf{z}^0$
20: $\quad \alpha^1 \leftarrow \max\left(0.01, \alpha^0 * \beta\right)$
21: **else**   # Accept step, decrease damping
22: $\quad \alpha^1 \leftarrow \min\left(0.01, \alpha^0 / \delta\right)$
23: **end if**
24: **return** $\mathbf{z}^1, \alpha^1$ # New gradients and damping

---

5.2.3 Backtracking

Consider a very flat region in the global residual space, such as a plateau of stability. In such situations, the gradient becomes very small, and the Newton step length can become very large. A full Newton step can actually overshoot the root in cases like these. However, Eq. 5.45 says that the Newton direction *must* decrease R for a sufficiently small step size. This is the idea behind backtracking. One knows that the global residual must decrease somewhere along the trajectory as defined by the Newton direction. To account for a possible overshoot, the algorithm backtracks along that direction until it finds that location. This could be particularly valuable near marginal stability, where slight overshoots of the solution can lead to very large errors. Instead of taking a full Newton step, backtracking allows for a scaled step:

$$\mathbf{z}^{n+1} = \mathbf{z}^n + \lambda \delta \mathbf{z}, \tag{5.66}$$

with the scale factor λ satisfying $0 < \lambda \leq 1$. Backtracking involves finding a value of λ for which $R(\mathbf{z}^n + \lambda \delta \mathbf{z}) < \xi R(\mathbf{z}^n)$, for some value of $\xi \leq 1$. The scale factor λ is similar to the relaxation parameter η of the original TGYRO scheme, with one stark difference: λ is a scalar, so that one always moves in the Newton direction. As η is a vector, it can scale the components of $\delta \mathbf{z}$ differently, effectively rotating the propagation vector away from the Newton direction. Backtracking exploits the fact that R must decrease in the Newton direction, so λ aims to keep the search along that direction.

One always begins by trying $\lambda = 1$, the full Newton step, to retain quadratic convergence near roots. Should $\lambda = 1$ not yield a sufficient reduction in the global residual, we apply techniques from one-dimensional minimization to find a new guess for λ that will minimize the residual along the Newton direction. TGYRO has been equipped with two possible methods of finding a suitable value of λ: parabolic backtracking and the golden ratio line search.

Parabolic Backtracking

The first method for finding λ, parabolic backtracking, exploits the square residual nature of R.

We define a linear function of λ along the Newton direction, which we are trying to minimize:

$$\mathcal{G}(\lambda) = R\left(\mathbf{z}^n + \lambda\delta\mathbf{z}^n\right). \tag{5.67}$$

This implies that

$$\mathcal{G}'(\lambda) = \nabla R \cdot \delta\mathbf{z}^n. \tag{5.68}$$

By starting with $\lambda = 1$, we have some initial conditions,

$$\mathcal{G}(0) = R\left(\mathbf{z}^n\right), \tag{5.69}$$

$$\mathcal{G}'(0) = \nabla R\left(\mathbf{z}^n\right) \cdot \delta\mathbf{z}^n, \tag{5.70}$$

as well as the residual from the full Newton step,

$$\mathcal{G}(1) = R\left(\mathbf{z}^n + \delta\mathbf{z}^n\right). \tag{5.71}$$

Near the solution to $\mathbf{F} = 0$, $\mathcal{G}(1) < \mathcal{G}(0)$, so that we are reducing the error in solution. However, as mentioned, this is not always the case, especially far from the root of $\mathbf{F}$, so we want to reduce λ until we find a minimum of $\mathcal{G}(\lambda)$ for $0 < \lambda \leq 1$. This is the one-dimensional minimization problem of the function $\mathcal{G}(\lambda)$.

To find an approximate minimum to $\mathcal{G}$, we expand $\mathcal{G}(\lambda)$ about $\mathcal{G}(0)$, such that:

$$\mathcal{G}(\lambda) = \mathcal{G}(0) + \lambda\mathcal{G}'(0) + \frac{1}{2}\lambda^2\mathcal{G}''(0) + \cdots. \tag{5.72}$$

We can attempt to find an optimal value of λ by recalling that

$$
\begin{aligned}
\mathcal{G}'(0) &= \nabla R(\mathbf{z}^n) \cdot \delta \mathbf{z}^n, \\
&= -\mathbf{F}(\mathbf{z}^n) \cdot \mathbf{F}(\mathbf{z}^n), \\
&= -2R(\mathbf{z}^n), \\
&= -2\mathcal{G}(0). \quad\quad (5.73)
\end{aligned}
$$

An approximate value of the second derivative $\mathcal{G}$ appears from some algebra:

$$
\begin{aligned}
\mathcal{G}''(0) &\approx 2\left[\frac{\mathcal{G}(\lambda) - \mathcal{G}(0) - \lambda\mathcal{G}'(0)}{\lambda^2}\right] \\
&\approx 2\left[\frac{\mathcal{G}(\lambda) - \mathcal{G}(0) + 2\lambda\mathcal{G}(0)}{\lambda^2}\right] \\
&\approx 2\left[\frac{\mathcal{G}(\lambda) + \mathcal{G}(0)[2\lambda - 1]}{\lambda^2}\right]. \quad\quad (5.74)
\end{aligned}
$$

Since we may need multiple backtracking steps to find the minimum of λ, we define everything in terms of the current estimate of the optimal value, λ_k. As with the Levenberg-Marquardt method, we start with a value of $\lambda_0 \leq 1$ that limits the maximum step size defined by $\Delta z_{\max}$, per Eq. 5.65. The kth apprixmation to the second derivative about $\lambda = 0$ is given by:

$$
\tilde{\mathcal{G}}_k''(0) = 2\left[\frac{\mathcal{G}(\lambda_k) + \mathcal{G}(0)[2\lambda_k - 1]}{\lambda_k^2}\right]. \quad\quad (5.75)
$$

One can now approximate the residual at the next guess for λ, $\tilde{\mathcal{G}}(\lambda_{k+1})$:

$$
\begin{aligned}
\tilde{\mathcal{G}}(\lambda_{k+1}) &= \mathcal{G}(0) + \lambda\mathcal{G}'(0) + \frac{1}{2}\lambda^2\mathcal{G}''(0) \\
&= \mathcal{G}(0)(1 - 2\lambda_{k+1}) + \left(\frac{\lambda_{k+1}}{\lambda_k}\right)^2 [\mathcal{G}(\lambda_k) + \mathcal{G}(0)(2\lambda_k - 1)]. \quad\quad (5.76)
\end{aligned}
$$

To find the value of λ_{k+1} that minimizes this parabolic approximation to the square residual, $\mathcal{G}$, we set $\tilde{\mathcal{G}}'(\lambda_{k+1}) = 0$, and find

$$\lambda_{k+1} = \frac{\lambda_k^2 \mathcal{G}(0)}{\mathcal{G}(\lambda_k) + \mathcal{G}(0)(2\lambda_k - 1)}. \tag{5.77}$$

The backtracking scheme is designed to find a value of λ_{k+1} that reduces the solution error sufficiently, until

$$\mathcal{G}(\lambda_{k+1}) \leq \xi \mathcal{G}(0). \tag{5.78}$$

What is a suitable condition on ξ? How much of a reduction is "good enough?" Having $\xi = 1$ is in some sense too loose of a condition, because we know that $\mathcal{G}$ can be approximated quadratically near $\mathcal{G}(0)$ and that $\mathcal{G}'(0) < 1$; we expect $\mathcal{G}$ to decrease by some finite amount in between $\mathcal{G}(0)$ and $\mathcal{G}(1)$. At some point it may not be worth trying to minimize $\mathcal{G}$, especially as $\lambda_k \to 0$, so it would be prudent to relax the condition in Eq. 5.78, as multiple guesses for λ_k fail.

Numerical Recipes [124] suggests $\xi = (1 - 2\epsilon\lambda_{k+1})$, with $\epsilon = 1 \times 10^{-4}$. This is known as the Armijo rule [125] and relaxes the constraint on each new step as $\lambda_k \to 0$. However, having $\epsilon = 1 \times 10^{-4}$ could be too constrictive: as $\mathcal{G}'(0) < 0$, the residual is expected to drop between 0 and λ_k. Indeed the parabolic fit suggests that there is some other minimum along the length of $\mathcal{G}$ that will be our next guess. Let's take a new step to this minimum if we expect the residual drop there to be a factor of $s > 1$ more than the residual drop at λ_k. Specifically, we'll take a new step λ_{k+1} if:

$$\mathcal{G}_0 - \mathcal{G}_{k+1} = s(\mathcal{G}_0 - \mathcal{G}_k). \tag{5.79}$$

For convenience, let $\mathcal{G}_k \doteq \mathcal{G}(\lambda_k)$. $\mathcal{G}_{k+1}$ can be rewritten in terms of λ_k by evaluating the parabolic equation for $\mathcal{G}_{k+1}$, Eq. 5.76, at its minimum, Eq. 5.77:

$$\mathcal{G}_{k+1} = \mathcal{G}_0 - \frac{\left(\mathcal{G}_0^2 \lambda_k\right)^2}{\mathcal{G}_k + \mathcal{G}_0(2\lambda_k - 1)}. \tag{5.80}$$

Therefore, Eq. 5.79 can be rewritten as:

$$\mathcal{G}_0 - \mathcal{G}_{k+1} = s\left(\mathcal{G}_0 - \mathcal{G}_k\right),$$
$$\frac{\left(\mathcal{G}_0\lambda_k\right)^2}{\mathcal{G}_k + \mathcal{G}_0\left(2\lambda_k - 1\right)} = s\left(\mathcal{G}_0 - \mathcal{G}_k\right). \tag{5.81}$$

To find a value of ϵ in the Armijo rule that satisfies this equation, let $\mathcal{G}_k = \mathcal{G}_0\left(1 - 2\epsilon\lambda_k\right)$. Then

$$\frac{\mathcal{G}_0^2\lambda_k^2}{-2\mathcal{G}_0\epsilon\lambda_k + 2\lambda_k\mathcal{G}_0} = 2s\mathcal{G}_0\epsilon\lambda_k,$$
$$4s\epsilon^2 - 4s\epsilon + 1 = 0,$$
$$\epsilon = \frac{1 \pm \sqrt{1 - {}^1/_s}}{2}. \tag{5.82}$$

As the Armijo condition is most restrictive for $\lambda_k = 1$, $\epsilon < 0.5$, thereby requiring the negative root:

$$\epsilon = \frac{1 - \sqrt{1 - s^{-1}}}{2}; \; s > 1 \tag{5.83}$$

For a value of $s = 2$ (that is, we expect a new parabolic iteration to reduce the error only by a factor of two over the present iteration), $\epsilon \approx 0.146$. We use this as a stopping condition. Namely, we accept a step along the Newton direction of length λ_k if

$$\mathcal{G}\left(\lambda_k\right) \leq \mathcal{G}\left(0\right)\left(1 - 0.29\lambda_k\right). \tag{5.84}$$

Otherwise, we pick a new λ_{k+1} according to Eq. 5.77, until we are satisfied with the error reduction. When the parabolic interpolation breaks down, the predicted λ_{k+1} can be quite small, so we limit each one to be no less than 10% of λ_k. Finally, we place a cap on the total number of allowable guesses, $k_{\max}$, and return the step size that yielded the smallest residual, in case Eq. 5.84 is never satisfied. This also prevents taking a step that increases the global residual, so that the algorithm will stay in one location if $\mathcal{G}(\lambda_k) > \mathcal{G}(0)\forall k < k_{\max}$. The full algorithm for the backtracking

line search is summarized in Algorithm 5.3, which takes a given search direction and attempts to minimize the residual along that direction using the parabolic interpolation for $\mathcal{G}$.

Algorithm 5.3 Parabolic backtracking algorithm for finding best step the search direction $\delta\mathbf{z}$ from an initial point $\mathbf{z}^0$.

Input: $\mathbf{z}^0$, $\delta\mathbf{z}$, $\Delta z_{\max}$, $k_{\max}$, $k = 0$
Output: $\mathbf{z}^{best}$

1: $R^0 \leftarrow R(\mathbf{z}^0)$
2: $R^{best} \leftarrow R^0$, $\mathbf{z}^{best} \leftarrow \mathbf{z}^0$ # Initialize best step
3: $\lambda \leftarrow \min\left(1, \Delta z_{\max}/\max_j |\delta z_j|\right)$ # Limit max step size
4: $\mathbf{z}^{new} \leftarrow \mathbf{z}^0 + \lambda\delta\mathbf{z}$ # First guess
5: $R^1 \leftarrow R\left(\mathbf{z}^{new}\right)$
6: **if** $R^1 < R^{best}$ **then**
7:    $R^{best} \leftarrow R^1$, $\mathbf{z}^{best} \leftarrow \mathbf{z}^{new}$
8: **end if**
9: $\lambda_{old} \leftarrow \lambda$
10: **while** $R^1 > R^0\left(1 - 0.29\lambda_{old}\right)$ **and** $k < k_{\max}$ **do**
11:    $\lambda \leftarrow \max\left(0.1\lambda_{old}, \frac{\lambda_{old}^2}{R^1+R^0(2\lambda_{old}-1)}\right)$ # New step size, not too small
12:    $\mathbf{z}^{new} \leftarrow \mathbf{z}^0 + \lambda\delta\mathbf{z}$
13:    $R^1 \leftarrow R\left(z^{new}\right)$
14:    **if** $R^1 < R^{best}$ **then**   # Store best step so far
15:       $R^{best} \leftarrow R^1$, $\mathbf{z}^{best} \leftarrow \mathbf{z}^{new}$
16:    **end if**
17:    $\lambda_{old} \leftarrow \lambda$, $k \leftarrow k + 1$
18: **end while**
19: **return** $\mathbf{z}^{best}$

Algorithm 5.3 can be incorporated into either the pure Newton iteration scheme or the Levenberg-Marquardt method. In the original Newton method, Algorithm 5.1, it supersedes the relaxation scheme, by replacing the lines of code following line 6. For the Levenberg-Marquardt method, the logic after finding the search direction is changed. If the first guess successfully decreases the residual, the algorithm decreases the damping factor and moves towards the Newton direction. Then, the algorithm tries the parabolic line search to find a λ that satisfies the condition in Eq. 5.84. However, should the search fail by exceeding the maximum number of allowed iterations without sufficiently reducing the residual, the damping factor α increases. The modified

---

Algorithm 5.4 Levenberg-Marquardt with a line search.

Input: $\delta\mathbf{z}'$ as found by Levenberg-Marquardt method, $\mathbf{z}^0$, α^0, δ, β
Output: $\mathbf{z}^1$, α^1
 1: $R^0 \leftarrow R\left(\mathbf{z}^0\right)$
 2: $R^1 \leftarrow R\left(\mathbf{z}^0 + \delta\mathbf{z}'\right)$
 3: **if** $R^1 < R^0$ **then**
 4:     $\alpha^1 \leftarrow \min\left(0.01, \alpha^0/\delta\right)$ # Decrease damping
 5: **end if**
 6: **while** residual not good enough **do**
 7:     search to find $\mathbf{z}^{best}$
 8: **end while**
 9: **if** line search fails **then**
10:     $\alpha^1 \leftarrow \max\left(0.01, \alpha^0 * \beta\right)$ # Increase damping
11: **end if**
12: $\mathbf{z}^1 \leftarrow \mathbf{z}^{best}$
13: **return** $\mathbf{z}^1, \alpha^1$

---

logic is in Algorithm 5.4, with the search loop beginning at line 6 given by that of line 10 of

Algorithm 5.3

Golden Ratio Bisection

An alternative way to find the minimum of $\mathcal{G}(\lambda)$ is to bracket the minimum by trying different

values of λ. Defining $\mathcal{G}_a \doteq \mathcal{G}\left(\lambda_a\right)$, a minimum of $\mathcal{G}$ lies on the interval (a, c) if there exists a

triplet of points $a < b < c$ such that $\mathcal{G}_a > \mathcal{G}_b$ and $\mathcal{G}_c > \mathcal{G}_b$. A bracketing method picks a new value

x, either between a and b or b and c. Choose $b < x < c$, then if $\mathcal{G}_b < \mathcal{G}_x$, we can move $c \rightarrow x$

and form a new triplet (a, b, x). On the other hand, if $\mathcal{G}_b > \mathcal{G}_x$, we can move $a \rightarrow b$ and form

a bracketing triplet of (b, x, c). The idea is to continually move the end points of the bracketing

triplet until the interval shrinks to the point where machine precision errors make $\mathcal{G}_x \approx \mathcal{G}_b$, or until

$\mathcal{G}$ drops below a pre-determined value.

To find an efficient guess for x, given (a, b, c), let b be a fraction w of the way between a and c, and x be an additional fraction z beyond b:

$$w = \frac{b - a}{c - a}, \tag{5.85}$$

$$z = \frac{x - b}{c - a}. \tag{5.86}$$

The next bracketing segment will either be of length $w + z$ relative to the current (if $c \to x$) or $1 - w$ (if $a \to b$). To minimize the number of guesses, pick a point x that makes these lengths equal, or

$$z = 1 - 2w. \tag{5.87}$$

An optimal choice x satisfies Eq. 5.87. Presumably though, the previous point picked, b, was also chosen optimally, so that the length of $b - a$ relative to $c - a$ is the same as that of $x - b$ relative to $c - b$:

$$\frac{b - a}{c - a} = \frac{x - b}{c - b},$$

$$w = z\frac{c - a}{c - b},$$

$$w = \frac{z}{1 - w}. \tag{5.88}$$

Together, Eqs. 5.87 and 5.88 combine into a quadratic equation for w:

$$w^2 - 3w + 1 = 0, \tag{5.89}$$

which can be solved for $w < 1$

$$w = \frac{3 - \sqrt{5}}{2} = 2 - \phi = (1 - \phi)^2 \approx 0.38197 \tag{5.90}$$

$\phi = (1 + \sqrt{5})/2$ is the golden ratio, which appears frequently in natural systems with scale simi-larities (such as Nautilus shells). It's role is similar in the minimization algorithm. To maintain the optimal scale similarity between successive bracketing choices, a point b should be chosen to lie a relative amount of $2 - \phi$ from the point a and a relative distance $\phi - 1$ from point c. Then x would be in the same relative positions on (b, c) and so on, producing an optimal bracketing algorithm. Even if the inital point b does not satisfy $w = 2 - \phi$, the algorithm converges quickly to picking the optimal ratios for future guesses.

The `TGYRO` implementation of the golden ratio section begins with an initial guess based on the parabolic interpolation for $\lambda = 1$, $\lambda_0 = R_0/(R_1 + R_0)$, and continues squeezing the bracketing region $(\lambda_a, \lambda_{k+1}, \lambda_c)$ until $|\lambda_a - \lambda_c| < 0.01$ or until $\mathcal{G}(\lambda_{k+1}) < \mathcal{G}(0)\left[1 - 1 \times 10^{-4}\lambda_k\right]$. The end points are λ_a and λ_c. λ_b lies between them and $\lambda_x = \lambda_{k+1}$ is the new guess. The full algorithm presented in Algorithm 5.5 switches the end points' order to always use the factor $b + w(c - a)$, instead of $b \pm w(c - a)$, depending on whether one should search to the right or left of the center point. The result is the same.

Like the parabolic backtracking method, the golden section search can be implemented into either a pure Newton iteration, by replacing the lines of code following line 6 in Algorithm 5.1, or in a Levenberg-Marquardt iteration, with the loop beginning at line 6 of Algorithm 5.4, replaced with the golden section code following line 6 in Algorithm 5.5.

5.2.4   Summary of new `TGYRO` algorithms

The previous section developed new algorithms for the steady-state transport solver `TGYRO`. These include a Levenberg-Marquardt minimization routine and two methods for line searches: parabolic backtracking and a golden section search.

`TGYRO` now has two methods of calculating a search direction: pure Newton iteration and Levenberg-Marquardt square residual minimization, which blends Newton with steepest-descent.

Algorithm 5.5 Golden ratio section search returns best step in direction $\delta \mathbf{z}$ from $\mathbf{z}^0$.

Input: $\mathbf{z}^0$, $\delta \mathbf{z}$, $\Delta z_{\max}$, $k_{\max}$, $k = 0$, $\phi = \left(1 + \sqrt{5}\right)/2$
Output: $\mathbf{z}^{best}$

1: $R^0 \leftarrow R(\mathbf{z}^0)$
2: $R^{best} \leftarrow R^0$, $\mathbf{z}^{best} \leftarrow \mathbf{z}^0$
3: $\lambda \leftarrow \min \left(1, \Delta z_{\max}/\max_j |\delta z_j| \right)$
4: $\mathbf{z}^{new} \leftarrow \mathbf{z}^0 + \lambda \delta \mathbf{z}$ # First step
5: $R^1 \leftarrow R\left(\mathbf{z}^{new}\right)$
6: **if** $R^1 < R^{best}$ **then**
7:     $R^{best} \leftarrow R^1$, $\mathbf{z}^{best} \leftarrow \mathbf{z}^{new}$
8: **end if**
9: **if** $R^1 < R^0 \left(1 - 0.29\lambda\right)$ **then**   # Step is ok. Don't backtrack.
10:     **return** $\mathbf{z}^{best}$
11: **end if**
12: $\lambda_a \leftarrow 0$, $\lambda_c \leftarrow 1$ # Initial end points
13: $\lambda_b \leftarrow R^0/(R^0 + R^1)$ # Parabolic first center point
14: $\mathbf{z}^b \leftarrow \mathbf{z}^0 + \lambda_b \delta \mathbf{z}$
15: $R^b \leftarrow R\left(\mathbf{z}^b\right)$
16: $\lambda_{old} \leftarrow \lambda_b$
17: **if** $R^b < R^{best}$ **then**
18:     $R^{best} \leftarrow R^b$, $\mathbf{z}^{best} \leftarrow \mathbf{z}^b$
19: **end if**
20: **while** $R^1 > R^0 \left(1 - 10^{-4}\lambda_{old}\right)$ **and** $|\lambda_a - \lambda_c| > 0.01$ **and** $k < k_{\max}$ **do**
21:     $\lambda_x \leftarrow \lambda_b + (1 - \phi)^2 \left(\lambda_c - \lambda_b\right)$ # New optimal center point
22:     $\mathbf{z}^{new} \leftarrow \mathbf{z}^0 + \lambda_x \delta \mathbf{z}$
23:     $R^1 \leftarrow R\left(\mathbf{z}^{new}\right)$
24:     **if** $R^1 < R^b$ **then**   # min between b and c, new triplet: (b, x, c)
25:        $\lambda_a \leftarrow \lambda_b$
26:        $\lambda_b \leftarrow \lambda_x$
27:        $R^b \leftarrow R^1$
28:     **else**   # min between a and x, new triplet: (x, b, a)
29:        $\lambda_c \leftarrow \lambda_a$
30:        $\lambda_a \leftarrow \lambda_x$
31:     **end if**
32:     **if** $R^1 < R^{best}$ **then**
33:        $R^{best} \leftarrow R^1$, $\mathbf{z}^{best} \leftarrow \mathbf{z}^{new}$
34:     **end if**
35:     $\lambda_{old} \leftarrow \lambda_x$, $k \leftarrow k + 1$
36: **end while**
37: **return** $\mathbf{z}^{best}$

This could be useful in regions where the Newton approximation breaks down, far from roots, to find a descent direction. Closer to a root, the algorithm dynamically switches to prefer the Newton direction, in an attempt to blend problem robustness (steepest-descent) with quick convergence (Newton).

Once a search direction is determined, should the global residual not decrease satisfactorily, the search vector can attempt to shrink to compensate. This may be useful near marginal stability, where slight overshoots in the search can lead to large errors in fluxes.

A final point is that the new methods focus on minimizing the global residual R, allowing for individual values of R_j to increase while searching for the solution. In so doing, a search direction, once found, is never altered: line searches only scale the magnitude of the search vector. Another difference with these algorithms is that they will never take a step that increases the global residual.

While a silver bullet is unlikely to exist for all transport problems, the new tools presented herein allow for greater flexibility when searching for stubborn solutions in a complex global problem. We now turn to a few examples to test these new methods.

5.3   Testing the new algorithms

Ultimately the feasibility of solving the transport problem comes down computational cost. Each evaluation of the function $\mathbf{F} = \mathbf{Q} - \mathbf{Q}^T$, corresponds to $N = N_{radii} \times N_{profiles}$ independent flux calculations. When using GYRO as the flux driver, these could each be a turbulence calculation. This has staggering implications: each new evaluation of the Jacobian requires N^2 flux calculations. Each new guess on a line search is another N. A successful root-finding algorithm will minimize the total number of calls to the flux driver, so a balance must be struck between speed and reliability. A quickly-converging method minimizes the number of iterations by moving towards the root as quickly as possible. A reliable root finder will always move towards the nearest root, instead of wandering in an alternate direction.

To determine how the new algorithms compare, we apply them to a few test problems from the NSTX and DIII-D machines, monitoring both the total number of turbulence calculations and the residual of the final converged solution.

5.3.1   Test Problems

As a test of the new algorithms we pick three steady-state transport problems: an NSTX ETG problem, a DIII-D L-mode plasma and a DIII-D H-mode plasma. We use `TGLF` as the flux driver and monitor the total number of calls to `TGLF`. This serves as not only a test of the `TGYRO`-`TGLF` system, but also of the `TGYRO` iteration scheme itself. A method that doesn't converge to a solution using `TGLF` is unlikely to quickly converge using `GYRO` (unless, of course, `TGLF` doesn't accurately describe the problem at all and is missing the root entirely). Also, the relative simplicity of the `TGYRO`-`TGLF` system allows for transport simulations that require only a few processors, as opposed to a few thousand.

NSTX 124948, 0.3 seconds
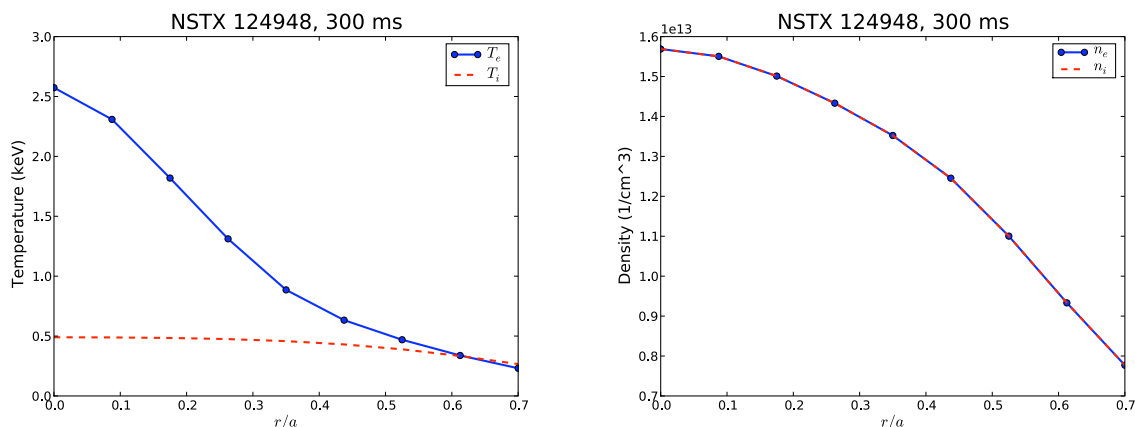
Figure 5.8: Electron and ion temperatures and densities for NSTX shot #124948 at 300 ms.
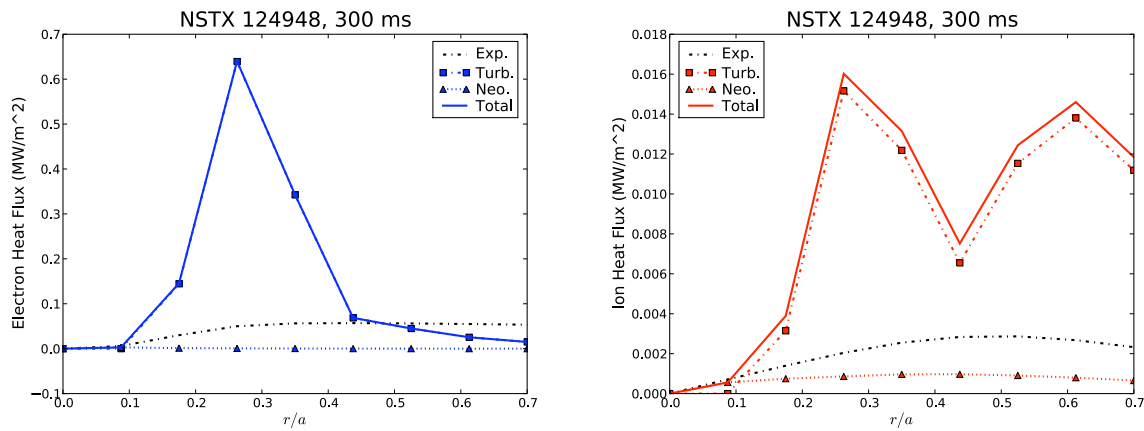
Figure 5.9: Electron and Ion Heat Fluxes for NSTX shot #124948 at 300 ms. The black dash-dot line indicates the experimental value, as calculated from `TRANSP`. The solid line is the sum of the `TGLF`-calculated turbulent flux (squares) and the `NEO`-calculated neoclassical flux (triangles), using the input temperature profiles.

The first test case for the new algorithms is NSTX shot number 124948 at 0.3 seconds, an R-F heated L-Mode with significant high-k fluctuations. Figure 5.8 shows the electron and ion temperature and density profiles at this time, while Fig. 5.9 shows the electron and ion heat flux profiles for these temperature and density profiles. For simplicity when testing the algorithms, we set $Z_{eff} = 1$ (and thus $n_e = n_i$), although `TGYRO` can more generally use multiple ion species, a feature used in Section 5.4. The heat fluxes shown include not only the experimentally measured value, as calculated from `TRANSP`, but also the turbulent and neoclassical fluxes as calculated by `TGLF` and `NEO`, respectively. These serve as essentially the baseline parameter, zeroth-iteration calculation from `TGYRO`. `TGYRO` will iterate on the temperature profiles to try and match the calculated (`TGLF`+`NEO`) fluxes with the target (`TRANSP`) fluxes. Since we are interested in turbulence driven by the electron temperature gradient, we will evolve only the electron temperature in this test up to $(r/a)_{max} = 0.7$.

An interesting thing to note about this problem is that `TGLF` significantly over-predicts the electron heat flux at the location of the peak gradients and under-predicts it near the edge of the

plasma. (The turbulence calculations of this shot in the previous chapter under-predicted the electron heat flux by a factor of two.) Also, in the core, $r/a < 0.1$, the measured, neoclassical and turbulent electron heat fluxes are all comparable. In fact, the magnitude of the neoclassical flux at $r/a = 0.0875$ is calculated to be much larger than the turbulent flux (1.2×10^{-2} vs. -3.2×10^{-5} ion gyroBohms). The interesting result, however, will be how the heat fluxes and temperature profiles compare after using `TGYRO` to attempt to match the `TRANSP` target fluxes and the `TGLF-NEO` fluxes.

DIII-D 128913, 1.5 seconds
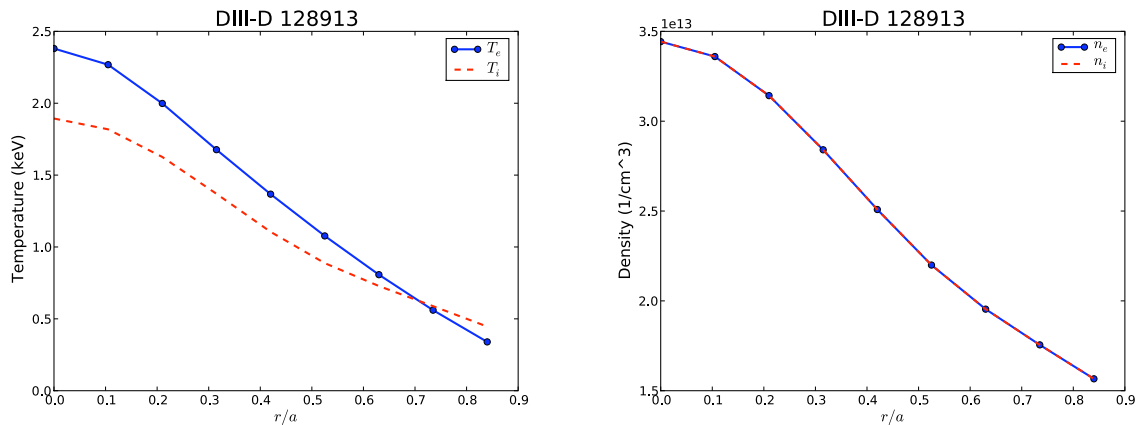
Figure 5.10: Electron and ion temperatures and densities for DIII-D shot #128913 at 1.5 s.

The next shot upon which to test the new `TGYRO` algorithms comes from the DIII-D tokamak. Shot 128913 at 1.5 seconds is an L-Mode discharge and one of the regression tests for `TGYRO` (`treg04`). For this case, we evolve T_e, T_i and n_e up to $(r/a)_{\max} = 0.84$, and use `TGYRO`'s implementation of the Hinton-Hazeltine Theory to calculate the neoclassical fluxes. Initial temperature, density and heat flux profiles are shown in Figs 5.10 and 5.11.
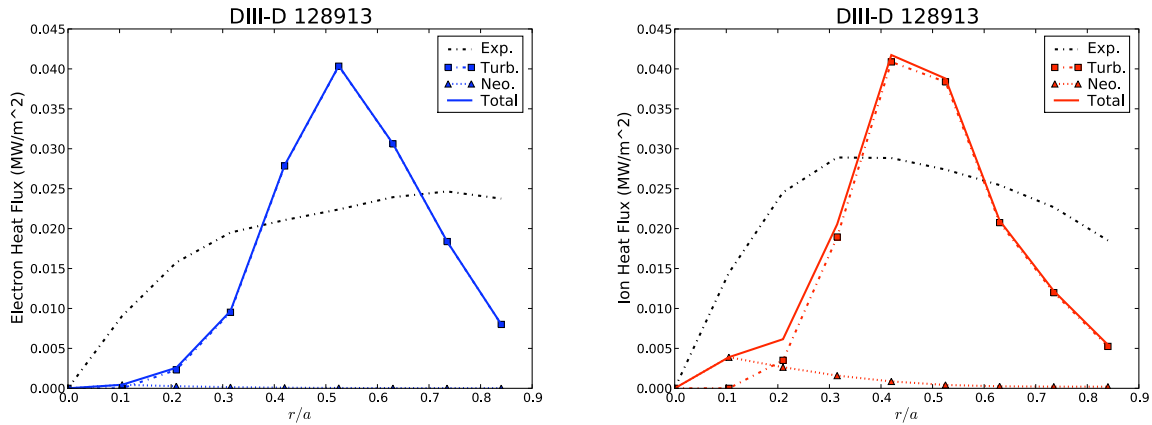
Figure 5.11: Electron and Ion Heat Fluxes for DIII-D shot #128913 at 1.5 s. The black dash-dot line indicates the experimental value, as calculated from `TRANSP`. The solid line is the sum of the `TGLF`-calculated turbulent flux (squares) and the Hinton-Hazeltine theory-calculated neoclassical flux (triangles), using the input temperature profiles.
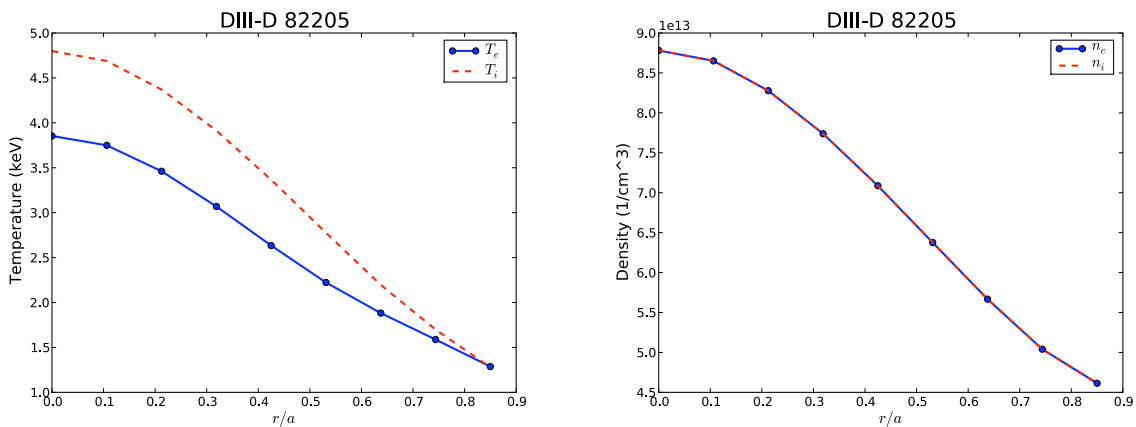
Figure 5.12: Electron and ion temperatures and densities for DIII-D shot #82205 at 2.5 s.
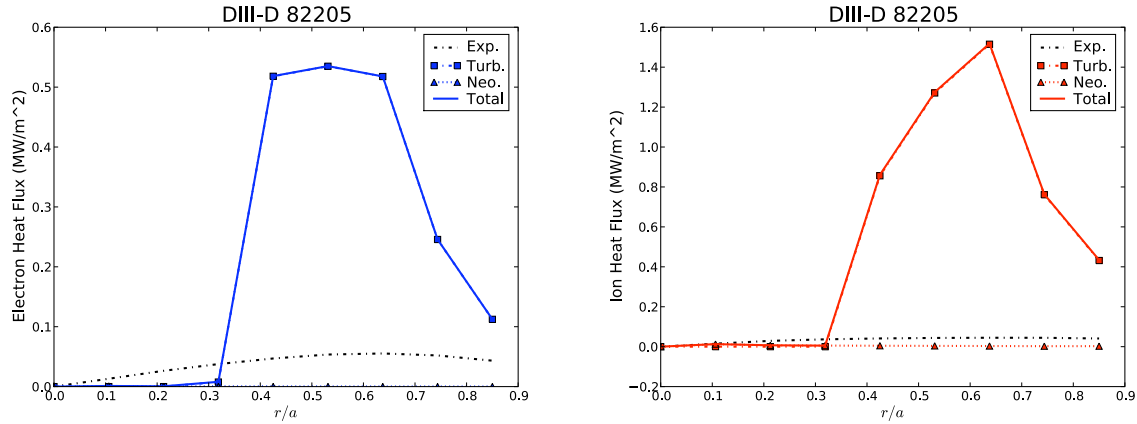
Figure 5.13: Electron and Ion Heat Fluxes for DIII-D shot #82205 at 2.5 s. The black dash-dot line indicates the experimental value, as calculated from `TRANSP`. The solid line is the sum of the `TGLF`-calculated turbulent flux (squares) and the Hinton-Hazeltine theory-calculated neoclassical flux (triangles), using the input temperature profiles.

DIII-D 82205, 2.5 seconds

The final test case for the new algorithms is DIII-D shot number 82205 at 2.5 seconds, whose temperature and density profiles can be seen in Fig. 5.12. This H-Mode shot shows a high core ion temperature. A key challenge for this case is that the core is nearly stable with respect to turbulent transport, as shown by the negligible levels of predicted flux from `TGLF` in Figure 5.13. In this case, we'll evolve T_e and T_i up to $(r/a)_{max} = 0.85$, to see if `TGYRO` can find a profile that account for the finite levels of flux in the plasma core.

For all of these test cases, we'll pick the reference radius for `TGYRO`, $r_\star$, as the furthest outward radial point in each domain. As in the original `TGYRO` work [120], we use a block-diagonal approximation to the flux part of the Jacobian, with a finite difference step size $\delta z/a = 1 \times 10^{-5}$ and $\Delta z_{max}/a = 1.0$ and limit ourselves to 100 iterations (Jacobian calculations) and 10 backtracking corrections per iteration, when backtracking ($k_{max} = 10$).

5.3.2   Finding Optimal Settings for Levenberg-Marquardt

The strength of the Levenberg-Marquardt algorithm comes from its active adjustment of its damping parameters. As such, the scaling factors for α (β and δ) directly impact the effectiveness of the method. A parameter scan in β and δ for the NSTX case might not only help determine some default values for β and δ but could also elucidate the sensitivity of the solution to these parameters.
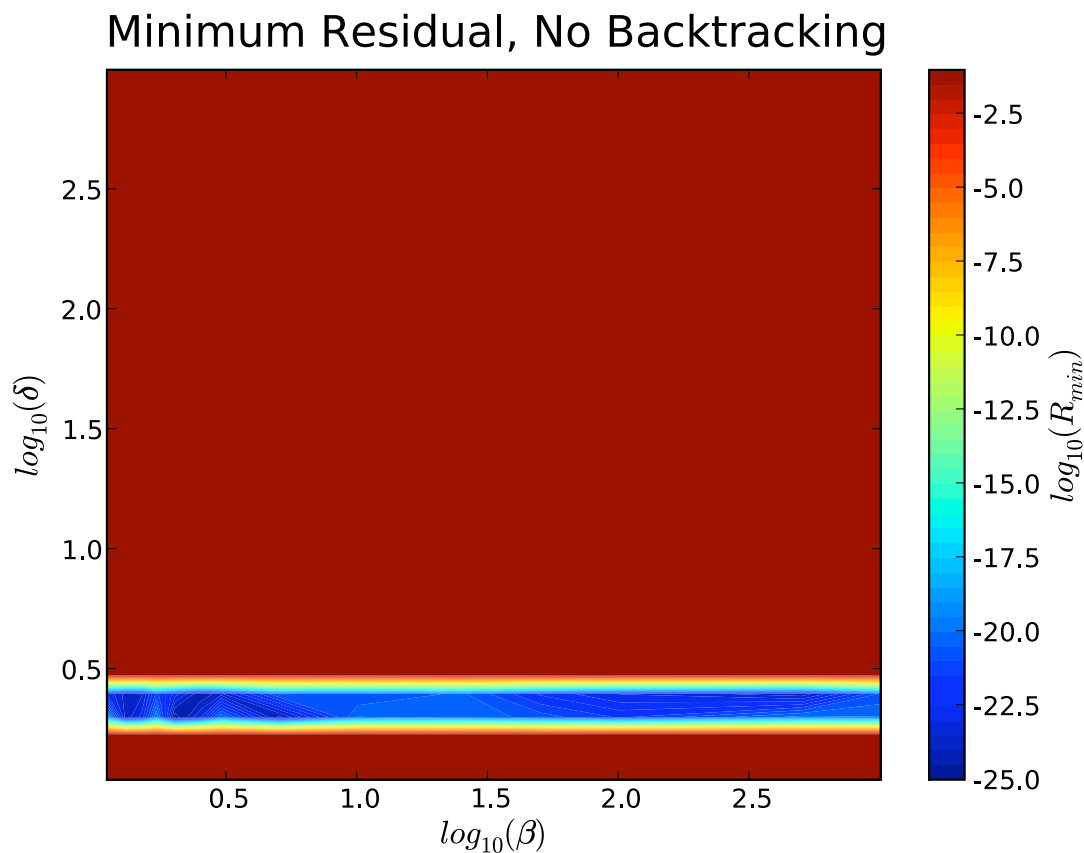
Figure 5.14: Contours of minimum residuals for a scan in β and δ for the NSTX test problem using the Levenberg-Marquardt algorithm without backtracking.

Figures 5.14 and 5.15 show the minimum global residual and the number of calls to `TGLF` to reach that minimum, respectively, for a scan in β and δ, using the Levenberg-Marquardt algorithm without any backtracking. A striking feature is that the total solution appears to be rather sensitive
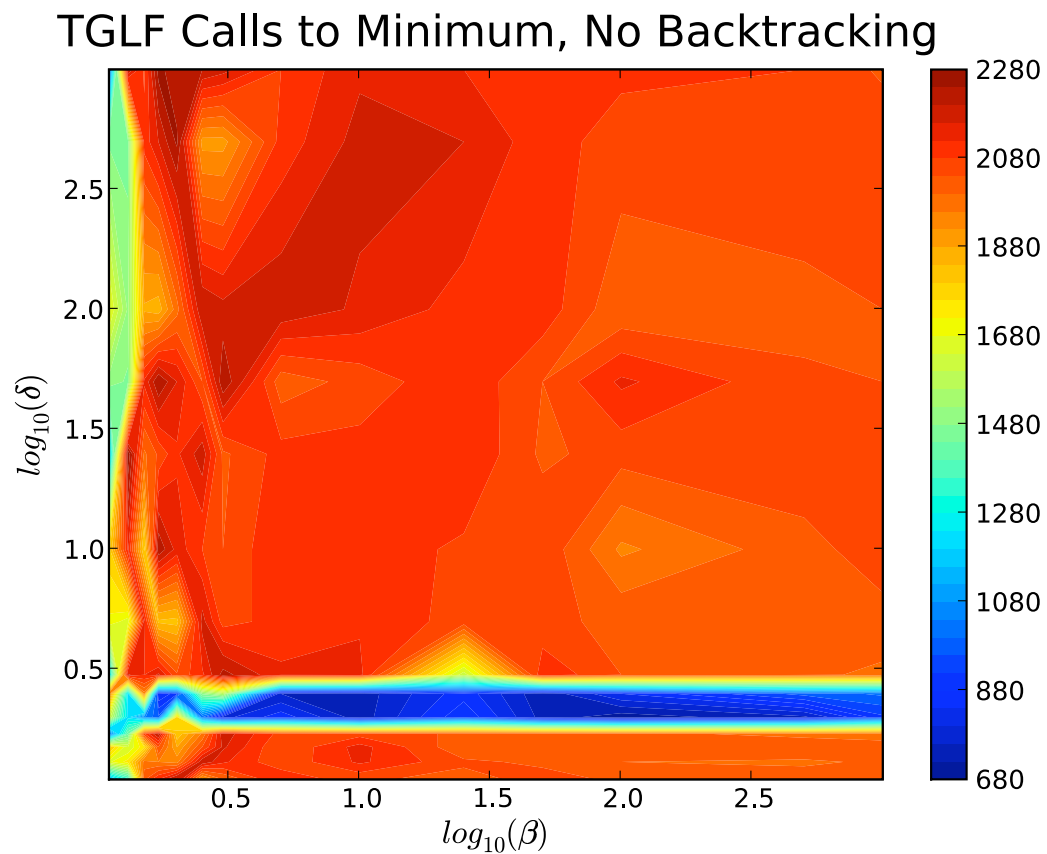
Figure 5.15: Contours of the number of calls to `TGLF` to reach the minimum global residual for a scan in β and δ for the NSTX test problem using the Levenberg-Marquardt algorithm without backtracking.

in δ, but not as much so in β, with the solution for low values of δ many orders of magnitude lower than the solution for higher values. Another interesting thing to note is that the minimum residual for the optimal parameters is $\sim 10^{-25}$. This is very small, and the algorithm can reach there in as few as ~ 700 calls to TGLF. The pure Levenberg-Marquardt algorithm is much more sensitive to the value of δ than of β, but, with the correct settings, can reach very low residual errors, very quickly. Since flux targets in gyrobohm units range from $\sim 10^{-2}$ in the core for this case to $\sim 10^2$ near the edge, a value of $R = 0.5\,(\mathbf{F} \cdot \mathbf{F}) = 10^{-25}$ corresponds to very small fractional errors: $\left(Q_0 - Q_0^T\right)/Q_0^T \sim 10^{-10}$, well below the uncertainties in experimental flux measurements.
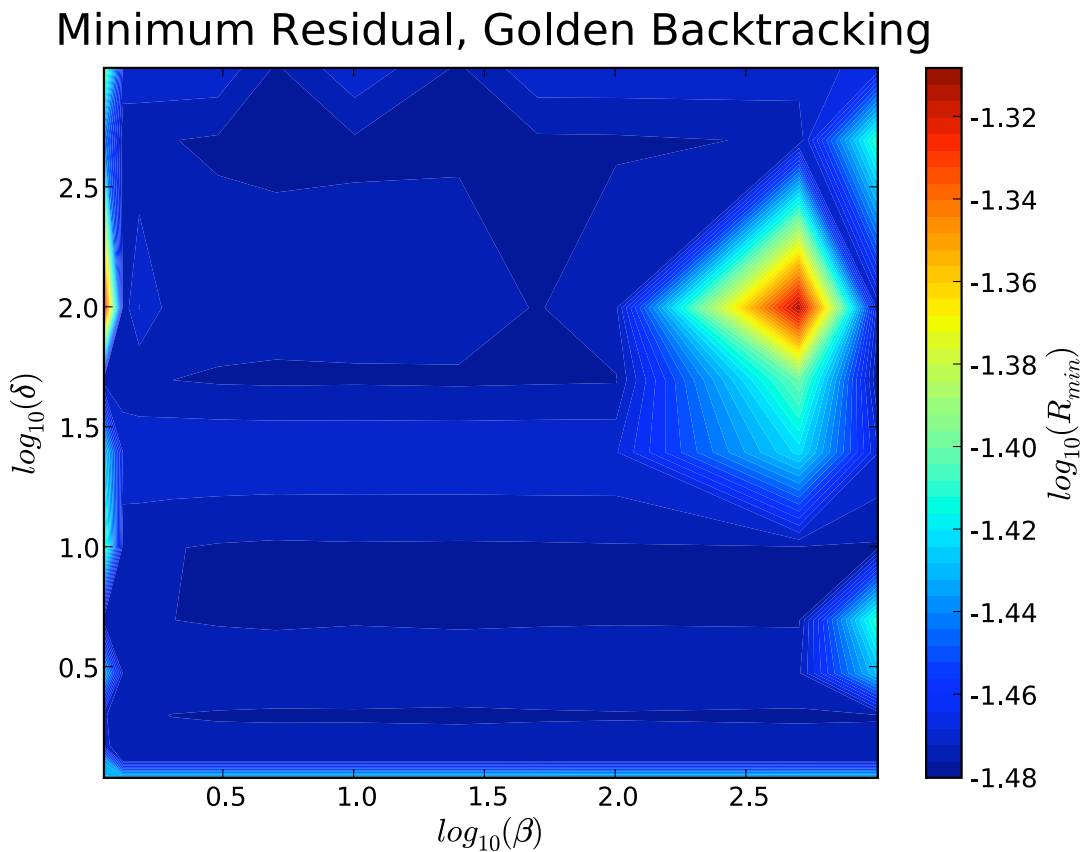
Figure 5.16: Contours of minimum residuals for a scan in β and δ for the NSTX test problem using the Levenberg-Marquardt algorithm with golden section search backtracking.
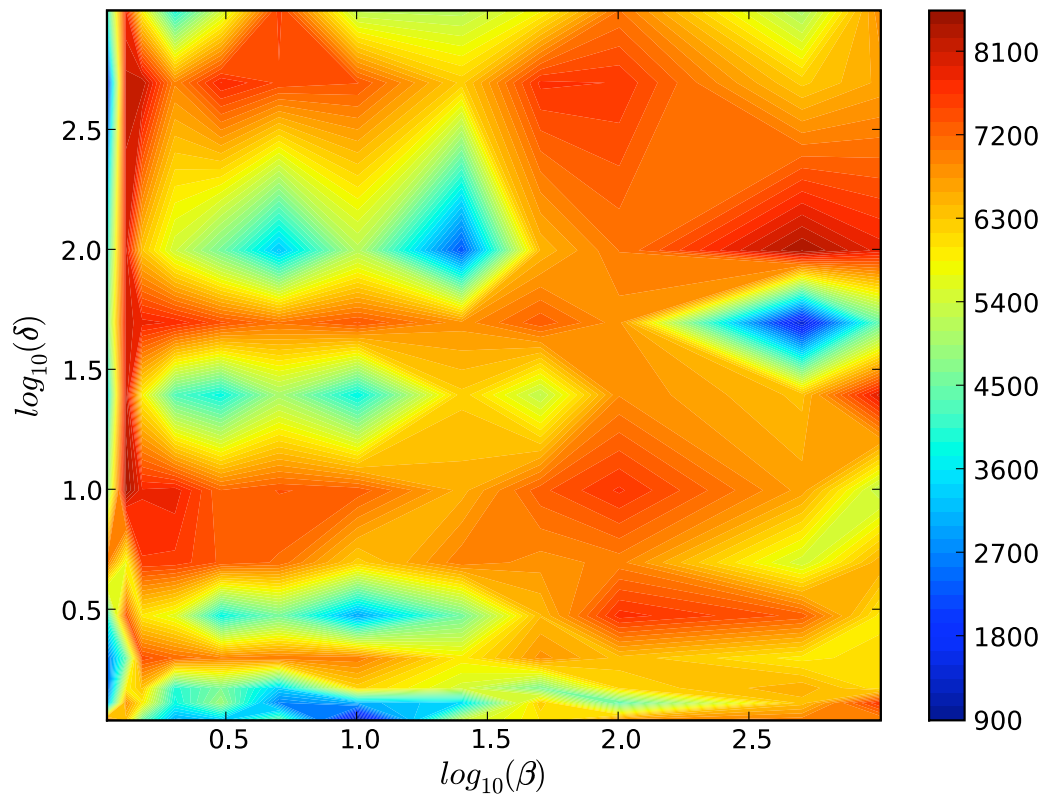
Figure 5.17: Contours of the number of calls to `TGLF` to reach the minimum global residual for a scan in β and δ for the NSTX test problem using the Levenberg-Marquardt algorithm with golden section search backtracking.
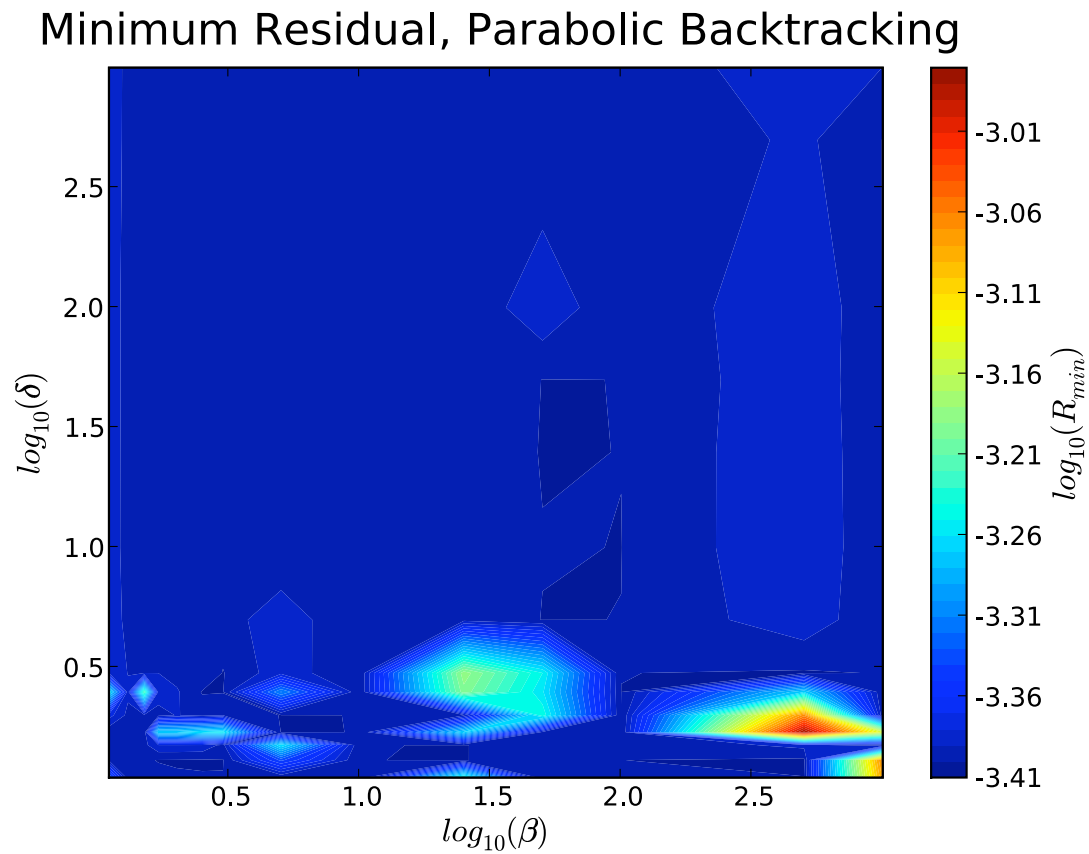
Figure 5.18: Contours of minimum residuals for a scan in β and δ for the NSTX test problem using the Levenberg-Marquardt algorithm with parabolic interploation backtracking.
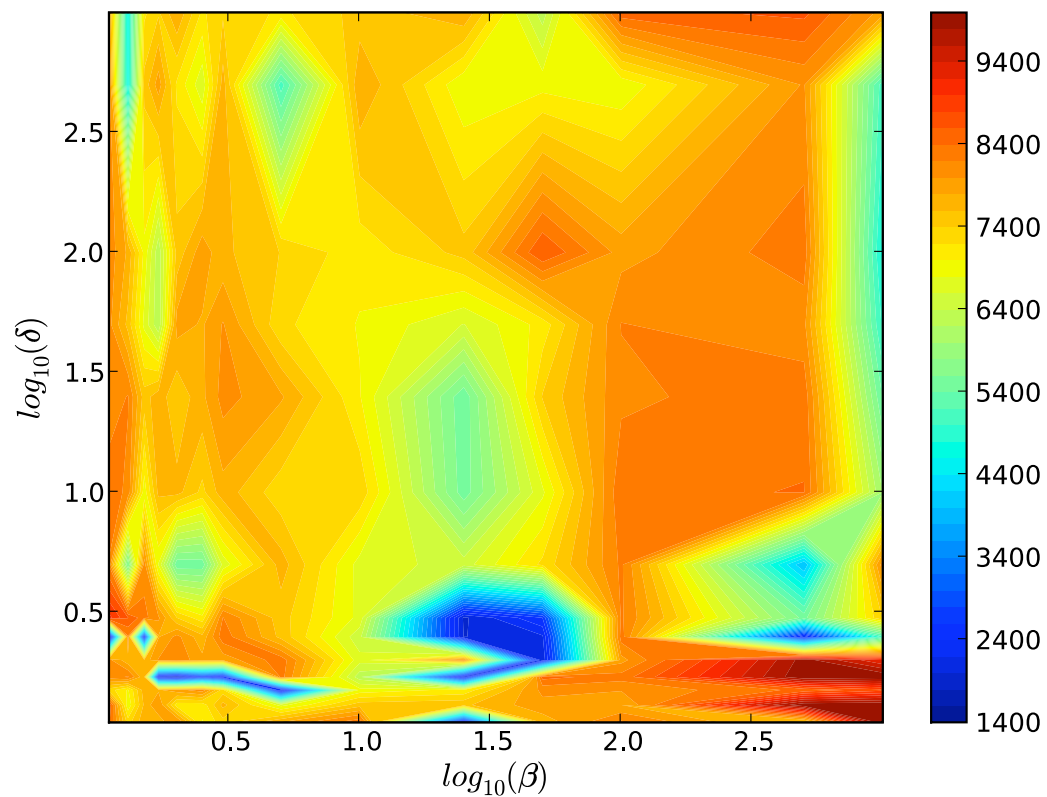
Figure 5.19: Contours of the number of calls to `TGLF` to reach the minimum global residual for a scan in β and δ for the NSTX test problem using the Levenberg-Marquardt algorithm with parabolic interpolation backtracking.

Adding backtracking to the Levenberg-Marquardt method changes the results. The sensitivity to β and δ is less pronounced for both golden section search and parabolic interpolation backtracking (Figs 5.16, 5.17 and 5.18, 5.19, respectively.) Furthermore, the final residual is much higher: the golden section search cannot reduce the residual beyond $\sim 10^{-1}$ and the parabolic line search cannot get below $\sim 10^{-3}$. The total number of calls to `TGLF` is also higher, as to be expected, since backtracking requires additional flux calls for each function evaluation along the search direction. Adding a line search to the Levenberg-Marquardt method does not appear in this case to improve either the efficiency or robustness of the solver. While other values of β and δ may yield some improvement, the uniform contours of the minimum residual suggest otherwise; although, some credit could be given to the fact that the golden section search only took ~ 900 flux calls to reach its solution for low values of δ.

We can draw some conclusions about the Levenberg-Marquardt algorithm from these tests. Based on the parameter scans in β and δ for the NSTX test problem, we choose $\beta = \delta = 2.5$ when using Levenberg-Marquardt. As to the question of whether or not to also use backtracking, it remains to be seen if in the other test cases it makes a difference. One complication when combining Levenberg-Marquardt with backtracking is that Levenberg-Marquardt changes not only the direction, but also the length, of the search vector. Since one never moves exactly in the Newton direction (as $\alpha > 0$), the assumption that one can always reduce the residual along the search direction (for sufficiently small step sizes) may not always hold. In cases like this, backtracking could needlessly add flux calls without improving the solution. Another possible conclusion is that the NSTX ETG problem has a local minimum that attracts the Levenberg-Marquardt iterator, making it difficult to find the global minimum: the ETG problem may just be very difficult. However, it is possible for the Levenberg-Marquardt method without backtracking to find a minimum with a very low global residual.

5.3.3   Algorithm Comparisons

To test the effectiveness of the new algorithms requires a broader ensemble of calculations, employing more than a single discharge. We now turn to a comparison of the `TGYRO` algorithms for not only the NSTX case used in the Levenberg-Marquardt parameter scan, but also the DIII-D L-Mode and H-Mode shots.

NSTX 124948, 0.3 seconds
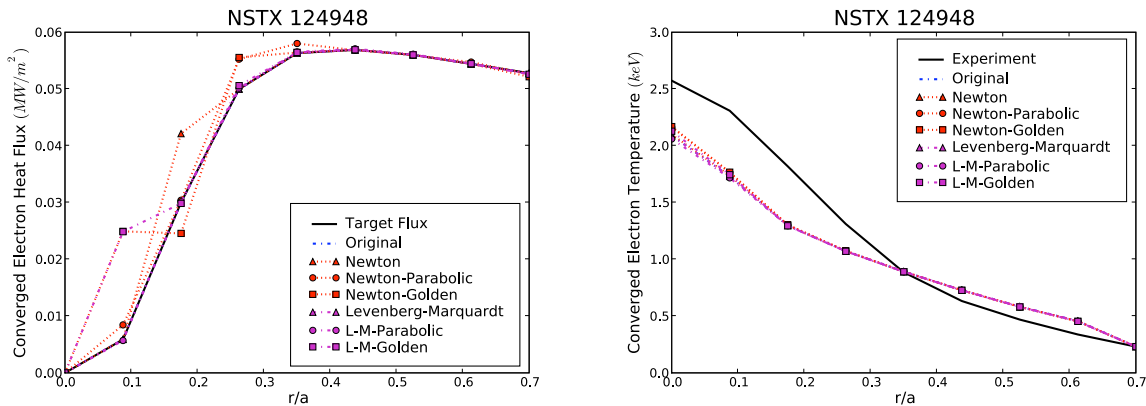
Figure 5.20: Converged electron heat fluxes (left) and temperatures (right) for the NSTX test case, using different algorithms after 100 `TGYRO` iterations. The solid black line is the experimental temperature profile or target heat flux. The solution using `TGYRO`'s original Newton-relaxation method is in blue dash-dot, without symbols. The red dashed lines are pure Newton methods, while the purple dashed-dotted lines are from Levenberg-Marquardt. Triangles represent no backtracking, while circles and squares indicate the parabolic interpolation and golden section search backtracking methods, respectively.

Figure 5.20 shows the electron heat fluxes and temperatures after 100 `TGYRO` iterations for the NSTX test case, using different iteration schemes. The solid black line is the experimental temperature profile or target heat flux. The solution using `TGYRO`'s original Newton-relaxation method is in blue dash-dot, without symbols. The red dashed lines are pure Newton methods, while the purple dashed-dotted lines are from Levenberg-Marquardt. Triangles represent no back-

tracking, while circles and squares indicate the parabolic interpolation and golden section search backtracking methods, respectively. Many of the methods' solutions overlap, making them hard to distinguish, but the Levenberg-Marquardt methods without backtracking and with parabolic backtracking overlay converge to the target heat flux at all radial points. The original method also does this, and the Newton methods are close, but not spot-on. While all methods have moved towards the target electron heat flux, matching much better than the pre-iterated solution in Fig. 5.11, they have not all yet converged to the target flux.

However, this variability in heat flux translates to small differences in temperature profiles. The electron temperatures all match to within 10% or so, and this variability is almost entirely confined to the inner two points in the plasma. All methods appear to be converging on the same electron temperature profile, which has a lower core electron temperature than the experimental method. This may be due to the forced quasineutrality constraint in the TGYRO simulation, with $n_e = n_i$ and no impurities, $Z_{eff} = 1$, while the experimental case likely has $Z_{eff} \sim 2.5$. If the ETG mode is governing this shot, it stands to reason that altering Z_{eff} can change the temperature profile, a phenomenon we'll explore with TGYRO later in this Chapter. The small differences in temperature profiles correlating with larger variability in heat fluxes further supports the idea of stiff electron transport.

Yet while these profiles appear to nearly match, the different algorithms have very different global residuals. Figure 5.21 shows the total global residual, $R = (\mathbf{F} \cdot \mathbf{F})/2$, as a function of the total calls to TGLF. The pure Levenberg-Marquardt method reaches a residual of $\sim 10^{-25}$. The original TGYRO method closely tracks the Levenberg-Marquardt method until below $\sim 10^{-23}$. At this point, however, it takes a step that increases the global residual by many orders of magnitude and continues to bounce around a solution with residual of $\sim 10^{-9}$. The pure Newton method, without backtracking, is the next closest solution, but appears to be stuck bouncing between two points around $R \sim 10^{-3}$. Unlike the pure Newton and the original Newton-Relaxation techniques,
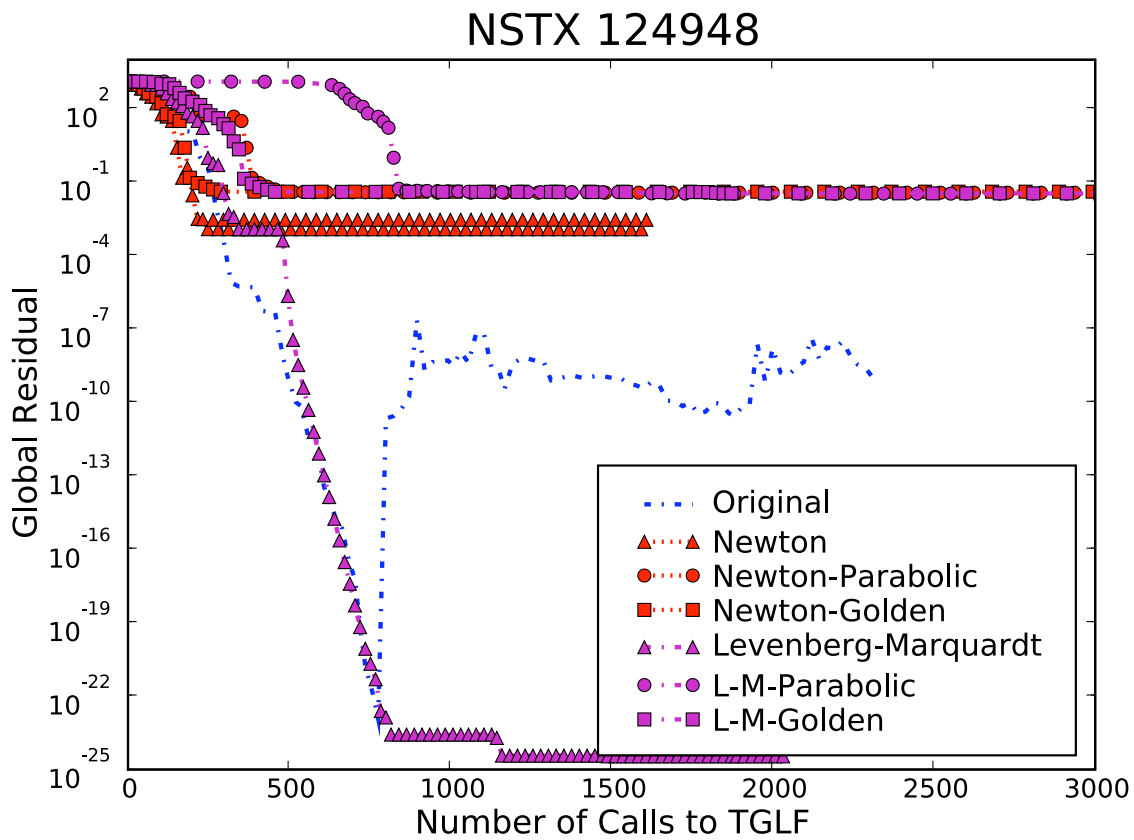
Figure 5.21: Global residual as a function of cumulative calls to `TGLF` for the NSTX test case, using different iteration methods.

no other method can take a step that increases the global residual. The rest converge to solutions with total global residual $\sim 4 \times 10^{-2}$.

In the NSTX test case, evolving only T_e in an attempt to match $\mathbf{Q}_e$ and $\mathbf{Q}_e^T$, the Levenberg-Marquardt method performs the best, by reaching the lowest total residual in the fewest number of calls to the flux driver. Neither the backtracking nor Levenberg-Marquardt methods take a step that increases the global residual, instead trying to alter the step direction and length until a suitable one is found. The pure Newton and the original Newton-Relaxation techniques, however, can, and do, take steps that increase the total global residual. In the case of the original scheme, a single misstep increases the error in the solution by many orders of magnitude. Each method finds a different local minima for the residual. The backtracking methods cannot find their way out of their minima, even after a few thousand different flux calls. The Levenberg-Marquardt-backtracking schemes are searching in a nearly steepest-descent direction at the end of the simulation, and still cannot find a suitable next step. The original and pure Newton methods bounce around a solution, with some steps increasing the residual, and others decreasing it. However, despite these orders-of-magnitude differences in global residual, the electron temperature profiles all match to within a few percent, reaffirming the notion of stiff transport.

DIII-D 128913, 1.5 seconds

The agreement amongst the different algorithms is even tighter for the DIII-D L-Mode case, that evolves both ion and electron temperatures and the electron density, in an attempt to match heat and particle fluxes. Figure 5.22 shows the fluxes (left) and profiles (right) after 100 iterations for the different iterative methods. The electron heat channel (top) and the ion channel (middle) show overlapping profiles and fluxes for all of the methods, although the electron heat flux at $r/a \approx 0.2$ is slightly lower for the pure Newton method. Each method matches the target heat fluxes very well, and the corresponding temperature profiles are near identical, with no visible difference between the methods' solutions, which each predict higher core temperatures than seen in the experiment.
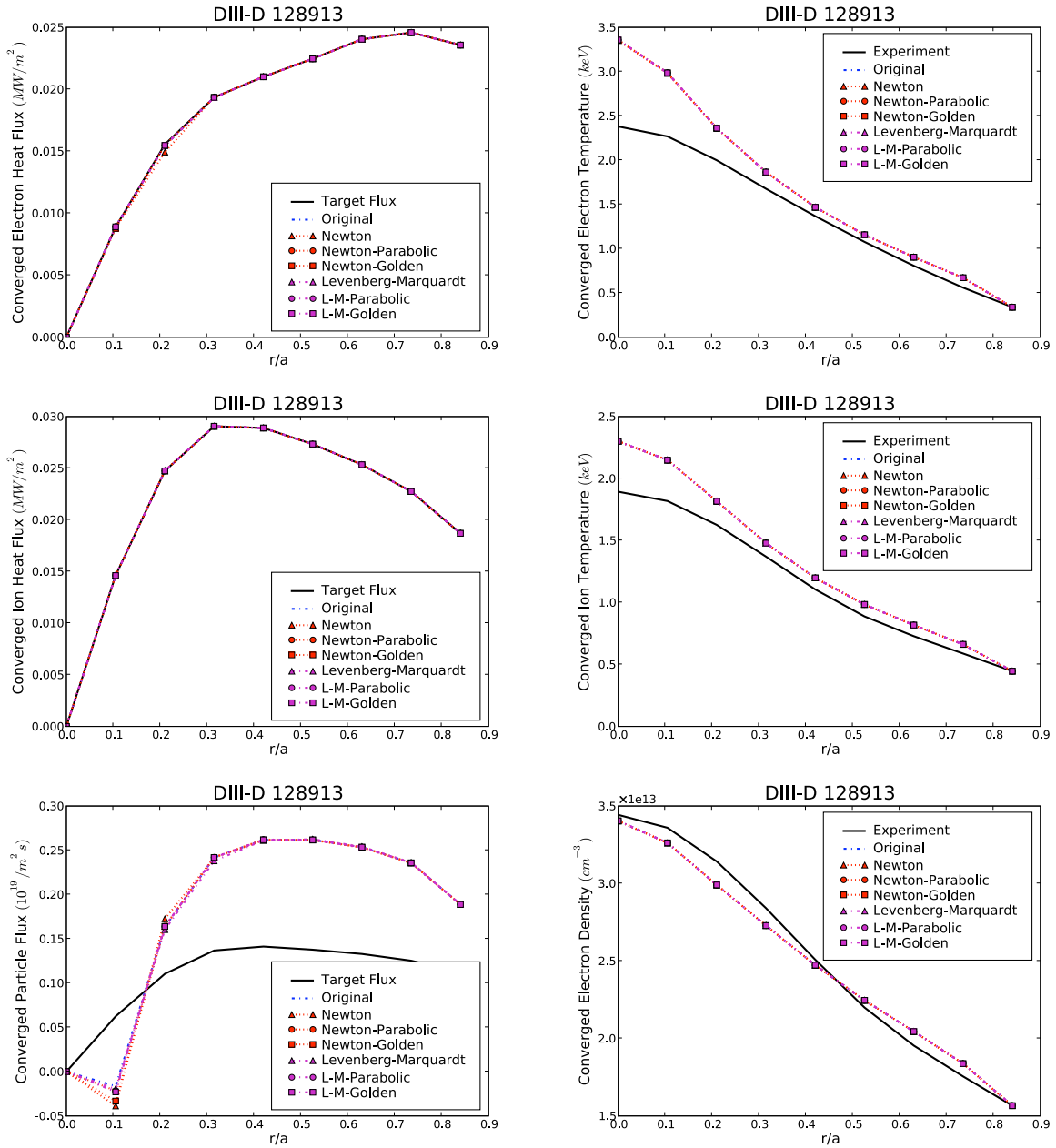
Figure 5.22: Converged fluxes (left) and profiles (right) for the DIII-D L-Mode test case, shot 128913, evolving both electron and ion temperatures and electron density, for different algorithms.
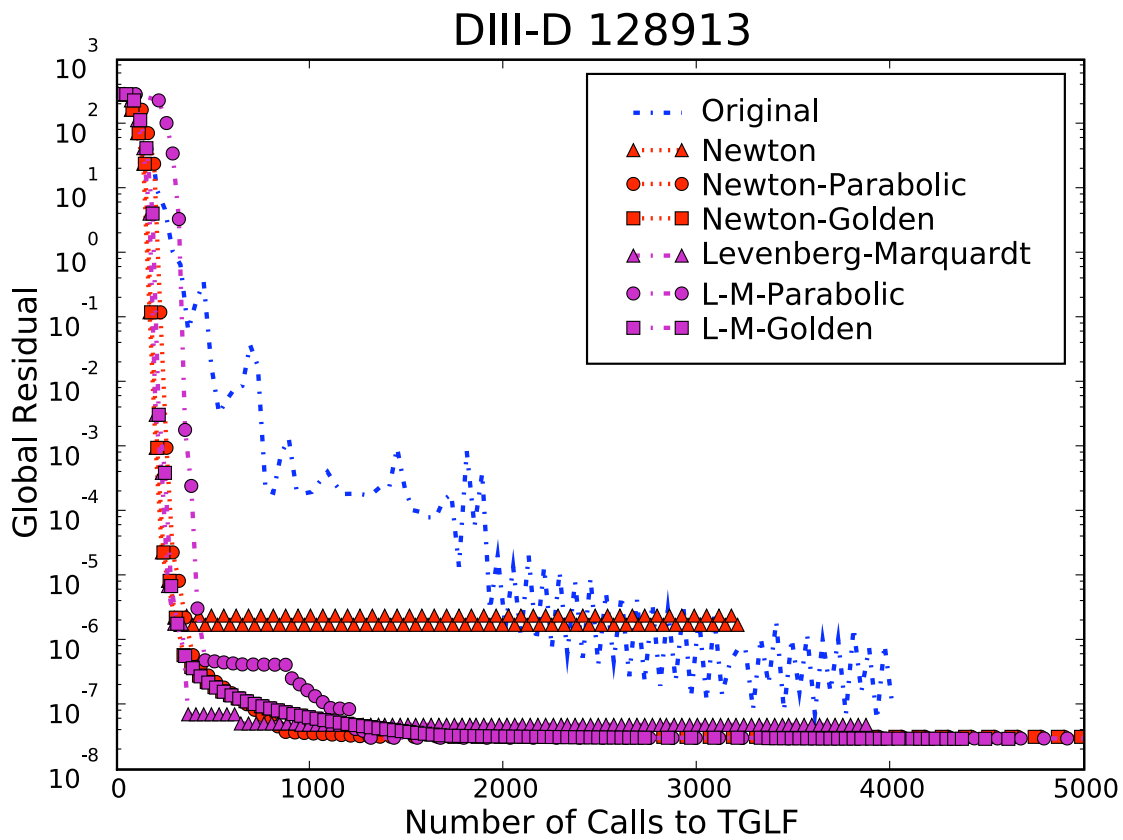
Figure 5.23: Global residual as a function of cumulative calls to TGLF for the DIII-D L-Mode test case, using different iteration methods.

However, the electron particle flux (bottom) does not match the target flux very well at all. Each method is converging to a flux profile that has roughly twice the target flux in the mid radius. Furthermore, they each predict a negative particle pinch at $r/a \approx 0.1$. Even still, the density profiles are very close to the experimental value. The time behavior of the residual shown in Fig. 5.23 is reminiscent of the NSTX results. The plain Newton method is stuck oscillating between two points, while the original method can take steps that increase the global residual, although in this case the trend is still downward. The Levenberg-Marquardt and Newton with backtracking methods converge the quickest and to the lowest residual, while never taking a step that makes the solution worse. Since the heat fluxes match extremely well, it suggests that the turbulent flux is preferentially controlled by the temperature profiles. Again, despite the differences in residual, the predicted temperature and density profiles match each other very well.

The new `TGYRO` algorithms behave similarly on the DIII-D L-Mode test case as they do the NSTX test case. The Levenberg-Marquard methods reach the lowest residual the quickest, and the Newton-with-backtracking schemes follow suit. None of these methods take steps that increase the residual. Little difference exists in the converged temperature and density profiles below global residuals of $\sim 10^{-6}$. The backtracking and Levenberg-Marquardt methods reach this residual level in under 500 calls to `TGLF`. The original `TGYRO` method takes over 2000 calls, and the pure Newton method never gets below $R = 10^{-6}$. Although no method matches the target particle flux, adjusting the Levenberg-Marquardt parameters β and δ may help these methods to converge, as was the case for NSTX. Another possibility is that the particle flux dynamics are not accurately modeled by `TGLF` for this case. In either case, the new algorithms converge to the found solution very quickly.

DIII-D 82205, 2.5 seconds

The final test for the new algorithms is a DIII-D H-Mode, shot #82205 at 2.5 seconds, in which we evolve the electron and ion temperatures. For this case, the non-iterated `TGLF` solution sig-

nificantly over-predicts both the ion and electron heat fluxes, as shown in Fig. 5.13. While the
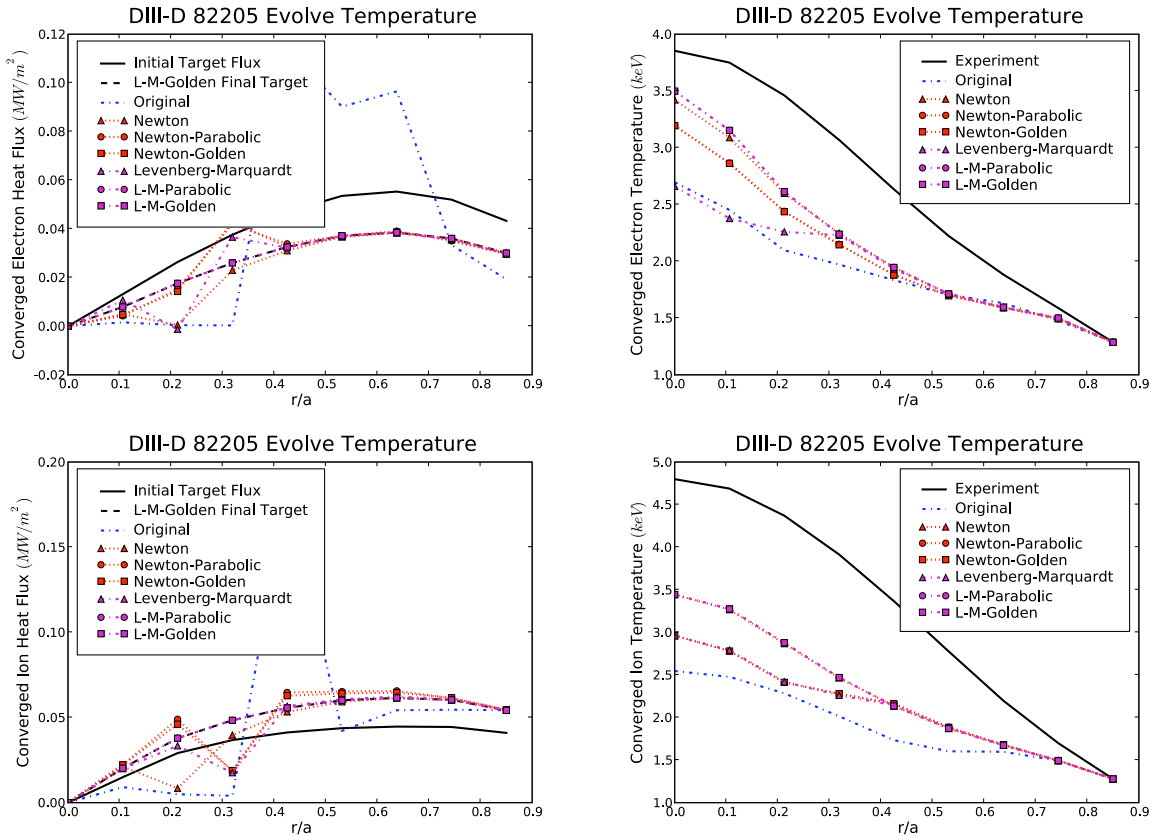
Figure 5.24: Converged fluxes (left) and profiles (right) for the DIII-D H-Mode test case, shot 82205, evolving the electron and ion temperatures, for different algorithms. In the electron flux plot (top left), the solid black line is the initial target flux for each algorithm. The dashed black line is the target for the Levenberg-Marquardt with golden section search algorithm after iterating.

pre-iterated profiles have $T_i > T_e$, the converged temperature profiles, shown in Fig. 5.24 with the

corresponding heat fluxes, appear to have $T_i \sim T_e$. Another interesting fact is that the algorithms

do not agree as to the solution nearly as well as they did for the previous test cases. Furthermore,

the heat flux profiles are not converging to the initial target flux. The solid black in in the heat flux

plots in Fig. 5.24 represents the target heat flux at iteration 0. The dashed black line, however, is

the target heat flux for the Levenberg-Marquardt-golden-section-search (L-M-Golden) method at

iteration 100. The fact that these are different is interesting, but not entirely unexpected. As illus-

trated in Eq. 5.9, since `TGYRO` solves for fluxes in gyro-Bohm normalized units, both the transport
and target fluxes are functions of the gradients. In this case, as the L-M-Golden method changed
the gradients, it changed not only the calculated transport fluxes, but also the target fluxes. That
is, `TGYRO` is shooting at a moving target, so to speak. The L-M-Golden method honed in on one
target flux and found a profile that matched it.
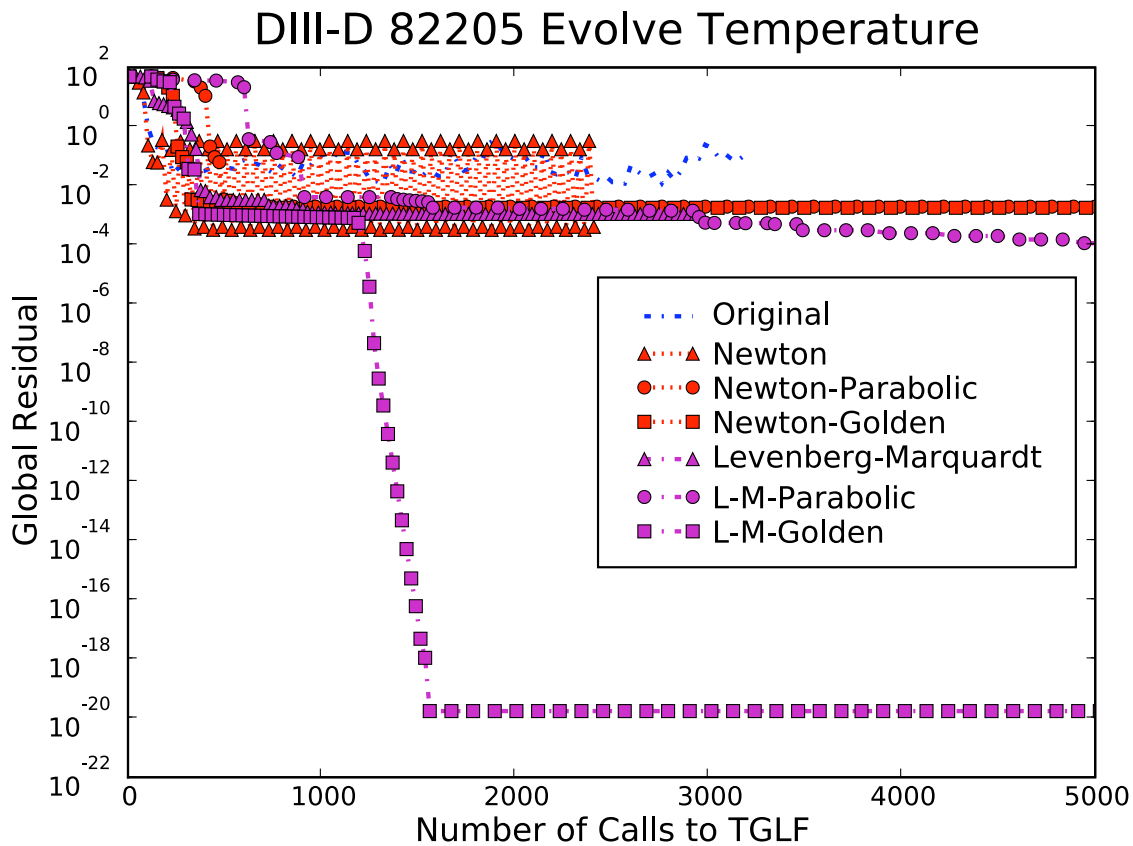
Figure 5.25: Global residual as a function of cumulative calls to `TGLF` for the DIII-D H-Mode
$T_e - T_i$ test case, using different iteration methods.

It is import to emphasize, however, that the solution found by the L-M-Golden method does in
fact solve the transport equations. Although, with core electron and ion temperatures each at about
3.5 keV and a higher (lower) ion (electron) heat flux, the profiles look more like those of the DIII-D
L-mode shot than of the H-mode initial conditions. Figure 5.25, the global residual as a function

of total calls to `TGLF`, confirms that the L-M-Golden solution solves the steady-state transport equations very well, finding a solution whose global residual is roughly 10^{-20}. Like the other test cases, the pure Newton and original methods take steps that increase the global residual, and the pure Newton method oscillates between a few solutions (in this case, four). None of the new methods increases the residual, and it appears as though both the Levenberg-Marquardt method with and without parabolic backtracking are still converging to a solution.
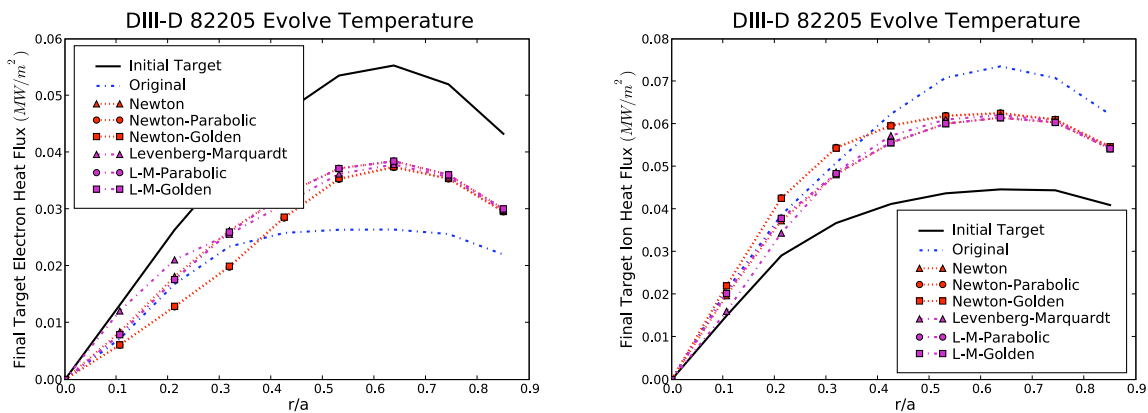
Figure 5.26: Target electron and ion heat fluxes at the end of 100 iterations for the different methods on the DIII-D H-Mode test case, evolving T_e and T_i. The solid black line is the target flux prior to iterating on the profiles.

While the H-Mode test case also shows that the new methods can converge to a transport solution relatively quickly, it also demonstrates the difficulty of this problem. Since both the transport and target fluxes are functions of the local gradients, as the iteration scheme changes the plasma profiles, it also can change the solution it's looking to match. Figure 5.26 shows the initial and final target fluxes for each of the tested algorithms. Every algorithm is searching for a solution with more ion heat flux and less electron heat flux than that of the initial target.

One possible explanation for the moving target phenomenon is that the H-Mode solution represented by the initial target fluxes does not exist for or cannot be captured by the currently employed transport model (evolving T_i and T_e with `TGLF` and the Hinton-Hazeltine neoclassical theory).
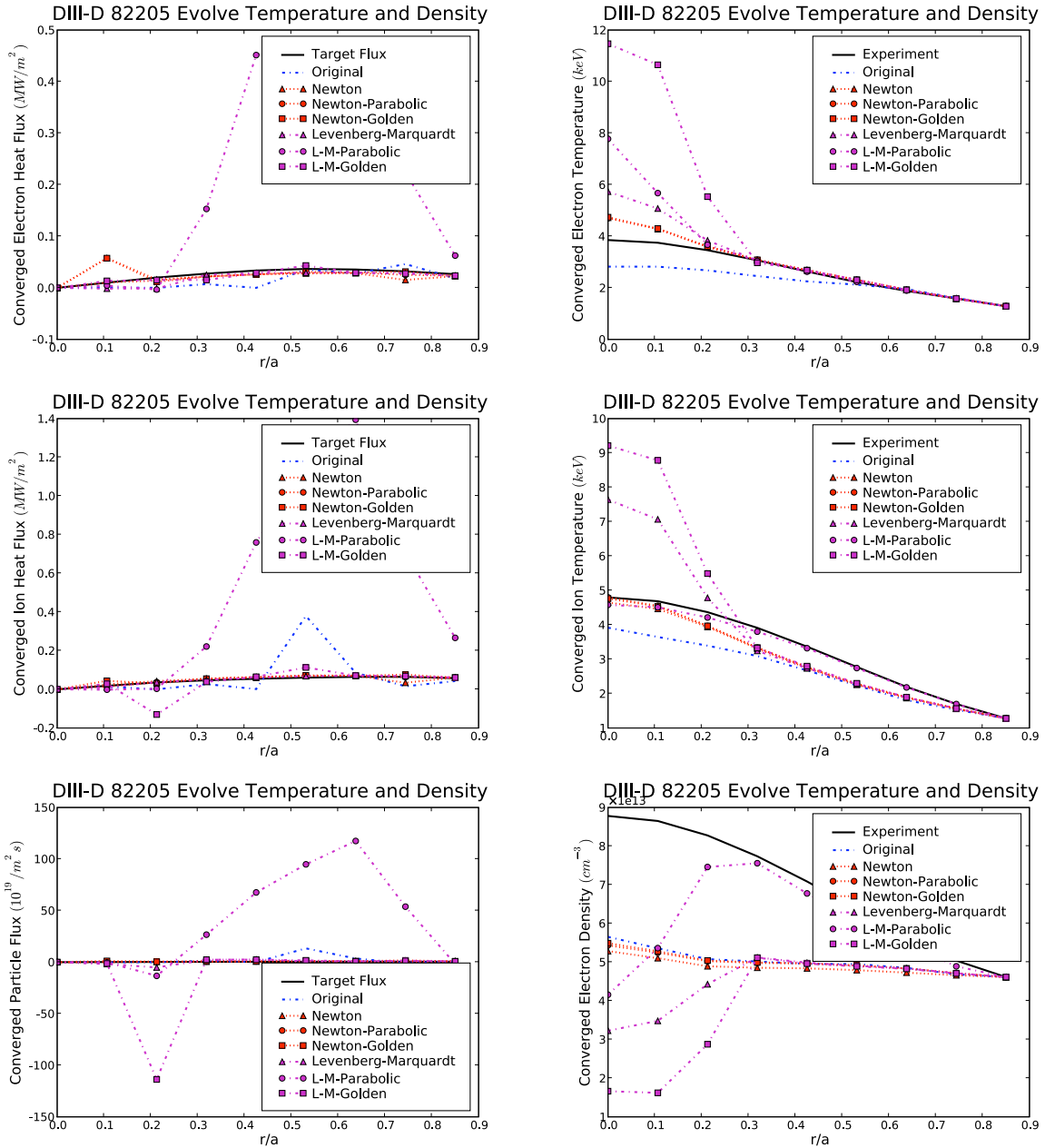
Figure 5.27: Fluxes (left) and profiles (right) for the DIII-D H-Mode test case, shot 82205, evolving both electron and ion temperatures and electron density, for different algorithms after 100 iterations.
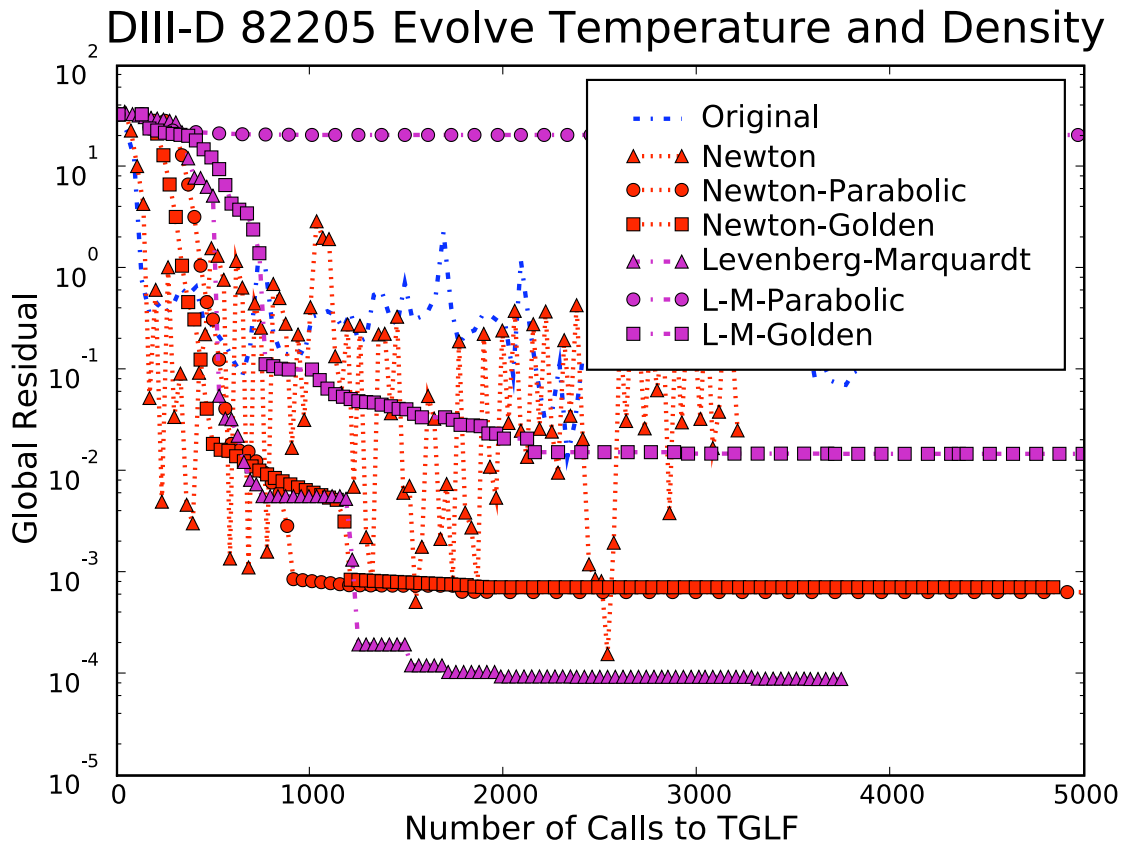
Figure 5.28: Global residual as a function of cumulative calls to `TGLF` for the DIII-D H-Mode case, evolving T_e, T_i and n_e, using different iteration methods.

Adding density evolution, however, does not improve the convergence, as in Figs. 5.27 and 5.28. The final residuals are not very good, with the best being $\sim 10^{-4}$, from the pure Levenberg-Marquardt method. While the algorithms may still be converging, the predicted profiles are very strange at this point, with flat and/or hollow density profiles and very strongly peaked core temperatures.

The DIII-D H-Mode test case displays some of the challenges in solving the formulated steady-state transport problem. Specifically, the target flux depends upon the local gradients and changes every iteration. The model problem examined earlier in this chapter already demonstrated the possibility of multiple solutions. Guaranteeing that an algorithm converges to the experimentally realized one is problematic.

However, the new algorithms, Levenberg-Marquardt minimization and backtracking, significantly improve TGYRO's ability to converge to a solution. In all test cases, the new methods converged to the lowest global residual without ever taking a step that increases it. Furthermore, they reach their solutions in fewer calls to TGLF than the original Newton-relaxation method. Since the performance of the Levenberg-Marquardt methods depend on the choices of damping parameters β and δ, they add flexibility to the algorithm. Cases that do not converge quickly may be helped by changing these values. The newly-implemented algorithms improve both the speed and robustness of the TGYRO transport solver, requiring fewer calls to TGLF than the original method and reaching solutions that better match the target and transport fluxes.

5.4 Transport Solutions for NSTX

Armed with a new algorithmic arsenal, we now predict some temperature profiles for the NSTX ETG test case and show not only how these predictions support the idea that the ETG mode is at work in NSTX but also some possible effects of attempting to mitigate that transport.

The shot in question is one of the first used to support the conclusion that high-k activity measures ETG transport. NSTX shot #124948 is an RF-heated discharge with a steep electron temperature gradient, linearly unstable to ETG. Recall from Fig. 5.20 that multiple iterative schemes converged to the experimental heat flux evolving T_e up $r/a = 0.7$. The predicted electron temperature in this case was slightly lower than the experimental value in the core (2.1 keV vs. 2.55 at $r/a = 0$) and slightly higher near the edge (0.45 vs. 0.3 keV at $r/a \approx 0.6$).

A solution can also be found by moving $(r/a)_{\mathrm{max}}$ to 0.8. In fact, multiple solutions exist, as predicted by the simple model discussed earlier. Figure 5.29 shows that two unique electron temperature profiles can match the exact same target heat flux, thereby demonstrating that the multiple solutions predicted by the simple transport model can appear in real applications. Solution 1's relation to solution 2 is also consistent with the simple model: matching outer gradients, but an inner gradient that is much steeper. It stands to reason that, like in the simple model, $F(r/a = 0.2)$, rolls over at high gradients. This further emphasizes the need for robust root-finding algorithms that will converge to solutions like solution 2, instead of solution 1. Allowing the algorithm to walk away from the nearest root (for instance, by letting Δz_{max} be large or by rotating off the descent direction) could lead to undesirable roots. Also as discussed with the model transport problem, solution 1 is unstable in a time-dependent sense. While the time-independent `TGYRO` formulation was able to find it, a time-dependent transport equilibrium solver would not rest on this solution.

Another interesting feature of Fig. 5.29 is solution 2, which is the closer of the two to the experimental measurement. This solution's matches the experiment actually very well, with the exception being at the edge, $r/a = 0.8$. Here, `TGYRO` predicts that a steep gradient is necessary to match the flux at this point. Since this is also the boundary condition, it's temperature is fixed. Elevating the local gradient here propagates that error throughout the profile, nearly uniformly raising up the interior temperatures, whose gradients otherwise closely match those of the experiment. This suggests that the `TGLF` model, while able to capture the core behavior fairly well, seriously under-predicts the transport at the edge; a steeper-than-experimental gradient implies that `TGLF`
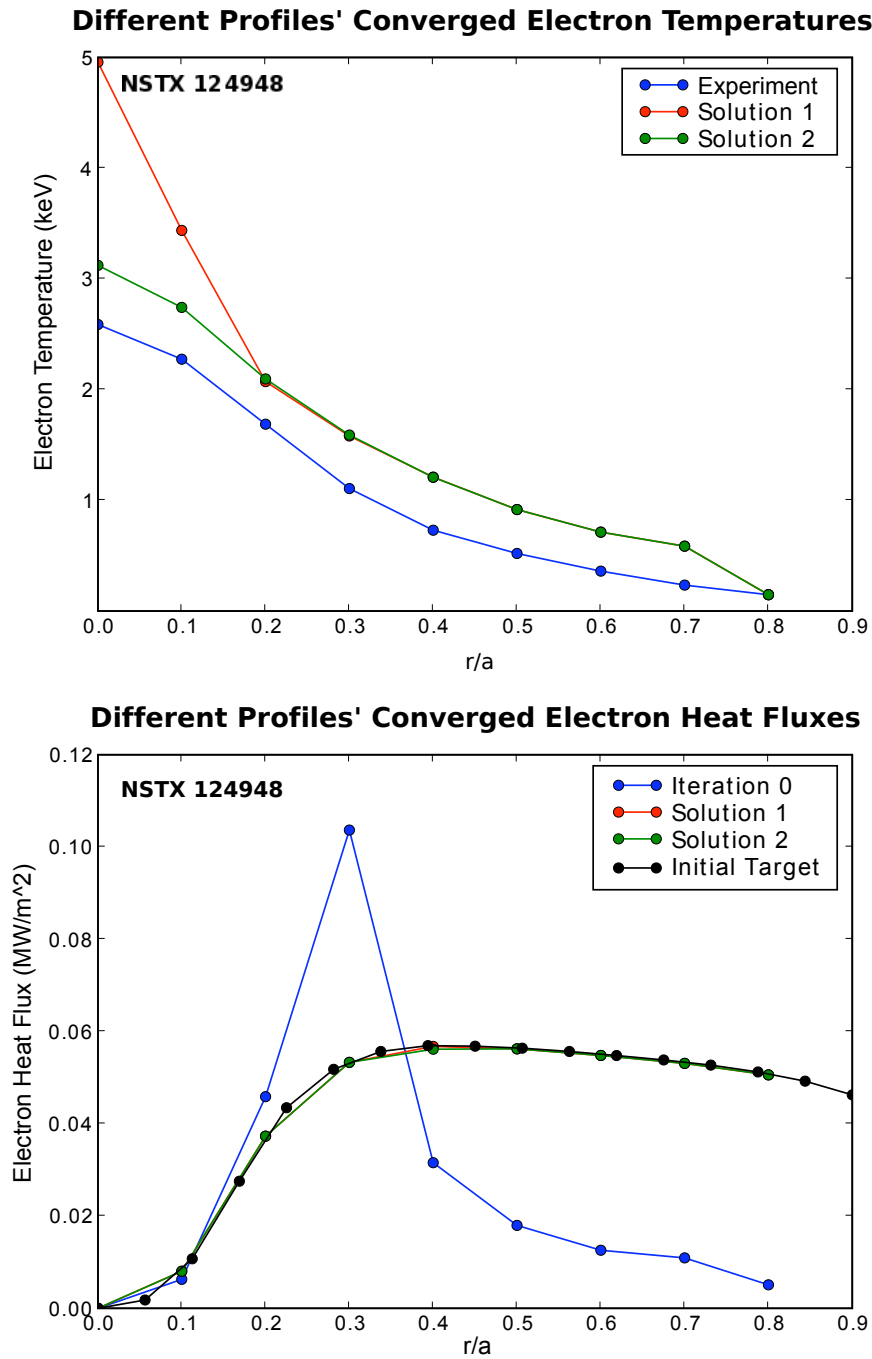
Figure 5.29: Converged electron temperatures (top) and heat fluxes (bottom) for NSTX shot #124948. Two different electron temperature profiles (red and green) iterate on the experimental profile (blue, top) to match the same target electron heat flux (black). For comparison, the non-iterated heat flux is also presented (blue, bottom).

must be driven harder to match the experimental flux. Therefore, it stands to reason that the physics represented by TGLF does not capture the transport properties of the edge plasma. However, the opposite is also true: since the interior gradients match those of the experiment much better, TGLF is a more accurate representation of the plasma here.

The discrepancy between the TGYRO-TGLF and experimental electron temperature profiles in Fig. 5.20 may be due to setting $n_i = n_e$. If the ETG mode is at play, then Z_{eff} should affect the system. Raising Z_{eff} linearly stabilizes the ETG mode. Setting $n_i = n_e$ effectively sets $Z_{eff} = 1$, which is an underestimate for NSTX. A lower Z_{eff} than the experimental value would mean increased ETG activity, so the profile gradients would become limited at a lower value. Translate this to the temperature profile itself, and it's little surprise that TGYRO predicts a steady-state with a lower overall core temperature.

In fact, it has been proposed to use Z_{eff} to control ETG transport. One experiment [126] would attempt to recreate this NSTX shot with different values of Z_{eff}. The idea would be to add neon gas into the deuterium plasma in sufficient concentrations to alter Z_{eff}. One would look for a decrease in high-k fluctuation amplitudes as Z_{eff} increased, the logic being if ETG is driving high-k measurements and if Z_{eff} shuts off the ETG mode, then Z_{eff} should also shut off the high-k signal. No high-k signal: no ETG-driven turbulence.

We can use TGYRO to predict the outcome of this experiment, by adding neon to increase the Z_{eff} of this shot (while enforcing quasi-neutrality by diluting the deuterium) and then evolving T_e until we match the target electron heat flux. Since the predicted effect of Z_{eff} on the ETG mode is thought to be due to linear physics (Z_{eff} alters the linear critical gradient for ETG instability), it may be captured by the quasi-linear-like TGLF model. Fig. 5.30 shows TGYRO-TGLF predictions for three values of Z_{eff}. As we raise Z_{eff} from 2 to 4 to 6, the edge temperature changes very little. However, inside $r/a = 0.5$ the electron temperature rises with Z_{eff}. For $Z_{eff} = 6$, $T_e(r = 0) > 3.5$ keV. This temperature profile starts to look like that of an e-ITB. TGYRO tells us that this experiment may trigger an e-ITB merely by altering Z_{eff}. Yet this result seems logical. Since the
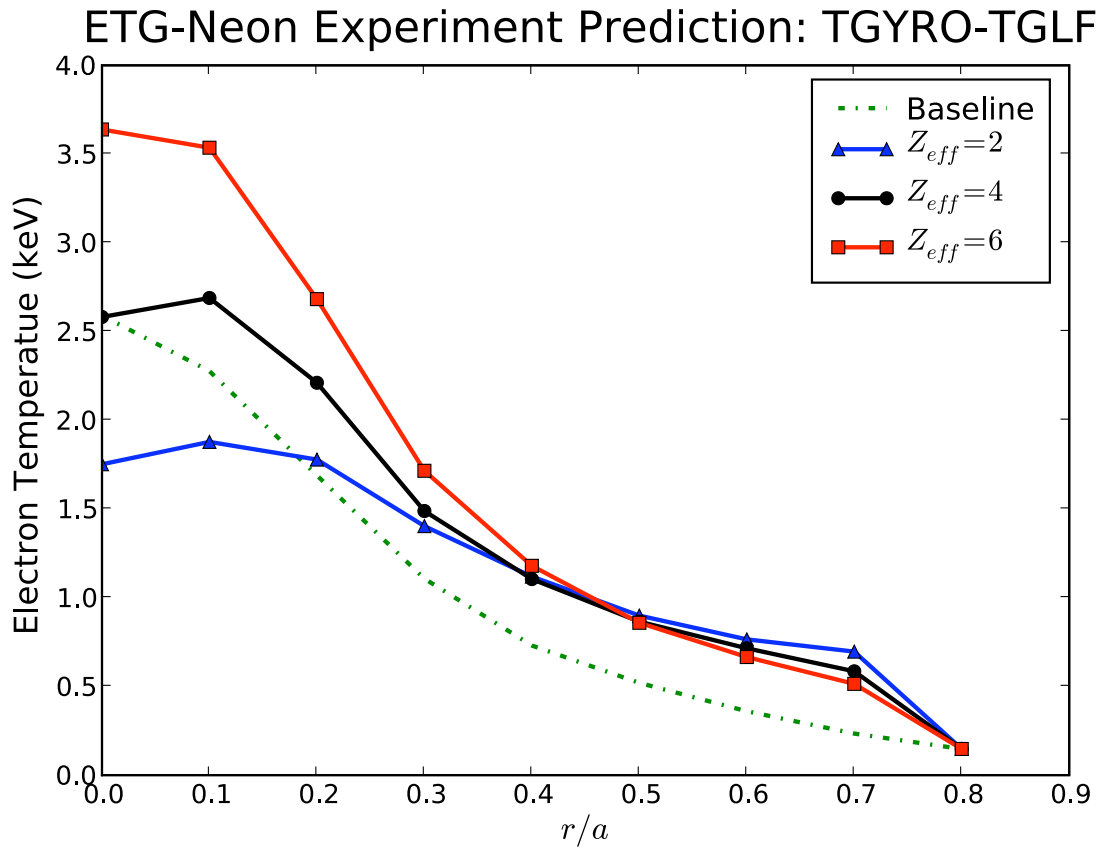
Figure 5.30: `TGYRO-TGLF` predicted electron temperature profiles for proposed ETG-Neon Z_{eff} experiment [126]. The baseline profile is the original experimentally measured value. The different values of Z_{eff} correspond to adding neon in different concentrations, but keeping n_e constant and diluting n_D to enforce quasineutrality.

heating source remains constant (the same RF power), the plasma must work harder to expel that heat.

Put another way, in steady-state, heat in equals heat out; the plasma will heat up until its gradients can drive enough turbulent flux to reach a steady-state, exactly matching the input source heat. Z_{eff} pushes up the critical gradient for ETG transport. As such, Fig. 5.30 supports the idea that the ETG mode is at least in part controlling the performance of these plasmas. In fact, it seems unlikely that these profiles will exhibit reduced high-k activity, if indeed high-k is measuring ETG-driven fluctuations. This is because the ETG mode hasn't been shut off in this experiment. Quite the opposite is true: its likely presence limits the profiles' shapes. e-ITBs triggered with reversed magnetic shear in NSTX still show high-k activity. These Z_{eff}-triggered ones very well could too.

To better pinpoint whether or not the increased electron temperature profiles from Z_{eff} are due to the suppression of the ETG mode, we compare two different TGYRO simulations, with and without TGLF's ETG model in Figure 5.31, evolving only $r/a < 0.6$, to avoid the effects of the poor fit near $r/a = 0.8$ in Fig. 5.30. One of the most interesting features is that *both* simulations show a steepening of the temperature profile with enhanced Z_{eff}. That is to say that this e-ITB-like feature is unlikely to distinguish between ETG- and non-ETG-driven turbulent transport. Z_{eff} suppress both high and low k turbulence in this case.

However, that's not to say that ETG does not play a role. Figure 5.32 shows a scatter plot of local temperature gradients and $\tau = Z_{eff}T_e/T_i$ for the different values of Z_{eff} and for every iteration, with and without the ETG model. The solid lines are the final iterated-to radial profiles, extending from $r/a = 0.6$ at the lowest value of τ (and the largest value of a/L_{T_e}) to $r/a = 0.0$ at the largest values of τ (and defined zero gradient on-axis). In all cases, including the ETG model reduces the final peak driving gradients, as defined by a/L_{T_e}, by approximately $a/L_{T_e} = 1.5 - 2$ (at $r/a = 0.6$). Interestingly enough, increasing Z_{eff} has the effect of reducing the peak a/L_{T_e} at $r/a = 0.6$ in all situations. This suggests that at this location increased Z_{eff} actually drives more transport. Since this occurs with or without the ETG model, it is very likely that another low-k
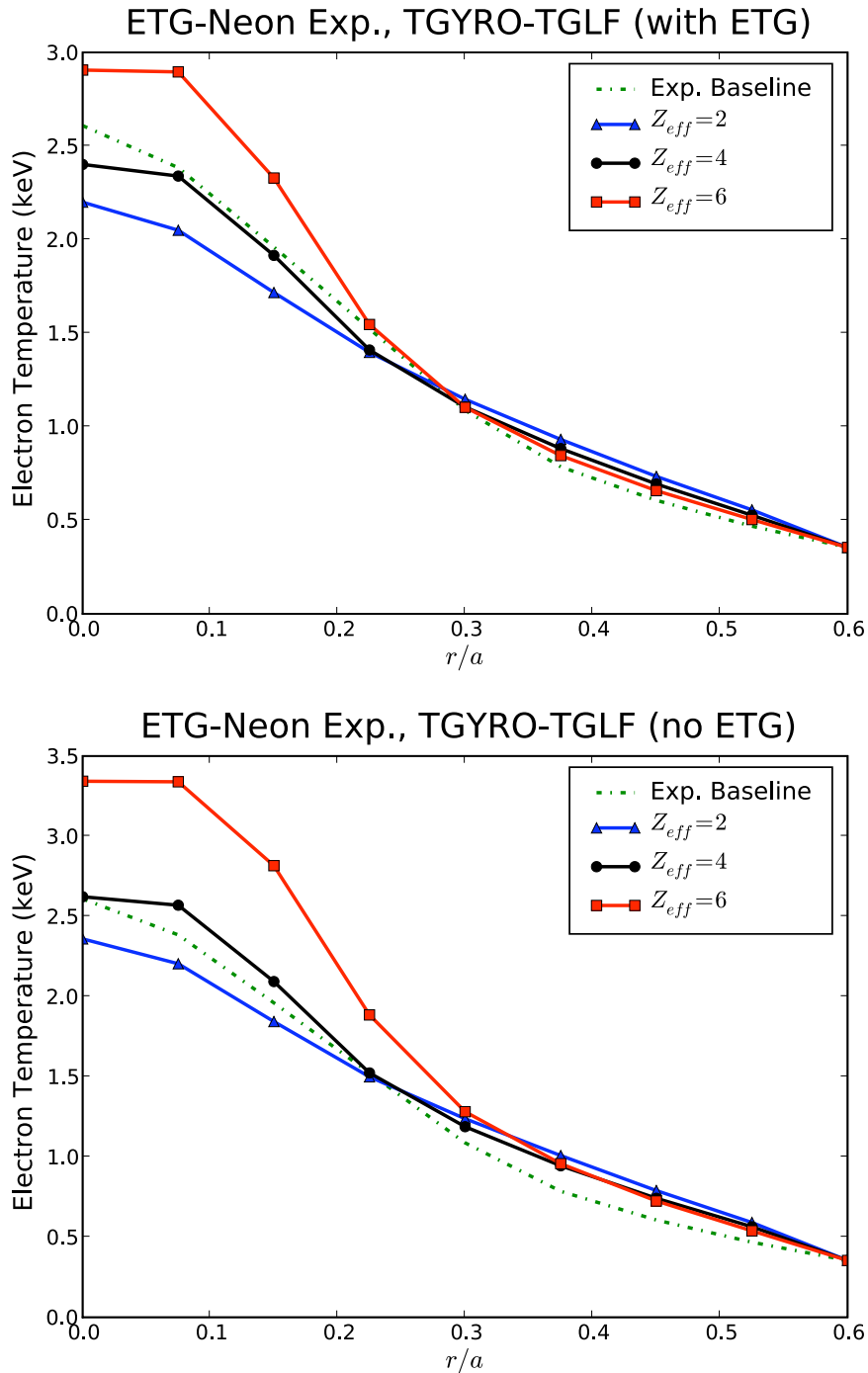
Figure 5.31: `TGYRO-TGLF` predicted electron temperature profiles for the proposed ETG-Neon Z_{eff} experiment (evolving up to $r/a = 0.6$, with and without including the ETG mode.
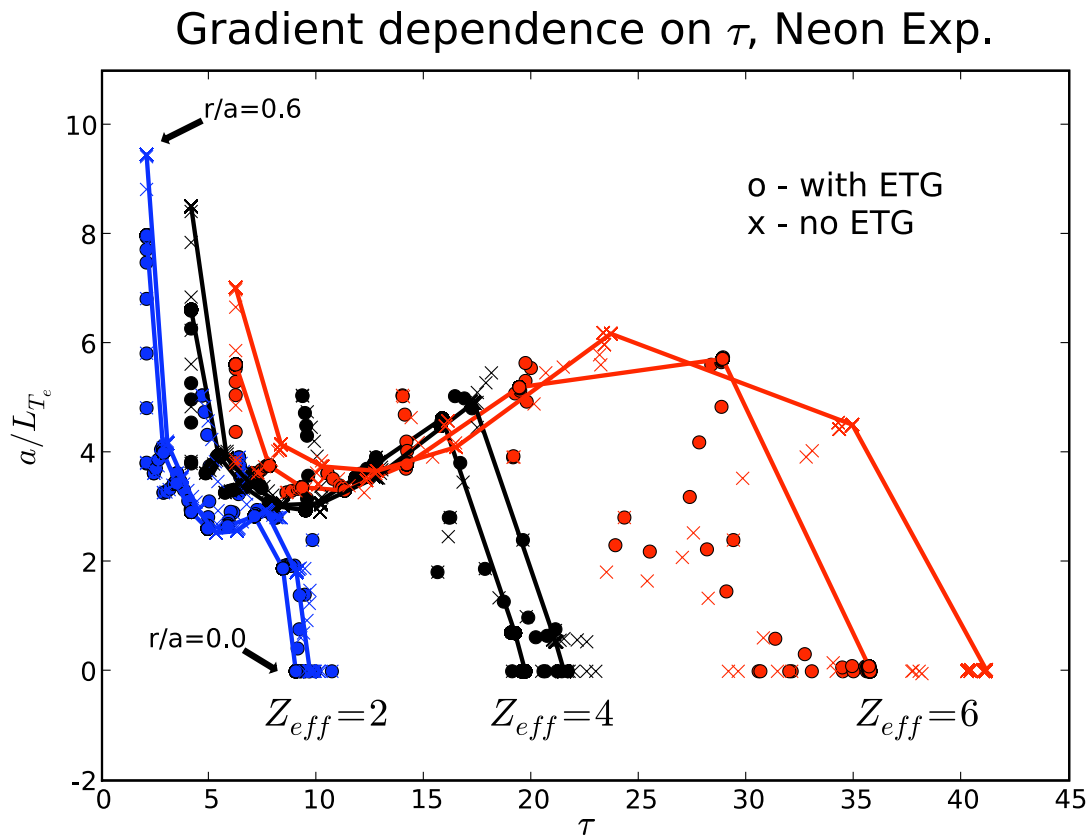
Figure 5.32: `TGYRO-TGLF` predicted electron temperature gradients as a function of $\tau = Z_{eff}T_e/T_i$ for the ETG-neon experiment for every iteration and radius. Solid lines indicate iterated-to profiles and connect consecutive radial locations. In all cases the largest values of a/L_{T_e} are at $r/a = 0.6$ and the largest values of τ are at $r/a = 0$.

mode exists at this radius. Additionally, the highest achievable values of τ (at $r/a = 0$) occur when ETG is not present, for all values of Z_{eff}. For $Z_{eff} = 6$, including ETG in the calculation drops the peak τ from 41 to 36, corresponding to T_e/T_i of 6.8 to 6. However, the local minimum present in each profile (the "dip") always occurs at $r/a = 0.3 - 0.45$, right at the location where ETG is thought to be active. The fact that increasing Z_{eff} increases the gradient at this location, even when not simulating ETG, suggests that Z_{eff} is suppressing something other than ETG in that region.

The picture that emerges is rather complicated. At some radial locations, increasing Z_{eff} lowers the achievable gradient, but at others, it increases it, particularly inside $r/a = 0.3$. The picture is further complicated by the value of the core temperature increase appearing to depend on the problem, since Fig. 5.30 shows the core T_e increasing from 1.75 keV (at $Z_{eff} = 2$) to over 3.5 keV (at $Z_{eff} = 6$) (when simulating $r/a < 0.8$), but Fig. 5.31 shows a more moderate increase if simulating $r/a < 0.6$, from roughly 2.2 to 2.9 keV with ETG and from 2.4 to 3.4 keV without ETG. However, the cumulative effect on the observed plasma profiles in all cases is an increased core temperature. Even though this predicted result is likely large enough to measure, it is unlikely to distinguish between ETG and non-ETG activity.

In conclusion, the `TGYRO-TGLF` model predicts that an experiment designed to suppress ETG activity in NSTX by raising Z_{eff} could trigger an electron internal transport barrier, whose temperature profile is still limited by thermal transport, but at a much higher critical temperature gradient. However, this effect is likely to occur independent of the existence of the ETG mode. But the predicted enhanced performance is attractive nonetheless. Since Z_{eff} is less transient than reversed magnetic shear, this could be a method for creating sustainable e-ITBs in NSTX.

5.5   Summary

To sum up, this chapter demonstrates how turbulence models integrate with plasma transport to govern the steady-state performance of tokamaks.

A simple two-point model of plasma transport shows why solving the steady-state transport problem is likely to be difficult: a combination of expensive function calls, complex residual terrain and multiple solutions. This motivates the development of advanced root-finding algorithms for `TGYRO`, which out-perform the original iterative scheme in three test cases (one from NSTX and two from DIII-D), reaching a lower global residual in fewer calls to `TGLF` while never increasing the global residual.

These tests also provide physical examples of some of the difficulties with steady-state transport equilibrium solvers, namely stiff transport (small differences in profiles corresponding to orders of magnitude differences in fluxes) and the possibility of multiple solutions (since the target flux changes during the course of iteration).

The existence of multiple solutions to the radially discretized steady-state transport problem is confirmed by the NSTX ETG case, in which the same electron heat flux profile could arise from two distinct temperature profiles, whose relationship qualitatively agrees with what the simple transport model expects (matching outer profiles with steeper inner gradients). These solutions also suggest that the `TGLF` model better captures the turbulent properties of the plasma core of the NSTX discharge than those of its plasma edge.

Finally, an application of the new algorithms to a proposed NSTX experiment, designed to suppress ETG-driven high-k fluctuations by introducing impurities into the plasma, predicts the formation of electron internal transport barriers from high values of Z_{eff}. This transport prediction is consistent with the theory that ETG turbulence is at least in part limiting the performance of these discharges, since Z_{eff} strongly affects the critical gradient for linear ETG drive, but the effect is likely to occur independent of the ETG mode's existence. The simulations also suggest not only

a way to control the profile-limiting effects of turbulent transport but also a tantalizing method to create and sustain longer lived e-ITBs than the transient ones triggered by reversed magnetic shear.

Further improvements to TGYRO are certainly possible. One could add time-dependence to the code, as in the TRINITY transport solver [127]. Since multiple steady-state solutions exist, time evolution could ensure the simulated plasma reaches the same steady-state as the experimentally realized plasma, although the time step required to do so may become transiently very small. Time-dependent evolution would also prevent the solver from resting on a physically unstable solution. Additionally, since multiple solutions arise from integrating the gradients to obtain the plasma profiles, one could either transition to having the profiles be the independent variables, or improve upon the integration scheme for T_j, replacing the trapezoidal rule (in which the temperature at radial location j depends upon its local gradient z_j) with one that were finite for $z_j \to \infty$ or independent of z_j. One possibility is a van Leer average:

$$\int_{r_1}^{r_2} z(r) dr = \frac{2z_1 z_2}{z_1 + z_2}. \tag{5.91}$$

This would ameliorate the drastic turn-over in F for large gradients that can lead to multiple (or non-existent) solutions.

A final, but potentially great, improvement could be the adaptation of quasi-Newton methods like those attributed to Broyden [128]. Broyden's method, like Levenberg-Marquardt, uses an approximation of the Hessian matrix to solve a nonlinear system of equations. However, instead of using the Jacobian to do so, it builds up the Hessian entirely from function evaluations from previous iterations. These Jacobian-free methods, if found to be robust enough, could drastically reduce the total number of transport function calls required to solve the transport problem, but the reduced accuracy of the Jacobian approximation may increase the number of iterations necessary for convergence. Since the Jacobian calculation is the single most computationally intensive

part of the transport problem, the Broyden family of algorithms is an attractive avenue of further investigation.

While not the final word, the algorithmic improvements to `TGYRO` developed in this chapter still serve as a significant step in the realization of tractable integrated transport simulations.

Chapter 6

Conclusions: From Computer Turbulence to Component Testing

Humanity's continued thirst for energy is not likely to be quenched without new sources of power. Nearly inexhaustible, environmentally friendly and politically tenable, controlled nuclear fusion would be a game changer on the world energy stage. Yet the technological challenges blocking the path towards commercial viability are numerous. Chief among magnetic fusion energy's obstacles is the problem of plasma confinement. In particular, understanding the interplay between plasma turbulence and transport is crucial to the development of magnetic fusion energy.

Electron turbulent transport is particularly poorly understood. The electrons' transport is large and could come from a variety of sources, which likely compete depending on the specific problem parameters. The question becomes, of those sources, can ETG turbulence account for the high levels of observed electron transport? This dissertation answers: yes, in some NSTX discharges, ETG turbulence can indeed cause experimentally relevant levels of turbulent flux. ETG is not likely to govern the performance of every discharge, as even those meant to drive ETG contain other instabilities. But, ETG is certainly important.

Although strong ETG turbulence can exist in NSTX, and there is some high-k fluctuation measurements appear when the ETG mode is thought to be active, universally interpreting high-k fluctuations as evidence of the ETG mode is nuanced, in particular because the diagnostic's present configuration measures only the tail-end of the spectrum. The analogy is of a riverboat captain who, after a faraway storm, sees his river swell. He cannot say exactly where the rains fell, because many streams feed into his river. The captain only knows that it must have rained somewhere upstream. The high-k measurements see the downstream flood, not the upstream storm. However, the next generation high-k diagnostic, to be installed on the upgraded NSTX-U, will have a different view of the plasma. Instead of observing the tail-end of the ETG spectrum, at large k_r and small k_θ, the new high-k system will zero in on ETG's spectral peak, at small k_r and large k_θ [100]. This new configuration will likely allow for a much more direct observation of ETG driven turbulence.

Because ETG turbulence can be strong, it is important to find ways of controlling it. One key method is through magnetic shear. Reversing the magnetic shear can prevent ETG turbulence from driving significant transport, thereby allowing plasmas to sustain gradients that would be otherwise unreachable. Reversed magnetic shear is so good at suppressing ETG transport that it can trigger high-confinement regimes in NSTX known as electron internal transport barriers (e-ITBs). The location of the barrier depends not on the minimum value of the safety factor q, but rather on the minimum of the magnetic shear $\hat{s}$. Within the barrier, where $\hat{s}$ is strongly negative, ETG is nonlinearly quenched, despite being linearly unstable. ETG turbulence that causes large amounts of thermal transport outside of the barrier cannot propagate inward past the e-ITB. Reversed magnetic shear is an extremely effective way of controlling electron turbulent transport.

Connecting gyrokinetic turbulence to machine performance is a complex problem. Transport's difficulty lies not only in the vast gulf in scales between turbulent fluctuations and profile evolution, but also in the nature of the beast itself. In particular, multiple roots can exist for the steady-state transport problem either because of physical bifurcation mechanisms or because of discretization effects. Efficiently and robustly finding the correct root is challenging. Advanced nonlinear root

finding algorithms, such as those developed herein, help, but much of the problem has to do with the problem formulation, in particular the discretization of plasma profiles defined by their local gradients. By using logarithmic derivatives as independent variables, integration errors get compounded by exponentiation. These errors can manifest themselves as multiple (or non-existent) solutions. Finding an equilibrium transport solution becomes either challenging, or impossible. In some situations, a correct equilibrium solution could perhaps be found by using a finite time step, but even this may fail to find an equilibrium, if a transport model is missing some mechanisms.

Despite its challenges, connecting turbulence to transport is an important step in the development of nuclear fusion as a commercial energy source.

6.1 Key Points

This dissertation touches on several topics regarding gyrokinetic turbulence and transport in NSTX. However, a number of key points stick out.

1. ETG turbulence can drive significant thermal transport in NSTX.

   Electron-temperature-gradient-driven turbulence can drive significant amounts of heat flux in NSTX. This flux is at levels much higher than simple ITG-ETG isomorphic estimates, consistent with other simulations of ETG turbulence, and consistent with levels measured within the experiment. ETG exists in some NSTX plasmas. It can be there and it can be strong. But comparing levels of fluxes between simulation and experiment is nuanced, because of the large uncertainties and sensitivities in both calculations.

2. High-k density measurements do not always imply ETG activity.

   Even though the ETG mode can appear in NSTX, it lives in an overcrowded zoo of instability, and is most likely not the sole arbiter of electron heat flux in NSTX. Pinning down the existence of ETG turbulence is further complicated because fluctuation readings on the

present configuration of the high-k scattering system do not always imply ETG mode activity. Because the high-k system measures the tail of the ETG-driven turbulent spectrum, interpreting fluctuations as caused by the ETG mode is nuanced. However, forthcoming upgrades to the diagnostic, which will move its sensitivity to the peak of the ETG spectrum, will strengthen the connection between high-k fluctuations and ETG activity. As it stands, if the high-k systems measures fluctuations, they are not necessarily unique signatures of the ETG mode. The flip side is that if the high-k system doesn't measure any fluctuations, the ETG mode could still be active.

3. Reversed magnetic shear triggers electron internal transport barriers.

The single greatest control for triggering electron internal transport barriers is reversed magnetic shear. Reversing magnetic shear strongly enhances the nonlinear critical gradient for the onset of ETG turbulent transport. This effect can allow plasmas to sustain very large electron temperature gradients within an electron internal transport barrier. The location of the barrier depends on the magnitude of the magnetic shear, not on the safety factor: e-ITBs formation depends on $\hat{s}_{\min}$, not $q_{\min}$. Presently, reversed magnetic shear is a transient plasma state. These results support the importance of finding ways of sustaining reversed magnetic shear.

4. Multiple roots exist for the steady-state transport problem.

The problem of steady-state transport is complicated by the potential existence of multiple solutions. In other words, a single heat flux profile can be explained by multiple plasma profiles. This is both interesting from a mathematical point of view and tantalizing from a practical point of view. Such a bifurcation in transport solutions could have applications for maximizing fusion gain, say by coaxing a plasma into a higher temperature state with the same amount of external heating. However, their existence complicates the transport problem. While some of these bifurcations may be real, such as the L-H split, many could be

purely numerical, artifacts of the problem discretization. Distinguishing between the two, and finding the "real" ones while avoiding the others, is algorithmically difficult. Problem formulation becomes extremely important. As is done in the `TRINITY` code [127], adding time-dependence and using profiles (instead of their gradients) as the independent variables may help, especially when combined with advanced root-finding algorithms, like those developed herein.

5. Some electron temperature profiles in NSTX can be explained by turbulent transport.

   Steady-state transport solutions exist for NSTX, with external heat sources balanced by turbulent heat losses. While this may not be the only rule governing the performance of NSTX plasmas, it lends credit to the theory of turbulence-dominated profiles. Reducing ETG turbulence, for instance with Z_{eff} or negative $\hat{s}$, could allow the plasma to achieve impressive temperature profiles.

6.2   Future Work

A clear path for this research lies in applications beyond NSTX. With the importance of electron transport confirmed for NSTX, it is only natural to wonder how electron transport could affect the performance of advanced spherical tori.

6.2.1   Simulate Coupled Ion-Electron Turbulence

Turbulent transport is an inherently nonlinear process. Linearly unstable modes can drive other sub-dominant modes, with drastic effects on the saturated turbulent state. This process is not limited to electron-scale turbulence. This work focused solely on electron-scales. How NSTX plasmas fare when electron and ion turbulence interacts remains an open question.

The successful simulation of coupled ion and electron turbulence will required advances in numerical techniques for the study of plasma turbulence. One of the major challenges is that ions and electrons presently exist in `GYRO` on the same spatial grid, so the resolution for ions is effectively much higher than for electrons (a grid spacing of ρ_e is $\rho_{sD}/60$). This extra resolution is unnecessary. Possible advances include new gyroaveraging techniques that work as efficiently for ions as electrons, different grids for different species and new levels of parallelization, which can take advantage of shared memory systems and GPU acceleration.

6.2.2   Update Reduced Models for NSTX Operating Space

The power of reduced models in solving the turbulent transport problem is clear: a full-blown turbulence simulation that takes tens of thousands of CPU-hours could be closely approximated in seconds with an appropriate reduced model. Gyrokinetic simulations of STs, such as those presented herein, should be used to re-calibrate models like `TGLF` to better capture turbulent electron behavior in spherical tori. This will greatly improve the tractability of whole-device simulation, especially if models of turbulent transport are to be integrated with other physics packages.

Currently, `TGLF` cannot capture the behavior of reversed shear e-ITBs. But, with a re-calibration based on ETG parameter scans in $\hat{s}$, Z_{eff} and q, it may be possible to use `TGLF` with `TGYRO` to predict e-ITB formation. One potential way to accomplish this would be to extend the saturation model used in `TGLF` to include the interaction with the secondary instabilities discussed in Chapter 2. This may better capture the importance of magnetic shear in ETG saturation.

At present, widespread use of `GYRO` as `TGYRO`'s turbulence engine remains challenging, especially since each turbulence calculation can take several tens of thousands of CPU hours. Even if parallelized, a single transport calculation could only be possible on leadership-class computing clusters, and only at a great cost. But by modeling turbulent transport with `TGLF` instead of `GYRO`, transport simulations could be run much more quickly on smaller computing clusters, thereby al-

lowing for a wider variety of experimental comparisons and parameter scans. Upgrading `TGLF` to better model nonlinear ETG turbulence would make transport simulations much more practical and accurate.

6.2.3 Predict Transport in ARIES-ST, ST CTF

The ST, while a relative newcomer to the MFE stage, has been considered as a candidate for future fusion devices. These ideas range from a component test facility (ST CTF [129]), where equipment could be tested in reactor-like conditions, to a full-blown power plant (such as ARIES-ST [130]). Applying improved models for electron turbulence and advanced transport algorithms to next-generation machines could help create a predictive model of advanced ST performance. The insights gained from transport studies on NSTX should serve as a stepping stone to future devices.

Gyrokinetic electron turbulence can transport enough heat to limit the performance of NSTX plasmas. Yet, understanding that turbulence and ways to mitigate its effects on transport has implications beyond the present machine. Magnetic shear's ability to control electron turbulent transport is an extremely powerful tool, whose application should not be limited to NSTX. Advanced tokamaks and stellarators could potentially use the same mechanism to enhance electron plasma confinement. With ITER poised to bring magnetic fusion research into the realm of net energy gain, and eyes turning to the next generation of machines, no piece of the transport puzzle is too small to solve. The world needs new energy sources now. It needed them yesterday. Turbulent transport in magnetically confined plasmas is one of the major obstacles standing in the way of controlled nuclear fusion. Although far from a solution to the confinement problem, the knowledge gained in this dissertation, on electron turbulence and how to control it and plasma transport and how to model it, is an important step in the quest for fusion energy.

Bibliography

[1] *Magnitude 9.0 - Near the East Coast of Honshu, Japan*, U. S. Geological Survey: March 11, 2011, Accessed Online: April 20, 2011, URL `http://earthquake.usgs.gov/earthquakes/eqinthenews/2011/usc0001xgp/`.

[2] *38-meter-high tsunami triggered by March 11 quake: survey*, Kyodo News: April 3, 2011, Accessed Online: April 20, 2011, URL `http://english.kyodonews.jp/news/2011/04/82888.html`.

[3] *Damage Situation and Police Countermeasures associated with 2011 Tohoku district - off the Pacific Ocean Easrthquake*, Japanese National Police Agency, Accessed Online: April 20, 2011, URL `http://www.npa.go.jp/archive/keibi/biki/higaijokyo_e.pdf`.

[4] The World Bank, East Asia and Pacific Economic Update **1** (2011), Accessed Online: April 20, 2011, URL `http://siteresources.worldbank.org/INTEAPHALFYEARLYUPDATE/Resources/550192-1300567391916/EAP_Update_March2011_japan.pdf?cid=EXTEAPMonth1`.

[5] *In Focus: Fukushima Nuclear Accident*, International Atomic Energy Agency, Accessed Online: April 20, 2011, URL `http://www.iaea.org/newscenter/focus/fukushima/index.html`.

[6] A. Nandakumar, *Hitachi submits plan to decommission Fukushima reactors*, Reuters: April 13, 2011, Accessed Online: April 20, 2011, URL `http://www.reuters.com/article/2011/04/12/hitachi-idUSL3E7FC2UE20110412`.

[7] E. Kirschbaum, *RPT-Germany's Greens come of age after Japan disaster*, Reuters: March 28, 2011, Accessed Online: May 3, 2011, URL `http://www.reuters.com/article/2011/03/28/germany-election-greens-idUSLDE72Q0KS20110328`.

[8] J. O'Halloran, *Fears rise in India of Fukushima-style nuclear disaster*, BBC News: April 27, 2011, Accessed Online: May 3, 2011, URL `http://www.bbc.co.uk/news/business-13205060`.

[9] J. Rockoff, *Potassium Iodide Runs Low as Americans Seek It Out*, The Wall Street Journal: March 15, 2011, Accessed Online: May 3, 2011, URL `http://online.wsj.com/article/SB10001424052748703363904576201013720213564.html`.

[10] B. Knight, *Merkel shuts down seven nuclear reactors*, Deutsche Welle: March 3, 2011, Accessed Online: March 15, 2011, URL `http://www.dw-world.de/dw/article/0,,14912184,00.html`.

[11] A. Breidthardt, *German government wants nuclear exit by 2022 at latest*, Reuters: May 31, 2011, Accessed Online: June 20, 2011, URL `http://www.reuters.com/article/2011/05/31/us-germany-nuclear-idUSTRE74Q2P120110531`.

[12] B. Montopoli, *Poll: Support for new nuclear plants drops*, CBS News: March 22, 2011, Accessed Online: March 22, 2011, URL `http://www.cbsnews.com/8301-503544_162-20046020-503544.html`.

[13] M. Wald, *Nuclear 'Renaissance' Is Short on Largess*, The New York Times: December 7, 2010, Accessed Online: May 3, 2011, URL `http://green.blogs.nytimes.com/2010/12/07/nuclear-renaissance-is-short-on-largess/`.

[14] M. Rapp and N. Lundeen, *German Nuclear Shift Hits E.ON*, The Wall Street Journal: May 3, 2011, Accessed Online: May 3, 2011, URL `http://online.wsj.com/article/SB10001424052748703922804576300671980875818.html`.

[15] S. Evans, *German nuclear review throws up new problems*, BBC News: May 2, 2011, Accessed Online: May 2, 2011, URL `http://www.bbc.co.uk/news/world-europe-13257804`.

[16] U.S. Energy Information Administration, Tech. Rep. DOE/EIA-0484(2010), U.S. Department of Energy (2010), Accessed Online: April 20, 2011, URL `http://www.eia.doe.gov/oiaf/ieo/index.html`.

[17] *World Development Indicators 2011*, The World Bank: March 22, 2011, Accessed Online: April 20, 2011, URL `http://data.worldbank.org/data-catalog/world-development-indicators`.

[18] Keepscases, *Aztec Calendar*, Creative Commons: October 21, 2009, accessed Online: May 18, 2011, URL `http://commons.wikimedia.org/wiki/File:Aztec_calendar.svg`.

[19] J. Lawson, Proceedings of the Physical Society B **70**, 6 (1957).

[20] J. Huba, Tech. Rep., Naval Research Laboratory (U.S.) (2009).

[21] H. Craig, Science **133**, 1702 (1961).

[22] B. Jaskula, Tech. Rep., U.S. Geological Survey (2011).

[23] K. Schwochau, in *Inorganic Chemistry* (Springer Berlin / Heidelberg, 1984), vol. 124 of *Topics in Current Chemistry*, pp. 91–133.

[24] R. C. Maninger and D. W. Dorn, IEEE Transactions on Nuclear Science **NS-30**, 571 (1983).

[25] R. J. Goldston, A. Glaser, and A. F. Ross, 9th IAEA Technical Meeting on Fusion Power Plant Safety (2009).

[26] J. Lindl, Physics of Plasmas **2**, 3933 (1995).

[27] J. Lindl, P. Amendt, R. Berger, S. Glendinning, S. Glenzer, S. Haan, R. Kauffman, O. Landen, and L. Suter, Physics of Plasmas **11**, 339 (2004).

[28] R. Rhodes, *Dark Sun: The Making of the Hydrogen Bomb* (Simon and Schuster, New York, 1996), 1st ed.

[29] E. C. Tanner, *Project Matterhon: An Informal History*, DE-AC02-76-CHO-3073 (Princeton University Plasma Physics Laboratory, Princeton, New Jersey, 1982).

[30] *Peaceful Uses of Atomic Energy*, vol. 1, Second International Conference on the Peaceful Uses of Atomic Energy (United Nations, Geneva, 1958).

[31] E. C. Tanner, *The First Princeton Tokamaks: An Informal History 1970-1980* (Princeton University Plasma Physics Laboratory, Princeton, New Jersey, 1982).

[32] N. J. Peacock, D. C. Robinson, M. J. Forrest, P. D. Wilcock, and V. V. Sannikov, Nature **224**, 488 (1969).

[33] J. Strachan et al., Physical Review Letters **72**, 3526 (1994).

[34] Fusion Power Associates, *US Fusion Budgets for MFE and ICF*, Accessed Online: June 3, 2011, URL `http://aries.ucsd.edu/FPA/OFESbudget.shtml`.

[35] Fusenet, *Fusion Research Today*, Accessed Online: June 3, 2011, URL `http://www.fusenet.eu/node/42`.

[36] Congressional Budget Office, Tech. Rep., The Congress of the United States (2004).

[37] ITER Organization, *ITER - the way to new energy*, Accessed Online: June 20, 2011, URL `http://www.iter.org/`.

[38] H. Y. Yuh, F. M. Levinton, R. E. Bell, J. C. Hosea, S. M. Kaye, B. P. LeBlanc, E. Mazzucato, J. L. Peterson, D. R. Smith, J. Candy, et al., Physics of Plasmas **16**, 056120 (2009).

[39] H. Y. Yuh, S. M. Kaye, F. M. Levinton, E. Mazzucato, D. R. Mikkelsen, D. R. Smith, R. E. Bell, J. C. Hosea, B. P. LeBlanc, J. L. Peterson, et al., Physical Review Letters **106**, 055003 (2011).

[40] J. Candy and E. A. Belli, General Atomics Report GA-A26818, General Atomics (2010).

[41] J. M. Greene and J. L. Johnson, Physics of Fluids **5**, 510 (1962).

[42] R. L. Miller, M. S. Chu, J. M. Greene, Y. R. Lin-Liu, and R. E. Waltz, Physics of Plasmas **5**, 973 (1998).

[43] A. Einstein, Annalen der Physik **322**, 132 (1905).

[44] A. Einstein, Annalen der Physik **322**, 891 (1905).

[45] A. Einstein, Annalen der Physik **323**, 639 (1905).

[46] A. Einstein, Annalen der Physik **322**, 549 (1905).

[47] R. J. Goldston and P. H. Rutherford, *Introduction to Plasma Physics* (Institute of Physics Publishing, Bristol and Philadelphia, 1995).

[48] A. J. Wootton, B. A. Carreras, H. Matsumoto, K. McGuire, W. A. Peebles, C. P. Ritz, P. W. Terry, and S. J. Zweben, Physics of Fluids B **2**, 2879 (1990).

[49] J. Krommes (2008), Conceptual Foundations of Plasma Kinetic Theory, Turbulence, and Transport.

[50] H. C. Spruit, Solar Physics **55**, 3 (1977).

[51] H. Sugama and W. Horton, Physics of Plasmas **5**, 2560 (1998).

[52] E. A. Frieman and L. Chen, Physics of Fluids **25**, 502 (1982).

[53] W. Lee, Physics of Fluids **26**, 556 (1983).

[54] H. Sugama and W. Horton, Physics of Plasmas **4**, 405 (1997).

[55] A. J. Brizard and T. S. Hahm, Reviews of Modern Physics **79**, 421 (2007).

[56] D. H. E. Dubin, J. A. Krommes, and W. Lee, Physics of Fluids **26**, 3524 (1983).

[57] H. Sugama, Physics of Plasmas **7**, 466 (2000).

[58] H. Qin, W. M. Tang, and W. Lee, Physics of Plasmas **7** (2000).

[59] J. A. Krommes, Annual Review of Fluid Mechanics **44**, 175 (2012).

[60] J. Candy and R. E. Waltz, Journal of Computational Physics **186**, 545 (2003).

[61] S. Cowley, R. M. Kulsrud, and R. Sudan, Physics of Fluids B **3**, 2767 (1991).

[62] M. A. Beer, S. C. Cowley, and G. W. Hammett, Physics of Plasmas **2**, 2687 (1995).

[63] J. Candy, R. E. Waltz, and W. Dorland, Physics of Plasmas **11**, L25 (2004).

[64] L. I. Rudakov and R. Z. Sagdeev, Soviet Physics Doklady **6**, 415 (1961).

[65] B. Coppi, Physics Letters **14**, 172 (1965).

[66] B. Coppi, M. N. Rosenbluth, and R. Z. Sagdeev, Physics of Fluids **10**, 582 (1967).

[67] M. N. Rosenbluth and F. L. Hinton, Physical Review Letters **80**, 724 (1998).

[68] B. N. Rogers, W. Dorland, and M. Kotschenreuther, Physical Review Letters **85**, 5336 (2000).

[69] G. W. Hammett, M. A. Beer, W. Dorland, S. C. Cowley, and S. A. Smith, Plasma Physics and Controlled Fusion **35**, 973 (1993).

[70] W. Dorland and G. W. Hammett, Physics of Fluids B **5**, 812 (1993).

[71] R. E. Waltz, G. R. Kerbel, and J. Milovich, Physics of Plasmas **1**, 2229 (1994).

[72] R. E. Waltz, G. R. Kerbel, J. Milovich, and G. W. Hammett, Physics of Plasmas **2**, 2408 (1995).

[73] M. A. Beer and G. W. Hammett, Physics of Plasmas **3**, 4046 (1996).

[74] A. M. Dimits, T. J. Williams, J. A. Byers, and B. I. Cohen, Physical Review Letters **77**, 71 (1996).

[75] A. Dimits, B. I. Cohen, N. Mattor, et al., in *Proceedings of the 17th IAEA Fusion Energy Conference* (1998).

[76] A. M. Dimits, G. Bateman, M. A. Beer, B. I. Cohen, W. Dorland, G. W. Hammett, C. Kim, J. E. Kinsey, M. Kotschenreuther, A. H. Kritz, et al., Physics of Plasmas **7**, 969 (2000).

[77] E. A. Belli, G. W. Hammett, and W. Dorland, Physics of Plasmas **15**, 092303 (2008).

[78] D. R. Mikkelsen and W. Dorland, Physical Review Letters **101**, 135003 (2008).

[79] A. G. Peeters, C. Angioni, and D. Strintzi, Physical Review Letters **98**, 265003 (2007).

[80] T. S. Hahm, P. H. Diamond, O. D. Gurcan, and G. Rewoldt, Physics of Plasmas **14**, 072303 (2007).

[81] R. E. Waltz, G. M. Staebler, J. Candy, and F. L. Hinton, Physics of Plasmas **14**, 122507 (2007).

[82] F. Parra, M. Barnes, and A. G. Peeters, Physics of Plasmas **18**, 062501 (2011).

[83] W. Dorland, F. Jenko, M. Kotschenreuther, and B. N. Rogers, Physical Review Letters **85**, 5579 (2000).

[84] F. Jenko, W. Dorland, M. Kotschenreuther, and B. N. Rogers, Physics of Plasmas **7**, 1904 (2000).

[85] F. Jenko and W. Dorland, Physical Review Letters **89**, 225001 (2002).

[86] F. Jenko, W. Dorland, and G. W. Hammett, Physics of Plasmas **8**, 4096 (2001).

[87] I. H. Hutchinson, *Principles of Plasma Diagnostics* (Cambridge University Press, 2002), 2nd ed.

[88] J. Candy, R. E. Waltz, M. R. Fahey, and C. Holland, Plasma Physics and Controlled Fusion **49**, 1209 (2007).

[89] W. M. Nevins, J. Candy, S. Cowley, T. Dannert, A. Dimits, W. Dorland, C. Estrada-Mila, G. W. Hammett, F. Jenko, M. J. Pueschel, et al., Physics of Plasmas **13**, 122306 (2006).

[90] C. M. Roach, I. G. Abel, R. J. Akers, W. Arter, et al., Plasma Physics and Controlled Fusion **51**, 124020 (2009).

[91] J. Candy, R. E. Waltz, M. R. Fahey, and C. Holland, Journal of Physics: Conference Series **78**, 012008 (2007).

[92] T. Görler and F. Jenko, Physical Review Letters **100**, 185002 (2008).

[93] M. Ono, S. Kaye, Y. Peng, G. Barnes, W. Blanchard, M. Carter, J. Chrzanowski, L. Dudek, R. Ewig, D. Gates, et al., Nuclear Fusion **40**, 557 (2000).

[94] J. B. Kallman, Ph.D. thesis, Princeton Universtiy (2011).

[95] S. M. Kaye, R. E. Bell, D. Gates, B. P. LeBlanc, F. M. Levinton, J. E. Menard, D. Mueller, G. Rewoldt, S. A. Sabbagh, W. Wang, et al., Physical Review Letters **98**, 175002 (2007).

[96] S. Kaye, F. Levinton, D. Stutman, K. Tritz, H. Yuh, M. Bell, R. Bell, C. Domier, D. Gates, W. Horton, et al., Nuclear Fusion **47**, 499 (2007).

[97] ITER Physics Basis Editors et al., Nuclear Fusion **39**, 2137 (1999).

[98] D. R. Smith, E. Mazzucato, W. Lee, H. K. Park, C. W. Domier, and J. Luhmann, Review of Scientific Instruments **79**, 123501 (2008).

[99] E. Mazzucato, Physics of Plasmas **10**, 753 (2003).

[100] Y. Ren, (private communication, 2011).

[101] E. Mazzucato, D. R. Smith, R. E. Bell, S. M. Kaye, J. C. Hosea, B. P. LeBlanc, J. R. Wilson, P. M. Ryan, C. W. Domier, J. Luhmann, et al., Physical Review Letters **101**, 075001 (2008).

[102] E. Mazzucato, R. Bell, S. Ethier, J. Hosea, S. Kaye, B. LeBlanc, W. Lee, P. Ryan, D. Smith, W. Wang, et al., Nuclear Fusion **49**, 055001 (2009).

[103] D. R. Smith, S. M. Kaye, W. Lee, E. Mazzucato, H. K. Park, R. E. Bell, C. W. Domier, B. P. LeBlanc, F. M. Levinton, N. C. Luhmann, et al., Physical Review Letters **102**, 225005 (2009).

[104] D. R. Smith, S. M. Kaye, W. Lee, E. Mazzucato, H. K. Park, R. E. Bell, C. W. Domier, N. C. L. Jr., J. E. Menard, and H. Y. Yuh, Physics of Plasmas **16**, 112507 (2009).

[105] G. M. Staebler, J. E. Kinsey, and R. E. Waltz, Physics of Plasmas **14**, 055909 (2007).

[106] G. M. Staebler and J. E. Kinsey, Physics of Plasmas **17**, 122309 (2010).

[107] E. A. Belli and J. Candy, Plasma Physics and Controlled Fusion **50**, 095010 (2008).

[108] E. A. Belli and J. Candy, Physics of Plasmas **17**, 112314 (2010).

[109] W. Guttenfelder, J. Candy, S. M. Kaye, W. M. Nevins, E. Wang, R. E. Bell, G. W. Hammett, B. P. LeBlanc, D. R. Mikkelsen, and H. Yuh, Physical Review Letters **106**, 155004 (2011).

[110] D. R. Smith, W. Guttenfelder, B. P. LeBlanc, and D. R. Mikkelsen, Plasma Physics and Controlled Fusion **53**, 035013 (2011).

[111] F. M. Poli, S. Ethier, W. Wang, T. S. Hahm, E. Mazzucato, and D. R. Smith, Physics of Plasmas **17**, 112514 (2010).

[112] F. Jenko and D. Told, (private communication, 2011).

[113] J. Candy, (private communication, 2011).

[114] T. M. Antonsen, J. F. Drake, P. N. Guzdar, A. B. Hassam, Y. T. Lau, C. S. Liu, and S. V. Novakovskii, Physics of Plasmas **3**, 2221 (1996).

[115] W. Guttenfelder and J. Candy, Physics of Plasmas **18**, 022506 (2011).

[116] R. E. Bell and H. Y. Yuh, (private communication, 2011).

[117] B. P. LeBlanc, (private communication, 2010).

[118] S. Kaye, (private communication, 2009).

[119] J. R. Taylor, *An Introduction to Error Analysis* (University Science Books, 1997), 2nd ed.

[120] J. Candy, C. Holland, R. E. Waltz, M. R. Fahey, and E. Belli, Physics of Plasmas **16**, 060704 (2009).

[121] R. E. Waltz and G. M. Staebler, Physics of Plasmas **15**, 014505 (2008).

[122] K. Levenberg, The Quarterly of Applied Mathmatics **2**, 164 (1944).

[123] D. Marquardt, SIAM Journal on Applied Mathematics **11**, 431 (1963).

[124] W. Press, S. A. Teukolsky, W. T. Vetterling, and B. P. Flannery, *Numerical Recipes in C: The Art of Scientific Computing* (Cambridge University Press, 1992), 2nd ed.

[125] L. Armijo, Pacific Journal of Mathematics **16**, 1 (1966).

[126] E. Mazzucato, NSTX Research Forum (2011).

[127] M. Barnes, I. G. Abel, W. Dorland, T. Görler, G. W. Hammett, and F. Jenko, Physics of Plasmas **17**, 056109 (2010).

[128] C. G. Broyden, Mathematics of Computation **19**, 577 (1965).

[129] Y. Peng et al., Plasma Physics and Controlled Fusion **47**, B263 (2005).

[130] F. Najmabadi et al., Journal of Fusion Energy and Design **65**, 141 (2003).